Title

High-Order Sideband Generation for Creating Optical Frequency Combs and Probing Bloch Wavefunctions

Author

Valovcin, Darren

Publication Date

2019

UNIVERSITY of CALIFORNIA
Santa Barbara

High-Order Sideband Generation for Creating Optical Frequency Combs and Probing Bloch Wavefunctions

A dissertation submitted in partial satisfaction of the
requirements for the degree of

Doctor of Philosophy

in

Physics

by

Darren Charles Valovcin

Committee in charge:

Professor Mark S. Sherwin, Chair
Professor David M. Weld
Professor Chetan Nayak

March 2019

The dissertation of Darren Charles Valovcin is approved:

Professor David M. Weld

Professor Chetan Nayak

Professor Mark S. Sherwin, Chair

February 2019

High-Order Sideband Generation for Creating Optical Frequency Combs and Probing Bloch Wavefunctions

Acknowledgements

Achieving a PhD in physics (or in any field) is never done in a vacuum. It requires the help and assistance of many people without without whom, none of this work would have been possible. I would first like to thank my advisor Mark Sherwin for giving me the opportunity to work in his lab and guiding me through the process of becoming a scientist. His knowledge and advice was invaluable during the countless walls and confusions I hit during my work, and his motivation, drive, and 'big-picture' kept us focused and able to discover some great physics. I truly appreciate his patience and understanding during my time here, and have greatly enjoyed the past five years in this group.

I would also like to thank the rest of the members of the Sherwin Group. Hunter Banks not only helped teach me how to ask questions to drive our research, but also how to intelligently tune optics instead of twisting random knobs. I'm also grateful for all of the Chick-fil-A dinners during the long nights taking data. Thank you to Jessica Clayton and Blake Wilson for countless sanity checks when tuning the FEL and always providing a sounding board for understanding the inevitable confusions which pop up in lab. I would also like to thank Chang, Marzieh, Joe, Seamus and Cocoa.

The Institute for THz Science and Technology, and especially my thesis, would be nothing without the FELs. I would like to thank Dave Enyeart for teaching me how to wrangle the beast and get it working for me and not against me (most of the time). His willingness to go above and beyond to help solve problems was invaluable. I would like to thank Nick Agaldze for taking up Dave's mantle after he 'retired' to make sure the FELs stayed operational. Thank you also to Gerry Ramien and the countless others who worked on and developed the FEL over the years.

The theoretical understanding of large parts of this thesis were far beyond what I would have been able to do, so I must express my greatest gratitudes for Qile Wu and the time he spent not only uncovering some of the secrets of sideband generation, but taking the time to explain it all to me. I appreciate the time we were able to work together during his short stay at UCSB, which greatly accelerated how quickly we were able to develop the theory, and his continued assistance after leaving.

I would like to thank the staff of the physics department for keeping everything running under the hood. Specifically, thank you to Jennifer Ferrar and Daniel Stack for always having answers to my questions, or at least advice on how to get them answered. Thank you to Mike Deal for keeping the building and labs as dry as can be, for always taking care of problems when they arise, and for the numerous entertaining diversions.

Thank you to the collaborators inside and outside of UCSB who enabled this work. Thank you to Kyle Seyler for providing the TMD samples, Weilu Gao for the CNTs, and Naveen Venkatesa for the perovskites. In addition to providing the samples which allowed one of the chapters of this thesis, each was always willing to answer the novice's questions about a material system I had previously never studied. I would also like to thank Rupert Huber for inviting me out to the University of Regensburg for a month, and his students Christoph Schmid and Stephan Schlauderer for hosting me. While none of the work I did there made it into this thesis, it was a wonderful experience participating in research in one of my favorite groups.

Thank you to the plethora of friends who have helped me throughout grad school. Thank you to Lucas Brady for getting me through first year and beyond, and Dan Ish for all our sidebars. Thank you to KS, ZG and RS from the Weld lab for their help in learning how to relax after a long week.

Finally, thank you to my family, without your support I never would have made it this far.

Curriculum Vitæ

Darren Charles Valovcin

Education

2019	Ph.D., Physics, University of California, Santa Barbara
2016	M.A., Physics, University of California, Santa Barbara
2013	B.S., Physics, University of New Hampshire, Durham
2009	Holliston High School, Holliston

Professional Experience

2014-2019	Graduate research assistant, Department of Physics, UCSB
2013-2014	Graduate teaching assistant, Department of Physics, UCSB
2011-2013	Mathematics assistance tutor, Department of Mathematics, UNH
2011-2013	Undergraduate research assistant, Department of Physics, UNH

Publications

"Optical Frequency Combs from High-Order Sideband Generation", **Darren C Valovcin**, et al. *Optics Express* **26**, (2018)

"Dynamical Birefringence: Electron-Hole Recollisions as Probes of Berry Curvature", Hunter B Banks, Qile Wu, **Darren C Valovcin**, et al. *Physical Review X* **7**, (2017)

Accepted

"Temporal and Spectral Fingerprint of Ultrafast All-Coherent Spin Switching", Stefan Schlauderer, Christoph Lange, Sebastian Baierl, Thomas Ebnet, Christoph Schmid, **Darren Valovcin**, Anatoly Zvezdin, Alexey Kimel, Rostislav Mikhaylovskiy *Nature Letters* (2019)

Abstract

High-Order Sideband Generation for Creating Optical Frequency Combs and Probing Bloch Wavefunctions

by

Darren Charles Valovcin

High-order sideband generation (HSG) is a recently discovered phenomenon in semiconductors simultaneously driven by a weak near infrared (NIR) laser and a strong THz electric field. The NIR field excites electrons out of the valence band into the conduction band, leaving behind holes. The strong THz field can then accelerates the electrons and holes apart before it switches directions to drive the electrons and holes back towards each other. If an electron and a hole recollide, they emit a photon. Since both particles gained energy from the THz field, the emitted photons are typically higher in energy than the original NIR photon. The narrow linewidth of both lasers result in these emitted photons being equally spaced from the NIR photon energy and each other by twice the THz frequency to generate frequency combs. More than 130 orders have been observed.

The intensities of the sidebands is typically difficult to simulate theoretically. However, a simple scaling law for the THz frequency and field strength can be used to predict the widths of the frequency combs. This provides greater tunability and control of HSG frequency combs than previously, opening technological applications of these combs. This

scaling relation is complicated, however, by the motion of holes as they travel within a complicated Brillouin zone. Berry's Curvature mixes the Bloch wavefunctions in momentum space, causing a hole to evolve into new states as it is accelerated by the THz field. When an electron recollides with a hole, these different wavefunctions are imprinted onto the intensity and polarization of the emitted sidebands. With careful polarimetry of the sidebands, information can be extracted about the material structure. For example, strain can be introduced to modify the band structure of the material, which significantly alters the measured polarizations of the sidebands. These techniques could lead to all-optical measurements of the band structure, and Berry Curvature of material systems.

In order to apply these techniques to understand novel material systems, HSG must first be observed in these materials. Any new material must be a semiconductor with a band gap near the NIR photon energy where electrons and holes can be created. However, finding systems with suitably small scattering rates and large enough coherence times remains a challenge.

Contents

Chapter 1

Introduction

In the late 1980's to early 1990's, there was an explosion of research into a phenomenon called high harmonic generation (HHG), wherein intense radiation focused onto an atomic or molecular gas is able to produce many harmonics of the incident frequency. Inspired by this work and the observation of 2$^{\text{nd}}$- and 4$^{\text{th}}$-order THz sideband generation [16, 56], a prediction was made in 2007 to see a sister process in solids termed high-order sideband generation (HSG) [67]. In 2012, the first experiments had been published by the Sherwin Group observing this prediction [133]. Since then, a significant amount of work has gone into understanding HSG, some of its applications, and how it differs greatly in some aspects from HHG [9, 60, 61, 124, 10].

This introduction will begin by discussing some of the basic properties of GaAs and the changes that occur when it is reduced from 3D to 2D in a quantum well. The phenomenon of high harmonic generation will be discussed, followed by the extension to high-order sideband generation. Berry's Curvature, which is turning out to be an important concept in understanding HSG, will be briefly introduced. Finally, I give a quick description of the UCSB Free Electron Lasers, which made this work possible.

1.1 Semiconductors, Bands and Quantization

As will be discussed in Sec. 1.2, an intuition for HSG comes from considering the semi-classical motion of electrons (and holes) driven by a strong electric field. A free electron (that is, an electron traveling without any external potential) can be treated as a plane wave with parabolic energy dispersion where the energy $E \propto k^2$, with k being electron quasi-momentum. The work presented here, however, is concerned with electrons and holes as quasi-particles which are confined to a physical solid. Clearly, imposing the periodic potential of the host crystal drastically changes the motion of the electron relative to a free electron. Here, I will briefly discuss the specifics of GaAs, which was the system where nearly all of this work was performed. This will be a coarse overview, and the interested reader may refer to more detailed discussions provided by many wonderful introduction to solid state physics books [25, 6, 130].

1.1.1 Bulk GaAs

GaAs is a semiconductor with a zincblende crystal structure, which can be viewed as two independent face-centered cubic (fcc) lattices for the Ga and As atoms which are then offset from each other along the diagonal by 1/4 the cell size. Figure 1.1 depicts a single

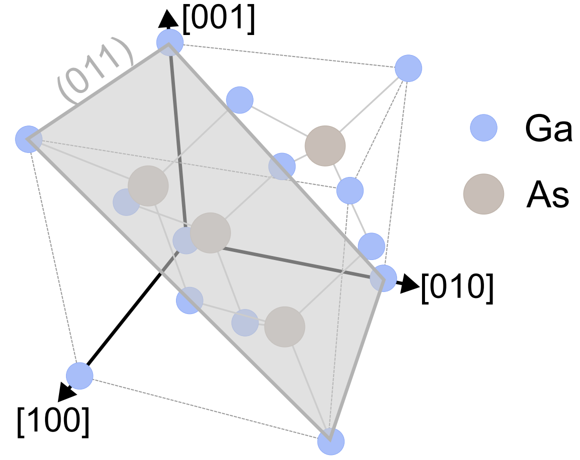

Figure 1.1: A unit cell of GaAs. Ga atoms (blue) are arranged in a face-centered cubic (fcc) lattice. As atoms (grey) are also arranged in an fcc lattice, but offset from the Ga atoms by 1/4 the unit cell diagonal. The Miller indices indicate the coordinate directions of the unit cell. An example Miller plane, the (011), is denoted in grey and is the plane with a surface normal of the [011] direction.

unit cell of GaAs. Miller indices can be used to describe directions in a crystal relative to the unit cell, where the notation $[ijk]$ denotes a direction (vector) relative to the axes of the unit cell. Each i, j, k is an integer which denotes the weight of each unit vector of the unit cell of the vector described the Miller index. That is, [100], [010], and [001] refer to the $x-$, $y-$, and $z-$axis of the unit cell, respectively, while [111] is the vector pointing across the diagonal of the unit cell. A negative direction is denoted by an over-bar, $[\bar{1}00]$ points opposite to [100]. Miller planes, denoted (ijk), refer to planes in the crystal whose surface normal is given by the vector $[ijk]$.

Electron Motion and Band Structure

An electron in a perfect crystal of GaAs will experience a periodic potential due to the regular arrangement of the Ga and As atoms. For such an electron, the time-independent

Schrödinger equation reads,

$$H\Psi(\mathbf{r}) = \left(\frac{\mathbf{p}^2}{2m} + V(\mathbf{r})\right)\Psi(\mathbf{r}) = E\Psi(\mathbf{r}) \tag{1.1}$$

with $V(r+a) = V(r)$, when a is the periodicity of the system, which includes the Coulomb potential of the atoms. Bloch's theorem allows one to extract the periodic part of the wavefunction by expressing the wavefunction as

$$\Psi(\mathbf{r}) = u_{n\mathbf{k}}(\mathbf{r})e^{i\mathbf{k}\cdot\mathbf{r}} \tag{1.2}$$

where $\mathbf{k}$ is the momentum, n labels the band, and $u_{n\mathbf{k}}(\mathbf{r})$ has the same periodicity as $V(\mathbf{r})$. Inserting Eq. 1.2 into Eq. 1.1 (and using $\mathbf{p} = -i\hbar\nabla$) results in

$$\left(\frac{\mathbf{p}^2}{2m} + \frac{\hbar\mathbf{k}\cdot\mathbf{p}}{m} + \frac{\hbar^2 k^2}{2m} + V(\mathbf{r})\right)u_{n\mathbf{k}} = E_{n\mathbf{k}}u_{n\mathbf{k}} \tag{1.3}$$

This equation defines the starting point for '$k \cdot p$' methods, named so for the second term on the left hand side. The eigenenergies of this equation are the band structure of the material, while the eigenfunctions are the wavefunctions of the electrons and holes at the band and momentum specified by n and $\mathbf{k}$. Typically, solving Eq. 1.3 begins by solving for the wavefunctions and energies at $\mathbf{k} = 0$. These $u_{n\mathbf{0}}$ provide a complete basis, and perturbation theory can be used to extend outward to non-zero $\mathbf{k}$. Because perturbation theory is applied, the results are best for small k, but certain techniques have been developed to extend it across the Brillouin Zone, see [121, 130] for more information. Methods based on $k \cdot p$ have been used for calculating the band structure and wavefunctions which were used in simulating many of the results in this work.

The wavefunctions near the band edge at $\mathbf{k} = 0$ are described by the symmetries of the atomic orbitals which give rise to the energy bands [25, 130]. The wavefunction at the bottom of the conduction band of a zincblende semiconductor has the same symmetries of an s atomic orbital, while the top of the valence band follows the p orbital symmetries. Because of this, is it common to refer to the bottom of the conduction band by $|S\rangle$, and the top of the valence band with $|X\rangle$, $|Y\rangle$, and $|Z\rangle$ mimicking the symmetries of the p_x, p_y, and p_z orbitals, respectively (see refs. [25, 130] for a more detailed discussion). However, when spin and spin-orbit coupling are included, these atomic orbital symmetry states are not sufficient to describe the electronic states at the top of the band and the angular momentum quantum numbers, $|j, j_z\rangle$ are used instead. In terms of these states, the wavefunctions at the Γ-point, $|u_{n\mathbf{0}}\rangle$, are given by,

$$\begin{aligned}
|u_{1\mathbf{0}}\rangle &= |S\uparrow\rangle \\
|u_{2\mathbf{0}}\rangle &= |S\downarrow\rangle \\
|u_{3\mathbf{0}}\rangle &= -\frac{1}{\sqrt{2}}\,|(X+iY)\uparrow\rangle = \left|\frac{3}{2},\frac{3}{2}\right\rangle = |HH+\rangle \\
|u_{4\mathbf{0}}\rangle &= -\frac{1}{\sqrt{6}}\,[|(X+iY)\downarrow\rangle - 2\,|Z\uparrow\rangle] = \left|\frac{3}{2},\frac{1}{2}\right\rangle = |LH+\rangle \\
|u_{5\mathbf{0}}\rangle &= \frac{1}{\sqrt{6}}\,[|(X-iY)\uparrow\rangle + 2\,|Z\downarrow\rangle] = \left|\frac{3}{2},-\frac{1}{2}\right\rangle = |LH-\rangle \qquad (1.4) \\
|u_{6\mathbf{0}}\rangle &= \frac{1}{\sqrt{2}}\,|(X-iY)\downarrow\rangle = \left|\frac{3}{2},-\frac{3}{2}\right\rangle = |HH-\rangle \\
|u_{7\mathbf{0}}\rangle &= \frac{1}{\sqrt{6}}\,[|Z\uparrow\rangle + 2\,|(X+iY)\downarrow\rangle] = \left|\frac{1}{2},\frac{1}{2}\right\rangle = |SO+\rangle \\
|u_{8\mathbf{0}}\rangle &= \frac{1}{\sqrt{6}}\,[|Z\downarrow\rangle - 2\,|(X-iY)\uparrow\rangle] = \left|\frac{1}{2},-\frac{1}{2}\right\rangle = |SO-\rangle
\end{aligned}$$

The first equality of each line defines the wavefunctions at Γ for the lowest conduction band and the highest 3 valence bands in terms of the symmetric s- and p-like states, respectively, along with the electron spin denoted by $\uparrow$ (spin up) and $\downarrow$ (spin down). For the valence band states, the next equality labels them by their total angular momentum and the $z-$component of the angular momentum. Finally, they are also listed in terms of their designation of 'heavy-hole', 'light-hole', or 'split-off hole'. The '+' and '$-$' are used to denote the sign of the j_z component, which has implications on allowed transitions that will be discussed later.

An extension of the $k \cdot p$ is to solve the Hamiltonian exactly under a restricted basis set. If one restricts the system to the 3/2-spin states, the Hamiltonian can be written as [25, 18, 118],

$$H_L = -\frac{\hbar^2}{2m}\left[(\gamma_1 + \frac{5}{2}\gamma_2)k^2 - 2\gamma_3(\mathbf{k}\cdot\mathbf{J})^2 + 2(\gamma_3 - \gamma_2)(k_x^2 J_x^2 + k_y^2 J_y^2 + k_z^2 J_z^2)\right] \tag{1.5}$$

which is known as the Luttinger Hamiltonian. **J** are the angular momentum operators on the 3/2 states, while the γ_i are the material dependent "Luttinger parameters", phenomenological fitting parameters. Determining the values of the Luttinger parameters from experiments therefore provide the Hamiltonian which can be solved to calculate the electronic band structure and particle wavefunctions. With these, the dynamics of charge carriers within the material can be determined, which is critical for understanding and controlling electronic devices.

The Luttinger Hamiltonian considers the 3/2-spin states, and is called a 4-band model

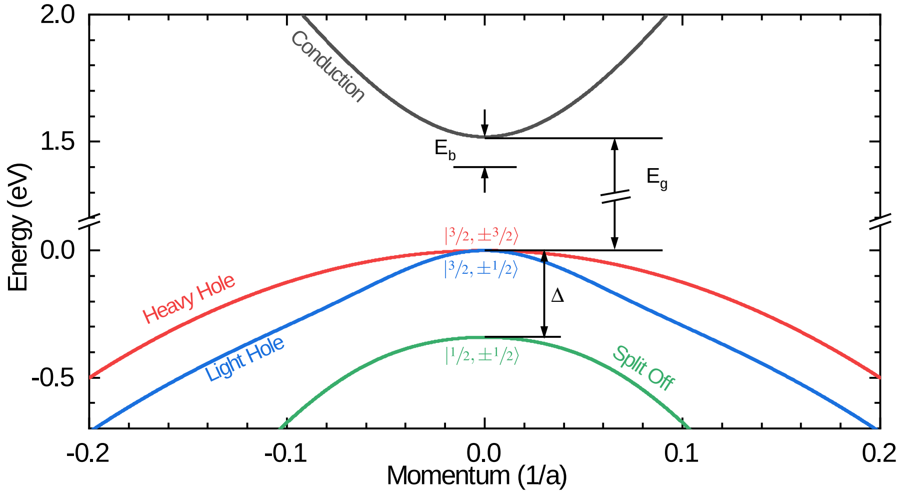

Figure 1.2: Partial band structure of GaAs from the 8-band Kane model, plotted along the [010] crystal direction. The lowest conduction band and highest three valence bands are shown near the Γ-point ($k = 0$). E_g (≈ 1.52 eV at low temperatures) is the band gap of GaAs, the separation between the highest valence band and lowest conduction band. The light hole and heavy hole are degenerate at $k = 0$, while spin-orbit coupling separates the split off band by Δ (≈ 341 meV). The exciton state is shown at the Γ-point below the band gap by its binding energy ($E_b \approx 4$ meV in low temperature bulk GaAs). The exciton state is not to scale for visibility. The valence bands are also labeled by their $k = 0$ angular momenta state, see Eq. 1.4

(for the $|\pm 3/2\rangle$ and $|\pm 1/2\rangle$ states). An extended model which includes the total angular momentum 1/2 states (which includes the lowest conduction band and the split-off band) is called the 8-band Kane model [25, 18, 11, 118]. Figure 1.2 shows the calculated band structure in bulk GaAs using the Kane model. The distinction between the light-hole and heavy-hole become clear as, near the Γ point, the heavy hole shows much heavier mass (lower curvature) that the light hole (higher curvature). It is also important to note that the bands are not parabolic throughout the Brillouin zone, which is especially clear around $k = 0.075/a$ for the light-hole band, due to the coupling between bands at finite $\mathbf{k}$. Furthermore, the bands are not spherically symmetric and the anisotropy is characterized by the ratio γ_3/γ_2 [25, 121, 130]

1.1.2 GaAs Quantum Wells

With the improvements in vacuum technologies and epitaxial surface preparation and characterization which came in the 1960's and 1970's, molecular beam epitaxy (MBE) became a technique capable of producing exceptionally high quality single crystal epitaxial layers of semiconductors [118, 21]. Since then, scientists have been using MBE to produce arbitrary semiconductor heterostructures and confining charge carriers from the bulk 3D structure into lower dimensions.

Calculating the states of a particle confined in a potential well is an elementary problem in quantum mechanics [25, 118, 94, 11]. The first step is to solve the more straightforward problem of an infinite square well where the potential of the well in Eq. 1.1 is given by,

$$V_\infty(z) = \begin{cases} \infty, & z < 0 \\ 0, & 0 < z < L \\ \infty, & z > L \end{cases} \tag{1.6}$$

where L is the width of the well. Inside the well, the Hamiltonian is the same as that of a free particle, and the wavefunction can be expressed as $\Psi(z) = A\sin(az) + B\cos(bz)$. In the barrier regions of the well, the only solution to Schrödinger's equation is $\Psi(z) = 0$. This specifies the boundary conditions for within the well, $\Psi(0) = \Psi(L) = 0$, restricting Ψ to the sine components (and $B = 0$) and quantizing the results:

$$\Psi_n(z) = \sqrt{\frac{2}{L}}\sin\left(\frac{n\pi}{L}z\right), \qquad E_n = \frac{\hbar^2}{2m}\left(\frac{n\pi}{L}\right)^2 \tag{1.7}$$

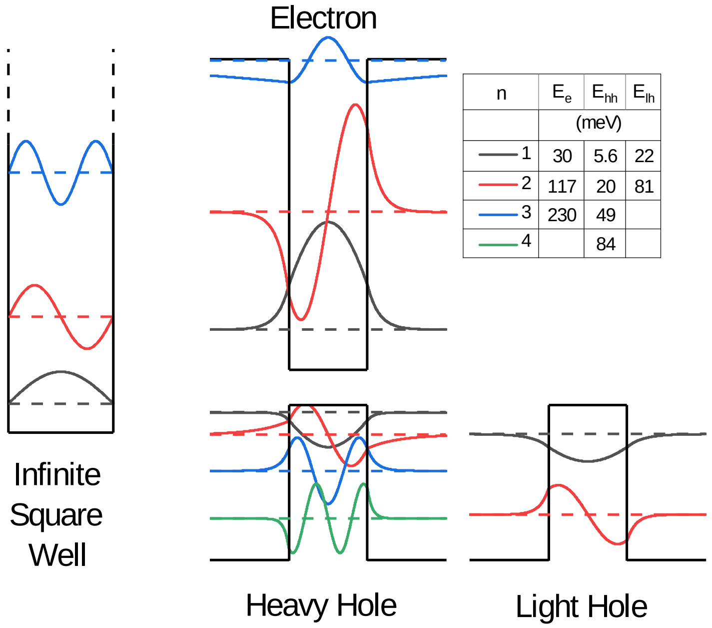

n	E_e	E_{hh}	E_{lh}
	(meV)		
— 1	30	5.6	22
— 2	117	20	81
— 3	230	49	
— 4		84	

Figure 1.3: Quantum well wavefunctions. The left shows the first three states of an infinite square well ($V(\mathbf{r}$ given by Eq. 1.6). Dashed lines show the energy of the state and are the zero-axis for the wavefunctions. Center and right show the calculated solutions for the parameters of a 10 nm GaAs/AlGaAs QW: (Electron) $V_b = 231$ meV, $m_w = 0.067m_0$, and $m_B = 0.092m_0$; (Heavy Hole) $V_b = 115$ meV, $m_w = 0.5m_0$, and $m_B = 0.5m_0$; (Light Hole) $V_b = 115$ meV, $m_w = 0.082m_0$, and $m_B = 0.103m_0$. Upper right tabulates the energies of the bound states for the electron (E_{e}), heavy hole (E_{hh}) and light hole (E_{lh})

Where m is the mass of the particle in the well. The first three levels of the infinite square well are sketched on the left of Fig. 1.3. In an infinitely deep potential well, there is an infinite number of these confined states.

$$V_f(z) = \begin{cases} V_b, & z < -L/2 \\ 0, & -L/2 < z < L/2 \\ V_b, & z > L/2 \end{cases} \tag{1.8}$$

In a finite square well, given by the potential of Eq. 1.8, the picture is significantly more complicated. Instead of the simple solution $\Psi(z) = 0$ in the barrier found in the infinite square well, the wave function within the barrier can be nonzero. The wavefunctions in each region are given by,

$$\Psi_n(z) = \begin{cases} A_n \exp\left(\kappa_n z\right), & z < -L/2 \\ B_n \left\{ \begin{matrix} \sin \\ \cos \end{matrix} \right\} \left(\dfrac{k_n L}{2} \right), & -L/2 < z < L/2 \\ -A_n \exp\left(-\kappa_n z\right), & z > L/2 \end{cases} \tag{1.9}$$

Where the A_n, B_n are normalization factors, and sin is used inside the well for even n while cos is used for odd n. These are determined by the boundary conditions where the wavefunction must be continuous,

$$\Psi(z \to \pm L/2^-) = \Psi(z \to \pm L/2^+) \tag{1.10}$$

and that the weighted (by effective masses) derivative must be continuous,

$$\left. \frac{1}{m_B} \frac{d\Psi}{dz} \right|_{z \to \pm L/2^B} = \left. \frac{1}{m_w} \frac{d\Psi}{dz} \right|_{z \to \pm L/2^w} \tag{1.11}$$

where m_B and m_w are the effective masses in the barrier and well region, respectively, and I have invented a lazy shorthand to indicate the limits are taken from the direction of the Barrier region or $w$ell region. Solving for all of the coefficients is a transcendental equation and must be done numerically. The upper center of Fig. 1.3 shows the solutions for $L = 10$ nm, $V_b = 231$ meV, $m_w = 0.067m_0$ and $m_B = 0.092m_0$, which correspond to an electron confined in a 10 nm QW of GaAs with barriers of $Al_{0.3}Ga_{0.7}As$. Below the solutions for the electron, the solutions for the heavy hole are plotted ($V_b = 115$ meV, $m_w = 0.5m_0$ and $m_B = 0.5m_0$), with the light hole beside it ($V_b = 115$ meV, $m_w = 0.082m_0$ and $m_B = 0.103m_0$). To determine the depths of the potentials for the conduction and valance band wells, Anderson's rule is applied [25], wherein the vacuum level of the electron affinities for each material are aligned, and the band offsets determined relative to the vacuum level. The effective masses in the barriers are linearly interpolated between the masses of GaAs and AlAs [25].

The first thing to note with the solutions to the finite well compared to the infinite well is the existence of a finite number of bound states. The table in the top right of Fig. 1.3 lists the eigenenergies for Schrödinger's equation with the finite square well potential of Eq. 1.8. The electron has three bound states (energies listed as E_e), the heavy hole has four bound states (E_{hh}), and the light hole has two bound states (E_{lh}). While the heavy- and light-hole both have the same confinement depth, the larger mass of the heavy hole causes the spacings between energy levels to be closer together, and allows more bound states. This is consistent with the result from the infinite square well where the energy spacings are inversely proportional to mass (Eq. 1.7).

Compared to the solutions to the infinite square well on the left side of Fig. 1.3, it can be seen that the wavefunctions in the finite potential are non-zero in the barrier region, instead of zero in the infinite square well. This is especially significant for the highest bound state for the electron (Fig. 1.3 center top, blue curve). The energy of the bound state is only 1 meV below the top of the barrier, which results in a very large portion of the electron state being in the barrier. In theoretical calculations, however, the simplicity of the analytic solutions to the infinite square well (Eq. 1.7) are far easier to work with relative to the transcendental equations which must be solved for in the finite square well (Eqs. 1.9-1.11). Thus, it is sometimes preferred to make the "infinite square well approximation" wherein an infinite square well is assumed with a modified

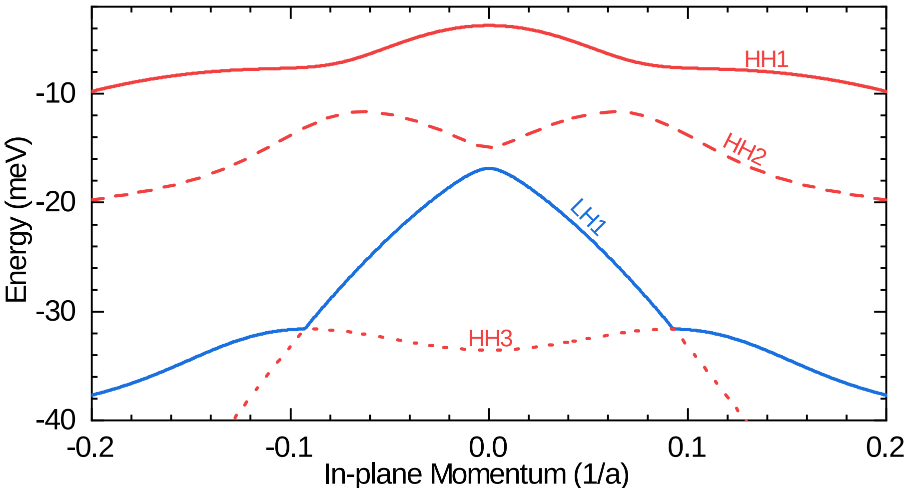

Figure 1.4: In-plane band structure of a 10 nm quantum well. The three highest heavy hole sub-bands (HHn, red) and highest light hold band (LH1, blue) are depicted. The bands are significantly warped relative to the bulk GaAs structure (Fig. 1.2), with negative effective masses visible in the HH2 and HH3 bands near the Γ point.

width so the spacing of the states equals the values found from experiments [9].

So far, this section has discussed the states of particles confined to a 1D potential, while Sec. 1.1.1 discussed the wavefunctions and dynamics of particles in bulk GaAs. Finally, we bring the two together, as the quantum well structures in the real world only confine one dimension while the two perpendicular directions retain their (nearly) bulk character. However, the in-plane dispersion does not follow the bulk, shown in Fig. 1.2. First, Fig. 1.3 shows that the energy levels of the heavy- and light-holes are different, so it should be expected the degeneracy at the Γ-point should now be lifted. Furthermore, the wavefunctions used in the Kane model (Eqs. 1.4) must now include the contributions from the $z-$confinement (Eqs. 1.9). The Kane model, for example, can be solved again using these modified wavefunctions. References [25, 118, 11] provide good discussions of this procedure.

As an example, Fig. 1.4 shows the calculated in-plane dispersion for the 10 nm QW discussed above, using the infinite square well approximation and a Luttinger Hamiltonian for simplicity. The dispersion relations are significantly more complicated than the bulk band structure, showing significant non-parabolicity at significantly lower momenta and even regions of negative mass (where the bands bend up).

1.1.3 Optical Selection Rules

Much of this thesis depends on the ability to excite electrons from the valence band to the conduction band using photons. Such transitions must obey optical selection rules where the difference in angular momentum of the two states must be ±1[130]. To begin, a photon can be represented in the circular basis of $\sigma_\pm$, where ± corresponds to a photon angular momentum of ±1 respectively. Compared with the momentum states of the conduction and valence bands at Γ given in Eq. 1.4, a $\sigma_\pm$ photon is able to excite different electron and hole states:

$$\begin{aligned} \sigma_+ \longleftrightarrow \left|\frac{1}{2}\right\rangle_e + \left|\frac{1}{2}\right\rangle_h, &\qquad \left|-\frac{1}{2}\right\rangle_e + \left|\frac{3}{2}\right\rangle_h \\ \sigma_- \longleftrightarrow \left|-\frac{1}{2}\right\rangle_e + \left|-\frac{1}{2}\right\rangle_h, &\qquad \left|\frac{1}{2}\right\rangle_e + \left|-\frac{3}{2}\right\rangle_h \end{aligned} \tag{1.12}$$

The e or h subscript on the state denotes electron or hole, and the total angular momenta have been dropped from the state labels. From these, we can see that both circular photons are able to excite either light holes ($\langle \pm 1/2|$) or heavy holes ($\langle \pm 3/2|$).

The effective of quantization from a quantum well adds an additional layer into the optical selection rules. Fermi's Golden Rule states the probability of a transition occurring depends on the overlap of wavefunctions of the initial and final states [25]. With the solutions to the infinite square well, Eq. 1.7, this adds an additional restriction to between subbands of the same parity.

A final point to these optical selection rules is that they apply equally to the inverse process. Namely, the emission of a photon due to the recombination of an electron and hole is restricted to equal parity in quantum wells and the dipole selection rules of Eqs. 1.12.

1.1.4 Exciton

Everything discussed so far has dealt with the general dynamics of particles in the bulk material or quantum well, but it is helpful to consider the dynamics of single particles. Consider a crystal of bulk GaAs with the band structure shown in Fig. 1.2, with the valence bands fully filled and the conduction band fully empty. If a photon is incident on the sample with a photon energy $\hbar\omega = E_g$ (ω is the photon frequency), it can promote an electron out of the valence band and into the conduction band. The valence band now has an empty space in the state it once occupied, the hole. The hole is effectively a positively charged quasi-particle, and the electron and hole will each experience a

Coulomb potential given by,

$$V_{eh}(\mathbf{r}_e, \mathbf{r}_h) = \frac{e^2}{4\pi\epsilon_0\epsilon_b}\frac{1}{|\mathbf{r}_e - \mathbf{r}_h|} \tag{1.13}$$

With $\mathbf{r}_e$ ($\mathbf{r}_h$) the position of the electron (hole), e the charge of the electron and hole, ϵ_0 the vacuum permittivity, and ϵ_b the relative permittivity ($\epsilon_b \approx 12.9$ in GaAs at low frequency). The two-particle Schrödinger equation is then,

$$\Bigg[\left(-\frac{\hbar^2}{2m_e}\nabla_e^2 - V_e(\mathbf{r}_e)\right) + \left(-\frac{\hbar^2}{2m_h}\nabla_h^2 - V_h(\mathbf{r}_h)\right) - \frac{e^2}{4\pi\epsilon_0\epsilon_b}\frac{1}{|\mathbf{r}_e - \mathbf{r}_h|}\Bigg]\psi(\mathbf{r}_e, \mathbf{r}_h) = E(\mathbf{r}_e, \mathbf{r}_h)\psi(\mathbf{r}_e, \mathbf{r}_h) \tag{1.14}$$

where m_e (m_h) is the reduced mass of the electron (hole), ∇_e (∇_h) is the gradient operator on the electron (hole) position, and the potentials are those due to the periodic array of atoms as discussed in previous sections. The standard procedure [25, 118, 130, 97] is to change to the center of mass coordinate system with,

$$\mathbf{R} = \frac{m_e\mathbf{r}_e + m_h\mathbf{r}_h}{m_e + m_h}, \qquad \mathbf{r} = \mathbf{r}_e - \mathbf{r}_h \tag{1.15}$$

To simplify the math, the conduction and valence bands are assumed to be parabolic, which is justified when considering the electron and hole created by a resonant excitation near the Γ-point. In this case, the center of mass and relative coordinates are separable, resulting in two different states to solve. The center of mass trivially solves to a free particle with a mass equal to the sum of electron and hole. For the relative coordinates in a bulk crystal, one finds

$$\left(-\frac{\hbar^2}{2\mu}\nabla^2 - \frac{e^2}{4\pi\epsilon_0\epsilon_b}\frac{1}{|\mathbf{r}|}\right)\Phi(\mathbf{r}) = E\Phi(\mathbf{r}) \tag{1.16}$$

where μ is now the reduced mass of the electron and hole, $1/\mu = 1/m_e + 1/m_h$. This equation is identical in form to the hydrogen atom, which can be solved in the standard way [94], and this bound state of an electron and hole is called an exciton. This results in a scaled Rydberg energy R_{exc} and Bohr radius a_{exc},

$$R_{\text{exc}} = \frac{\mu}{2}\left(\frac{e^2}{4\pi\epsilon_0\epsilon_b\hbar}\right)^2 \qquad a_{\text{exc}} = \frac{4\pi\epsilon_0\epsilon_b\hbar^2}{e^2\mu} \tag{1.17}$$

In GaAs, these numbers work out to $R_{\text{exc}} \approx 4$ meV and $a_{\text{exc}} \approx 10$ nm at low temperatures. As with the hydrogen atom, there exists a set of bound states whose binding energies are given by $E_n = R_{\text{exc}}/n^2$.

In the band structure diagram of Fig. 1.2, the conduction and valence bands both describe the motion of "free" electrons and holes. Since a bound electron and hole pair is a lower energy configuration than a free electron and hole, however, it is often useful to include this bound excitonic state in the band structure as a state in the gap at the Γ-point, separated from the conduction band by the binding energy of the exciton. The inclusion of this state has significant impact on the absorption spectra, resulting in a strong absorption peak slightly below the band gap of the material [25, 118].

When reducing dimensionality to two dimensions, the calculation above can be repeated to determine the new energies in reduced dimensionality. The main result is the scaling of the binding energies to $E_{\text{2D},n} = R_{\text{exc}}/(n - \frac{1}{2})^2$. A quantum well structure, however, is not perfectly 2 dimensional. The 3D Hamiltonian must be solved, Eq. 1.14, with the quantum well confinement explicitly included in a z-dependent potential. Under such treatment, the full separation into center of mass and relative coordinates (Eqs. 1.15) is no longer allowed, and a complete solution requires numerical simulations [25, 118]. One interesting point worth noting concerns the wavefunction of the exciton under increased confinement; as the width of the barrier shrinks, the in-plane wavefunction does not increase as a squished ball of rubber would, but instead shrinks as well, similar to a toy Hoberman sphere.

1.1.5 Berry Curvature

Consider a system whose Hamiltonian H is a function of some set of parameters which vary with time, $\mathbf{R}(t)$, so that the Hamiltonian can be written as $H = H(\mathbf{R}(t))$. The solutions to the eigenvalue problem can be defined for each value in the parameter space by,

$$H(\mathbf{R}(t)) \left| n(\mathbf{R}(t)) \right\rangle = \varepsilon_n(\mathbf{R}(t)) \left| n(\mathbf{R}(t)) \right\rangle$$

Next, consider the state $|\psi(t)\rangle$ which starts in an eigenstate of the above Hamiltonian, $|\psi(0)\rangle = |n(\mathbf{R}(0))\rangle$. When the parameter $\mathbf{R}$ is varied adiabatically through some path in its parameter space, the state $|\psi(t)\rangle$ will remain in the instantaneous eigenstate of the Hamiltonian with an additional phase,

$$|\psi(t)\rangle = \exp\left[-\frac{i}{\hbar}\int_0^t \varepsilon_n(\mathbf{R}(t'))dt'\right] e^{i\gamma_n(t)} \left| n(\mathbf{R}(t)) \right\rangle \tag{1.18}$$

The first phase is the standard dynamical phase, while the second is an arbitrary phase allowed by the stipulation of adiabatic evolution. The state in Eq. 1.18 must satisfy the time-dependent Schrödinger equation, $H(\mathbf{R}(t))\,|\psi(\mathbf{R}(t))\rangle = i\hbar\,\frac{\mathrm{d}}{\mathrm{d}t}\,|\psi(\mathbf{R}(t))\rangle$. Inserting the expression for $|\psi(t)\rangle$ from Eq. 1.18 into the time dependent equation and simplifying finds the following relation for the "arbitrary" phase,

$$\frac{\mathrm{d}\gamma_n}{\mathrm{d}t} = i\langle n(\mathbf{R}(t))|\nabla_{\mathbf{R}} n(\mathbf{R}(t))\rangle \cdot \frac{\mathrm{d}\mathbf{R}}{\mathrm{d}t} \tag{1.19}$$

When the path is taken along a closed loop such that after time T, $\mathbf{R}(0) = \mathbf{R}(T)$, Eq. 1.19 can be re-expressed as,

$$\gamma_n = i\oint_C \langle n(\mathbf{R}(t))|\nabla_{\mathbf{R}} n(\mathbf{R}(t))\rangle \cdot \mathrm{d}\mathbf{R} = \oint_C \mathcal{A}_n(\mathbf{R}) \cdot \mathrm{d}\mathbf{R} \tag{1.20}$$

Where C is the closed loop traced by $\mathbf{R}$, and the second equality defines the Berry Connection [123, 18, 13],

$$\mathcal{A}_n = i\langle n(\mathbf{R}(t))|\nabla_{\mathbf{R}} n(\mathbf{R}(t))\rangle \tag{1.21}$$

The Berry Connection itself is not gauge-invariant [123], and the Berry Curvature is instead used,

$$\mathbf{\Omega}_n(\mathbf{R}) = \nabla_{\mathbf{R}} \times \mathcal{A}_n \tag{1.22}$$

Where Stokes Theorem allows Eq. 1.20 to be rewritten instead as,

$$\gamma_n = \int_S \mathbf{\Omega}_n(\mathbf{R}) \cdot \mathrm{d}\mathbf{S} \tag{1.23}$$

with S being the surface defined by the contour of Eq. 1.20. This work first done by Berry [13] to derive γ_n, which is now known as the Berry Phase, has had a significant impact on solid state and condensed matter physics and drawn interest as being a purely geometric phase. The Berry Phase has been used to explain anomalous velocity [18], the anomalous Hall effect [17], to describe the microscope origin of polarization and magnetization in materials [92, 113], and many other phenomena in condensed matter physics [123, 18, 113]. The Berry Connections and Berry Curvatures in solid state materials, which give rise to Berry Phases, have become widely accepted as a necessary component in modeling and understanding the motion of carriers in solids, alongside the electronic band structure [123, 18].

Sections 1.1.1 and 1.1.2 derived the wavefunctions of GaAs-based materials, $|u_{n\mathbf{k}}\rangle$. With the momentum $\mathbf{k}$ now playing the role of the parameter space used in the definitions of the Berry parameters, $\mathbf{R}$, it is possible to define a Berry Curvature for GaAs as,

$$\boldsymbol{\Omega}_n(\mathbf{k}) = i\nabla \times \langle u_{n\mathbf{k}}|\nabla_{\mathbf{k}} u_{n\mathbf{k}}\rangle \tag{1.24}$$

where the $|u_{n\mathbf{k}}\rangle$ states are the wavefunctions found, for example, from the Kane method described in Sec. 1.1.1. When this system is driven by an electromagnetic wave, the equations of motions for a particle of charge e are given by [123],

$$\dot{\mathbf{r}} = \frac{1}{\hbar}\frac{\partial \varepsilon_n(\mathbf{k})}{\partial \mathbf{k}} - \hbar\dot{\mathbf{k}} \times \boldsymbol{\Omega}_n(\mathbf{k}) \tag{1.25}$$

$$\hbar\dot{\mathbf{k}} = -e\mathbf{E}(\mathbf{r},t) - e\dot{\mathbf{r}} \times \mathbf{B}(\mathbf{r},t) \tag{1.26}$$

With the exception of the $\hbar\dot{\mathbf{k}} \times \boldsymbol{\Omega}_n(\mathbf{k})$ term, the above equations are the standard equations used to describe the motion of electrons in solids [6]. This additional term results in the anomalous velocity, and shows how the Berry Curvature can be viewed analogously to a magnetic field in momentum space [123, 18].

A rather significant caveat to this description so far has been in an implicit non-degenerate, single-band picture, where there is no mixing between the various eigenstates of the Hamiltonian. In this instance, the Berry physics is described as Abelian. However, when there is mixing or degeneracy, the physics becomes non-Abelian and significantly more complicated. Instead of the simple scalar description of the Berry Connection (Eq. 1.21), it must be described by a matrix,

$$\mathbf{A}_{mn} = \langle u_{m\mathbf{k}} | \nabla_{\mathbf{k}} u_{n\mathbf{k}} \rangle \tag{1.27}$$

The definition of the Berry Curvature is modified to,

$$\boldsymbol{\Omega}(\mathbf{k}) = \nabla_{\mathbf{k}} \times \mathbf{A} - i\mathbf{A} \times \mathbf{A} \tag{1.28}$$

For details on these changes between Abelian and non-Abelian Berry physics, several review papers exist with more detail [123, 18]. In general, when discussing Berry Curvature in GaAs, the non-Abelian case must be used due to the coupling between the various bands and the 2-fold degeneracy due to spin.

1.2 Recollisions

During the 1970's and 1980's, researchers were studying harmonic generation in gases as a method for generating ever shorter wavelengths of light [120, 73, 91]. An atomic gas would be subject to a strong laser field (10^{13}-10^{16} W/cm^2) with a fundamental frequency between roughly 200 nm and 1.6 μm, resulting in radiation whose spectral components contained several odd harmonics of the driving frequency. These harmonics were found to be perturbative in nature, with the power of each harmonic scaling with the power of the harmonic order and the intensity falling off near-exponentially as a function of harmonic order [14, 96]. By the late 1980's, however, a distinct shift occurred where some combinations of driving field strength and frequency could produce large numbers of harmonics whose intensities reached a "plateau" where the intensities did not significantly drop, until a cutoff energy was reached [31, 68]. This phenomenon has since been called High-Order Harmonic Generation (HHG). HHG has been investigated as a technique for a wide variety of applications, such as ultra-fast attosecond pulses [24, 58], optical arbitrary waveform generation [33], imaging of molecular orbitals [74], or a table-top source of x-rays [51]. As we will see in the following section, this phenomenon can be explained by the collisions of an ionized electron with its parent ion. Then, this process will be extended into solid systems to see how an analogous process occurs with collisions between electrons and holes.

1.2.1 Electron-ion recollisions

In order to describe the highly non-linear, non-perturbative process observed in HHG, an elegant semiclassical theory was first described which views HHG as a recollision between ionized electrons and their parent atom [23]. Starting with the gas of neutral atoms (or molecules), the theory is broken into three main steps: (1) a strong laser field tunnel ionizes an electron from the parent atom, which is then free to (2) be accelerated away from the parent ion before the field changes direction, accelerating the electron back to the parent ion, wherein they may (3) recollide, re-emitting a photon with energy greater than the driving field's photon energy as the electron gains energy from the field. Despite the simplicity of this "three-step model", it is able to accurately reproduce the plateau feature and the cutoff of the plateau at,

$$\hbar\omega N_{\max} \approx 3.2U_p + I_p, \qquad U_p = \frac{e^2F^2}{4m\omega^2} \tag{1.29}$$

where $N_{\max}$ is the largest number of harmonics observed, ω is the frequency of the driving field, I_p is the ionization potential of the gas studied, and U_p is the ponderomotive or quiver energy, which is related to the average energy gained by a charged particle in an oscillating field. In the year following the publication of this semiclassical model, a fully quantum mechanical model was published which agrees with the simple, semiclassical three-step model [63].

The mechanism of the first step in the three-step model, ionization of the atom by the driving field, was first investigated by Keldysh in the middle of the 20th century. He found [53] a parameter which distinguishes whether an electric field is able to ionize an atom via multi-photon absorption (for large photon energies but low field strengths) versus tunnel ionization (which occurs for low photon energies but large field strengths). This parameter, now called the Keldysh parameter, γ, is given by

$$\gamma = \frac{\omega\sqrt{2mI_0}}{eF} = \sqrt{\frac{I_0}{2U_p}} \tag{1.30}$$

with ω and F the frequency and field strength of the driving field, e and m are the charge and mass of an electron, and I_0 is the ionization potential of the atom in question. The

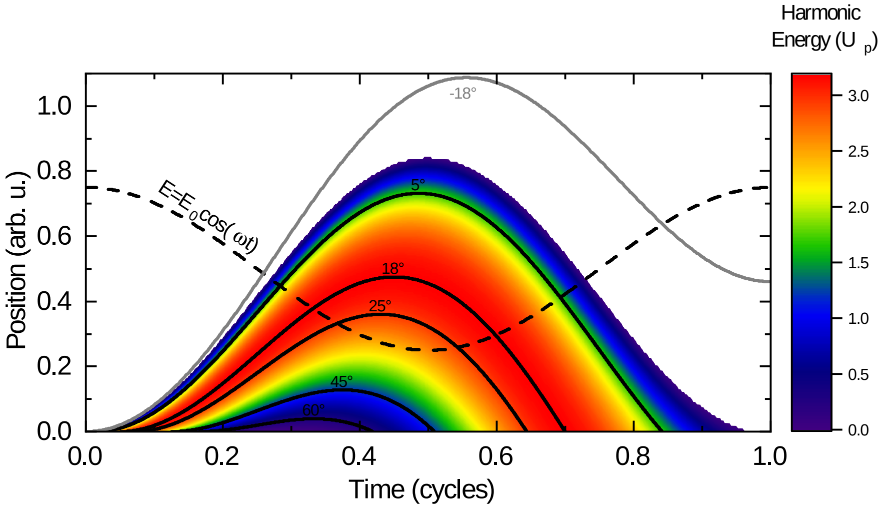

Figure 1.5: Classical electron trajectories in a oscillating driving field. The driving field is shown as the dashed line. An electron which is ionized from an atom at a given phase of the electric field can be accelerated away and back towards the parent atom. Contours of color show these path, with 5 arbitrary phases shown in black curves as an aide. The energy emitted when the electron recollides with the parent ion is encoded in the color of the path. The grey curve is the trajectory for an electron ionized before the field crest ($-18°$) shows that not all ionization times are able to drive the electron back towards the ion, instead driving the electron far from the ion.

second equality shows how the Keldysh parameter is related to the ratio of the ionization potential to the ponderomotive energy, as defined in Eq. 1.29. In experiments of HHG, $\gamma < 1$ which corresponds to the regime of tunnel ionization (while $\gamma > 1$ corresponds to the multi-photon ionization).

Once the electron is freed from the parent atom, its dynamics can be described simply as a free particle in an oscillatory electric field:

$$
\begin{aligned}
\ddot{x}(t) &= \frac{eE_0}{m}\cos(2\pi f t + \phi_i) \\
\dot{x}(t) &= \frac{eE_0}{2\pi f m}\sin(2\pi f t + \phi_i) - \frac{eE_0}{2\pi f m}\sin(\phi_i) \\
x(t) &= -\frac{eE_0}{(2\pi f)^2 m}\cos(2\pi f t + \phi_i) - \frac{eE_0}{2\pi f m}\cos(\phi_i)t \\
&\qquad + \frac{eE_0}{(2\pi f)^2 m}\cos(\phi_i)
\end{aligned}
\tag{1.31}
$$

The phase of the field, ϕ_i, is defined for these dynamics by what point of the driving field the atom is ionized and the free motion of the electron begins (the ionized atom, which is several orders of magnitude more massive than the electron, gains significantly less energy from the electric field and is ignored). The constants of integration can be found by the initial conditions of a stationary electron at the origin ($\ddot{x}(0) = \dot{x}(0) = 0$).

Figure 1.5 shows a family of trajectories for an electron from various ionization times for the driving field shown by the dashed curve. Each contour of constant color corresponds to a different electron trajectory for different ionization times. Five contour lines are shown for ionization times $\phi_i = 5^\circ,\ 18^\circ,\ 25^\circ,\ 45^\circ,$ and 60°. The color of the contour line denotes the energy of the photon emitted when the electron recollides with the ion, in units of U_p.

If an electron is ionized right around the electric field crest ($\sim 1^\circ$), the electron is accelerated far away from its atom. By the time the electric field reverses direction, the electron has gained significant momentum and it takes nearly a full half cycle before the electron is returned to the atom (at position 0). The result is a very long trajectory and large electron excursion, but a very low energy electron which then emits a low energy photon.

As the electron is ionized at increasing phases, the energy of the electron when it returns to the ion increases, up to a maximum energy of $\sim 3.2U_p$ when ionized near $\sim 18°$. The energy gained by the electron agrees with Eq. 1.29 and experimentally observed cutoffs [68, 77]. Further increases in the ionization phase now lead to a decrease in emitted photon energy, and at shorter excursion times relative to ionizations before 18°. Figure 1.5 also shows the existence of 'long-paths' and 'short-paths'; two different ionization phases result in the same electron energy, such as an ionization phase at 5° or 37.8° both result in $1.7U_p$ electron energies. However, ionization times between the field crest and 18° result in longer travel times and longer travel distances compared to the companion trajectory occurring after 18°.

Not all ionization phases allow the electron to return to the parent ion. After a quarter of a cycle following the field crest ($\phi_i > 90°$), the electron is freed while the electric field is increasing in magnitude. This provides the electron with too much momentum to have its direction be reversed after the field switches polarity. The grey curve in Fig. 1.5 shows the electron trajectory for $\phi_i = -18°$, where after a full cycle of the electric field the electron is not returned to the ion and no recollision occurs.

In 2011, high-order harmonic generation was observed in solid materials [35]. Due to the complexities introduced by a periodic crystalline structure (such as band structures,

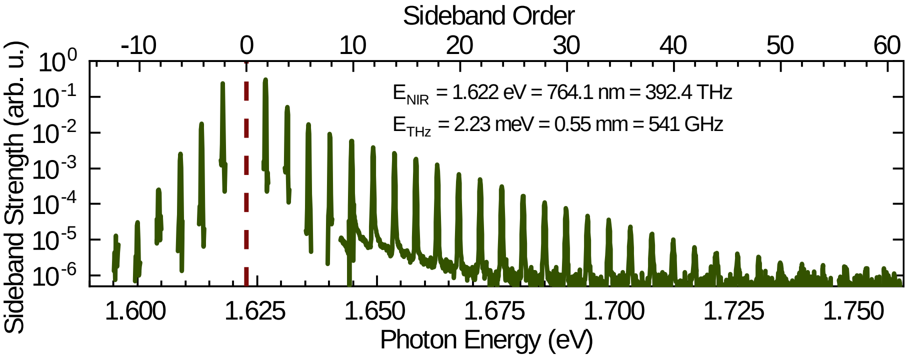

Figure 1.6: Example HSG spectrum from a 10 nm $Al_{0.05}Ga_{0.95}As$ QW. The NIR laser energy is set to the heavy hole exciton resonance (red dashed line), and THz set to 541 GHz. Sidebands are visible off the NIR energy, spaced by twice the THz photon energy. Negative order sidebands (lower in energy than the NIR) decay quickly, while positive orders decay much more slowly.

electron screening, many-body effects, ...), the theory describing solid-based HHG is much more complicated [111, 104, 43, 47]. One dominant mechanism for HHG in solids mimics that of the gaseous experiments; the strong field on a solid is able to excite an electron from the valence band into the conduction band (leaving behind a hole), which can be accelerated around the conduction bands before recolliding. This is called an 'inter-band' mechanisms as it relates to the dipole moment (which dictates the recollision process) between the valence and conduction bands. However, since the band structure in solids is highly non-parabolic (such as Figs. 1.2 and 1.4 depict), the electron and hole will generate non-linear currents which radiate harmonics of the driving field. This is called an 'intra-band' mechanisms as it relates to the individual motions of the electrons and holes in their respective bands [36, 47].

1.2.2 Electron-hole recollisions

A recently discovered phenomenon which decouples the intra- and inter-band mechanisms is high-order sideband generation (HSG) [67, 133], a sister process of HHG. In HHG, a single field responsible for both the inter-band electron excitation and intra-band driving. In HSG, however, a NIR laser tuned to the exciton energy creates an electron-hole pair, while a second strong laser field is responsible for ionizing the exciton, accelerating the electron and hole and causing them to recollide. When the NIR laser creates an exciton, the exciton plays the role of an atom in the description of HHG above, with the electron mass and the ionization energy of the atom of Eq. 1.29 scaled to the reduced electron-hole mass and the exciton binding energy, respectively. Once scaled, one finds a field oscillating in the THz regime (100's GHz to a few THz) with modest field intensities ($\sim 10^6$ W/cm^2) are able to ionize, accelerate and recollide an exciton, significantly lower than the $\sim 10^{16}$ W/cm^2 of NIR light used for HHG.

An example sideband spectrum is shown in Fig. 1.6 for a 10 nm $Al_{0.05}Ga_{0.95}As$ QW. The NIR photon energy (red line) creates the exciton and sets the overall energy scale. Sidebands are visible around the NIR excitation, spaced by twice the THz frequency as inversion symmetry prevents odd order sidebands. The negative order sidebands fall off near-exponentially, arising from cascaded non-linear frequency mixing. The positive orders decay much more slowly, extending to much higher energies than the negative orders, and are the result of electron-hole recollisions driven by the THz field. Recent work used short NIR pulses to inject electron-hole pairs at specific phases of the driving

THz field and observed a time delay between optimal injection and the field crest of the driving field, consistent with the electron hole recollision picture [60].

The electron-hole recollisions which result in Fig. 1.6 arise from holes which are driven throughout a complicated band structure, such as the one shown in Fig. 1.4. As the hole travels through this complicated band structure, it accumulates various phases, both dynamical and geometrical (Sec. 1.1.5), which have significant impact on the resulting spectra [9]. The focus of this thesis is how the parameters of the NIR and THz fields (such as photon energies, polarizations or field strengths) can be changed to alter sideband spectra. Furthermore, the Berry phase accumulated in the wavefunctions of the holes as they travel through the band structures is imprinted in the polarization of the sidebands. Chapter 3 focuses on first steps to extract information about the local properties of the GaAs material investigated and develop the foundation for further measurements of Luttinger parameters and Berry Curvature.

1.3 UCSB Free Electron Lasers

As a final introduction, there are a pair of instruments unique to the University of California, Santa Barbara which have enabled this work: The UCSB Free Electron Lasers (FELs). Depicted in Fig. 1.7, an FEL first generates a relativistic electron beam which is then steered through an oscillating magnetic field [48]. The oscillating electric charges produce synchrotron radiation as it passes through the magnetic field (termed an undulator for the UCSB FELs, see [48] for the definition relative to a wiggler). When the

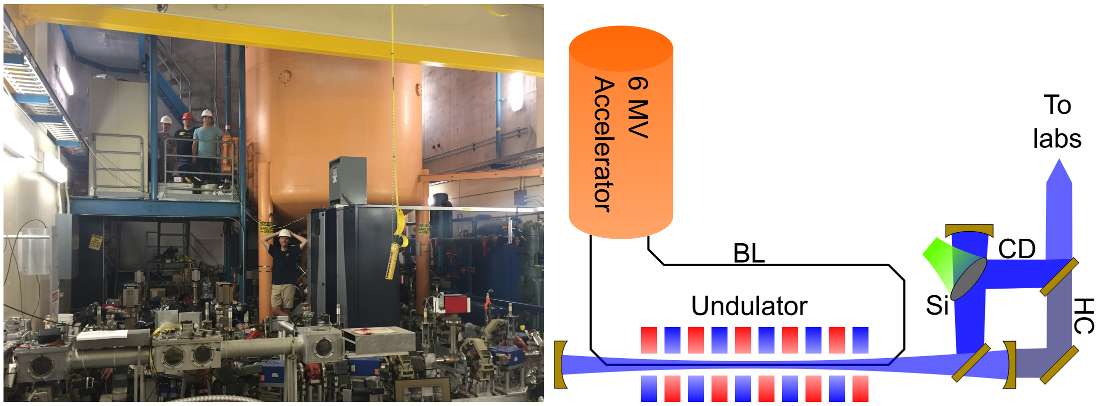

Figure 1.7: The UCSB FELs. (Left) Picture of the UCSB FELs, with the orange accelerator clearly visible. Four graduate students provide a sense of scale. The optical transport system is seen in the foreground along the bottom left. These evacuated steel tubes with plastic windows transport the THz radiation to the various user labs. (Right) Schematic overview of the FELs (only one undulator pictured). The 6 MV accelerator generates a relativistic electron beam. The electrons get steered through the electron beam line (BL) and sent into the undulator. The electrons oscillate in the undulator and THz is produced via synchrotron radiation. The THz is out-coupled through the hole coupler (HC), or cavity dumped (CD) by illumination of a silicon (Si) wafer with an intense visible laser pulse. A movable mirror in the THz cavity switches between the HC or CD.

undulator is enclosed in an optical cavity, the spontaneous synchrotron radiation can build up and coherently stimulate further synchrotron radiation to generate large optical powers.

The right side of Fig. 1.7 shows a schematic representation of the UCSB FELs. To generate the relativistic electron beam, a 6-MV linear electrostatic accelerator is used to produce several microsecond long electron pulses. This long pulse is able to produce coherent THz pulses of $1 - 2$ μs, which leads to very narrow linewidths across a wide tuning range [100, 109] (see Chapter 2). At UCSB, two undulators are currently in use and tuning the electron energy varies the radiation produced for each [90]: the millimeter-wave (MM) FEL produces radiation from 240 GHz to 700 GHz, while the far infrared

(FIR) FEL produces radiation from 1 THz to 4.5 THz. In standard operation of the UCSB FELs, a small portion of the light couples out of the cavity through a hole in the end-mirror of the cavity, known as the hole coupler. In the cavity dump coupler (CDC) available to the MM FEL, an insulating silicon wafer is inserted into the cavity near Brewster's angle allowing full transmission of the THz radiation as it builds up in the cavity [101, 50, 90]. Once sufficient radiation buildup has occurred, a 532 nm pulsed laser illuminates the silicon wafer generating a dense electron-hole plasma. This turns the silicon wafer into a THz mirror, allowing all of the radiation to be out-coupled within one round trip of the cavity (∼40 ns) and boosts the output powers from several kW to low 10's of kW up to 100 kW [109]. Unless otherwise specified, the FEL is operated in the CDC mode for all experiments in this work to access the larger available field strengths.

Chapter 2

High-Order Sideband Generation for Tunable Optical Frequency Combs

A frequency comb is a spectrum of light composed of many discrete peaks in frequency which are equally spaced apart. From the example spectrum of high-order sidebands in Fig. 1.6, high-order sideband generation (HSG) produces these equally spaced, discrete frequencies, making it a possible technique for generating optical frequency combs (OFCs). In this chapter, a brief introduction to frequency combs will be given. The utility of OFCs from HSG due to their wide tunability will then be demonstrated. Following this, a simple model for controlling the parameters of an HSG frequency comb will be derived. Finally, these combs will be used to characterize the NIR and THz laser sources used to generate the combs to show their utility.

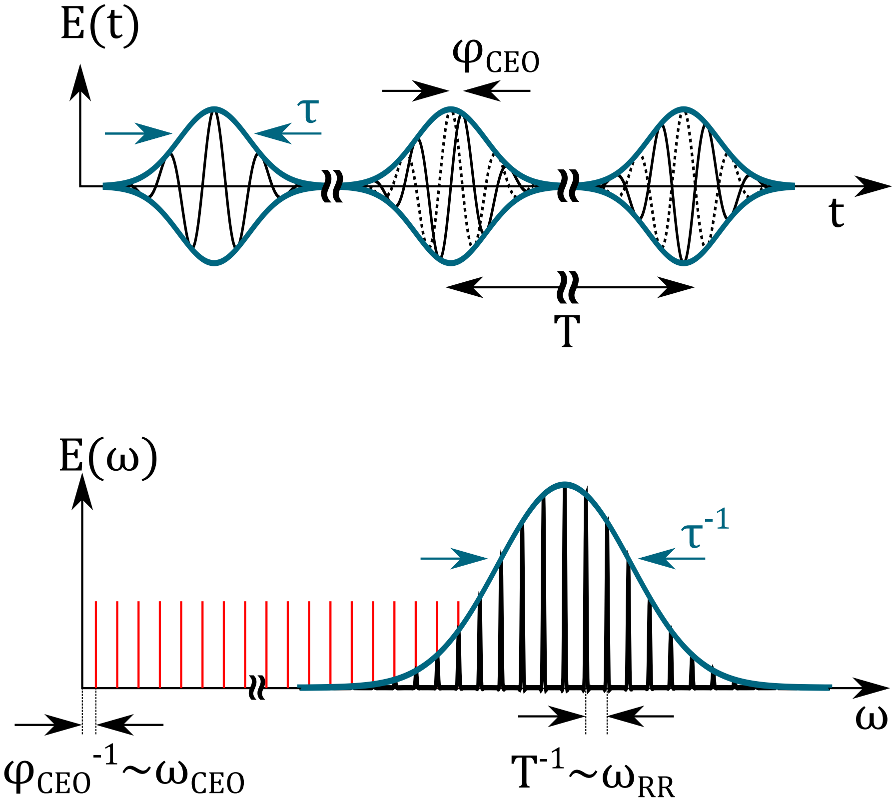

Figure 2.1: Schematic representation of the (top) time domain and (bottom) corresponding frequency domain for a frequency comb. Adapted from [127, 79]. φ_{CEO} is the carrier envelope offset phase, describing the relative shift between maxima of the electric field and envelope function. τ defines the width of the envelope of each pulse, and each pulse is separated by a period T. In frequency, the inverse of τ is related to the bandwidth of the comb, or how large of a frequency it spans. The inverse of the period is proportional to the repetition rate, ω_{RR}, which is the spacing between each of the teeth in the comb. When the teeth of the comb are extrapolated to zero frequency, it is possible for there to be an offset relative to zero. This offset is ω_{CEO} and is proportional to the inverse of the carrier envelope offset phase.

2.1 Fundamentals of Frequency Combs

Frequency combs results from a periodic train of short laser pulses, where the time between consecutive pulses is shorter than the duration of each pulse. If the phase difference between consecutive pulses in the train is constant (but not necessarily zero), this train of pulses results in a set of equally spaced Dirac peaks in frequency. These peaks look like the teeth of a comb, giving them the name frequency comb. Figure 2.1 depicts how the time-domain parameters of the pulse pulse train are related to the frequency parameters of the comb. The period between pulses, T, is the inverse of the repetition rate of the laser, ω_{RR}, which determines the spacing between the comb teeth. A drift between the relative maxima of the envelope function of the short pulse and the maxima of the electric field is called the carrier envelope offset phase, φ_{CEO}. In frequency, this causes non-zero offset between the first tooth of the comb and DC frequency. Any frequency in the comb is given in terms of these parameters by,

$$\omega_n = \omega_{\mathrm{CEO}} + n\omega_{\mathrm{RR}} \tag{2.1}$$

Optical frequency combs are used for a wide variety of applications such as calibration in astronomical spectrograms [99], use in high-resolution metrology [107], telecommunications [128], various other applications which are discussed in many review papers [54, 80]. The values of ω_{RR} and ω_{CEO} determine which applications a comb is best suited for. Different techniques for generating OFCs, as discussed below, can be used to create combs with repetition rates from several MHz to THz.

There are three primary methods commonly used for creating OFCs: mode-locked lasers (MLLs), nonlinear interactions with microresonators, and electro-optic modulation (EOM) of a continuous-wave laser. MLLs were used for the first [54, 88] realization of a frequency comb which could be stabilized for use in high precision measurements. To understand how a mode-locked laser operates, it is instructive to imagine the light traveling in the optical cavity of the laser in the time domain. When the light in the cavity is a single short coherent pulse bouncing back and forth within, the laser is called mode-locked. The duration of the pulse is much less than the round-trip time of the pulse circulating in the cavity. Each time the pulse reaches one end of the cavity, a small fraction of the power can be allowed to leak out into an output pulse. The period between each output pulse is therefore determined by the cavity length, and the width of each pulse is determined by the width of the wavepacket in the laser cavity.

Several methods exist for realizing this kind of discrete wavepacket in a laser cavity for creating OFCs. They are broken into two categories of active or passive mode-locking. In passive mode-locking, a nonlinear material exhibiting relatively high loss for low intensity light but lower loss for high intensity light, such as saturable absorbers or Kerr lensing, is inserted into the cavity of the laser. This medium causes the weaker spontaneous emission to be suppressed by high losses while the stronger, in-phase portions of the electric field are not significantly attenuated. In active mode-locking, an active component such as a piezo-controlled cavity mirror is used to modulate the cavity to permit ultra-short pulses. For an extensive overview of mode-locked lasers and applications, see [127].

Microresonator combs are created through nonlinear interaction of laser light with an ultra-high quality factor toroidal, spheroidal, or ring microresonator [27, 84]. By bringing a continuous-wave (CW) NIR laser close to the resonator, often through near-field coupling of a tapered fiber, the whispering-gallery modes in the resonator are excited. Through Kerr-nonlinear four-wave mixing, two pump photons from the CW laser can create a signal and idler photon pair, where each is separated from the CW laser by the free spectral range (FSR) of the resonator. Through cascaded four-wave mixings between the pump laser and the initial comb teeth, an equally space optical frequency comb is produced.

The final common scheme for generating OFCs, electro-optic modulation, starts with a phase modulator. Typically, a nonlinear crystal which permits the Pockels effect is used [106, 78] so that when a strong voltage is applied to the crystal, the index of refraction of the material is changed. A varying voltage is then applied at radio-frequencies (RFs) which modulates the index of refraction at this driving frequency. If a CW laser is sent through this RF modulated material, the changing index of refraction will result in new frequencies separated from the laser's wavelength by the frequency of the RF drive. Cascading multiple consecutive phase modulators can be used to create wide comb bandwidths [117, 106, 78].

The most widely used sources, MLLs, dominate the field because their combs easily span an optical octave, meaning the highest frequency tooth is at least twice the lowest frequency tooth. This is a significant feature for an OFC because the comb can be stabilized by mixing the second harmonic of a low frequency tooth with the tooth at twice the frequency [28], and feeding the resulting beat frequency to control electronics. However, the spacing of the teeth for MLLs, which is 100's of MHz to low GHz, and their overall offset are very difficult to tune since they depend on the cavity length of the laser [106, 88]. Microresonator combs, on the other hand, provide much larger comb spacings on the order of several 100's of GHz. Furthermore, the offset of the comb is determined by the CW laser which makes the center comb frequency continuously tunable. In order to change the comb spacing, however, a different device must be used with different dimensions to change the resonant frequencies of the microresonator [84]. In contrast to MLLs and microresonators, larger tunability in the comb spacing can be achieved with EOM frequency combs by simply changing the frequency of the voltage driving the crystal. EOM-based combs also provide continuously tunable center frequency by changing the CW laser's frequency. The tooth spacing, however, is still limited to 10's of GHz due to the difficulty of driving electronics at higher frequencies. Furthermore, generating large bandwidths requires carefully cascading several phase modulators together, which is a non-trivial process [106, 78]. High-order sideband generation, similar to combs from EOM, provides widely tunable center and spacing frequencies since both are controlled by separate, fully tunable lasers. Here, I introduce such HSG frequency combs and then develop a method for determining the bandwidths of these combs depending on the driving field parameters.

2.2 Optical Frequency Combs from HSG

To demonstrate the tunability of HSG frequency combs, Figure 2.2 shows OFCs produced from a 10 nm GaAs QW for several THz and NIR frequencies. In Fig. 2.2(a-e), the THz frequency was tuned between 247 GHz to 633 GHz, and the peak field strength listed corresponds to the highest achieved field strength from the FEL in the sample. The frequencies were chosen to correspond to the maximum field enhancements from the sample cavity (see Sec. B.1 and Ref. [9]). The spectra in Fig. 2.2(a-e) were taken with the EMCCD attached to the imaging spectrometer, which had a bandwidth of approximately 50 nm in each image. To capture the full bandwidth of each comb, multiple images were required with the spectrometer center bandwidth changed, depicted by the grey, red and blue curves in Fig. 2.2(a-e). Additionally, longer exposures were performed for the higher-order sidebands to lower the noise floor. Each spectrum was normalized to the number of FEL pulses so they can be directly compared.

In Fig. 2.2(a), a THz driving field 7 kV/cm at 247 GHz was used. The low field strength and frequency resulted in a comb which was only 30 meV wide and was captured in a single image. At 24 kV/cm of 341 GHz, Fig. 2.2(b), a much larger 140 meV wide comb was produced, requiring two spectrometer steps. The largest comb was 330 meV wide and produced by 54 kV/cm at 633 GHz, requiring stitching three spectrometer steps, Fig. 2.2(e).

To compare the combs from different THz field strengths and frequencies, each peak

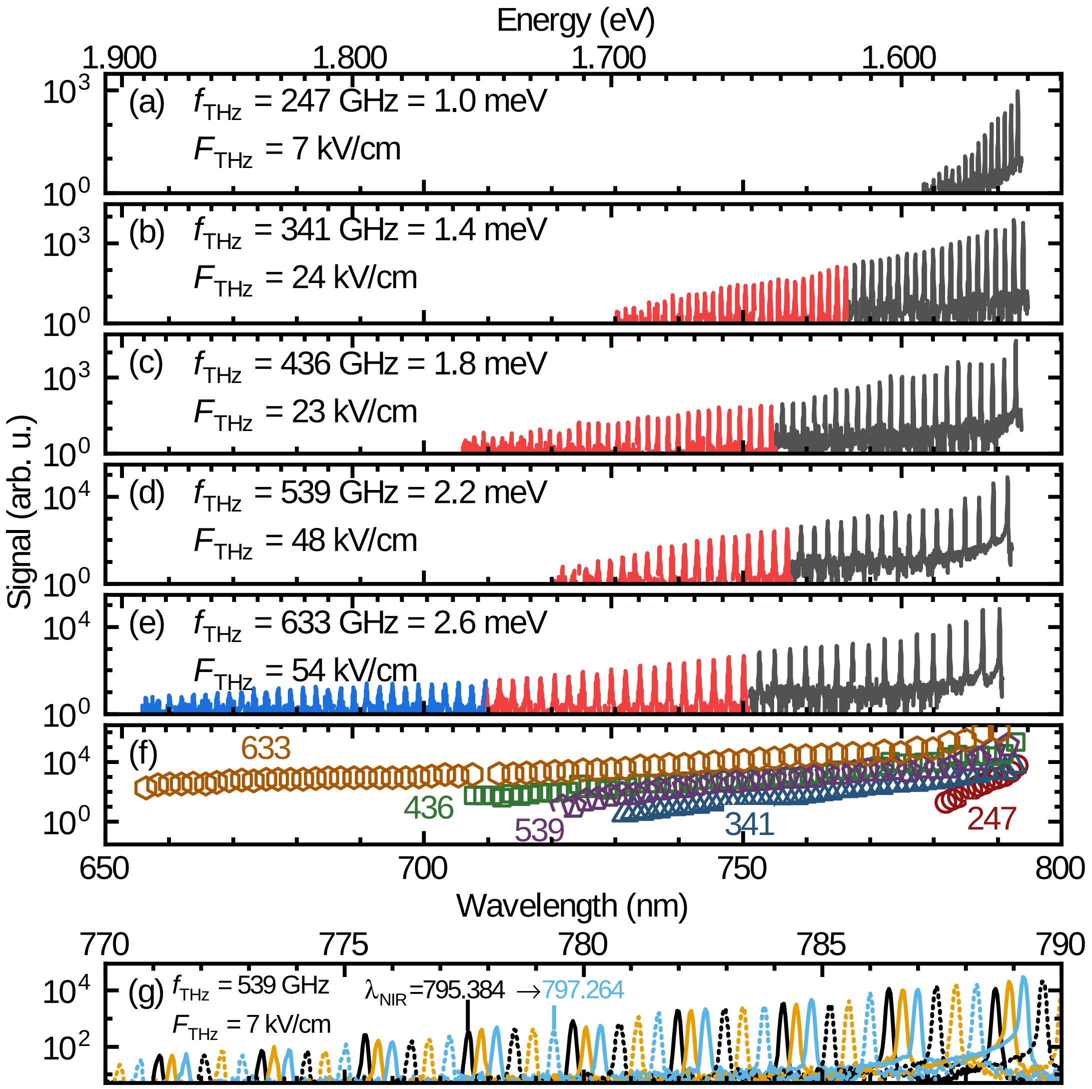

Figure 2.2: Optical frequency combs with variable tooth spacing and offset frequency from HSG in 10 nm GaAs quantum wells. (a-e) Spectra of positive order sidebands measured by the CCD for increasing THz frequencies, where the frequency and field strength are listed in the top left of each plot. The different colors correspond to spectra taken with different grating positions in the monochromator, and integration times ranging from ∼25 to ∼250 FEL pulses. (f) Strength of each sideband (area under Gaussian fit) vs. wavelength for HSG spectra generated by THz fields at 247 GHz (red circles), 341 GHz (blue triangles), 436 GHz (green squares), 539 GHz (purple pentagons), and 633 GHz (gold hexagons). Spectra are offset slightly for visibility. For each comb, the tooth spacing is $2 \times f_{\mathrm{THz}}$. (g) Spectra measured by the CCD for a THz field of 7 kV/cm at 539 GHz with several NIR excitation wavelengths spaced by roughly 0.4 nm. Values of λ_{NIR}, in nm, are indicated for the smallest (solid black) and largest (dashed teal) NIR laser excitation wavelengths used.

in the comb was fit to a Gaussian, and the area of those Gaussians is shown in Fig. 2.2(f). While each spectrum in Fig. 2.2(f) displays a roughly exponential decay with increasing order, the rate of decay for each spectrum varies drastically. At 247 GHz, the low frequency and field strength resulted in a rapid fall-off in sideband strength with order compared to the higher driving frequencies.

In addition to continuously tuning the comb spacing by changing the THz frequency, it was also possible to continuously tune the comb offset frequency by changing the NIR laser excitation frequency. Figure 2.2(g) shows an example of different OFCs produced with identical THz fields of 7 kV/cm and 539 GHz, but various NIR frequencies. When exciting near 800 nm and driving at 539 GHz, the comb spacing is approximately 2.3 nm. By tuning the excitation frequency through 2 nm around the heavy hole exciton resonance, it was possible to achieve arbitrary comb frequencies.

Larger changes in the center frequency were also accomplished by performing HSG in a material with a different band gap. Figure 2.3 shows the frequency combs resulting from a 5 nm GaAs QW, whose band gap was roughly 764 nm. Figure 2.3(a) shows a 240 meV wide comb produced from 61 kV/cm at 633 GHz, which was centered at 760 nm instead of 800 nm shown in Fig. 2.2(e). Figure 2.3(b) shows a comb produced driving at 736 GHz with 35 kV/cm, further demonstrating the wide tooth spacing possible simply from tuning the THz frequency. The field strength used in this data had to be reduced from the maximum achievable fields (roughly 50 kV/cm) to prevent damage to the sample.

Figure 2.3(c) shows the integrated sideband intensities versus wavelength for similar

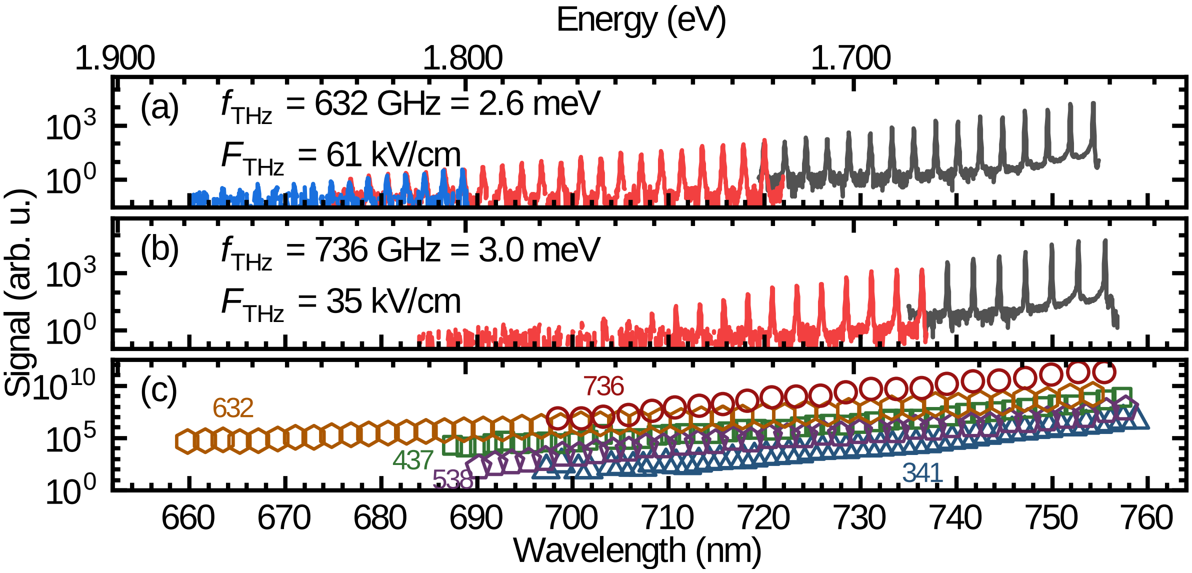

Figure 2.3: Optical frequency combs with variable tooth spacing from HSG in 5 nm GaAs quantum wells, demonstrating a large offset in comb center is possible with material design. (a,b) Raw spectra for driving with (a) 632 GHz at 61 kV/cm and (b) 736 GHz at 35 kV/cm. (c) Strength of each sideband (area under Gaussian fit) vs. wavelength for HSG spectra generated by THz fields at 341 GHz (blue triangles), 437 GHz (green squares), 538 GHz (purple pentagons), 632 GHz (gold hexagons) and 736 GHz (red circles). Spectra are offset slightly for visibility.

fields to Fig. 2.2(g), with 21 kV/cm at 341 GHz, 22 kV/cm at 437 GHz, 50 kV/cm at 538 GHz, 61 kV/cm at 633 GHz, and 35 kV/cm at 736 GHz. The 736 GHz data had a much higher noise floor as no long integration data was taken due to sample damage. Each spectra in Fig. 2.3(c) shows an exponential decay, again at different rates at different frequencies. Interestingly, the combs do not extend beyond roughly 660 nm, similar to Fig. 2.2(f). The barrier in both the 10 nm GaAs QW (Fig. 2.2) and the 5 nm GaAs QW (Fig. 2.3) was $\mathrm{Al}_{0.3}\mathrm{Ga}_{0.7}\mathrm{As}$, which has a low temperature band gap of 1.9 eV (653 nm). Electrons and holes may begin scattering into the barrier regions when they have enough energy to emit this high energy sidebands, resulting in significantly reduced signal. It is also possible that the absorbance is significantly increased below ∼650 nm as the barrier regions begin absorbing more, providing another mechanism for reducing sideband signal at higher energies[1].

2.3 Controlled Manipulation of Comb Bandwidths

As can be seen from Fig. 2.2(f) and Fig. 2.3(c), the sidebands produced from various THz field strengths and frequencies can produce a wide variety of comb bandwidths. In high-harmonic generation, the three step model predicts a maximum harmonic energy, E_{max}, which scales with the strong laser's electric field, F, and frequency, ω, as discussed in Sec. 1.2. This simple cutoff relation has been observed in experiments [57]. For HSG, such

---

[1] Unfortunately, the loss of signal around 650 nm may also result from the optics. All optics used after the sample utilize Thorlab's '-B' AR coatings, which extend 630-1050 nm, quite close to the signal cutoff observed.

cutoffs are predicted by theory in the absence of scattering [67, 125, 124], but have not been observed in experiment [133, 9, 10]. In the presence of scattering, electrons and holes may be scattered and prevented from coherently recolliding to create a sideband. Because the time between electron-hole excitation and recollision increases with increasing order, the attenuation of sidebands due to scattering increases with increasing order, making it difficult to observe the predicted plateau and cutoff. For the spectra shown in Fig. 2.2 and Fig. 2.3, the predicted cutoff wavelength at the field strengths listed is nearly 520 nm at 247 GHz or 150 nm at 633 GHz, which would have produced much larger bandwidths than those observed. One should not expect to observe sidebands associated with recollisions that take much longer than than typical scattering times, which are $\sim$ 200 fs in these samples [10].

If scattering is the dominant mechanism for determining the rate of decay of sideband intensity, one might expect that, for sidebands associated with similar duration electron hole recollisions occurring during analogous electric field profiles, should display similar intensities. To illustrate this, the top of Fig. 2.4 depicts a portion of a period of the THz waveform at four different field strength and frequency combinations chosen to give identical electric fields, $F_{\mathrm{THz}}(t)$ near the zero-crossing of the THz field. The left side shows lower peak field strengths compared to the right.

The dynamics from the three-step model [23], assuming simple parabolic bands with conduction band effective mass $0.063m_e$ and a valence band effective mass $0.1m_e$ (m_e is the free electron mass) [10] can be solved numerically to find the recollision times

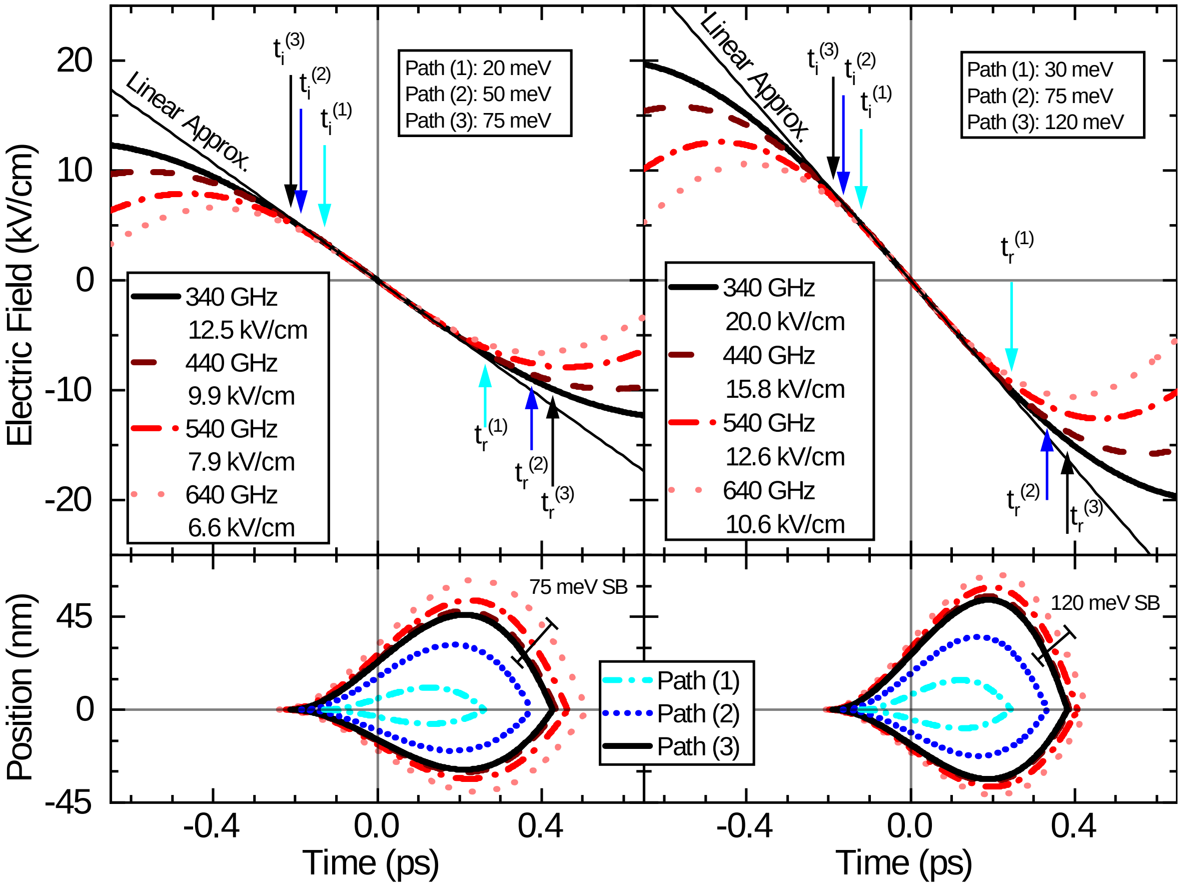

Figure 2.4: Classical carrier dynamics. (top) THz field for four driving fields chosen such that the field-frequency products at the zero crossings are equivalent, (left) $f_{\text{THz}}F_{\text{THz}} \approx$ 4.3 THz $\cdot$ kV/cm (right) $f_{\text{THz}}F_{\text{THz}} \approx$ 6.8 THz $\cdot$ kV/cm. The ionization times, $t_i^{(m)}$, and and recollision times, $t_f^{(m)}$, are specified for various sideband energy offsets: (left) (1) 20 meV (2) 50 meV and (3) 75 meV, (right) (1) 30 meV (2) 75 meV and (3) 125 meV. Sideband energies calculated from the semiclassical three-step model under a 340 GHz, (left) 12.5 kV/cm, (right) 20 kV/cm driving field using Eqs. 1.31. Each of the three steps of the recollision model occur during portion of the driving field when the electric field is approximately linear in time, as shown by the Linear Approx. line. (bottom) Classical trajectories for low-energy sideband (cyan dash-dot), mid-energy sideband (blue dotted) and high-energy sideband (solid black) for the offset energies specified in the top panel (calculated using the full sinusoidal electric field profile). The solid black, dashed deep red, dash-dot red, and dotted pink lines show the trajectories for a (left) 75 meV or (right) 120 meV energy offset sideband when driven at 340 GHz, 440 GHz, 540 GHz and 640 GHz, respectively.

and trajectories (see Fig 2.4, bottom and Sec. 1.2) for the injection times associated with various sideband offset frequencies at these fields. The three arrows in the top two panels of Fig. 2.4 show the ionization ($t_i^{(m)}$) and recollision ($t_r^{(m)}$) times for three different sideband offset energies.

At lower electric fields, top left, these energies correspond to 20 meV ($n \approx 14$ at $f_{\mathrm{THz}} = 340$ GHz), 50 meV ($n \approx 36$), and 75 meV ($n \approx 54$), as calculated for the 12.5 kV/cm field at 340 GHz. At higher electric fields, top right, these energies correspond to 30 meV ($n \approx 20$), 75 meV ($n \approx 54$), and 120 meV ($n \approx 86$), as calculated for the 20 kV/cm field at 340 GHz. In the frequency comb spectra of Fig. 2.2 and Fig. 2.3 when driven at 340 GHz and ~ 20 kV/cm, the largest sideband offset energy was approximately 140 meV and 155 meV, respectively. Compared with the top right of Fig. 2.4, most of these sidebands were therefore created during the linear portion of the driving field where,

$$F_{\mathrm{THz}}(t) = F_{\mathrm{THz}} \sin(2\pi f_{\mathrm{THz}} t) \approx F_{\mathrm{THz}} 2\pi f_{\mathrm{THz}} t \tag{2.2}$$

with F_{THz} and f_{THz} being the electric field's amplitude and frequency, respectively.

For THz fields satisfying $F_{\mathrm{THz}} f_{\mathrm{THz}} \approx$ constant, if an electron and hole are injected and recollide while the THz field is close to linear in time, they should produce sidebands with roughly the same strength for different THz frequencies. If typical scattering times are sufficiently short, one also expects similar comb bandwidths. Since the driving frequency is changing, however, the spacing between comb teeth will vary, and this scaling would provide a knob for controlling comb spacings while keeping the bandwidths consistent.

To test this scaling law, two quantum well (QW) samples were driven with several

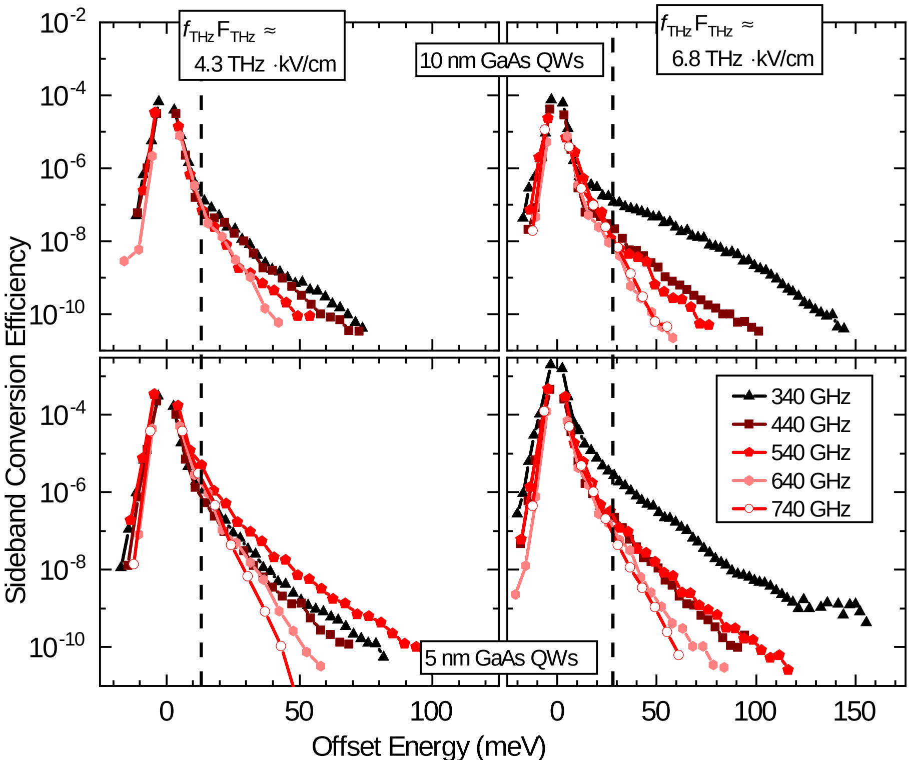

Figure 2.5: Sideband conversion efficiency for (top) a 10 nm GaAs QW structure and (bottom) a 5 nm GaAs QW sample when the driving THz is tuned such that $f_{\mathrm{THz}}F_{\mathrm{THz}} \approx$ Const. (Left) Field strengths are 12.5 kV/cm at 340 GHz, 9.9 kV/cm at 440 GHz, 7.9 kV/cm at 540 GHz, 6.6 kV/cm at 640 GHz, 5.7 kV/cm at 740 GHz, corresponding to $f_{\mathrm{THz}}F_{\mathrm{THz}} \approx 4.3$ THz · kV/cm. (Right) Field strengths are 20.0 kV/cm at 340 GHz, 15.8 kV/cm at 440 GHz, 12.6 kV/cm at 540 GHz, 10.6 kV/cm at 640 GHz, 9.2 kV/cm at 740 GHz, corresponding to $f_{\mathrm{THz}}F_{\mathrm{THz}} \approx 6.8$ THz · kV/cm. Dashed lines indicate the offset frequency of a sideband emitted at time when the 640 GHz field profile deviates from the linear approximation by 10%, 13 meV for the low field and 28 meV for high field. The hole coupler on the FEL was used for the 640 and 740 GHz data.

combinations of frequency and field with different products $F_{\mathrm{THz}} f_{\mathrm{THz}}$. The resulting sideband conversion efficiencies[2] are shown in Fig. 2.5. The top two plots show the results from a clean 10 nm GaAs QW with a heavy-hole exciton (HHX) linewidth of of approximately 2.0 meV, while the bottom plots show the results from a 5 nm QW in which the well-width fluctuations result in a proportionally broadened HHX linewidth of 6.3 meV (see Sec. A.1 and Ref. [9] for details on the samples). For each quantum well studied, the left (right) plots show the sideband conversion efficiencies for $f_{\mathrm{THz}} F_{\mathrm{THz}}$=4.3 (6.8) THz·kV/cm.

In the 10 nm QW sample at lower electric fields (Fig. 2.5 upper left), each frequency and field combination resulted in equal sideband conversion efficiencies up to around a 13 meV sideband offset frequency (vertical dashed line). Above a 13 meV offset, the 340 GHz comb and 440 GHz combs resulted in higher sideband powers than the 540 and 640 GHz combs. At 340 and 440 GHz, a ∼70 meV wide comb was observed, but only 50 meV and 40 meV were observed at a 540 and 640 GHz driving frequency, respectively. Generally, the lower frequency driving fields resulted in combs with a larger sideband strength bandwidth relative to higher frequencies.

To understand why each comb produced slightly different sideband strengths and comb bandwidths, counter to the initial hypothesis, consider where the linear electric field approximation begins to break down. Figure 2.4 shows that higher frequencies deviate from the linear approximation more quickly than lower frequencies. For 7 kV/cm at 640 GHz, the time at which the field deviates from the linear approximation by 10%

---

[2] Sideband conversion efficiency is the normalized sideband power to the incident NIR power

corresponds to the recollision of an electron-hole pair responsible for the emission of a 13 meV sideband (depicted by a vertical dashed line in the left side of Fig. 2.5). Below this sideband offset, all combs for the low-field driven 10 nm GaAs sample agreed quite well. Above this offset, the deviation from a linear field at higher frequencies results in longer times required to recollide electrons and holes for an equivalent sideband energy relative to lower frequencies.

The bottom left of Fig. 2.4 shows the recollision trajectories for an electron and hole which would emit a 75 meV sideband at 340 GHz (solid black), 440 GHz (dashed crimson), 540 GHz (dash-dot red) and 640 GHz (long dot pink). At 640 GHz, it takes nearly 100 fs longer than at 340 GHz for the electron and hole to recollide, substantially increasing the chance for the electron or hole to scatter. This results in lower sideband signal and comb bandwidths, which matches the observed trends in the top left of Fig. 2.5.

These trends are also evident in the other panels of Fig. 2.5, with three notable exceptions. For the 5 nm QW at low field (lower left, Fig. 2.5) sidebands were similar in efficiency below the 13 meV offset, and most of the lower driving frequencies produced stronger sidebands than higher frequencies. In this sample, 740 GHz data was taken which follows the previous trends by producing the weakest combs. The exception with this sample at the lower fields was the comb produced from the 540 GHz field was stronger than the others.

At higher fields, Fig. 2.5 right, a 10% deviation of the 640 GHz electric field from the linear approximation now corresponds to a 28 meV sideband. 740 GHz data was also taken for both samples at high field (the high field data was taken before the low field, and damage occurred to the 10 nm GaAs QW during the low field before low field 740 GHz data could be taken). The sidebands from the 440, 540, 640, and 740 GHz combs were similar in power below 28 meV offset. Above this offset, higher frequencies yielded narrower combs and weaker sidebands in both samples for all but the 540 GHz comb in the 5 nm QW which equaled the 440 GHz comb. The major exceptions at the higher fields were that the 340 GHz combs were significantly stronger and wider for both samples.

While the proposed scaling law, with adjustments to account for deviations from the linear approximation, captures many observed trends, it is clearly insufficient to describe all of the data. The assumption that electrons and holes each travel in a single, parabolic band may be one of the problems. In GaAs QWs, there are several closely-spaced and strongly-mixed valence subbands, with several low-energy avoided crossings (see Fig. 1.4). It has been shown that sideband polarizations and intensities are sensitive to the motion of holes through these avoided crossings sidebands [9] (and see Chapter 3). Accounting for the influence of the complexity of the valence subbands on the scaling of HSG was outside the scope of the work performed in this section.

2.4 Measuring the free electron laser

As an application of these frequency combs, I use them here to characterize the Free Electron Laser (FEL) used in these experiments. While the optical and infrared regions

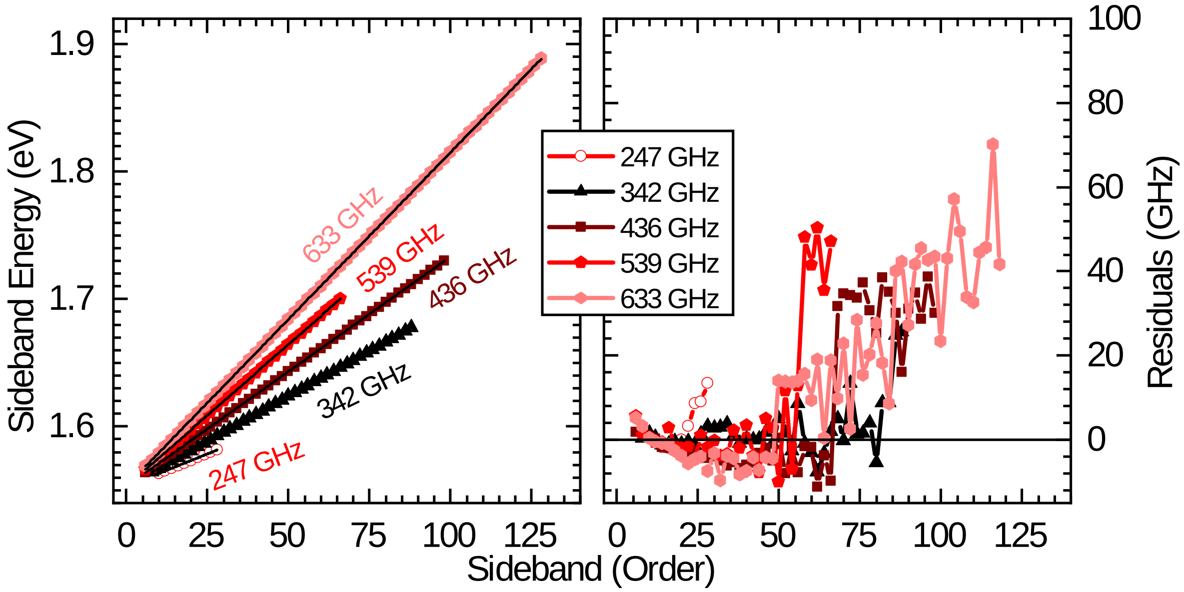

Figure 2.6: Determining the frequency of the FEL. (a) The frequency of each sideband vs sideband order, with linear fits. Sidebands are taken from the combs shown in Fig. 2.2. (b) The residuals of the fits from (a)

of radiation benefit from a myriad of methods of measuring their spectral properties over a large bandwidth, the THz regime lacks a similar ease of these measurements. Often, specialized setups are designed for specific applications. For example, the UCSB high-field electron paramagnetic resonance lab makes use of heterodyne mixing scheme [100, 101], but is limited to a narrow bandwidth; electro-optic sampling (EOS) is a phase-sensitive technique and widely used for performing THz spectroscopy [122], but requires phase stable source to average over many pulses; and holographic Fourier transform techniques have been demonstrated [1], but it requires high powers and expensive array detectors. HSG, however, is a technique for measuring the frequency and, as will be shown, linewidth of the driving THz field over a large operating bandwidth, on a phase-unstable source, while being robust to alignment.

High-order sideband generation serves to map THz frequencies onto NIR frequencies, which allows it to use the superior optical detectors to extract parameters about the THz field. Similar techniques, such as first-order, perturbative sideband generation based on the linear electro-optic effect, in which $f_{\mathrm{SB}} = f_{\mathrm{NIR}} \pm f_{\mathrm{THz}}$, have been used to measure THz frequencies [135, 134]. In these single-sideband measurements, if the uncertainty in the NIR laser frequency is negligible, the uncertainty in the THz frequency δf_{THz} is limited by the resolution of the sideband frequency δf_{SB}, which is determined by the monochromator and CCD. In an HSG spectrum, the sidebands are seen at $f_{\mathrm{SB}} = f_{\mathrm{NIR}} + n f_{\mathrm{THz}}$ (n even), and the corresponding uncertainty of the THz frequency, δf_{THz}, is $\frac{1}{n}[\delta f_{\mathrm{NIR}}^2 + \delta f_{\mathrm{SB}}^2]^{1/2}$. If the frequency of the NIR laser is measured or known to high precision, $\delta f_{\mathrm{NIR}} \ll \delta f_{\mathrm{SB}}$, the uncertainty in the THz frequency is then approximately $\frac{1}{n}\delta f_{\mathrm{SB}}$, more than 100 times smaller than δf_{SB} if $n > 100$. Each of the frequencies reported in Fig. 2.2 comes from the slope of the linear fit of sideband frequency versus sideband order, shown in Fig. 2.6. The covariance from the fits indicate the uncertainty of the frequency is within 1 GHz. The shape of the residuals in Fig. 2.6 indicates the calibration on spectrometer could be improved slightly.

The linewidth of the UCSB FEL output is too small to measure using first-order, perturbative sideband generation. However, it can be measured using HSG. The linewidth of each sideband, Γ_{SB}, depends on the resolution of the spectrometer, Γ_{spec}, as well as the linewidth of the FEL, Γ_{FEL}. A THz pulse from the UCSB FEL contains contributions from multiple longitudinal modes of the cavity, resulting in each pulse containing several

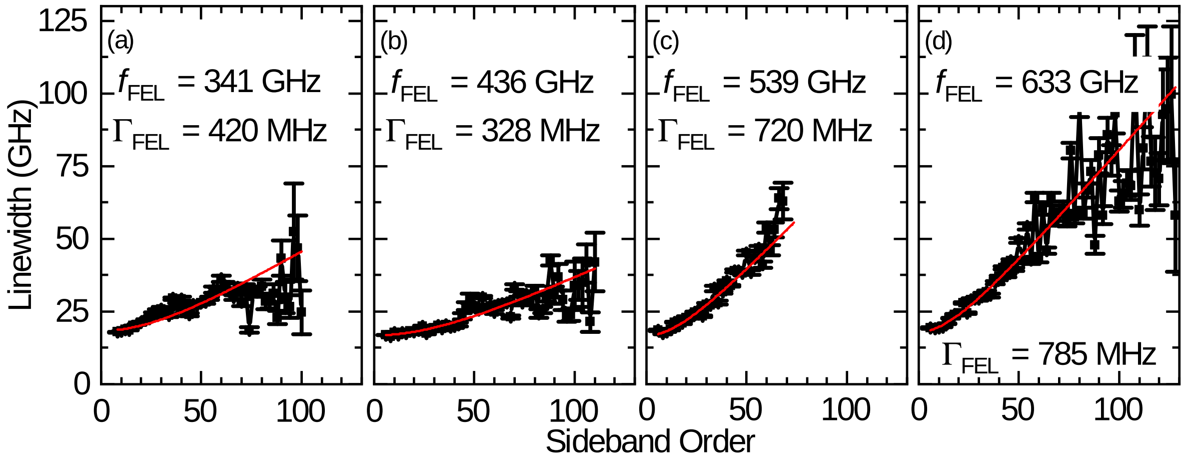

Figure 2.7: Linewidths of sidebands taken as the Gaussian widths from the fit of the spectra shown in Fig. 2.2. Each spectra is fit to Eq. 2.3 to extract the linewidth of the FEL at each frequency.

of these modes simultaneously. Competition between each mode causes pulse-to-pulse fluctuations in the spectral contents of each pulse [100], in addition to fluctuations in radiated power. This inhomogeneous broadening results in a sideband linewidth given by

$$\Gamma_{\mathrm{SB}} = \sqrt{\Gamma_{\mathrm{spec}}^2 + n^2\Gamma_{\mathrm{FEL}}^2} \tag{2.3}$$

Figure 2.7 shows the linewidths of the sidebands from the combs shown in Fig. 2.2, and the corresponding fits to Eq. 2.3. At low orders, $n \lesssim 20$, the linewidths are limited by the resolution of the spectrometer, which is approximately 20 GHz depending on experimental conditions (such as the width of the entrance slits and adequate f-matching with the spectrometer). The FEL linewidth contributes to the measured linewidth of sidebands only above about 20th-order. From Fig. 2.7, the extracted FEL linewidths are $\Gamma_{\text{FEL, 341 GHz}} = 420 \pm 21$ MHz, $\Gamma_{\text{FEL, 436 GHz}} = 328 \pm 12$ MHz, $\Gamma_{\text{FEL, 539 GHz}} = 720 \pm 16$ MHz, and $\Gamma_{\text{FEL, 633 GHz}} = 785 \pm 15$ MHz with errors taken as the covariance of the fits to Eq. 2.3. At 247 GHz, the low field strength and low frequency resulted in too few sidebands observed to accurately determine the FEL linewidth. At the remaining THz frequencies, the FEL linewidth is well resolved and below 1 GHz, matching previous measurements with a sub-band harmonic mixer, which only works in a very small frequency range [100].

2.5 Conclusion

High-order sideband generation provides a mechanism for generating optical frequency combs with bandwidths exceeding 330 meV with continuous control the offset frequency and comb spacing. These results demonstrate the ability to tune the comb offset frequency throughout the comb spacing by varying the NIR laser frequency near the band gap of the GaAs QWs used. Combs centered at different frequencies can be created by choosing materials with band gaps in the desired frequency range, for example by choosing quantum wells with different widths or compositions, as demonstrated here, or using altogether different semiconductors [60, 132], and Chapter 4. Furthermore, Fig. 2.2 and Fig. 2.3 show the ability to tune the comb spacing between 480 GHz to 1470 GHz. Much higher spacings of 3 THz [133] or even 60 THz [60] are possible with higher frequency driving field. I have shown that OFCs based on HSG are practical for measuring the linewidth of our THz source over a large frequency range. While the high power of an FEL was utilized in this work, careful microwave engineering [133] or use of antenna structures [8] can provide comparable fields using compact sources with much lower power than the FEL. Demonstration of HSG using such a compact source would open the door to applications of OFCs based on HSG in metrology, spectroscopy, telecommunications, and other areas. The results of this chapter illustrate some of the trade-offs between THz field and frequency that will be required in the design of OFCs based on HSG.

Chapter 3

Polarimetry of High Order Sidebands

In the three-step recollision model of high-order sideband generation (HSG) discussed in Sec. 1.2.2, the process of HSG was described by the collision between electrons and holes after each is driven through their respective momentum bands. Chapter 2 used simplified two parabolic bands for the dispersion to describe the dynamics, as shown in Fig. 2.4. We have discovered, however, that the full band structure of the material (such as those depicted in Figs. 1.2 and 1.4) is required to understand some of the features of HSG. Namely, the phenomenon of "dynamical birefringence" (DBR) [9] refers to the features of HSG wherein (1) the intensities of the sidebands depend on the polarization of the NIR and THz polarizations and (2) the polarization of the sidebands also depend on the laser polarizations and can deviate significantly from the NIR laser polarization.

The initial observations of dynamical birefringence [9] were restricted in their ability to carefully control and measure the NIR polarizations used. While it was sufficient to observe the sideband intensity dependences on the NIR polarization, the NIR polarizations were limited to nearly parallel or perpendicular to the THz field. Furthermore, the polarization states of the sidebands were only measured when the THz field was parallel to a high symmetry axis of the crystals studied, which caused the direction of the THz to be a “dynamical optical axis”. Similar to the optical axis of linearly birefringent materials where a polarization parallel or perpendicular to the optical axis is unchanged, a dynamical optical axis indicates the direction which, when the NIR polarization is parallel or perpendicular to, results in unchanged sideband polarizations. The end result is that when exciting with NIR polarizations nearly parallel or perpendicular to the dynamical optical axis, the polarizations of the sidebands change by only a few degrees.

Recent experiments in high-harmonic generation (HHG) have measured the polarization of harmonics to observe a 90° flip in even versus odd order harmonics [66, 59, 61]. Further experiments have measured the polarization to observe a rotation of the harmonics related to the crystal symmetry [129], or used multiple excitation sources with carefully controlled polarizations to control the polarization of the harmonics [46]. Some experiments have also hoped to extract information about the Berry Curvature with these methods [66], however the theoretical modeling in HHG is complicated by the interplay of inter- and intra-band currents (see Sec. 1.2.1).

High-order sideband generation, on the other hand, decouples the inter-band and intra-band components and may provide easier access to the underlying physics. For example, Section 1.1.1 introduced the Kane model and Bloch functions in GaAs to describe the band structure and wavefunctions throughout the Brillouin zone. Coupling between the Bloch wavefunctions causes the wavefunctions at finite momentum to be superpositions of the various $\mathbf{k} = 0$ Bloch functions. When momentum is considered as a parameter of the Hamiltonian, this mixing of wavefunctions with momentum is a manifestation of Berry Curvature, as described in Sec. 1.1.5 and Eq. 1.28. As the hole travels through momentum space and its wavefunction becomes a mixture of Bloch wavefunctions of different angular momenta (Eq. 1.4), the recollision with its electron emits different polarization states, depending on the optical selection rules in Section 1.1.3. Therefore, measuring the polarization of the sidebands and correlating these changes in polarization with the evolution of the Bloch wavefunctions provides a pathway for extracting Berry Curvature from HSG.

In this chapter, I will discuss observations of DBR from a substantially improved experimental setup. This includes results for NIR polarizations not strictly parallel or perpendicular to the dynamical optical axis, and with the THz polarized away from a high symmetry axis. The results were then used to introduce the utility of dynamical Jones calculus to quantitatively describe dynamical birefringence. A theoretical model will be describe to compare with the experimental results and introduced as a method for extracting strain and the Luttinger parameters from GaAs as first steps to measuring Berry Curvature directly.

3.1 Improved Polarization Measurements

The new experimental apparatus which enabled the work of this chapter is describe in detail in Appendix A. One of the substantial additions was an off-the-shelf polarimeter from Thorlabs (PAX1000IR1) which provided instantaneous read-out of the NIR polarization used in experiments. The second significant improvement was to use both a quarter-wave and half-wave plate pair (instead of a single half-wave plate as in Ref. [9]). The two wave plates in tandem were able to provide any polarization state at the sample, as measured quickly and accurately (with $\lesssim 0.2^\circ$ error on rotation and ellipticity) from the PAX. This removed the uncertainties on the NIR polarization which may have previously skewed the agreement between theory and experiment as well as allowing the study of more interesting excitation polarizations.

Figure 3.1 shows the measured polarization states of the sidebands for two different samples (sideband polarization measurements still required the use of a custom polarimeter, see Appendix D). Polarizations are reported using the polarization ellipse shown in Fig. D.2, where α denotes the rotation angle and γ denotes the ellipticity. The left side of Fig. 3.1 shows the polarization states for the same 10 nm AlGaAs quantum well (QW) sample used in Ref. [9][1], excited at λ_{NIR} =765.00 nm with 50 mW power, and driven by 30 kV/cm at 540 GHz. The right side shows the results for 500 nm of bulk GaAs excited with 50 mW of λ_{NIR} =815.750 nm and driven by 35 kV/cm at 540 GHz. The THz polarization was fixed at horizontal with respect to the lab frame, but the sample

---

[1] The sample here is actually a different fabrication run, but from the same wafer

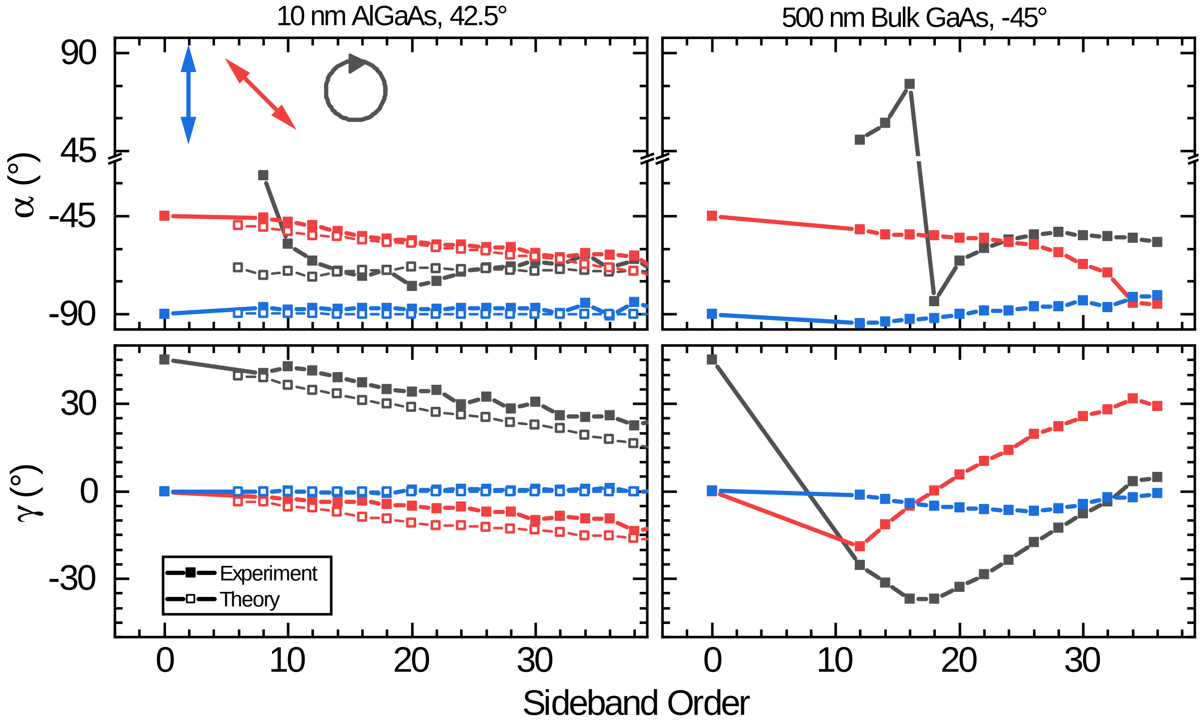

Figure 3.1: Polarimetry from two different samples, a 10 nm AlGaAs QW (left) and a 500 nm bulk GaAs (right). The top plot shows the rotation angle of the sidebands, α, and the bottom shows the ellipticity, γ. Sideband order $n = 0$ corresponds to the laser line. The THz was at an angle of 42.5° with respect to the [010] axis in the AlGaAs sample and $-45°$ for the bulk GaAs (measured positive angles are counter-clockwise). Each sample was excited by three different NIR polarizations, schematically shown in the top-left plot: perpendicular to the THz (blue curves), $-45°$ with respect to the THz (red curves) and right-hand circularly polarized light (grey curves). α for the NIR laser for the circular polarizations is omitted as it is undefined. The theoretical points (open squares for the AlGaAs sample) were calculated for the theory describe in Ref. [9]. Polarizations remain relatively unchanged when the NIR is polarized parallel to the THz. Sideband polarizations change significantly more when the NIR polarization is changed, and the change is more drastic for the bulk sample than the quantum well.

was rotated to change the relative THz polarization with respect to the crystal. For the AlGaAs sample, the THz field was at an angle of 42.5° with respect to the [010] crystal direction[2] and the bulk GaAs sample had the THz at −45° with respect to the [010] direction. Each sample was excited by NIR polarization perpendicular to the THz field ($\alpha_{\text{NIR}} = 90°$, $\gamma_{\text{NIR}} = 0°$, blue curves), at an angle of $\alpha_{\text{NIR}} = -45°$ with respect to the THz ($\gamma_{\text{NIR}} = 0°$, red curve) which makes the NIR nearly parallel to the [010] or [001] directions of the crystal. Finally, they were excited by right-hand circular polarizations, as viewed along the propagation direction ($\gamma_{\text{NIR}} = 45°$, grey curve). Each NIR polarization state is depicted schematically in the upper left of the image. The top of Fig. 3.1 shows the angle of the major axis of the polarization ellipse, α, for each sideband, and the bottom shows the ellipticity, γ.

In the 10 nm AlGaAs sample, we can see the clear dynamical optical axis in the sideband polarizations for the perpendicular excitation (blue curve). The angle of the sidebands, α, closely followed the NIR laser and stayed within a few degrees of −90° and the ellipticity γ stayed close to 0°. To observe a more pronounced effect from dynamical birefringence, one must change the NIR polarization to be at 45° with respect to the dynamical optical axis, similar to achieving the maximal phase retardation in a standard quarter-wave or half-wave plate. In this scenario (red curve), the sideband polarizations deviated significantly from the NIR polarization. The sidebands rotated monotonically away from the NIR laser, reaching a 20° deviation at the 40th-order. Similarly, the

---

[2] Note that these angles definitions are different from Ref. [9] where the angles were defined between the THz field and the [011] direction

ellipticity of the sidebands increased monotonically to a value of $-15°$ at the 40^{th}-order. The final significant NIR polarization depicted is the circularly polarized light. Circular NIR polarizations selectively excite the heavy-hole spin states, which would simplify the pathway-interference which gives rise to DBR [9]. As with the 45° NIR polarization, the sideband polarizations were significantly different than that of the excitation; the sidebands became monotonically more linear, with only an ellipticity of $\sim 22°$ by the 40^{th}-order. As the sidebands became linear, they rotated towards $\sim -70°$.

To further test the theory put forth in Ref. [9], it was applied to the experimental conditions for the data shown on the left of Fig. 3.1 (with the exception that it assumed the THz was exactly parallel to the [011] crystal direction and not 2.5° off). The results are shown as the open squares in Fig. 3.1. Overall, there is very good agreement between the theory and experiments, with the theory correctly reproducing the overall magnitude of the sideband rotations and ellipticities. It is interesting to note the agreement between the α angles for the circular polarization; circular polarization has an undefined α angle, and yet both the experiment and theory indicate the sidebands rotate to the same orientation. Understanding the significance of this rotation and what it may indicate about the crystal or its symmetries is still under investigation.

In addition to the QW sample, a bulk GaAs sample was also investigated. Comparing Fig. 1.2 to Fig. 1.4, the in-plane band structure of bulk GaAs is simpler than the quantum well. Without the additional subbands from the quantized hole states, which resulted in significantly more complicated band bending, bulk GaAs may be easier to theoretically model. Further, using bulk GaAs over QWs removes the need for the infinite square well approximation which was applied in Ref. [9] and believed to be the cause of some of the discrepancy between theory and experiment. However, the system is slightly more complicated in that when a NIR photon is resonant with the band gap of the material, it must excited both light- and heavy-hole components since the degeneracy is no longer lifted by confinement.

The right side of Fig. 3.1 shows the resulting sideband polarizations for 500 nm of bulk GaAs when excited by the same NIR polarizations as the QW. As in the QW, the perpendicular polarization showed only small deflections of the sidebands relative to the NIR and minimal ellipticity changes. The 45° excitation, however, showed a much stronger effect in the bulk than in the QW. The sidebands rotated several 10's of degrees, while the ellipticity changed from negative to positive, indicating a change in helicity, and achieved a large magnitude of 30° at the 32nd-order. The DBR from a circular excitation similarly showed a stronger effect in bulk than in the QWs. When excited by a right-hand circular polarization, the the polarization became almost entirely left-hand circular polarization by the 16th-order sideband, before decreasing in ellipticity. The angle α of the sidebands began around 50°, flipped directions as the sidebands become nearly circular at the 16th-order, then rotated towards $-60°$, nearly perpendicular to the lower order sidebands. Figure 3.1 indicates the bulk GaAs shows larger effects from dynamical birefringence relative to a quantum well sample under similar experimental conditions. Understanding how the simpler band structure of GaAs results in larger birefringences

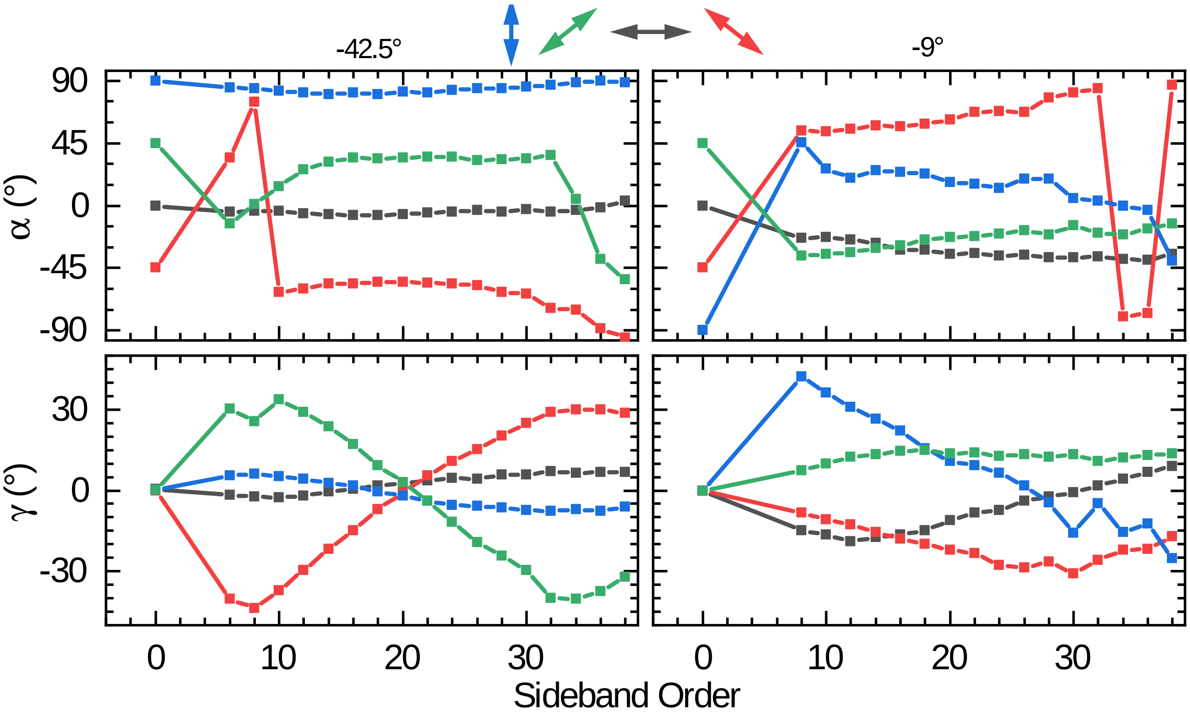

Figure 3.2: Polarimetry of bulk GaAs when the THz was $-42.5°$ (left) or $-9°$ (right) with respect to the [010] axis of the crystal. Each orientation was excited by four different NIR polarizations relative to the THz field, shown schematically at the top of the figure: perpendicular (blue), parallel (grey), $+45°$ (green) and $-45°$ (red). Each experiment was performed with 50 mW of λ_{NIR} =815.764 nm excitation and driven by 35 kV/cm at 541 GHz. When the THz was nearly parallel to the $[01\bar{1}]$ direction (left side), the parallel and perpendicular excitations resulted in sidebands nearly parallel to the NIR, while NIR polarizations of $\pm 45°$ resulted in large ellipticities. When the THz was not parallel to a high symmetry axis (right side), all of the sideband polarizations rotated and changed ellipticity.

requires further theoretical modeling, which could be useful in maximizing the effects of dynamical birefringence.

To investigate the notion of the dynamical optical axis, such as whether it is defined by the THz direction or the high symmetry directions of the GaAs crystal, it is instructive to consider when the THz is no longer parallel to a high symmetry axis of the crystal. The left side of Fig. 3.2 shows the polarization of the sidebands for various excitation polarizations when the THz was nearly parallel to the high symmetry axis $[01\bar{1}]$. The right side shows the results when the crystal was rotated so the THz was 9° away from the [010] crystal axis and excited by the same NIR polarizations.

When the THz was parallel to a high symmetry axis, the results were similar to those discussed for Fig. 3.1. When the NIR polarization was parallel (grey curve) or perpendicular (blue curve) to the THz, the sideband polarizations closely followed the NIR laser. The ellipticities for each excitation remained small, although some finite ellipticity was gained by the sidebands, likely do to the imperfect alignment of the THz to the $[01\bar{1}]$ direction. When excited with a NIR polarization which was rotated ±45° from the THz (green and red curves), large changes in the angle and ellipticity of the sidebands were seen. Remarkably, α and γ of the sidebands for $\alpha_{\text{NIR}} = \pm 90^\circ$ appeared as mirrors of each other about the 0° line, and similarly for $\alpha_{\text{NIR}} = \pm 45^\circ$. There appears to be some disagreement for the α angles of the sidebands for $\alpha_{\text{NIR}} = \pm 45^\circ$ around the $6-8^{\text{th}}$-orders and again at $> 32^{\text{nd}}$-order, but this is because the sidebands became largely elliptical ($\gamma \gtrsim 30^\circ$) and α is less well defined (and certainly harder to measure). This presence of a mirror axis around 0° is another result of the dynamical optical axis along the THz and crystal symmetry axis.

When the crystal was rotated off a symmetry axis and the experiment repeated, the results were significantly different, see the right side of Fig. 3.2. At no α_{NIR} measured did the sidebands follow the NIR polarization. Each set of sidebands showed large changes in their ellipticities, and the sidebands rotated significantly. For $\alpha_{\text{NIR}} = 90^\circ$, the sidebands quickly rotated significantly away from the NIR polarization and gained significant ellipticity by the 8th-order, the first observed. Increasing orders monotonically rotated towards 0° by the 36th-order, while simultaneously decreasing ellipticity to linear polarizations around the mid-20th-orders, and then gaining large left-handed ellipticities at higher orders. For these data sets, there is no longer evidence for a mirror axis for the polarization states, as observed when the THz is driven along the high symmetry $[01\bar{1}]$ direction.

One argument for the lack of observation of the dynamical optical axis (DOA) in the $-9°$ data of Fig. 3.2 could be that the DOA is oriented along a direction which was not measured. Therefore, further α_{NIR} should be measured to determine whether the DOA exists. Instead of cluttering Fig. 3.2 with more curves for additional measurements of α_{NIR}, Fig. 3.3 introduces a 'fan diagram' for polarimetry. The circular image plot on the the left side of Fig. 3.3 shows the polarization states of the sidebands when the THz is nearly parallel to the $[01\bar{1}]$ direction, the same as the left side of Fig. 3.2. Each azimuthal slice shows the results for a given α_{NIR} which were rotated from 90° to $-85°$ in 5° steps. Each radial ring corresponds to the measured sideband state for the given NIR excitation. The left half of the plot depicts the γ angles of the sidebands with white corresponding to linearly polarized, blue is right-hand circularly and red is left-hand circularly polarized, with increasing color saturation corresponding to the magnitude of the ellipticity. The right hand of the color plot corresponds to the α angles of the sidebands. White corresponds to horizontally polarized, green values are positive

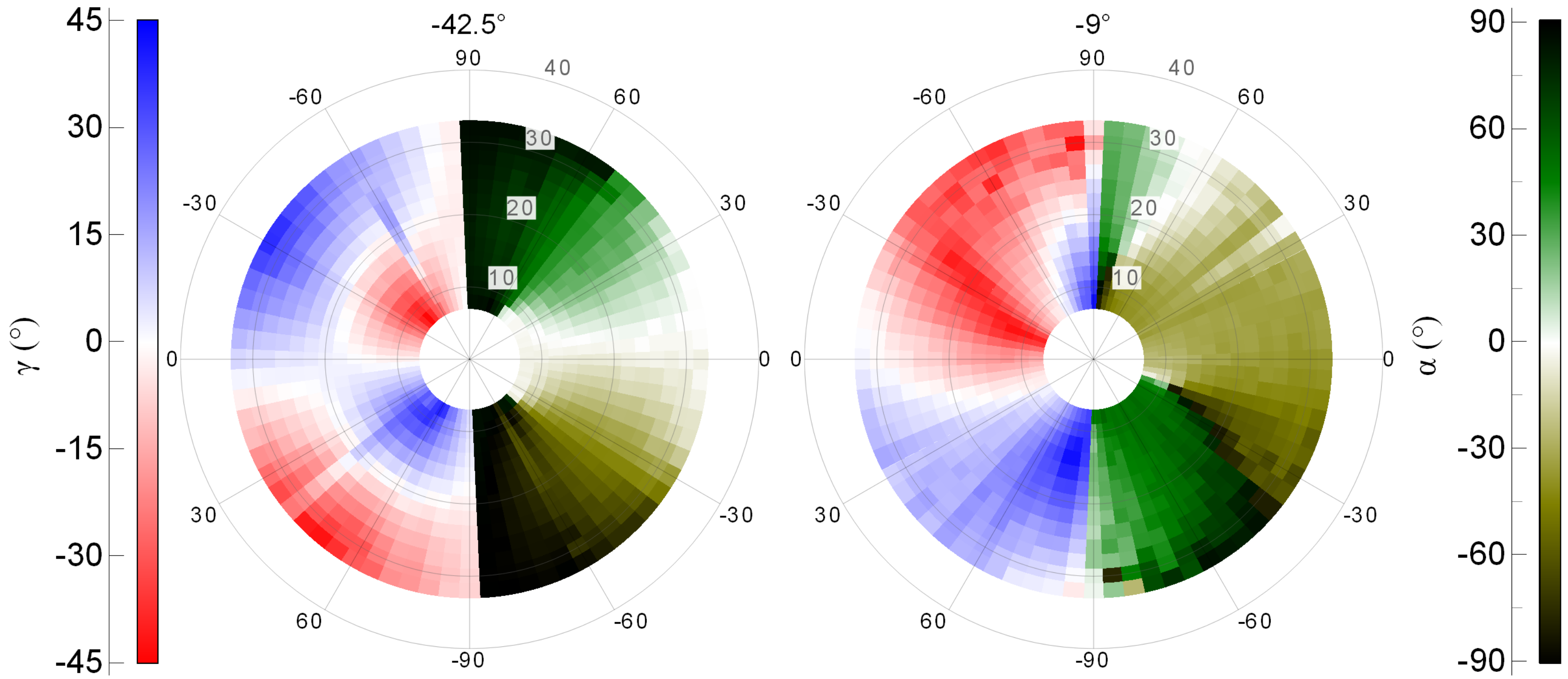

Figure 3.3: Fan diagrams for the experimental settings of Fig. 3.2. The α angle of the sidebands is shown on the right side of each circle, mapped to a color space where $\alpha = \pm 90°$ is black, $\alpha < 0°$ is gold, $\alpha = 0°$ is white, and $\alpha > 0°$ is green. γ is shown on the left side with right-handed polarizations ($\gamma > 0°$) in blue, left-handed polarization ($\gamma < 0°$) in red, and linearly polarized ($\gamma = 0°$) is white. An azimuthal slice across the diameter of the circle corresponds to the sideband polarizations from a single experiment where the azimuthal angle is the NIR polarization, α_{NIR}. Moving radially outward corresponds to increasing sideband order. NIR polarizations are all linearly polarized. When the THz is nearly parallel to the high symmetry axis (left), the sideband α roughly follows the NIR polarization, but the ellipticity changes drastically when $\alpha_{\mathrm{NIR}} \neq 0°$ or $90°$. When the THz is not along a high symmetry axis (right), no dynamical optical axis is seen and the sideband polarizations change significantly from that of the NIR laser.

rotations and gold are negative rotations, while ±90° corresponds to perpendicular polarizations. Since the system displays a 2-fold symmetry, $\alpha_{\text{NIR}} \in (-90°, 90°]$ are equivalent to $\alpha_{\text{NIR}} \in [-90°, -180°] \cup [90°, 180°]$. This allows the α and γ results for the sidebands to be placed side-by-side[3], with a full azimuthal slice (across the center of the circle) marking the sideband states for the same α_{NIR}.

When displayed as a fan diagram, the dynamical optical axis in the high symmetry axis data is easy to pick out; along the $\alpha_{\text{NIR}} = 0°$ slice, the sideband states $\alpha \approx \gamma \approx 0°$ is a clear white strip. Similarly, the $\alpha_{\text{NIR}} = 90°$ shows a nearly white strip for γ, indicating low ellipticity, and the α slice is black to indicate the sidebands are nearly parallel to the NIR. For α_{NIR} which were not parallel or perpendicular to the DOA showed ellipticities which flipped between the two circular handedness', but the 20^{th}-order appeared to be linearly polarized for all α_{NIR} excitations. Meanwhile, the sideband α's followed the NIR laser's polarization without significant change across sideband orders.

To contrast the high-symmetry data, the right side of Fig. 3.3 shows the corresponding fan diagram for the THz polarization off of a high-symmetry axis. Along $\alpha_{\text{NIR}} = 0°$, the white strip which previously indicated the DOA was no longer observed. From the γ angles, there was a twist in the fan diagram, observed in the $\gamma = 0°$ slice which started at sideband $n = 8$ for $\alpha_{\text{NIR}} = -60°$ and moving radially outward (increasing sideband order) sees increasing α_{NIR} are needed to see $\gamma = 0°$. From this fan diagram, there is no clear α_{NIR} where each sideband showed the same polarization state as the laser,

---

[3] The α_{NIR} for the γ data is mapped to $\alpha_{\text{NIR}} \rightarrow \alpha_{\text{NIR}} + 180°$ to allow the two halves of the fan to be shown side-by-side

which emphasizes that the observation of a DOA requires the THz direction to be nearly parallel to a high symmetry axis of the crystal.

3.2 Dynamical Jones Calculus

To provide a method of quantitatively understanding fan diagrams, and for comparing experiment to theory (see Sec. 3.4), I now introduce the concept of dynamical Jones calculus. In standard Jones calculus, one starts with the complex 2-component electric field vector, $\vec{E}_{\text{in}} = (E_x, E_y)^{\text{T}}$. When this electric field is sent through some optically active material (typically polarizers or wave-retarders), it is transformed into an output electric field, $\vec{E}_{\text{out}}$ as,

$$\vec{E}_{\text{out}} = \mathcal{J}\vec{E}_{\text{in}} \tag{3.1}$$

Here, $\mathcal{J}$ is the Jones matrix, a 2×2 complex vector which describe the optical element, see Reference [37] for details.

This formalism can be extended to sideband polarimetry where $\vec{E}_{\text{in}}$ is the NIR electric field, $\vec{E}_{\text{out}}$ are the sideband electric fields which can be determined from polarimetry, and $\mathcal{J}_n$ is a matrix which describes the effect of HSG,

$$\vec{E}_{\text{n}} = \begin{pmatrix} \mathcal{J}_{xx} & \mathcal{J}_{xy} \\ \mathcal{J}_{yx} & \mathcal{J}_{yy} \end{pmatrix}_n \vec{E}_{\text{NIR}} \tag{3.2}$$

$\mathcal{J}_n$ is now a dynamical Jones matrix where one is defined for each sideband order. The components of $\mathcal{J}_n$ can be extracted using Eq. 3.2. To start, experiments measure α and γ of the sidebands and NIR. By Eq. D.10, the Jones vectors can be written in terms of these polarization states as,

$$\vec{E}_{\rm n} = \begin{pmatrix} \cos\alpha & -\sin\alpha \\ \sin\alpha & \cos\alpha \end{pmatrix} \begin{pmatrix} \cos\gamma \\ i\sin\gamma \end{pmatrix} \equiv \begin{pmatrix} \cos\phi_n \\ e^{i\delta_n}\sin\phi_n \end{pmatrix} \tag{3.3}$$

The left hand side defines the vector in terms of the relative magnitude, ϕ, and phase, δ, the components of the electric field for each sideband, n, with $n = 0$ corresponding to the NIR laser. Substituting the Jones vectors of Eq. 3.3 into the matrix equation of Eq. 3.2 and simplifying provides,

$$\cos\phi_n \left(\frac{\mathcal{J}_{yx}}{\mathcal{J}_{xx}} \cos\phi_0 + \frac{\mathcal{J}_{yy}}{\mathcal{J}_{xx}} e^{i\delta_0} \sin\phi_0 \right) - \sin\phi_n \left(\cos\phi_0 + \frac{\mathcal{J}_{xy}}{\mathcal{J}_{xx}} e^{i\delta_0} \sin\phi_0 \right) = 0 \tag{3.4}$$

Equation 3.4 is passed to a standard least-squares fitting routine to calculate $\mathcal{J}$. Equation 3.3 shows that each polarization measurement for a sideband provides two inputs to the minimization, while Eq. 3.4 has six unknowns, $\mathcal{J}_{xy}/\mathcal{J}_{xx}$, $\mathcal{J}_{yx}/\mathcal{J}_{xx}$ and $\mathcal{J}_{yy}/\mathcal{J}_{xx}$, each of which is complex. Therefore, a minimum of three data sets are required, which come from different $\alpha_{\rm NIR}$, to calculate the ratios of the $\mathcal{J}$ matrix. While the normalized elements are calculated, the magnitudes can be determined by sideband intensity data: measuring the x-projection sideband intensity when the NIR is parallel to the THz field measures $|\mathcal{J}_{xx}|$.

Once the $\mathcal{J}$ matrices are known, they can be used to predict the polarization state of the sidebands given any input NIR polarization by simply using Eq. 3.2. To demonstrate this, the left side of Fig. 3.4 shows the same experimental fan diagram as Fig. 3.3. The data for $\alpha_{\rm NIR} = 90°$, $\pm 45°$, and $0°$ were used to calculate the $\mathcal{J}$ matrices for each sideband as described above. These matrices were then used to reconstruct the fan diagram for

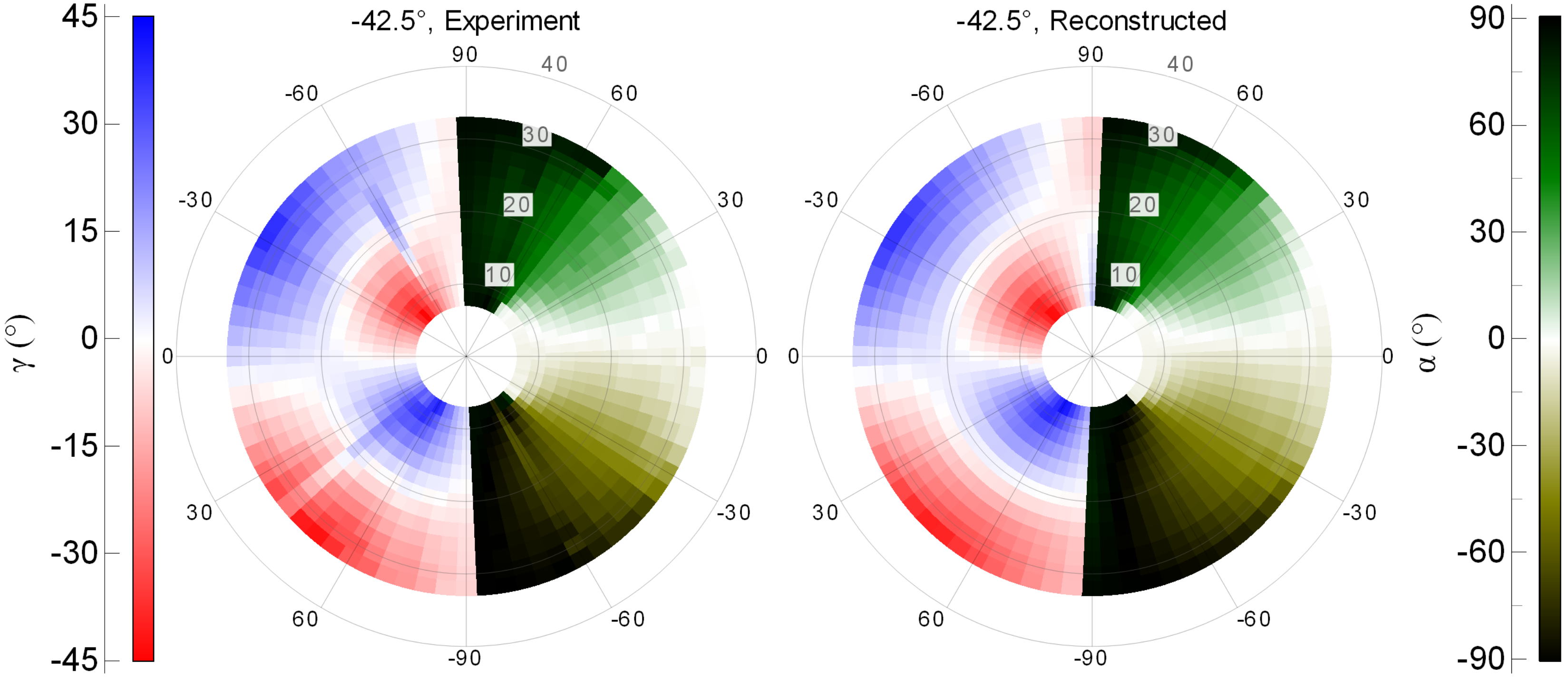

Figure 3.4: Robustness of the $\mathcal{J}$ matrix extraction and reconstruction. The left side shows the same fan diagram as the left side of Fig. 3.3. For the left side, the data from $\alpha_{\text{NIR}} = 0°, 90°, \pm45°$ were used to construct the $\mathcal{J}$ matrices by minimizing Eq. 3.4. The $\mathcal{J}$ matrices were then used to calculate what the fan diagram would look like for all other α_{NIR} angles, plotted on the right. The agreement between the two fans shows only four α_{NIR} measurements are required to calculate the $\mathcal{J}$ matrices and accurately produce a fan diagram.

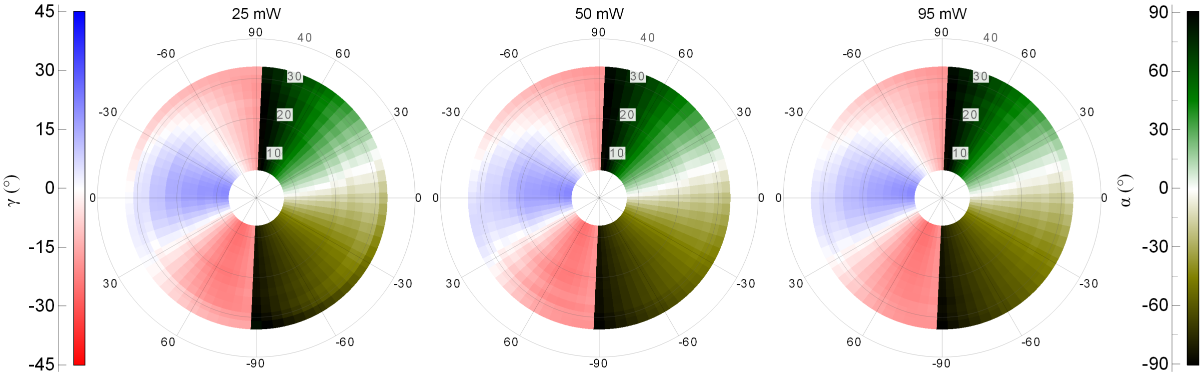

Figure 3.5: NIR power dependence of fan diagrams. Three fan diagrams were measured for 25 mW (left), 50 mW (center) and 95 mW (right) of NIR power at λ_{NIR} =816.590 nm, 35 kV/cm and 540 GHz. The THz was parallel to the [010] direction, and the sample was measured at Spot R of Fig. 3.7, which is why the fan looks considerably different from the previous fans. The consistency between each of the three fans indicate measurements were in the linear response region with respect to NIR power.

α_{NIR} from $-90°$ to $85°$, which is shown on the right of Fig. 3.4. This "reconstructed" fan cleanly reproduces the experimental results which confirms dynamical Jones calculus is valid to describe the polarization changes which occur from DBR. It further indicates only 4 experimental data sets are required to determine the Jones matrix and calculate a Fan diagram.

One final check to confirm the validity of the Jones formalism to HSG is to check the polarization dependence on the NIR power. Jones calculus is valid for processes linear in the electric field being transformed by a Jones matrix. While high-order sideband is an extremely non-linear phenomenon in the THz electric field, it is often linear in the NIR electric field[4]. Figure 3.5 shows three fan diagrams taken with different NIR powers. On the left is the results of 25 mW of NIR, which was the lowest power to see reasonable signal for measuring a fan diagram. 50 mW is shown in the center and is the

---

[4] See Chapter 4 of the thesis of Hunter Banks for data when HSG is not linear in the NIR field

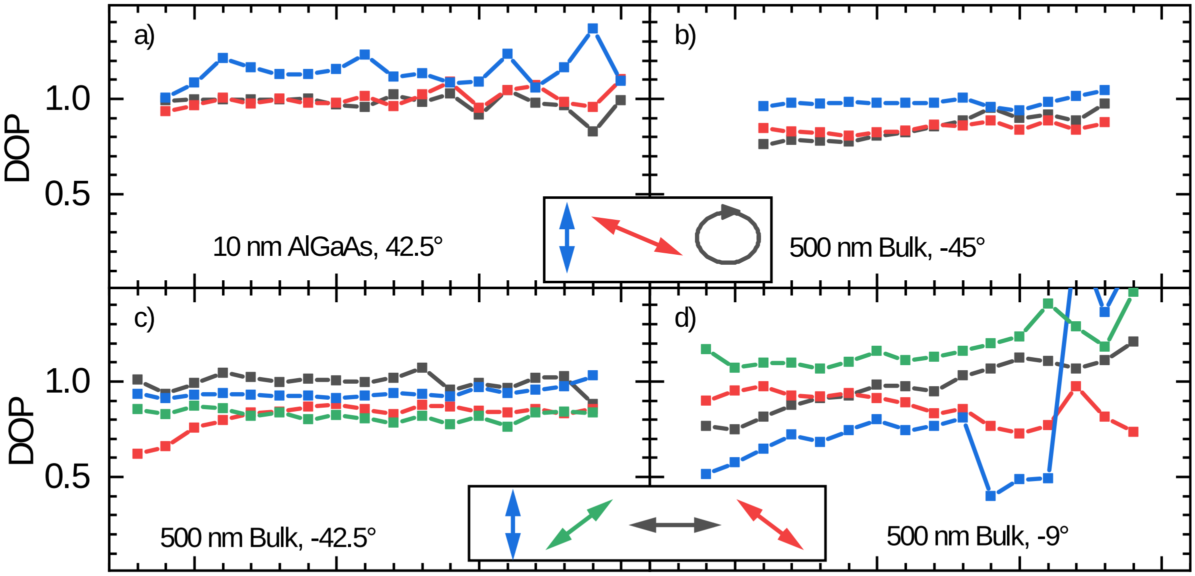

Figure 3.6: Degree of polarization (DOP) of sidebands. (a,b) DOP for the data shown in Fig. 3.1 left and right, respectively. (c,d) DOP for the data of Fig. 3.2 left and right, respectively. The quantum well sample had well polarized sidebands, while the bulk polarizations depended on the incident NIR polarization.

standard power used throughout this thesis. On the right, 95 mW is shown which was the maximum power achievable at the sample. While higher powers did produce stronger sideband signals (the intensities are not shown here), the polarizations were unchanged.

Given the validity of the Jones calculus for the polarization states of the sidebands, all of the following fan diagrams were calculated by measuring four α_{NIR} excitations to calculate the Jones matrix and calculating the remaining states. While this means there is no additional information in the fan of Fig. 3.3 compared to the raw data in Fig. 3.2, a comparison between the two shows the power of the fan diagram to quickly give comparisons between polarization spectra at a glance, without having to quantitatively compare spectra.

There is one final note to be made with regards to this dynamical Jones calculus.

Standard Jones calculus can only be applied to perfectly polarized light. The polarimeter used in experiments is a full Stokes polarimeter, see Appendix D, which allows measuring the degree of polarization (DOP) of the sideband. Figure 3.6 shows the degree of polarization for the data of Figs. 3.1 and 3.2. The cause for the lack of perfect polarization will be discussed in the following section. The DOP shown in Fig. 3.6(c) corresponds with the polarization states used to calculate the dynamical Jones matrices and resulting fan diagram of Fig. 3.4. The good agreement in the reconstruction of Fig. 3.4 indicates there is some validity to using applying the Jones formalism to the partially polarized data for extracting information from the system. What is lost, however, is exactly this depolarization: the dynamical Jones matrices can not be used to calculate the degree of polarization for a sideband of a given NIR excitation polarization. Experiments are ongoing to fully investigate the source of the depolarization, its effects on HSG, and how to fully remove it.

3.3 Strained Polarization

Figure 3.3 shows how the fan diagrams are sensitive to the electronic structure of the crystal as the band structure of GaAs is anisotropic along different crystal axes [25]. This is an important first step in observing the influence of Berry Curvature on HSG. However, another method for modifying the band structure of the material would be useful for further controlling and understanding the effects of the Berry Curvature on the sideband polarizations. Straining a semiconductor provides such a control for modifying the band structure of the material [25, 130, 121]. When subjected to some strain[5], ε_{ij} $(i, j = x, y, z)$, the valence bands will shift and the light hole-heavy hole degeneracy can be lifted. For example, a uniaxial strain (such as from lattice mismatches) induces an in-plane strain such that $\varepsilon_{xx} = \varepsilon_{yy}$ which shifts the valence bands by [121],

$$2a\left(1 - \frac{C_{12}}{C_{11}}\right)\varepsilon_{xx} \tag{3.5}$$

and splits the top two valence bands by,

$$-b\left(1 + 2\frac{C_{12}}{C_{11}}\right)\varepsilon_{xx} \tag{3.6}$$

where a and b are deformation potentials, and C_{11} and C_{12} are components of the stiffness tensor.

Figure 3.7(a) shows the bulk band structures near the Γ-point calculated from the modified $k \cdot p$ method to include three different values of stress applied. The red curves are the bands where the $k = 0$ wavefunction has the ±1/2 spin component, while they grey is the ±3/2 spin[6]. The solid lines are the unstrained bands which show the $k = 0$ degeneracy. Under 90 MPa of compressive stress (double-lines), the 3/2-hole is shifted to higher energy while the 1/2-hole is shifted down, resulting in a splitting of ~ 5 meV. Coupling between the bands also causes the mass of the 3/2-hole band to decrease while the 1/2-hole band increases near the Γ-point. When tensile strain is applied (dashed lines), the ordering of the bands is flipped with the 1/2-hole lying roughly 5 meV above the 3/2 band. The effective masses of the bands are nearly reverse with respect to the

---

[5] Recall the distinction between *strain*, the differential length change, and *stress*, the force per area applied. They are related through the compliance and stiffness tensors [121]

[6] Note that these labels are only valid at the Γ-point, but it is useful to have some method for distinguishing the bands.

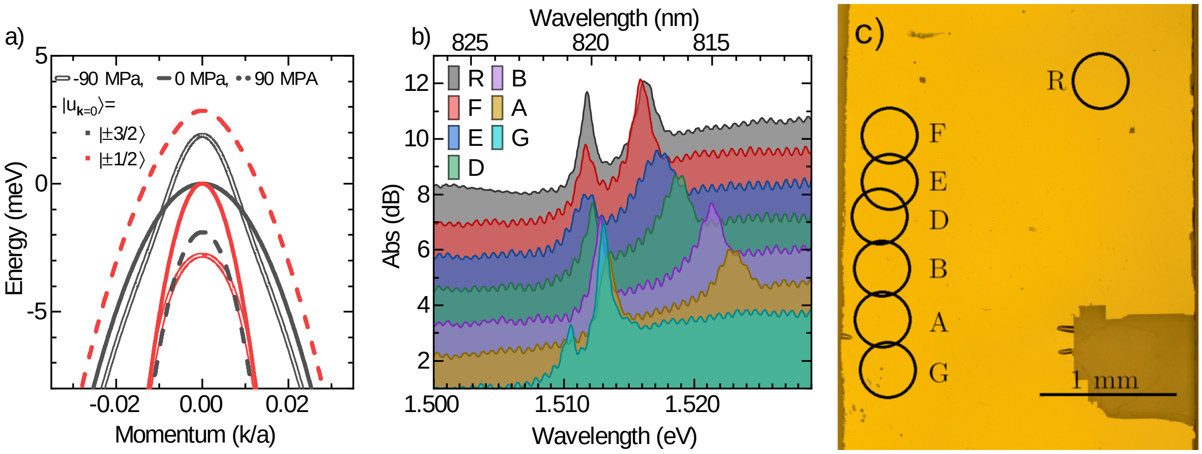

Figure 3.7: Stress in the bulk GaAs sample used in experiments. (a) Calculated band structure from the $k \cdot p$ method under various strains where the grey curves have spin 3/2 at $k = 0$ and red have spin 1/2 at $k = 0$. The unstrained band structure is shown in solid lines. When compressive (double-lines) or tensile (dashed lines) strain is applied, the valence bands shift and the degeneracy is lifted. (b) Measured absorbances of the sample at the positions marked in the real space image of (c). The splitting of the valence bands results in two peaks corresponding to the light-hole and heavy-hole excitons. Additional oscillations in the spectra are due to a Fabry-Perot cavity from the sample geometry, see Sec. B.2. Absorbances are offset for visibility. The spot size during absorbance was roughly the spot sizes in (c), roughly 400 μm diameter.

unstrained effective masses. These shifts in the band structure due to strain significantly alter the mixing and bending between the various valence bands, altering the Berry Curvature which should result in drastically different HSG spectra and fan diagrams.

Strain was introduced to the bulk GaAs sample via a difference in thermal expansion coefficients between the GaAs epitaxial layer and the sapphire substrate[7] [71, 70]. Figure 3.7(b) shows the absorbance spectra at various positions in the sample which are marked in the microscope image of the sample in Fig. 3.7(c). The strain splits the exciton lines by ~ 4 meV at positions R and F, and up to ~ 10 meV at spot A, corresponding to maximum magnitudes of the stresses at ~ 150 MPa. From the image of the sample in Fig. 3.7(c), the strain in the sample varied drastically on the order of hundreds of microns (the spot size of the NIR used for HSG experiments was roughly 200 μm in diameter, while the THz spot size was 500 μm). Note that, while the strain is visible in the splitting of the exciton peaks in absorbance, it was not strong enough to introduce a linear NIR birefringence, and the NIR polarization did not change when passed through the sample.

Figure 3.8 shows the fan diagrams resulting from identical experimental conditions (95 mW at λ_{NIR}=816.595 nm and driving with 540 GHz with maximum field strengths of 35 kV/cm and the THz parallel to [010]), but the sample was excited at two different positions of the sample[8]. On the left side of Fig. 3.8, the sample was excited at the overlap of Spot A and Spot B as labeled in Fig. 3.7, while the right side of Fig. 3.8 was

---

[7] The reason for the spatial inhomogeneity of the strain, seen in the position dependent splittings of Fig. 3.7(b), is unclear.

[8] The fans of Fig. 3.3 were both taken at Spot D

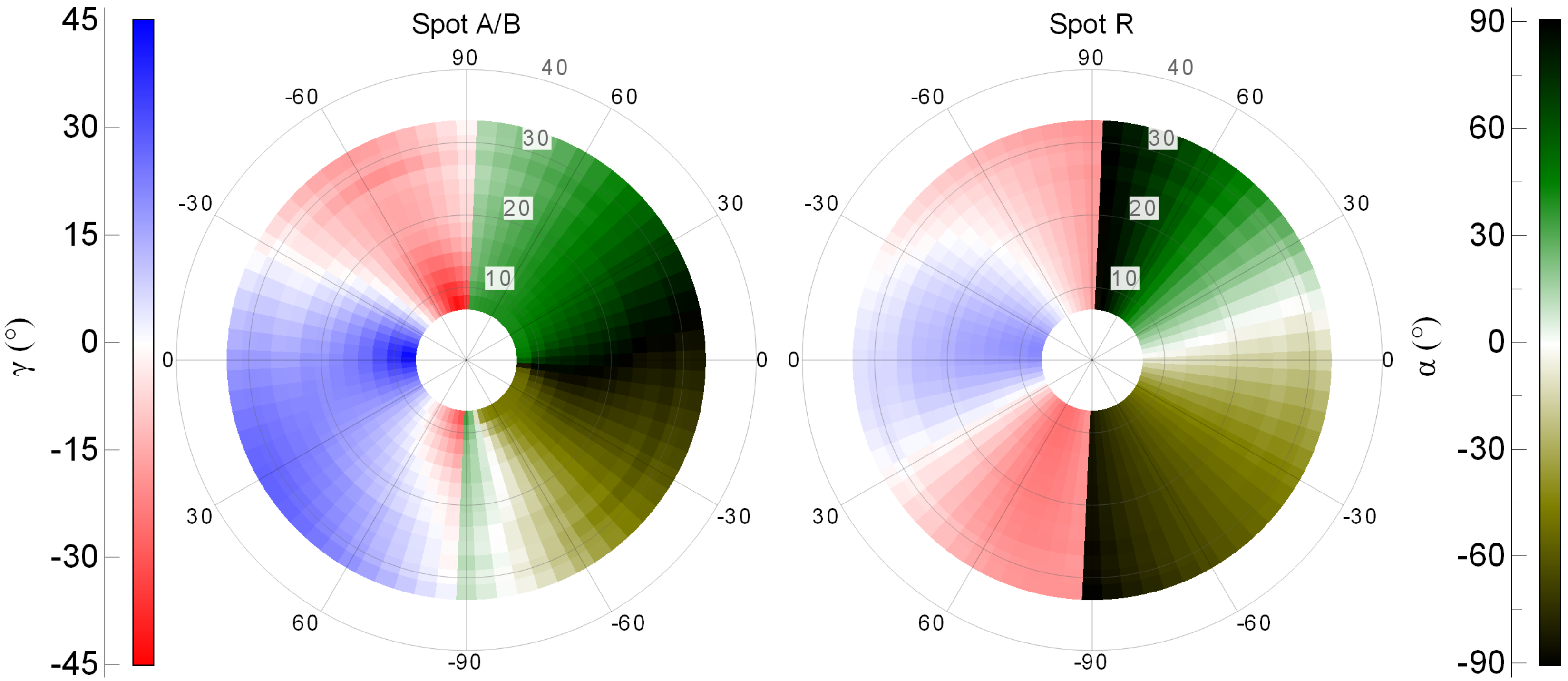

Figure 3.8: Strain dependence on fan diagrams by measuring at two different positions of the sample. Both experiments were performed with 95 mW of λ_{NIR} =816.595 nm excitation and driven by 35kV/cm at 540 GHz. The THz polarization was parallel to the [010] axis. The left side was measured at the overlap of Spots A and B, while the right side was measured at Spot R, see Fig. 3.7. The sidebands from Spot A/B were not always fully polarized, see Fig. 3.9, likely from accidental inhomogeneous averaging over strains. Spot R shows $\alpha_{\mathrm{SB}} \approx 0^\circ$ when $\alpha_{\mathrm{NIR}} = 0^\circ$, while Spot A/B observed $\alpha_{\mathrm{SB}} \approx 90^\circ$ for the same excitation polarization. Spot A/B also observed greater ellipticities at lower-order sidebands than observed at Spot R.

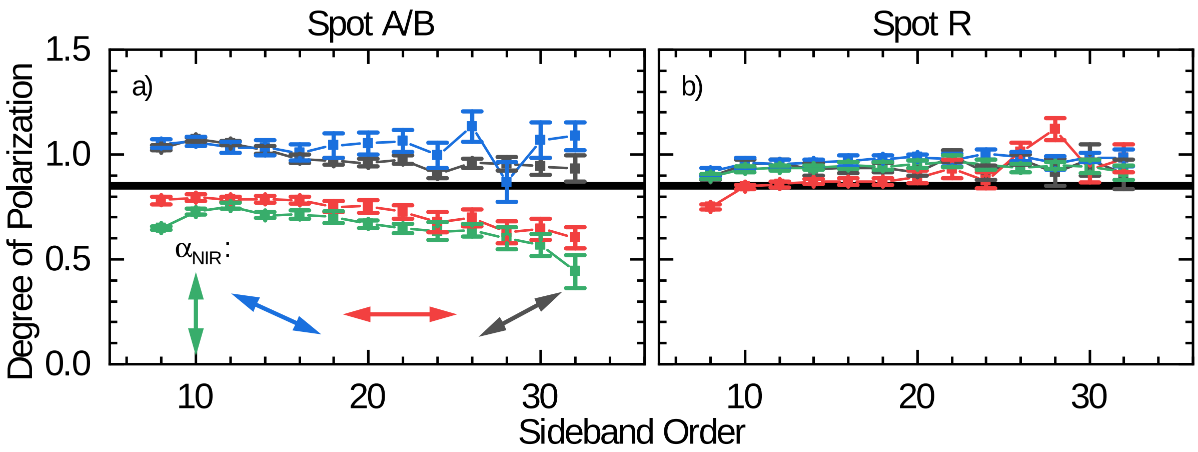

Figure 3.9: Degree of polarization for the data sets used to create the fan diagrams of Fig. 3.8. Four curves are shown for each fan corresponding to the α_{NIR} measured to produce the fan (shown schematically on the bottom left). (a) The DOP for Spot A/B, where $\alpha_{\text{NIR}} = \pm 45°$ (grey and blue, respectively) were well polarized, while $\alpha_{\text{NIR}} = 0°/90°$ were not perfectly polarized. (b) Spot R was well polarized for all measurements taken. The black line is at 85% polarized as a guide for well polarized sidebands. DOP values greater than 100% result from artifacts in the numerical fitting and errors come from the errors to the fits, see Appendix D.

taken at Spot R.

Strain produced striking difference in the fans of Fig. 3.8. Neither fan showed evidence for a dynamical optical axis. Spot R showed high degrees of ellipticity for low order sidebands near $\alpha_{\text{NIR}} = -30°$ and $\alpha_{\text{NIR}} = 65°$, with the ellipticity decreasing at higher orders. It can be roughly seen that $\alpha_{\text{NIR}} > 0°$ ($\alpha_{\text{NIR}} < 0°$) resulted in $\alpha > 0°$ ($\alpha < 0°$), although there did appear a twist in α. The 8$^{\text{th}}$-order sideband was roughly parallel with the NIR laser at $\alpha_{\text{NIR}} = 0°$, but the 30$^{\text{th}}$-order had $\alpha = 0°$ for $\alpha_{\text{NIR}} \sim 15°$. This is similar to the twist observed in the $-9°$ fan shown in Fig. 3.2, to a smaller extent. By comparison, the excitation at Spot A/B produced a significantly different fan. Firstly, the sidebands from $\alpha_{\text{NIR}} = 90°$ and $\alpha_{\text{NIR}} = 0°$ were not fully polarized, see Fig. 3.9. Figure 3.9(a) shows the degree of polarization (DOP) of the sidebands for the four α_{NIR}

datasets measured, with each α_{NIR} shown schematically. For $\alpha_{\text{NIR}} = 0°,90°$, the DOP for all the sidebands is between 50% and 85%. The remaining $\alpha_{\text{NIR}} = \pm 45°$ excitations were fully polarized. By contrast, Fig. 3.9(b) shows the DOP for Spot R, which shows the sidebands were all well polarized (DOP> 85%). However, as four α_{NIR} data sets were measured and section 3.2 showed that only three sets are necessary to create a fan diagram, subsets of the measurements can be used to check the consistency of the fan. When subsets of three data sets of the four are used to produce a fan diagram for the data from Spot A/B, each fan is similar to the one shown in Fig. 3.8, indicating the lack of perfect polarization on two of the data sets does not significantly alter the polarizations.

The polarizations from Spot A/B were also drastically different from Spot R. At $\alpha_{\text{NIR}} = 0°$, the sidebands had larger magnitudes of ellipticity at lower orders, and that ellipticity remained larger at higher orders relative to that of Spot R. Furthermore, α from $\alpha_{\text{NIR}} = 0°$ is at $\pm 90°$, flipped significantly from the exciting NIR polarization, and quite different from the results from Spot R where the sidebands for $\alpha_{\text{NIR}} = 0°$ were almost parallel to the lasers.

The lack of perfect polarization seen in Fig. 3.9(a) was likely a result of inhomogeneously integrating over various strain profiles. If the NIR excites excitons which experience significantly different strain fields, Fig. 3.8 shows the polarizations from the different strains can be quite different. However, the polarimeter used integrates over all of the signal and is unable to distinguish sidebands which are generated from different strains, resulting in partially polarized light. Furthermore, Fig. 3.8 shows there are strain values which can produce sidebands which are nearly perpendicular, such as the $\alpha_{\mathrm{NIR}} = 0^\circ$ data for Spot A/B compared to Spot R. Averaging over these strain regions which would result in partially polarized light. For $\alpha_{\mathrm{NIR}} = \pm 45^\circ$, however, the sidebands are of similar polarization between the two fans, which wouldn't be distinguished in the degree of polarization. This result is consistent with the degrees of polarization measured in Fig. 3.9(a).

3.4 Extracting Material Parameters

The experimental results so far have shown the sideband polarizations to be extremely sensitive to slight changes of the material being studied. In this final section, I will discuss progress being made to use this polarization data to extract information about GaAs directly. The theory discussed here is a modified version from the original observation of dynamical birefringence[9] [9], and a more detailed description for the evolution of the electrons and holes can be found there.

Overview of the Theory

From the optical selection rules discussed in Sec. 1.1.3, a circularly polarized photon excites a subset of the Bloch wavefunctions at Γ. For example, a σ_- photon will create a $|1/2\rangle$ and $|-3/2\rangle$ electron heavy-hole pair, or a $|-1/2\rangle$ and $|-1/2\rangle$ electron light-hole pair. Similarly, a σ_+ photon will create a $|-1/2\rangle$ and $|3/2\rangle$ electron heavy-hole pair, or a

---

[9] This theory and code have been developed entirely by Qile Wu during a short post-doc study at UCSB. The theory will only be briefly outlined here, and the details can be found in future publications.

$|1/2\rangle$ and $|1/2\rangle$ electron light-hole pair. Because the initial particle states depend on the components of circular polarization of the NIR, the theory begins by breaking a linearly polarized NIR photon into the superposition of two circularly polarized photons,

$$\sigma_{\pm} = \pm\frac{\hat{x} \pm i\hat{y}}{2} \tag{3.7}$$

where $\hat{x}$ ($\hat{y}$) is the unit vector along the [010] ([001]) direction of the crystal. This lets one separate the dynamics from the two different excitation pathways to simplify calculations.

While in experiments it is natural to use the Jones formalism from Eq. 3.2 in a Cartesian basis, it is not a convenient form when discussing the theory. Instead, these Jones matrices can also be written in the circular basis as,

$$\begin{pmatrix} \sigma_+ \\ \sigma_- \end{pmatrix}_n = \begin{pmatrix} \mathcal{T}_{++} & \mathcal{T}_{+-} \\ \mathcal{T}_{-+} & \mathcal{T}_{--} \end{pmatrix}_n \begin{pmatrix} \sigma_+ \\ \sigma_- \end{pmatrix}_{\text{NIR}} \tag{3.8}$$

where $\sigma_{\pm}$ corresponds to a photon with angular momentum ± 1, respectively. Converting between the $\mathcal{J}$ and $\mathcal{T}$ matrices can be done with the basis change,

$$\mathcal{T} = \begin{pmatrix} \mathcal{T}_{++} & \mathcal{T}_{+-} \\ \mathcal{T}_{-+} & \mathcal{T}_{--} \end{pmatrix} = \frac{1}{2}\begin{pmatrix} e^{-i\theta} & -e^{i\theta} \\ ie^{-i\theta} & ie^{i\theta} \end{pmatrix}^{\dagger} \mathcal{J} \begin{pmatrix} e^{-i\theta} & -e^{i\theta} \\ ie^{-i\theta} & ie^{i\theta} \end{pmatrix} \tag{3.9}$$

where θ is the orientation of the sample, $\theta = 0^\circ$ corresponds to the THz parallel to the [010] crystal direction. This transformation matrix comes from the basis change of Eq. 3.7, and the sample orientation enters into Eq. 3.9 since the $\mathcal{J}$ matrices are defined with respect to lab coordinates and not sample coordinates.

After the NIR photon creates an electron hole pair at some point within a THz period, the second step of the calculations propagate the electron and hole through their respective bands. The 8-band Kane Hamiltonian, discussed in Sec. 1.1.1, is used for calculating the band structure and wavefunctions throughout the Brillouin zone. Minimal coupling with the conduction bands result in the electron remaining in the same wavefunction in which they start, whereas significant coupling between the valence bands cause the angular momentum of the hole to become a superposition of all the valence band angular momentum states, which is a manifestation of the Berry Curvature in the sample (Sec. 1.1.5). When the electron and hole recollide, a superposition of left- and right-handed photons can be emitted based on the final state of the hole and the selection rules of Sec. 1.1.3.

The propagation of the particles through momentum space is a computationally difficult task, and several approximations were made to simplify the calculations. A constant dephasing factor was applied during the particle accelerations, which does not account for LO phonons [10] nor for increased scattering rates proportional to the density of states. It is also assumed that the Coulomb potential between electron and hole pairs is too weak to affect polarization [126]. Furthermore, each electron-hole pair is considered independent of other electron-hole pairs due to the low NIR intensities and the observed linear NIR power dependence of Fig. 3.5.

A more significant approximation was to only include the paths through momentum space for the hole which pass through the Γ-point. To understand the implications of this assumption, consider the band structure of GaAs shown in Fig. 1.2. When a NIR photon is incident with $\hbar\omega_{\mathrm{NIR}} = E_g$[10], a population of electrons and holes will be excited

---

[10] For the sake of description, ignore the exciton and its binding energy

at exactly the Γ-point. When driven by the THz field, the quasi-particles will move in one dimension in the Brillouin zone along the direction of the THz. If the NIR photon energy is greater than the band gap, $\hbar\omega_{\mathrm{NIR}} > E_g$, the electron-hole populations will no longer be localized to a single point in momentum space, but instead will be a ring in momentum space. When this population is driven by the THz field, the majority of the ring will not pass through Γ. Including all of these states in the calculations introduces significant complexity and should contribute little to the overall dynamics for certain experimental conditions which will be discussed below.

Extracting Strain

To best compare with the theory, experiments were performed using the hole coupler of the FEL (see Sec. 1.3). This limited the field strengths to ~6.5 kV/cm in the sample. Furthermore, the NIR wavelength was set to λ_{NIR}=820.190 nm, which was lower in energy than the dominant exciton of Spot G of Fig. 3.7, ensuring most of the electron-hole populations were at Γ. The crystal orientation was such that the THz polarization was nearly parallel to the [010] direction. The resulting fan diagram is shown on the left of Fig. 3.10. A dynamical optical axis was seen at $\alpha_{\mathrm{NIR}} = 0°$ and $\alpha_{\mathrm{NIR}} = 90°$ where the sideband polarizations followed the NIR polarization, similar to Fig. 3.3 when the THz was parallel to the $[01\bar{1}]$. Another similarity was the flipping in chirality of the sideband ellipticity for $\alpha_{\mathrm{NIR}} = \pm 45°$. In this dataset, however, the chirality is now seen to flip twice, instead of just once. For $\alpha_{\mathrm{NIR}} = 45°$, the 8^{th}-order sideband started with right-handed light, flipped to left-hand in the next sideband, before swapping back to

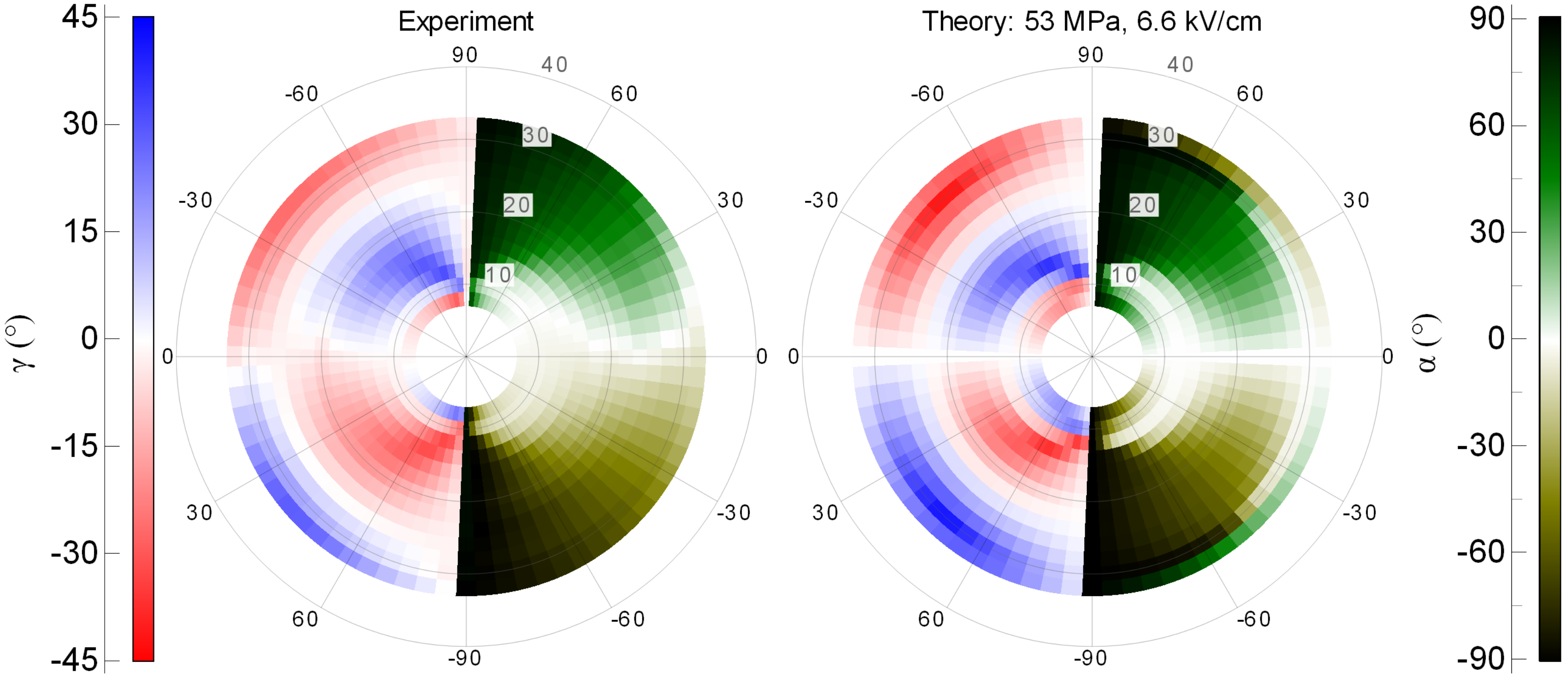

Figure 3.10: Fan diagrams comparing (left) experiment to (right) theory. The experimental fan was taken near Spot G in Fig. 3.7 with the THz parallel to [010], and 50 mW of NIR at λ_{NIR} =820.19 nm, to create excitons near Γ. The sample was driven by 6.5 kV/cm at 540 GHz. The theory fan was the best fit to the experiment varying the THz field strength and stress, minimizing the quantity in Eq. 3.10. The theory accurately reproduces the sign of γ and the multiple changes in handedness, though it predicts larger magnitudes of γ.

right-handed at the 28$^{\text{th}}$-order sideband.

As an initial attempt at calculating the corresponding theoretical fan diagram, the typical Luttinger parameters for GaAs were used for the Kane Hamiltonian, $\gamma_1 = 6.85$, $\gamma_2 = 2.06$, and $\gamma_3 = 2.93$ [25, 121, 9]. Uniaxial strain, denoted by X, was introduced to the Hamiltonian using deformation potentials [121], but the value of the stress was left as a free parameter[11]. The THz electric field strength was also left as a free parameter to account for errors in experimentally calculating its value. The stress and field strength were then varied to fit the theory to the experiment.

To fit the theory to experiment, the experimental $\mathcal{T}$ matrix was first extracted from the polarimetry data. A corresponding $\mathcal{T}$ was calculated from theory for a given field strength and stress and the difference in normalized $\mathcal{T}$ matrices between theory and experiment was minimized:

$$\min_{F_{\text{THz}},X} \sum_n \left| \left(\frac{\mathcal{T}_{+-,n}}{\mathcal{T}_{++,n}} \right)^T - \left(\frac{\mathcal{T}_{+-,n}}{\mathcal{T}_{++,n}} \right)^E \right| \tag{3.10}$$

The sum is over the $\mathcal{T}$ matrix for each sideband and the T and E superscripts correspond to the $\mathcal{T}$ for the theoretical calculation and experiment, respectively. The $\mathcal{T}$ matrices are normalized to the respective $\mathcal{T}_{++}$ to account for differences in the normalization factors which are not well accounted for between theory and experiment, but should not affect fan diagrams. The justification for only using only one element of the $\mathcal{T}$ matrices will be given below.

---

[11] Typically, one should be able to know the stress from the exciton splittings. Unfortunately, the exciton lines shown in Fig. 3.7(b) for the spot used in experiments (Spot G) for Fig. 3.10 do not match up with Eq. 3.6. It is unclear why this occurred, as the other absorbance spots do match Eq. 3.6.

Calculating the $\mathcal{T}$ matrices for a single set of experimental conditions is lengthy, taking about 10 minutes for each set of experimental conditions. For standard numerical minimization techniques which would be used on Eq. 3.10, the function must be evaluated at several positions. Instead of calculating the $\mathcal{T}$ matrices at every point during the minimization for the field strengths and strains required, the theory was instead first solved on a grid of field strength and strain values. For each step in the minimization, the $\mathcal{T}$ matrices were then interpolated from the values in the grid[12], and those $\mathcal{T}$ matrices were used in Eq. 3.10.

When this calculation was performed, a minimum was found for a field strength of 6.6 kV/cm and a strain of 53 MPa. Unfortunately, the error function of Eq. 3.10 did not yield a unique minimum, where increasing field strengths and stresses would show a minimum valley. However, given the agreement between the field strengths and the small splitting of exciton peaks in Fig. 3.7, which would indicate a small stress, the values extracted from the theory are reasonable.

The calculated fan diagram for the $\mathcal{T}$ matrices which minimized Eq. 3.10 is shown on the right side of Fig. 3.10. The main features of the experiment are well reproduced by the theory. The dynamical optical axis is seen at $\alpha_{\mathrm{NIR}} = 0°$ and $90°$. The γ angles of the sidebands for $\alpha_{\mathrm{NIR}} = 45°$ started right-handed at the 8th-order, flipped to left-handed, and flipped back to right-handed by the 30th-order. However, the experiment observed a greater number of sidebands which were left-handed (roughly the 10th - 22nd-orders) than the theory (12th - 20th-orders). The α angles were also well reproduced by the theory,

---

[12] 2D interpolation was performed using `scipy.interpolate.Rbf`

where α of the sidebands roughly followed that of the the NIR. The theory even captures the $\sim 12^{\text{th}}$-order sideband remaining at $\alpha = 0^\circ$ for most α_{NIR}.

The agreement seen in Fig. 3.10 between the theory and experiment supports the validity of the assumptions made in the theory. In these experimental conditions, including only the trajectories which pass through the Γ-point appears justified, as does ignoring multi-particle interactions. Overall, this provides substantial evidence that the theory includes the key components of the electron-hole dynamics. With this agreement in hand, it can now be asked what else can be extracted from the theoretical model.

Extracting Luttinger Parameters

While using HSG to extract the stress of the system is valuable, it is also possible to measure stress using more straightforward methods such as absorption [95, 112], differential reflectance [71, 70], or birefringence [112, 22]. However, the $\mathcal{T}$ matrices include all of the information about the dynamics of the quasi-particles, including the Hamiltonian of the system. Is it possible to extract parameters of the Hamiltonian, such as the Luttinger parameters in Eq. 1.5?

Under the assumptions of non-interacting particles and that the trajectories passing through Γ dominate, it turns out some simple relations of the $\mathcal{T}$ matrices appear. In these instances, one finds[13],

---

[13] The derivation of these equations is left for a future publication

$$\mathcal{T}_{++} = \mathcal{T}_{--} \tag{3.11}$$

$$(\gamma_2 \cos(2\theta) - i\gamma_3 \sin(2\theta))T_{+-} = (\gamma_2 \cos(2\theta) + i\gamma_3 \sin(2\theta))T_{-+} \tag{3.12}$$

where γ_2, γ_3 are the Luttinger parameters, θ is the angle of the THz polarization to the [010] crystal direction. Equations 3.11 and 3.12 should also be independent of strain and sideband order. These relations show the diagonal elements of the $\mathcal{T}$ matrices are equal, and the off-diagonal elements are related simply by the Luttinger parameters and crystal orientation. Therefore, a large amount of information on the polarization is contained in their ratio, which is why the error function of Eq. 3.10 was justified in using only that ratio. Looking at Eq. 3.12, it indicates the ratio of the off-diagonal elements of the $\mathcal{T}$ matrices could be used for extracting information about γ_3/γ_2.

To check the experimental agreement with these equations, Fig. 3.11 shows the ratios of extracted experimental $\mathcal{T}$ matrices for three of the fans shown in this chapter. Since these ratios are complex valued, Fig. 3.11(a) shows the magnitude of the ratios, while Fig. 3.11(b) shows their complex phase. The ratios of the diagonal elements is shown in grey curves and the off-diagonal is shown in red. The $\mathcal{T}$ matrices for the experiment in Fig. 3.10, where good agreement between the theoretical and experimental fan diagrams was observed, is shown as the solid curves with solid squares. The magnitudes of the ratios of both the diagonal and off-diagonal elements are close to 1, in agreement with Eqs. 3.11 and 3.12. The phases of the ratios ares also nearly 0°, again in agreement with

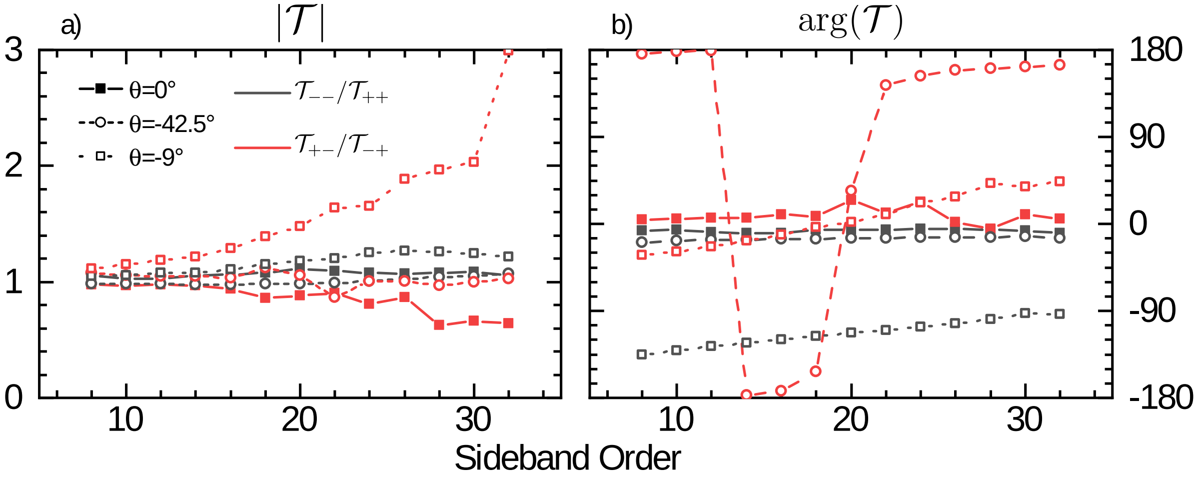

Figure 3.11: Ratios of components of the $\mathcal{T}$ matrices from experiment. $\theta = 0°$ (solid squares, solid line) is from the data in Fig. 3.10, while $\theta = -42.5°$ (open circles, dashed lines) and $\theta = -9°$ (open squares, dotted lines) come from the left and right side Fig. 3.3, respectively. The ratios of the diagonal elements are plotted in grey and the off-diagonal elements in red. (a) Magnitudes of the ratios of elements. Eq. 3.11 predicts all curves should be 1, in rough agreement with all curves except the off-diagonal components for $\theta = -9°$. (b) The complex phases of the ratios of elements of the $\mathcal{T}$ matrix. Eq. 3.11 predicts all $\arg(\mathcal{T}_{--}/\mathcal{T}_{++})=0°$, while $\arg(\mathcal{T}_{+-}/\mathcal{T}_{-+})$ depends on the crystal orientation: it should be near 0° for $\theta = 0°$, $-50°$ for $\theta = -9°$ and $-180°$ for $\theta = -42.5°$.

Eqs. 3.11 and 3.12.

Since the experiment of Fig. 3.10 was taken at $\theta = 0°$, it unfortunately means that it is not possible to extract information about the Luttinger parameters from this data set via Eq. 3.12. Therefore, data at different crystal axis is also shown in Fig. 3.11: the open circles shows data from the left side of Fig. 3.3, where $\theta = -42.5°$, and the open squares is for the experiment shown on the right side of Fig. 3.3 where $\theta = -9°$.

For both datasets, Eqs. 3.11 and 3.12 expect $|\mathcal{T}_{--}/\mathcal{T}_{++}| = |\mathcal{T}_{+-}/\mathcal{T}_{-+}| = 1$. This agrees with the observed values for the $\theta = -42.5°$, and for $|\mathcal{T}_{--}/\mathcal{T}_{++}|$ for $\theta = -9°$. While it also agrees for the low-orders of $|\mathcal{T}_{+-}/\mathcal{T}_{-+}|$ for $\theta = -9°$, the ratio of the off-diagonal elements increased in magnitude at higher orders, which is counter to the prediction that Eq. 3.12 holds for all sidebands.

For the phases of the ratios, Fig. 3.11(b), Eq. 3.11 predicts all phases for the diagonal components to be 0°. For the off-diagonal components, and assuming $\gamma_2 = 2.06$, $\gamma_3 = 2.93$, Eq. 3.12 predicts $\arg(\mathcal{T}_{+-}/\mathcal{T}_{-+})|_{\theta=-9°} = -49.6°$ and $\arg(\mathcal{T}_{+-}/\mathcal{T}_{-+})|_{\theta=-42.5°} = -173.0°$. This appears to agree well for $\theta = -42.5°$; $\arg(\mathcal{T}_{--}/\mathcal{T}_{++})$ is near 0° across all sidebands, and $\arg(\mathcal{T}_{+-}/\mathcal{T}_{-+})$ is moderately close when accounting for the phase wrap around 180°. The agreement of $\theta = -9°$ is less convincing, where $\arg(\mathcal{T}_{--}/\mathcal{T}_{++})$ is far from 0°, and $\arg(\mathcal{T}_{+-}/\mathcal{T}_{-+})$ is only $\sim -39°$ at low orders. Furthermore, there is clearly a dependence on sideband order for both ratios.

These disagreements of the experimental $\mathcal{T}$ matrices from Eqs. 3.11 and 3.12 make it difficult to reasonably extract information about the Luttinger parameters from these datasets. These data were taken with λ_{NIR} =815.794 nm, which is a relatively large photon energy and certainly larger than the band gap. In Fig. 3.7, the $\theta = -42.5°$ was taken in the overlap of Spots E and D, while the $\theta = -9°$ data was taken at Spot D, both of which have at least one band edge lower in energy than the NIR photon energy used. This violates the assumption that only paths through Γ are significant, and if additional paths must be considered for $\mathcal{T}$ matrices, then Eqs. 3.11 and 3.12 may no longer be valid for these data. Furthermore, these data were taken at a relatively large THz field strength, and it may be that other effects are not properly taken into account, such as sample heating or exploring outside the valid regions of the Brillouin zone. However, the agreement of the 0° data with Eqs. 3.11 and 3.12 provides a promising path forward to using polarimetry data from HSG for extracting material parameters.

3.5 Conclusion

This chapter has introduced a vastly improved apparatus for measuring sideband polarization and has shown the usefulness of dynamical Jones calculus for extracting information about the materials studied. Figure 3.1 showed how sensitive the polarization of the sidebands could be to different samples, while Figure 3.2 shows how sensitive they are to crystal symmetries. The dynamical Jones matrices introduced in Figure 3.4 provide a tool for determining sideband polarization states for any given NIR polarizations, which could be technologically relevant for tailoring polarization states of the teeth in a frequency comb.

Significant progress has been made to theoretically understand the underlying electron-hole recollisions which result in the various fan diagrams observed. Improved sample preparation to reduce the inhomogeneous strain to produce better quality data is required to fully test the predicted relations between $\mathcal{T}$ matrices, Equations 3.11 and 3.12, to prevent inhomogeneously averaging over strain, as in Fig. 3.8 and Fig. 3.9. Alternatively, intentionally strained samples, such as quantum well structures with mismatched lattices, could provide another control over sideband polarizations by tailoring the strain directly. Furthermore, if sufficient strain is introduced to significantly split the valence bands, it would be easier to theoretically study an effective two-band model. High-order sideband generation is well on its way to providing all optical measurements of band-structure and material properties.

Chapter 4

Beyond GaAs

All of the results discussed so far have come from a single family of materials, GaAs based systems. GaAs and its heterostructures are well studied materials which provides the benefit of an expansive amount of literature to compare results and better understand the dynamics of the material. However, moving outside of this relatively simple material would be extremely beneficial; different material would expand the viability of HSG frequency combs as different materials with varying band gaps would greatly shift the center frequency of the combs (see Chapter 2). Furthermore, a technique of measuring material parameters (as discussed in Chapter 3) could be invaluable in new, less well understood materials.

In order to observe high-order sidebands from a new material system, two fundamental criteria must be met. The band gap of the material in question must be within the tuning range of our excitation laser, 700-1000 nm (1.24 - 1.77 eV), and the Coulomb potential must not be so great that the exciton binding energy is too large to allow tunnel ionized by the field strengths allowed in the FEL (as defined in Eq. 1.30). Three new materials follow these criteria while being easily acquired: $MoSe_2$ and WSe_2 in the family of transition-metal dichalcogenides, lead-halide perovskites and carbon nanotubes (CNTs). In this chapter, each of these material systems will be briefly introduced, followed by the results of experiments to see HSG in each. Each section will wrap up with a discussion of how the experiments could be improved and future steps towards observing HSG in these materials at UCSB.

4.1 Transition-Metal Dichalcogenides

Transition-metal dichalcogenides (TMDs or TMDCs) fall under the realm of 2D Van der Waals bonded materials which have regained significant interest since the isolation of monolayer graphene [34]. With the ability to exfoliate high quality monolayers in the same fashion as graphene, there is significant promise of making Van der Waals heterostructures or ultra-thin electronics based on these materials [34, 116, 82]. These TMDs exhibit a wide range of unique properties which make them interesting candidates for investigating. For example, when taking these materials from bulk to discrete layers, one finds the electronic properties depend significantly on the number of layers; as the dimensionality is reduced by lowering the number of layers in a sample, the band gap blue shifts and its character changes from indirect to direct at one layer [69, 138].

Two TMDs are of interest here, the 2D semiconductors WSe_2 and $MoSe_2$. The crystal structure of each is of layered hexagonal planes of Se-M-Se (M being tungsten or molybdenum) [116]. In momentum space, this results in a direct band gap at the K and K' points in both bulk and monolayer (note that in the bulk, the minimum in the conduction band shifts in momentum leading to an overall indirect band gap semiconductor [116]). These materials also exhibit a large spin-orbit couping (SOC) which splits the valence bands at the K points by $\sim$180 meV in $MoSe_2$ [93] and $\sim$380 meV in WSe_2 [131]. The strong SOC results in differing optical selection rules for the K and K' valleys [82], and has been an active area of research for ultra-fast valleytronics for communication [82, 61]. This also results in two classes of excitons, the A and B excitons, which arise from holes generated from the upper or lower valence band in the K valleys [131, 139, 138].

For both WSe_2 and $MoSe_2$, it is important to know whether experiments should be performed at room temperature or low temperatures, and in bulk or monolayers. Table 4.1 lists the band gap of each material (defined relative to the exciton state, not the valence-conduction band splitting), the excitonic binding energy (E_b) for a neutral exciton (X^0) is shown. Furthermore, it is possible for a 'trion' to form in TMDs, discussed below. The negative trion (X^-) is also listed in Table 4.1, along with the Keldysh parameter (γ, Eq. 1.30), and the maximum number of sidebands expected from the three step model (N_{max}, Eq. 1.29). The effective masses used in calculations were $m_e = 0.70m_0$, $m_h = 0.55m_0$ for $MoSe_2$, $m_e = 0.53m_0$, $m_h = 0.52m_0$ for WSe_2 [89], and a driving field of 540 GHz at 50 kV/cm in the material were used.

In both materials, in the bulk and monolayer limits and at room temperature or low

		Band Gap[1] (eV)	Exciton E_b (meV)	γ	N_{Max}
MoSe$_2$	300 K	∼1.56 [5]	X^0 ∼50 [19][2]	X^0 ∼0.284	X^0 ∼460
	Low T	∼1.63 [5]			
ML MoSe$_2$	300 K	1.58 [93]	X^0 ∼100 [5];[3] 550 [108]	X^0 ∼0.942 X$^-$ ∼0.220	X^0 ∼680 X$^-$ ∼450
	Low T	∼1.64 [93]	X$^-$ ∼30 [93]		
WSe$_2$	300 K	1.621 [61, 4]	X^0 ∼60 [4]	X^0 ∼0.287	X^0 ∼540
	Low T	1.692 [4]			
ML WSe$_2$	300 K	1.665 [61, 4]	X^0 ∼370 [4] X$^-$ ∼30 [4, 49]	X^0 ∼0.713 X$^-$ ∼0.203	X^0 ∼680 X$^-$ ∼530
	Low T	1.744 [4]			

Table 4.1: Parameters of two TMDs relevant to HSG. Lists the band gap and exciton energy which are two important material parameters for HSG in the current experimental setup. γ is the Keldysh Parameter, Eq. 1.30, which determines the ionization of the exciton. N_{max} is the maximum number of sidebands expected from the three-step model, see Sec. 1.2 for reference. Assumes a 540 GHz driving field at 50 kV/cm in the material. X^0 refers to parameters of the neutral exciton, while X$^-$ is the negative trion.

---

[1] Measured from the valence band to the exciton state, *e.g.* $E_g - E_b$, the relevant value for HSG to generate an exciton.

[2] This is an order of magnitude estimate, based on the scaling from screening in 3D compared to the monolayer case

[3] This value assumed the spacings between the 1s-2p states of the exciton follow the 2D Rydberg, which is a bad assumption, as stated in the main text.

temperature, the required NIR photon energy to create an exciton was available by the laser available during this work. In the bulk materials, the exciton binding energies are significantly larger than even the quantum wells studied so far, but the Keldysh parameter for reasonable fields from the FEL should be sufficient to tunnel ionize them. When reduced to a single monolayer, the Coulomb potential is increased which results in more tightly bound excitons [4, 5, 108] where tunnel ionization of the neutral excitons with the fields available to the UCSB FEL is less probable. However, the increased Coulomb interaction allows for the formation of trions, a negatively or positively charged exciton which mimics H^- or H_2^+ [93, 82, 49, 4, 5]. TMDs are often intrinsically n-doped [115], so the trion is often associated with the negative state (X^-). The binding energy of the trion is small enough that it is often thermally ionized at room temperature [115, 93]. While the binding energies of the trion can be easily reported by the difference in energy of the trion to neutral exciton peak (in absorbance spectra, for example), the neutral exciton binding energy is slightly more difficult to measure. This is because the monolayer TMD excitons cannot be described by 2D Rydberg states and less straightforward methods must be used to estimate their binding energy [4, 5, 40, 64].

From Table 4.1, room temperature experiments on bulk WSe_2 or $MoSe_2$ or low temperature monolayers (to access the trion) would be good targets for experiments with minimal modification to the experimental apparatus of the rest of this thesis. Furthermore, HSG has been recently observed in bulk [60] and monolayer [61] WSe_2. While these reported studies were done at significantly higher THz frequencies and fields (20-40

THz and 17-18 MV cm^{-1}), it shows HSG is possible in these materials. Experiments at lower field strengths and frequencies, such as those attempted here, may be useful and yield more information about these material systems, especially around the K-points.

4.1.1 Attempts at HSG

Several samples of $MoSe_2$ and WSe_2 were provided by Kyle Seyler of Xiaodong Xu's group from University of Washington, transfered to 500 μm sapphire substrates with an ITO backside coating. In the first set of experiments, monolayers of $MoSe_2$ and WSe_2 were exfoliated and protected by an exfoliated layer of hexagonal boron nitride (hBN), see Fig. 4.1. The top left of Fig. 4.1 shows a relatively large ($\sim 15 \times 40$ μm) WSe_2 flake capped by the hBN. The $MoSe_2$ flake is shown on the top center, which fractured into several small pieces. The low temperature photoluminescence (PL) signal for both samples is shown below, using a confocal microscope objective at the University of Washington for signal collection[1]. Both flakes show the clear neutral exciton and trion, in good agreement with Table 4.1. The WSe_2 flake sees an additional broad feature is seen peaked around 750 nm, which arises from defect bound excitons [4, 86, 105].

Initial experiments on these samples at UCSB were unsuccessful. The $MoSe_2$ flake was investigated first due to the proximity of the trion with the GaAs systems studied in previous chapters. Experiments used 0.1 μW/μm^2 of 1.625 eV (763 nm) excitation at 15 K with a driving field strength of 100 kV/cm in air at 540 GHz. Before any signal

---

[1] The relatively large NIR spot sizes and slow optics used at UCSB made it difficult to characterize these samples, see Appendix A.2.5

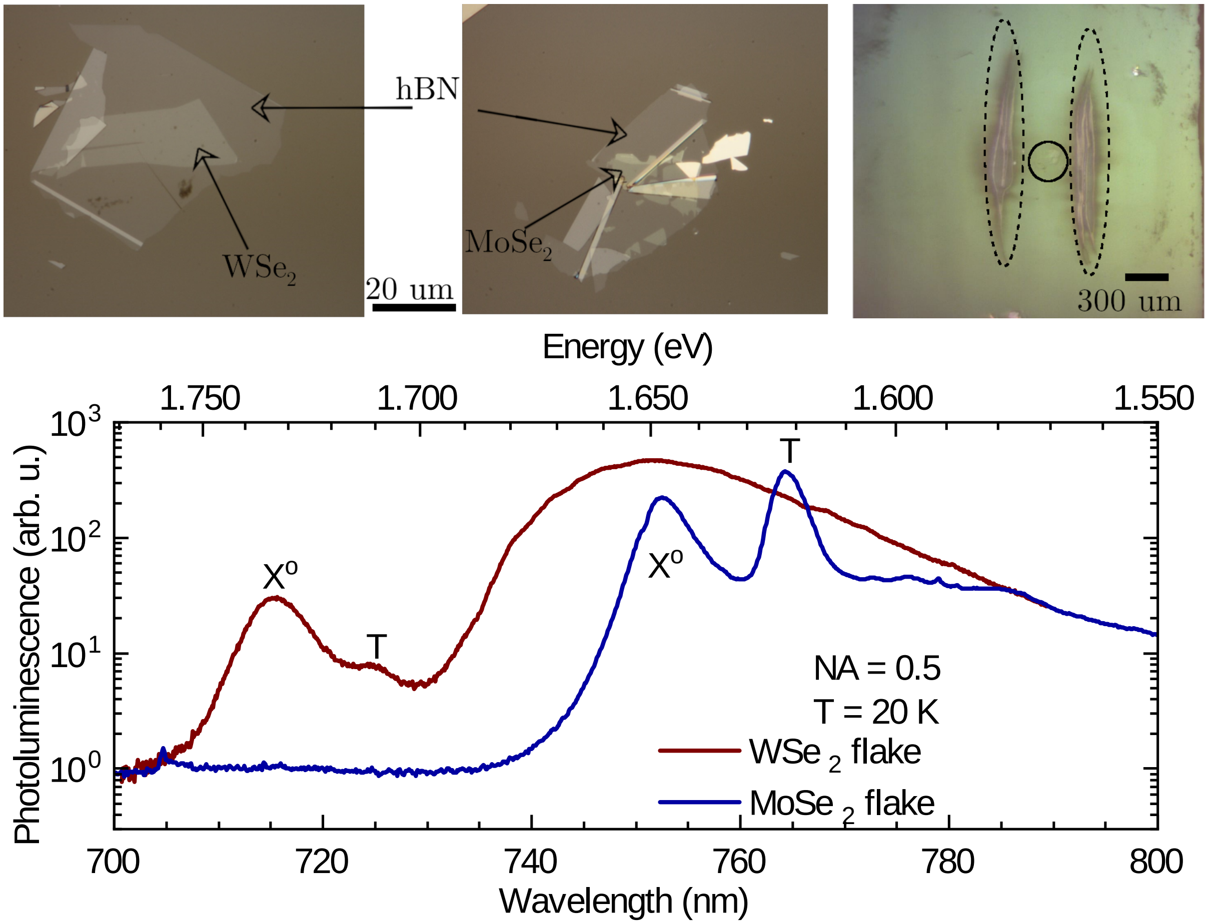

Figure 4.1: Samples of WSe_2 and $MoSe_2$ used for HSG experiments. Top left and center show the monolayer flakes of WSe_2 (left) and $MoSe_2$ (center). Each is covered by a monolayer of hexagonal boron nitride (hBN) to protect the monolayers. 20 μm scale bar corresponds to both the WSe_2 and $MoSe_2$ figures. The top right shows the WSe_2 flake (circled) in the cryostat after attempts to see sidebands. The dashed ovals highlight the damage to the ITO film. (Bottom) Low temperature photoluminescence of both samples, measured at the University of Washington. Measured with a 0.5 numerical aperture (NA) objective.

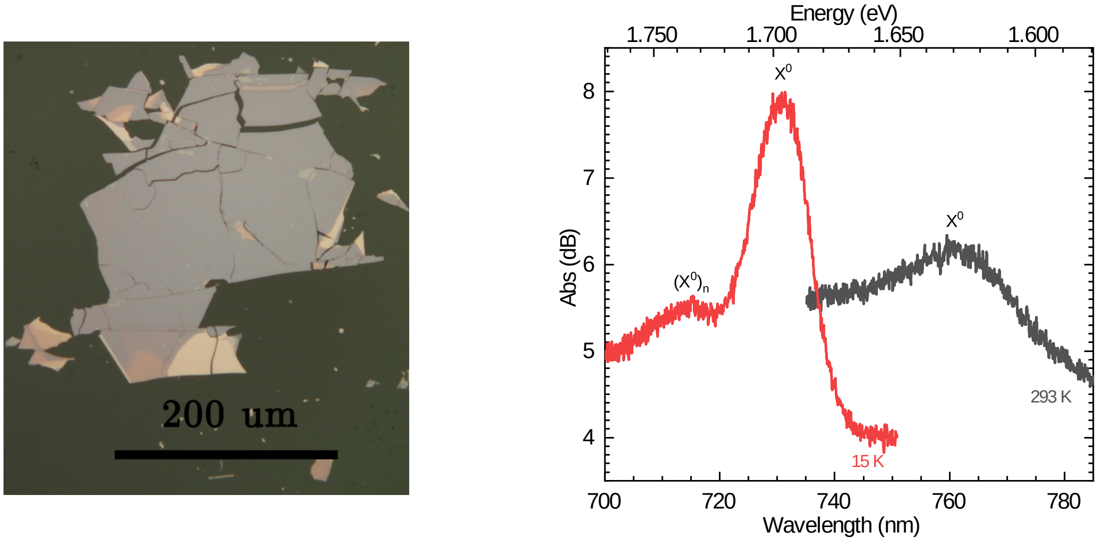

Figure 4.2: Bulk sample used for second attempts of HSG. (Left) Microscope image of the bulk (60 nm, ∼ 85 layers) sample of WSe_2 . (Right) Temperature dependence of the absorbance spectra of the sample. At 293 K (grey curve) a broad neutral exciton (X^0) is observed. At low temperature (15 K), the neutral exciton blue shifts. A shoulder is observed which is attributed to excited states of the exciton (See ref. [4]), labeled $(X^0)_n$.

could be seen, THz induced damage to the ITO layer occurred [2], as shown in the top right of Fig. 4.1. Before looking at the WSe_2 sample, it was realized that the typical NIR radius at the sample was ∼200 μm (see Appendix A) which was far larger than the sample sizes as seen in Fig. 4.1. Faster NIR (f = 60 mm) focusing optics were inserted which reduced the NIR spot radius to ∼10 μm. While the faster optics improved the signal of PL due to a higher collection efficiency, HSG attempts were still unsuccessful. One of the biggest concerns is the closed-cycle cryostat introduces vibrations which move the sample by ∼10 μm, on the order of the lateral dimensions of the sample and the NIR spot size. This made it difficult to ensure the NIR was hitting the sample during a THz pulse.

As it is easier to fabricate bulk samples which are larger than monolayers, and therefore easier to excite with optics and lasers, and the bulk exciton should be ionizable at room temperature with the UCSB FEL, a second round of experiments was attempted on exfoliated bulk samples. Figure 4.2 shows the optical microscope image of a 60 nm thick flake of WSe_2 with lateral dimensions of hundreds of microns. The large size made it significantly easier to measure the absorbance at both room temperature and low temperature, right side of Fig. 4.2. At room temperature, the neutral exciton peak was visible, which was enhanced and blue shifted when it was cooled low temperature, agreeing with Table 4.1. The peak around 715 nm is attributed to the excited states of the exciton ($2p$ etc.).

Figure 4.3 shows the experimental results for the bulk WSe_2 flakes for room temperature excitations with a NIR excitation intensity of 2 μW/μm^2, with 100 kV/cm of 540 GHz driving radiation. Figure 4.3(a) shows the integrated strength of the 2$^{\text{nd}}$-order sideband as a function of NIR excitation frequency, while the intensity of the excitation was kept fixed. Similar to reference [60], the sideband strength roughly followed the excitonic resonance. However, additional oscillations were observed due to the presence of a strong NIR Fabry-Perot cavity from the substrate which lacked an anti-reflection coating, see Sec. B.2.

The optimal NIR frequency was then used to determine how many sidebands could be observed. Figure 4.3(b) shows the resulting spectra for a NIR excitation of 761.6 nm (1.628 eV). To understand potential influences from dynamical birefringence on the sideband strengths (see Chapter 3), sideband signal was measured for the NIR polarization

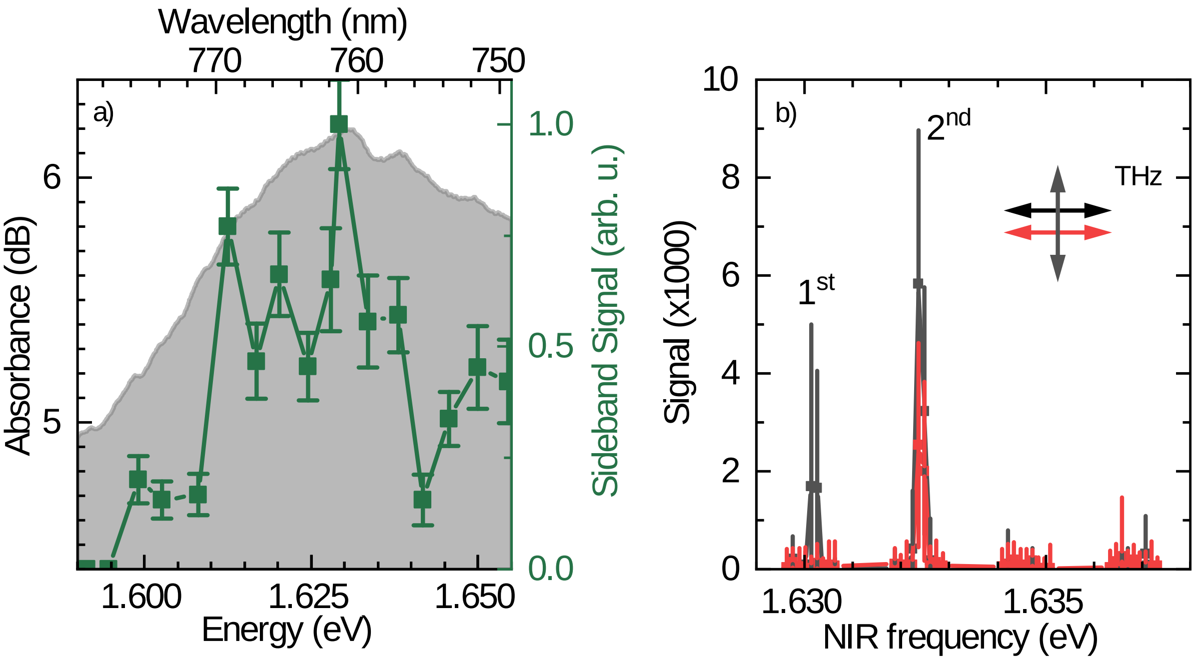

Figure 4.3: Results of sideband experiments from the bulk WSe_2 sample of Fig. 4.2. (a) Normalized signal of the 2^{nd}-order sideband as a function of the frequency of the NIR excitation (green curve, right axis). Overlain is the absorbance around the neutral exciton (shaded grey, left axis). The polarization of the NIR laser was parallel to the THz polarization. The signal roughly follows the absorbance peak, but is strongly modulated by the sapphire-ITO substrate cavity. (b) Raw spectra of the low-order sidebands for the NIR polarization parallel (red) and perpendicular (grey) to the THz polarization. NIR frequency was set to 761 nm. Vertical lines at each point denote the error bars (standard error of the mean). The laser was measured for each polarization (not shown) and signal was normalized to the maximum of the laser signal. Inset schematic shows the relative NIR to THz polarizations (THz was kept horizontally polarized).

parallel (perpendicular) to the THz polarization in red (grey)[2] with detection parallel to the excitation laser. With parallel laser fields, only the second order sideband was observed. With perpendicular excitation, a stronger 2^{nd}-order sideband was observed, as well as a 1^{st}-order. Unfortunately, the signal was too weak to adequately measure the THz field strength scaling to reproduce Fig. 1 of Ref. [60]. After only a few hours of measurements, damage occurred to the ITO substrate, similar to the top right of Fig. 4.1, and no further experiments were possible.

4.1.2 Future Direction

It is unclear how fruitful continued investigations of the monolayer TMDs would be in the current setup, where vibrations are too large. Figure 4.3 indicates, however, there may be more to be learned from studying the bulk material. As a first step, improvements to the ITO coating to prevent destruction of the samples would be necessary, see Sec. B.1. Another significant enhancement can come from greatly increased NIR intensities. Experiments here were limited to $\sim 2\mu\text{W}/\mu\text{m}^2$, while it is possible to excite monolayers with at least an order of magnitude larger intensities [108] or two orders for bulk [5]. If low temperature experiments are desired, a liquid helium flow cryostat may be preferred to prevent sample positional shifts due to vibrations, or better design of vibrational isolation in the current system.

Unfortunately, even with these improvements, it is not certain whether non-perturbative

---

[2] Note that it was not possible to determine the crystal axes of the sample, making it unclear what the polarizations were with respect to the symmetry axes of the crystal. However, Reference [60] indicates it should not matter for HSG.

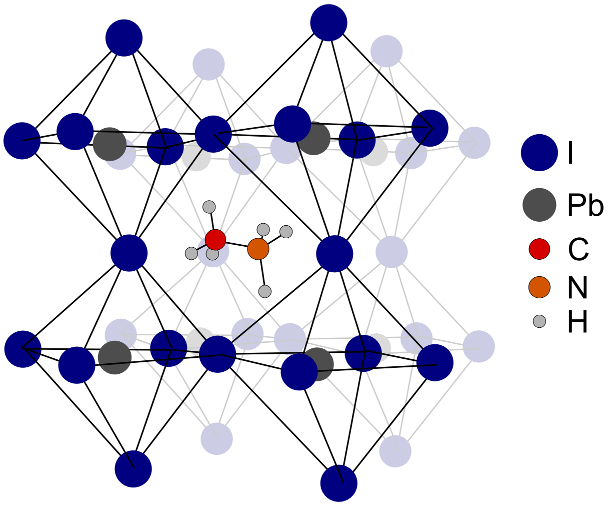

Figure 4.4: Crystal structure of methylammonium lead iodide. The iodide atoms form an octahedron with a lead atom at the center. A methylammonium group sits at the center of a grouping of these octahedron. Adapted from [32].

sidebands (*e.g.* those arising from HSG) could be observed with the THz driving fields available at the UCSB FELs. Langer, *et al* showed that non-perturbative sidebands from bulk WSe_2 , which is an indicator of HSG [133], took field strengths in excess of 1 MV/cm. Furthermore, the scattering rates of TMDs are estimated on the order of 150 fs^{-1} [86], which would scatter electrons and holes well before they can recollide for the time scales from the UCSB FELs (Sec. 1.2 and Chapter 2).

4.2 Lead-Halide Perovskites

Another class of materials investigated was the family of hybrid halide perovskites, with a schematic chemical formula ABX_3 where A is an organic complex, B is a heavy metal, and X is an element from the halides. One of the most common forms is $CH_3NH_3PbI_3$, also known as methylammonium lead iodide, or $MAPbI_3$. The crystal structure of the perovskites is depicted in Fig 4.4. $MAPbI_3$ and related materials have been of significant interest due to to their potential applications in solar cells [72, 30, 81] or LEDs [102]. Hybrid perovskites are processed at relatively low temperatures and from solutions, which make them significantly more straightforward to manufacture than typical solar cell materials [102].

At room temperature, $MAPbI_3$ has a tetragonal symmetry structure with a band gap around 1.60 [102]-1.64 eV [29]. As the temperature decreases, the band edge red-shifts (counter to typical expectations with semiconductors [25]) [29]. Around 160 K, the crystal undergoes a phase transition from the tetragonal symmetry to an orthorhombic phase [32, 75, 29, 42], blue shifting the band edge by $\sim$60 meV [29]. Further decreases in temperature again red-shift the band edge to roughly 1.64 eV at 4.2 K [29]. The overall band gap as a function of temperature spans between 1.6 - 1.7 eV [29], well within the range accessible to experiments at UCSB. In addition to changes in the band gap by temperature, it can also be tuned by changing the organic compound [30, 81, 42] or the halide [39, 42].

The binding energy of an exciton in these materials, the second important parameter for determining the efficacy of HSG, is not well understood. Early experiments attempted to extract the low temperature exciton binding energy from magneto-absorption experiments [44, 103], and yield a binding energy of 37-50 meV. These measurements, however, depended on the value of the dielectric screening in the material. The high-frequency dielectric value ($\epsilon_\infty \approx 6.5$ [44, 15]) was used, claiming the binding energy is lower than the

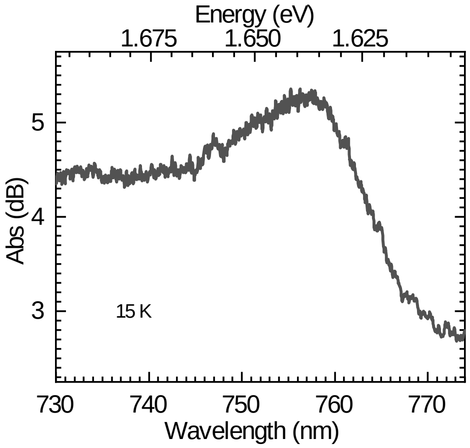

Figure 4.5: Low temperature absorbance of the $\mathrm{MAPbI_3}$. The exciton peak is readily visible around 755 nm.

LO phonon energy ($E_{\mathrm{LO}} \approx 38.4$ meV [75]), which justifies the use of ϵ_∞ (see Section 9.2 of [55], or Section 2 of [42]). If the static dielectric value is used ($\epsilon_0 \approx 25.7$ [15, 32, 75]), the binding energy of the exciton would only be 2 meV [75].

Other techniques for measuring the binding energy of the exciton also result in a significant spread of energies [42]. The structural phase transition also further complicates the measurements as the binding energy may change in the different phases. However, assuming the higher binding energy of 50 meV, and a reduced mass around $0.2m_0$ [32, 75, 103, 44, 42], the Keldysh parameter (Eq. 1.30) is $\gamma \approx 0.23$ for 35 kV/cm at 540 GHz and any exciton should be readily ionizable by the fields used in experiments.

4.2.1 Attempts at HSG

A polycrystalline sample of $\mathrm{MAPbI_3}$ on 500 μm unprocessed sapphire was provided by the Chabynic Group in the Materials department at UCSB. Figure 4.5 shows the mea-

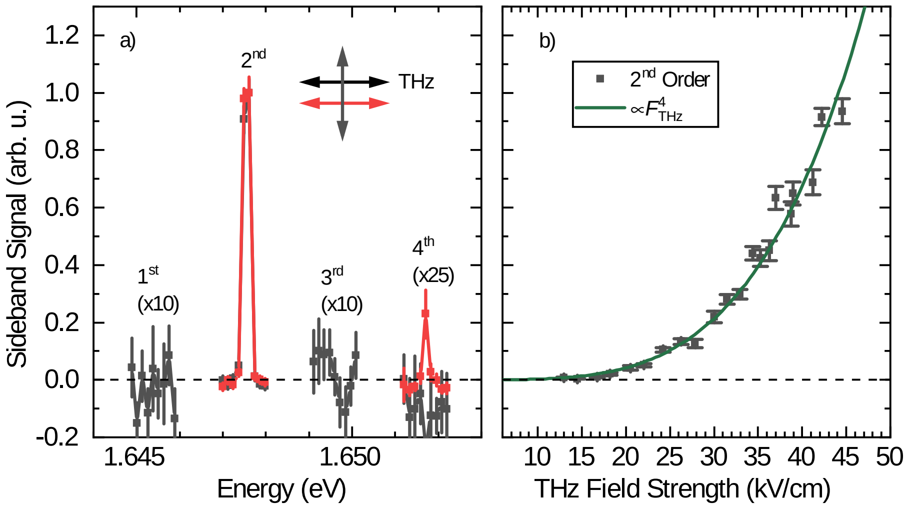

Figure 4.6: Results of HSG experiments in $MAPbI_3$. (a) Raw low-order sideband spectra for the NIR polarization parallel (red) and perpendicular (grey) to the THz laser. Inset schematically shows the relative polarizations of the NIR to the THz. Signal was normalized to the maximum of the 2^{nd}-order sideband. The THz field strength was ∼45 kV/cm (in air), NIR wavelength was 755 nm, and NIR power of 75 mW. Both orientations observe a 2^{nd}-order sideband. Parallel polarization shows hints of a 4^{th}-order. (b) Dependence of the sideband signal (the signal is proportional to the power in each sideband) on the THz field strength, F_{THz}. The sideband signal was well fit to F^4_{THz}, indicating the perturbative nature of the sideband signal. Dashed lines in (a), (b) mark the zero-signal offset.

sured low temperature absorbance spectrum. The peak near 755 nm is attributed to the exciton, and its position and width agree well with published low temperature values [29]. Experiments were performed at low temperatures so the quantum well samples discussed in previous chapters could be used to align the optics and lasers.

Preliminary experiments were performed using 600 GHz with the NIR laser tuned to 755 nm with 75 mW of NIR power ($\sim$ 600 mW/mm^2). The substrate used for the experiments was not coated in ITO which resulted in lower maximum field strengths available (See Appendix B). The results of the sideband experiments are highlighted in Fig. 4.6.

Figure 4.6(a) shows the signal of the first four sideband orders for the NIR polarization perpendicular to the THz polarization (grey) and the 2nd- and 4th-orders when the polarizations are parallel (red). The maximum THz field strength was used, and the signal in each spectra was normalized to the maximum of the second order sideband. While a second order sideband was observed in both polarization orientations, no further sidebands were observed for the perpendicular polarization. The parallel polarization shows hints of a 4th-order sideband.

To help determine the physical origin of the sidebands, the power in the second order sideband is plotted as a function of THz field strength in Fig. 4.6(b) for the laser field polarizations perpendicular to one another. The measured sideband signal was proportional to the power in each sideband. If the sidebands were perturbative in nature, the signal in the 2nd-order sideband should scale with the 4th-power of the THz field (F_{THz}) [14, 96]. A fit of the data to F_{THz}^4 is overlain in green, and the good agreement between the data and fit indicates this signal is likely the result of perturbative nonlinearities. An extraction of the nonlinear parameter, $\chi^{(3)}$ is not directly available from this data due to a lack of appropriate normalization of detectors such as done for the TMDs in Fig. 4.2, but to repeat experiments and properly normalize would be relatively straightforward. Note that the field strength reported in Fig. 4.6 is the in-air field strength (counter to the in-material convention used in previous chapters). Scaling the field strength to the material requires knowledge of the permittivity of the material at that frequency. However, the permittivity is strongly frequency dependent [110, 65] and there is no good measurement of the permittivity at these frequencies.

No further experiments were performed with this sample. These materials degrade quickly in the presence of water [32, 26] and the sample quality deteriorated significantly before other experiments were possible.

4.2.2 Future Direction

One of the most significant improvements for future experiments would be to request single-crystal $MAPbI_3$ [110] instead of polycrystalline. The grain size in these samples is estimated to be a few hundred nanometers[3]. With a relatively large NIR spot size several orders of magnitude larger than the grain size could result in incoherent averaging over the various grains, reducing the signal quality. Another significant improvement would be to use the ITO backed substrates which have been successful previously, and could push the signal out of the perturbative regime.

It is difficult to find literature on the scattering rates of these materials due to their relatively recent rise in interest. Recent experiments of THz time-domain spectroscopy observed optical conductivities which were well described by the Drude model [110]. The scattering rate extracted from these experiments result in a rather short $\tau \approx 70$ fs, which would be problematic for the long trajectories in HSG. However, it is possible investigating other materials in the hybrid-metal perovskite family could be beneficial; experiments replacing the methylammonium with formamidinium (creating $FAPbI_3$) observed a 5-fold increase in carrier lifetimes at room temperature [140]. If the short lifetimes of $MAPbI_3$

---

[3] As estimated by the grower

is one of the limiting factors in observing HSG, $FAPbI_3$ would be a promising avenue to explore.

4.3 Carbon Nanotubes

The final foray into new materials also attempted to investigated lower dimensionality effects on HSG. Graphene, the well-known 2-dimensional atomic layer of graphene, can be rolled along an axis to produce nanotubes, often called carbon-nanotubes (CNTs), see Fig. 4.7. Figure 4.7(a) depicts a single layer of graphene where $\vec{R}_1$ and $\vec{R}_2$ are the unit vectors. Various lattice vectors describe by a sum of these unit vectors, $\vec{R} = m\vec{R}_1 + n\vec{R}_2$ are given the shorthand notation (m, n). A CNT is formed when the graphene is rolled along one of these unit vectors (*i.e.* the vector $\vec{R}$ is tangent to the circumference of the nanorod), Fig. 4.7(b). Higher symmetry CNTs are formed when along the $(n, 0)$ (zigzag) or (n, n) (armchair) directions. CNTs have been of great interest in applications such as 1D electronics [3], broadband optical components [41], or using their high-strength composites [12].

The density of states of CNTs exhibits van Hove singularities due to its 1D nature [25, 76]. When $m - n = 3l$, where l is an integer, the CNT will display metallic characteristic where there are a finite number of states at the Fermi energy, otherwise they are semiconducting [76]. Figure 4.7(c) displays a schematic DOS for carbon nanotubes using the forms derived by Mintmire and White [76], while the relative spacing between energies is from Kataura *et al* [52]. The semiconducting character (grey curve)

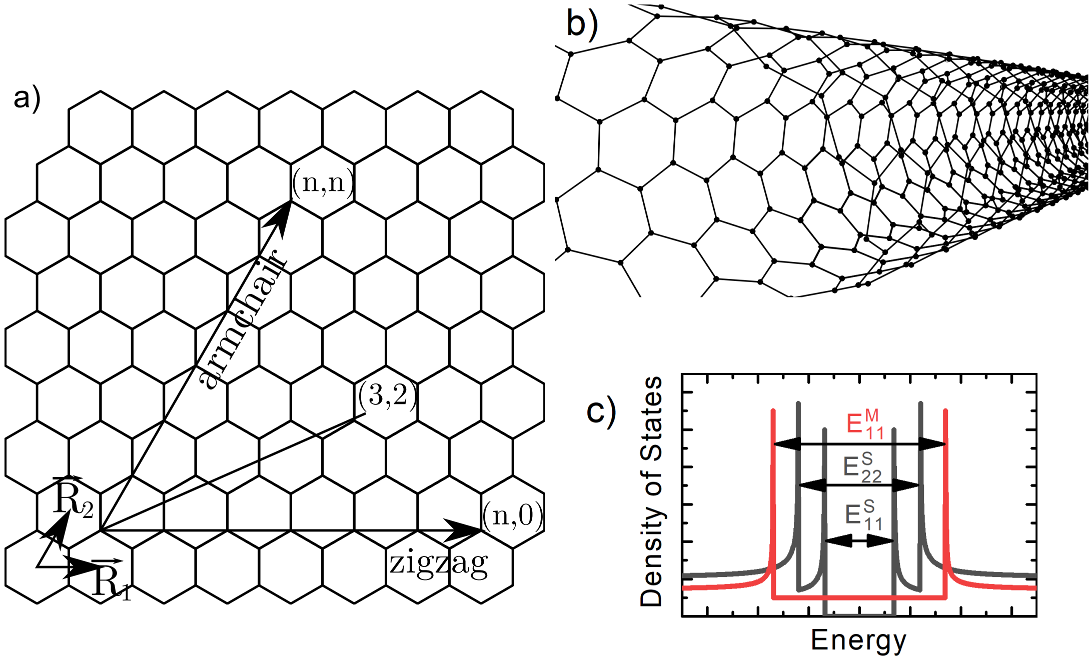

Figure 4.7: Description of carbon nanotubes (CNT). (a) 2D graphene lattice with the unit vectors $\vec{R}_1$ and $\vec{R}_2$. An arbitrary vector between graphene unit cells can be written as a linear combination of the two unit cell vectors, $\vec{R} = m\vec{R}_1 + n\vec{R}_2$, which can be written with the shorthand (m, n). When the graphene sheet is wrapped around one of these unit vectors, a CNT is formed. If the wrapping vector is described by (m, n) with $m = n$, it is called an armchair CNT. If $n = 0$, it is called a zigzag CNT. (b) Depiction of a (3, 0) zigzag CNT. (c) Schematic of the density of states of for a collection of CNTs of various (m, n) values. The distinction between the metallic states (red) and semiconducting (grey) is shown. Relative energy scales taken from [52] and functional form follows [76]. E^{S}_{11} denotes the first exciton gap of the semiconducting tubes, E^{S}_{22} denotes the second-highest, resulting from the second quantized levels of the CNT, not the excited exciton states. E^{M}_{11} is the first metallic exciton. Semiconducting CNTs show a zero density of states in band gap while the metallic states show a finite density of states.

shows no states exist in the center of the gap, and the lowest energy transition is the E_{11}^{S} corresponding to the highest hole band to lowest electron band transition. The metallic character (red curve) shows a finite density of states, and the lowest energy transition E_{11}^{M} is larger than the semiconducting character. In general, decreasing the tube diameter will increase $E_{11}^{\mathrm{M/S}}$, while for an equal tube diameter, $E_{11}^{\mathrm{M}} > E_{11}^{\mathrm{S}}$ [76, 52, 119].

The wide tunability of CNTs through their diameter and chirality enables them to be ideal candidates for testing HSG in 1D. Several small tube diameters, d_t, of various (n, m) yield E_{11}^{S} (for $d_t \approx 5$Å) or E_{22}^{S} (for $d_t \approx 12$Å) in the energy range of 1.5-2 eV [119]. The binding energy of the excitons in these systems is also highly dependent on the tube diameter and chirality. Theoretical predictions expect the binding energy to range between ~100 meV to ~1 eV [98, 85, 87, 137]. Experiments measuring the exciton binding energy agree with this sensitive dependence on tube parameters, but there is no consensus on magnitudes [114, 87, 137]. Furthermore, determining the effective mass is difficult, as it also depends on the tube dimensions [85], and the dielectric screening to determine the electric field within the material (for calculating the Keldysh parameter) is not well established for all tubes [85]. However, for an order of magnitude estimate, assuming an effective reduced mass of $m \approx 0.1 m_0$ [114, 3], a reasonable binding energy of $E_b = 500$ meV and a relative dielectric constant $\varepsilon = 1$[4], the Keldysh parameter for a 100 kV/cm, 540 GHz field is $\gamma \approx 0.2$, which indicates tunnel ionization should be possible.

---

[4] A valid assumption for the thin films used for experiments below, according to communications with Jun Kono

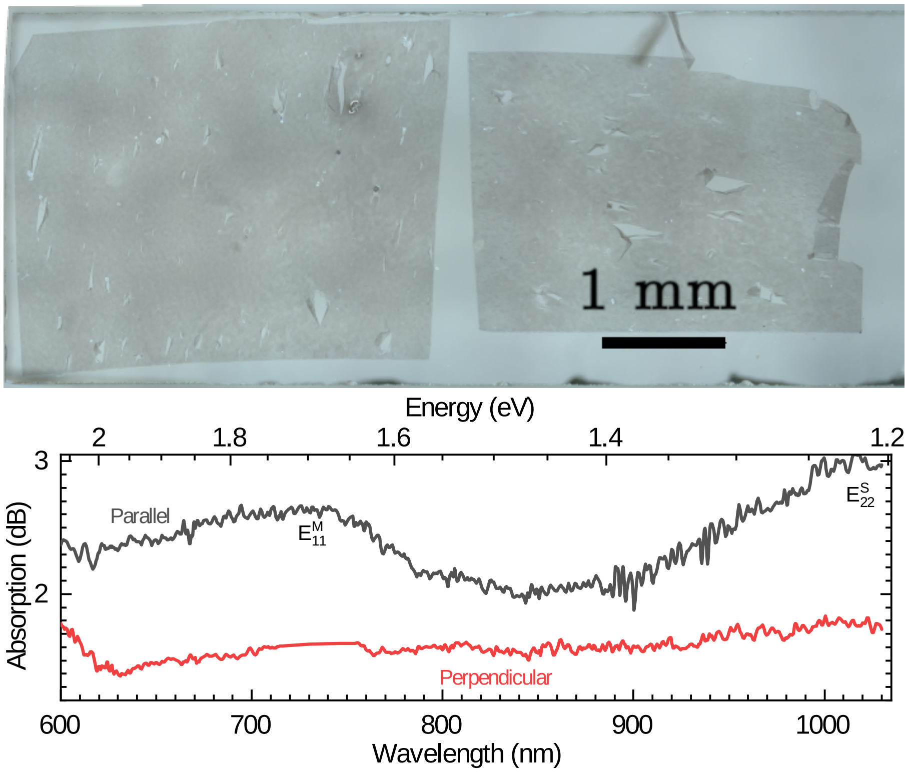

Figure 4.8: CNT samples used for HSG experiments. (Top) Microscope image of the CNTs. On the left side, the tubes are parallel to the short-axis of the substrate, while those on the right are parallel to the long axis (THz polarization is parallel to the short axis). (Bottom) Polarization sensitive absorbance spectra of the CNTs. When perpendicular to the tube axis (red), no significant spectral features were observed. When parallel (grey), peaks were seen attributed to the first exciton of the metallic state (E_{11}^{M}) and the second of the semiconducting (E_{22}^{S}), as labeled.

4.3.1 Attempts at HSG

Thin film (~200 nm) sheets of aligned carbon nanotubes on 500 μm sapphire with an ITO backside were provided by Weilu Gao from Jun Kono's group at Rice University. The top of Fig. 4.8 shows a microscope image of the nanotube films. Using a novel technique for generating large domains of homogeneously aligned tube [41], two domains were provided which provided the opportunity for the tubes to be parallel or perpendicular to the driving THz polarization. The bottom of Fig. 4.8 shows the polarization sensitive room temperature absorbance of one of the films. When the light was polarized perpendicular to the long axis of the tubes there was no significant absorbance or any features, while peaks are clearly present when parallel to the tube direction [41, 62]. These films were produced by arc discharge methods, which produce a variety of (n, m) tube configurations with an average tube diameter of 1.4 nm [52, 41]. In the absorbance spectrum taken, the first metallic transition E_{11}^{M} was visible around 720 nm and the second semiconducting transition E_{22}^{S} at 1000 nm, and both were very broad due to the large assortment of tubes. The first semiconducting transition E_{11}^{S} would occur around 0.65 eV (2 μm) and is outside the range of the detector.

Initial experiments were performed at 15 K (to allow alignment with quantum well samples), and quick low-temperature absorbance measurements did not show the transition energies shifting significantly. The NIR laser was tuned to 731 nm, polarized parallel to the axis of the rods, with 15 mW of power[5]. The THz frequency was set to 540 GHz. At ∼45 kV/cm in air, damage to the sample seemed to appear. The THz field was lowered to 10 kV/cm (using the hole coupler of the FEL) to prevent further damage. The NIR frequency was swept from 700-760 nm while monitoring for a 2$^{\mathrm{nd}}$-order sideband, but no signal was observed. Given the lower THz field strength, the Keldysh parameter was 1.8 for these experimental conditions, which would not be significant enough to ionize an exciton in this system.

Upon warming the sample, the "damage" vanished, indicating there was likely an ice

---

[5] The laser was unable to provide sufficient power to have 50 mW as in previous experiments.

Figure 4.9: Microscope image of the CNT samples after a few rounds of experiments. The top left corner of the sample has been blackened after extended exposure to THz radiation. The blue circle depicts the rough position and size of the THz which caused the damage. The THz polarization was parallel to the short edge of the sample.

layer formed on the sample, which the THz was able to vaporize. A second attempt at observing sidebands was performed at room temperature to better match the absorbance peaks. Furthermore, the thermal conductivity of CNTs at room temperature is higher than low temperatures [45], which was believed to lessen potential damage from the FEL.

Experiments were again performed with 15 mW of 731 nm NIR excitation. The THz field was increased to the maximum of 100 kV/cm in air at 540 GHz. As before, the NIR excitation frequency was swept across the E_{11}^{M} resonance from 700-740 nm while monitoring for a 2^{nd}-order sideband, with no signal seen. The NIR laser was then kept at the peak of the E_{11}^{M} resonance and no sidebands were observed from $n = 1$ to $n = 12$. After an hour of measurements, significant damage started to occur to the sample, see Fig. 4.9. The cyan circle represents the rough position of the THz beam during experiments. The top left edge of the sample has been blackened due to THz heating of the sample, destroying the CNTs and forming graphite.

4.3.2 Future Direction

Any further experiments on CNTs would greatly benefit from a different selection of CNT diameters and chiralities. Firstly, it is unclear what the effect of the metallic states were on experiments; while it is expected the metallic states support the existence of excitons [98], the presence of low-energy states which can be excited and driven by the THz field directly may lead to significant heating effects which would not be present in the semiconducting tubes alone. Furthermore, a single species of CNTs has a rather narrow absorption peak [62, 41]. The broad peaks observed in Fig. 4.8 are inhomogeneously broadened due to the large variety of tubes present. The narrow frequency NIR laser is therefore only exciting a small portion of the CNTs and lowering potential signal. Thus, purified CNTs which contain only one chirality (which is chosen to be semiconducting) would be a significant improvement and would provide a cleaner system to study.

The tubes should also be chosen to have resonances which better match the current setup (alternatively, new optics and lasers and detectors could be purchased to enable investigations at the wavelengths required for the tubes studied here). For example, HiPco (a process of forming CNTs under high pressure carbon monoxide) produces tubes with diameters of 0.9-1 nm [41], which provides a better match of the E_{22}^{S} transition. One caveat may be that a narrower tube will also result in tighter exciton binding [114, 137].

4.4 Conclusion

High-order sideband generation in three novel material systems has been studied. While none of the systems produced high order sidebands at UCSB, WSe_2 and $MAPbI_3$ both showed perturbative second order sidebands. Improvements to the setup and, more importantly for $MAPbI_3$, improvements to sample quality are promising avenues forward. No signal was observed from carbon nanotubes, but higher-quality samples should be feasible and would be a superior testing ground for observing HSG.

Appendix A

Experimental Procedures

Here, I will provide a rough outline of various components for doing a typical day of experiments. Appendix C will discuss the details of the data collection/processing software, and Appendix D will discuss the setup and calibration of the polarimeter used for all of the Dynamical Birefringence work we've done. Hunter Banks' PhD. thesis has an overview of many of the same instruments, in some cases in more details.

A.1 Sample Details

	5 nm GaAs QWs	10 nm AlGaAs QWs	10 nm GaAs QWs		500 nm Bulk GaAs
PC	50 nm GaAs	50 nm GaAs	150 nm GaAs		
	50 nm $Al_{0.3}Ga_{0.7}As$	50 nm $Al_{0.3}Ga_{0.7}As$	50 nm $Al_{0.3}Ga_{0.7}As$		
	10 nm $Al_{0.3}Ga_{0.7}As$	10 nm $Al_{0.3}Ga_{0.7}As$	15 nm $Al_{0.3}Ga_{0.7}As$	} N	
QW	5 nm GaAs	10 nm $Al_{0.05}Ga_{0.95}As$[1]			500 nm GaAs
	10 nm $Al_{0.3}Ga_{0.7}As$	10 nm $Al_{0.3}Ga_{0.7}As$	10 nm $Al_{0.3}Ga_{0.7}As$		
	50 nm $Al_{0.3}Ga_{0.7}As$	50 nm $Al_{0.3}Ga_{0.7}As$	65 nm $Al_{0.3}Ga_{0.7}As$		
PC	50 nm GaAs	50 nm GaAs	150 nm GaAs		
ES	300 nm $Al_{0.7}Ga_{0.3}As$	300 nm $Al_{0.7}Ga_{0.3}As$	300 nm $Al_{0.73}Ga_{0.27}As$		300 nm $Al_{0.72}Ga_{0.28}As$
	50 nm GaAs	50 nm GaAs	100 nm GaAs		100 nm GaAs
S	500 μm SI GaAs	500 μm SI GaAs	500 μm SI GaAs		500 μm SI GaAs

Table A.1: Details of the MBE grown samples used in all experiments. (S) substrate, (ES) etch stop, (PC) protective cap preventing oxidation of high content aluminum layers, (QW) quantum well. The 5 nm GaAs and 10 nm AlGaAs have N=20 repetitions of the quantum well and were grown by Shawn Mack of Art Gossard's group. The 10 nm GaAs QW has N=10 repetitions. The 10 nm GaAs and bulk GaAs were grown by Kenneth West and Loren Pfeiffer.

---

[1] This well region is grown digitally as 8 layers of 1.042 nm of GaAs and 7 layers of 0.238 nm of $Al_{0.3}Ga_{0.7}As$

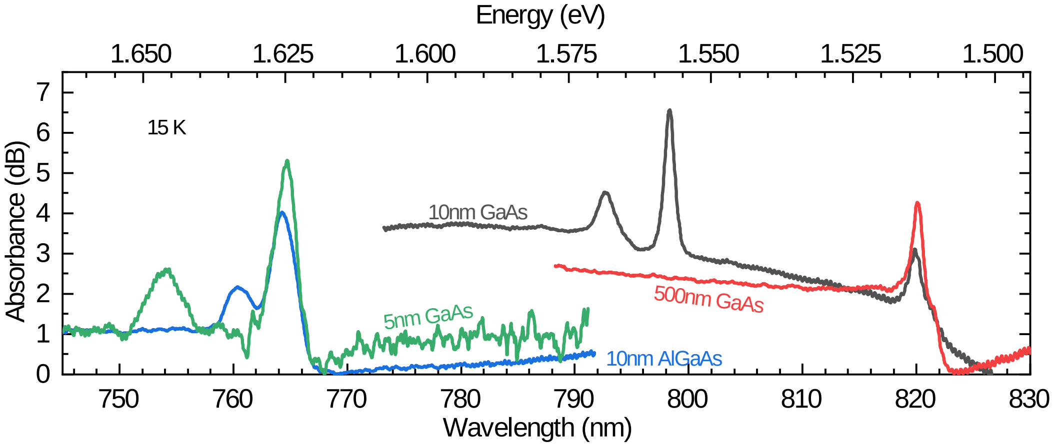

Figure A.1: Absorbances of the four samples listed in Table A.1 at 15 K. The samples have been transfered to a sapphire substrate, as describe in Appendix B.

Four GaAs based quantum well systems have been studied extensively in this work. The details of the growths are listed in Table A.1. After processing the samples as described in Appendix B, the absorbance spectra of each sample is shown in Fig. A.1. The peak at 820 nm for the 10 nm GaAs QW arises from the 150 nm GaAs protective caps.

A.2 Optical Setups

A.2.1 Standard experiment setup

Figure A.2 provides an overview of the optical table used in all experiments. NIR radiation (red lines) is produced by an M^2 SolsTiS pumped by a Lighthouse 7W-Sprout. Immediately at the output of the SolsTiS is a mirror on a flip mount (**arrow 1** in Fig. A.2) which can send the output into a power meter to measure the full laser power, for di-

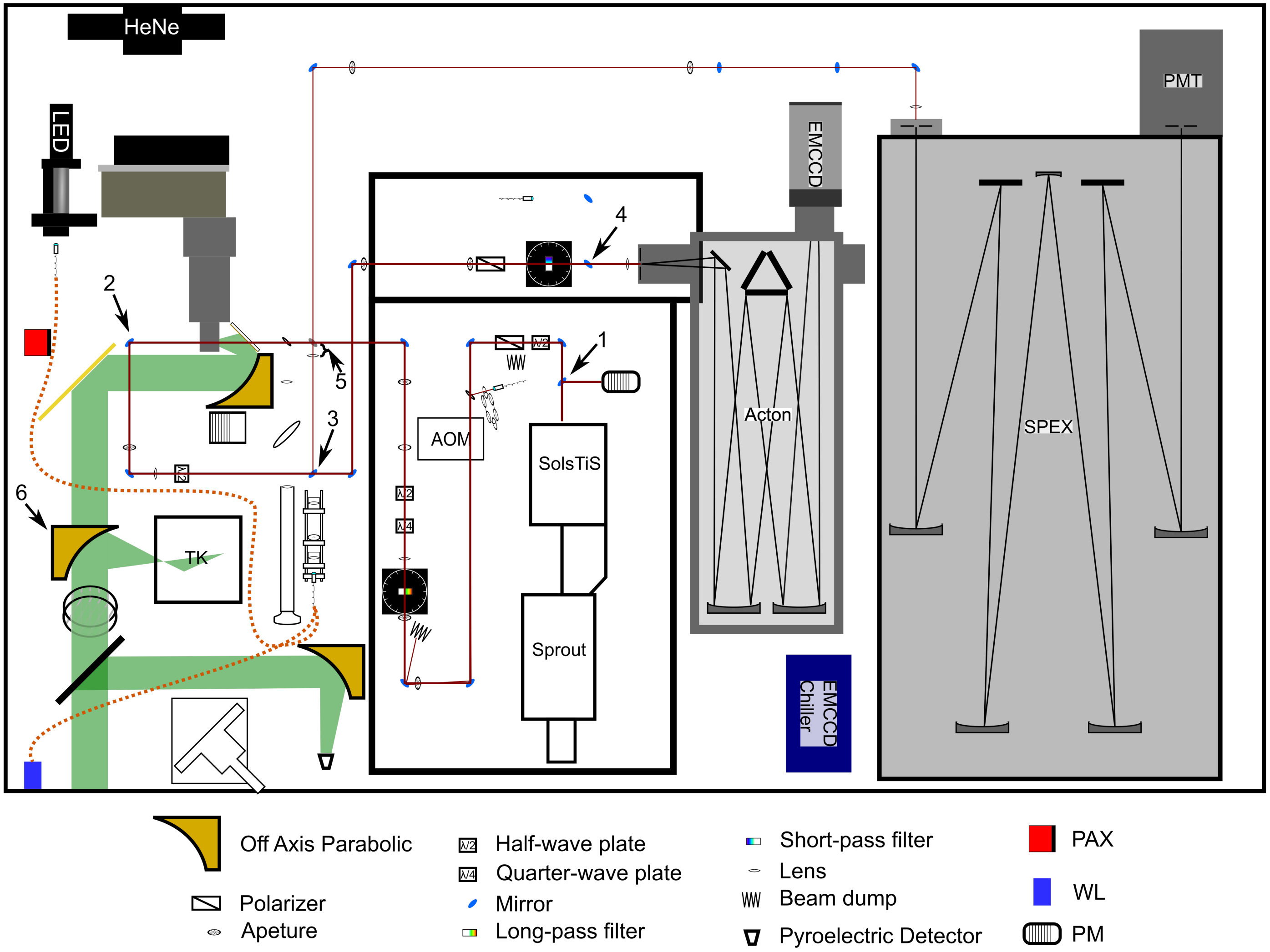

Figure A.2: A (mostly) scale schematic of the optical table used for all experiments. Green beam depicts the THz, red depicts the NIR (black when within the Acton spectrometer or SPEX). (PAX) Thorlabs PAX1000IR1 polarimeter. (WL) Tungsten white light source. (PM) power meter (with 1000:1 attenuator). Numbered arrows indicate kinematic mirrors to swap between beam orientations.

agnostics. When the mirror is not in, the light is sent through a half-wave plate and polarizer[1], which serve to attenuate the laser. The rejected light from the polarizer is sent into a beam dump (LBM1). A small amount of light is picked off and fiber coupled into a WS6-600 wavemeter for monitoring the wavelength, see Sec. A.5.2. An AOM is used to temporally overlap the NIR with the FEL, and the 0^{th}-order beam is clipped by an iris and another beam dump.

A long pass spectral filter removes amplified spontaneous emission from the SolsTiS which can affect sideband signal. In the majority of experiments, an $f = 500$ mm focuses the NIR laser onto the sample, resulting in a spot diameter of $\sim 250\ \mu$m at the sample. After the lens, a set of a quarter-wave plate and half-wave plate are used to provide any polarization state at the sample. The beam is sent through an ITO coated slide which collinearizes the NIR with the THz. After the sample, a 500 mm lens[2] collimates the signal and a half-wave plate matches the polarization of the signal. A smaller focus at the sample can be accomplished by swapping the 500 mm focusing lens with a shorter focal length. **Arrow 3** points to a flip-mounted mirror which controls sending the light between the SPEX and PMT, or the Acton spectrometer and EMCCD.

When sent towards the EMCCD, a polarizer is used to ensure high-quality polarization, which improves the function of the short-pass filter immediately after it. This short-pass filter serves to remove the laser before sending the signal with sidebands into

---

[1] The beam is periscoped from the 65 cm output of the SolsTiS to the 5 inch table standard before the attenuation section

[2] Arrow 2 points to a removable mirror for the PAX, see Sec. A.2.3

the EMCCD. A lens[3] matching the f-number of the spectrometer focuses the signal onto the spectrometer slits, where it can be imaged on the EMCCD.

When sent to the SPEX, the signal is simply routed into the SPEX monochromator (Arrow 5 points to components of Sec. A.2.4). As with the other spectrometer, a lens is used to focus onto the slits of the SPEX.

THz radiation (green beam) is coupled in from the FEL optical transport system, entering in from the lower-left of the figure. A beam splitter picks off a small portion to be sent to a pyroelectric detector (pyro) for reference. A pair of wiregrid polarizers are placed after the beam splitter which are used for attenuation. The first polarizer is free to rotate, while the second is fixed to pass horizontal polarization. The attenuator is placed after the beam splitter so the pyro will always measure the full beam power. A 5" off-axis parabolic mirror focuses the THz spot to a nearly diffraction limited spot of 0.5 mm diameter (at 540 GHz). The ITO has roughly a 70% reflectance.

A.2.2 Measuring THz power

For measuring the absolute THz power, a magnetically mounted off-axis parabolic can be inserted (**Arrow 6**) which focuses and directs the THz radiation onto the Thomas Keating (TK) power meter. Note that the FEL should never be focused directly on the film. As depicted in Fig. A.2, the focus of the FEL is slightly before the TK and a diverging beam is what is incident on the TK film. The mirror for the TK is placed after the attenuator so the power going to the sample can be measured directly.

---

[3] Mirror 4 is discussed in Sec. A.2.5

In experiments, it is often more useful to discuss the electric field strength in the material. Since the TK measures the power of the FEL in the entire pulse in air, the electric field strength must be calculated. Throughout this work, a modified version of the calculation used in the original HSG paper [133] has been used

$$F_{\mathrm{THz}} = E_{\mathrm{eff}} \sqrt{\frac{2 R_{\mathrm{ITO}} T_{\mathrm{window}} P}{A \varepsilon_0 c n}} \tag{A.1}$$

Here, F_{THz} is the electric field strength in the sample; E_{eff} is the electric field enhancement from the ITO, see Sec. B.1; R_{ITO} is the reflectance of the ITO used to combine the NIR and THz beams, see the previous section; T_{window} is the power transmission of the cryostat window; P is the power measured by the TK, A is the area of the THz spot; n is the index of refraction; ε and c are the standard constants.

Towards the end of this thesis, I began to suspect Eq. A.1 is not correct for the experiments performed here[4]. Furthermore, the presence of a cavity from the sapphire and ITO on the sample (see Appendix B) make it difficult to apply a single iteration of the Fresnel Equations at the sample surface. Instead, a full transfer matrix analysis was performed [136]. To apply transfer matrices to the system, the thickness of each layer and the optical impedance as a function of frequency must both be known. While this is moderately well known for the sapphire, the properties of the ITO coating are less well understood, as it is grown on campus (see Appendix B).

Instead of measuring the properties directly (potentially through ellipsometry), I thought it easier to extract the parameters of the sapphire and ITO cavity using the

---

[4] Nor in our DBR [9] or OE [109] papers

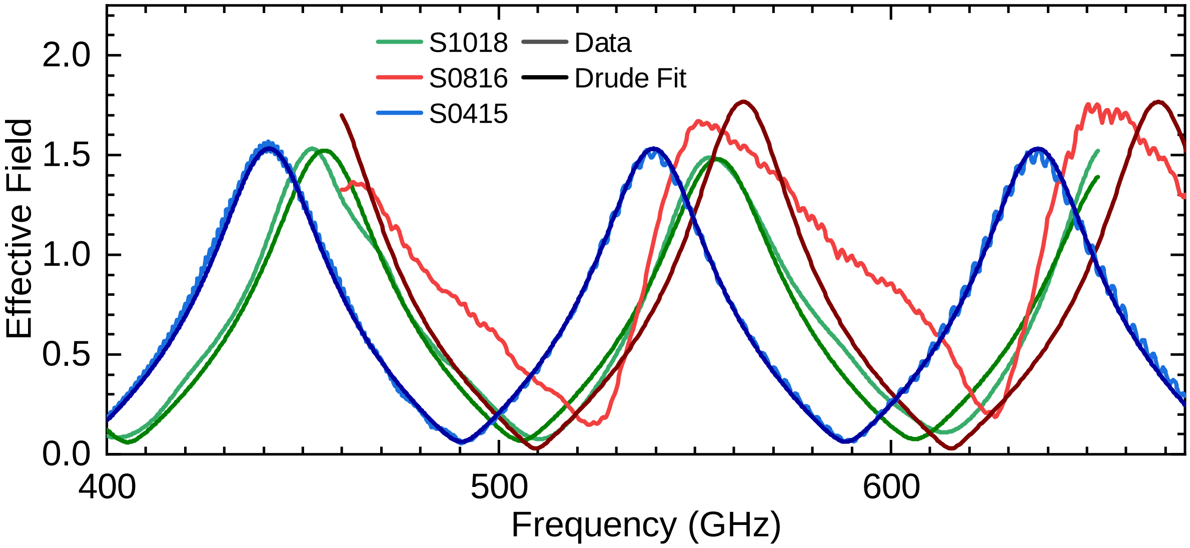

Figure A.3: Extracting sample substrate cavity parameters. Three sapphire substrates have been fabricated over the course of this work. The light colors show the measured data for the three substrates, fabricated in April 2015 (blue), August 2016 (red) and October 2018 (green). The darker colors correspond to fits to extract the parameters of the transfer matrices for each, assuming the ITO is described by the Drude model. Only the data from 2015 is accurately fit by this model.

field enhancements measured from the VNA. The transfer matrices were defined by,

$$T = \begin{pmatrix} \cos\phi & -iZ\sin\phi \\ -iZ^{-1}\sin\phi & \cos\phi \end{pmatrix} \tag{A.2}$$

where Z is the optical impedance and $\phi = n * d * \omega / c$ with n and d the index of refraction and thickness of the material, respectively. The index of sapphire was taken to be 3.06 and constant in this frequency range [83, 38], and the thickness was a free parameter. The index of refraction of the ITO was fit to the Drude model,

$$n^2 = \varepsilon = \varepsilon_\infty - \frac{\omega_p^2}{\omega^2 - i\omega/\tau} \tag{A.3}$$

ε_∞ is the high-frequency permittivity, ω_p and τ are the plasma frequency and scattering rate, respectively [20]. ω_p, τ and the thickness of the ITO were left as free parameters.

Figure A.3 shows the VNA measured reflectance for three different substrates in light colors. The corresponding dark colors are the fitted reflectances for each data set to determine the transfer matrix corresponding to the sapphire/ITO cavity. While the fit is good for the S0415 substrate[5], it is not a good fit for the other two substrates. It is unclear why this is the case, but the good fit can be used to analyze the effects of the substrate.

Using the fitted transfer matrix for the cavity for S0415 from Fig. A.3, Fig. A.4 shows the comparison with and without the sample, where the sample index of refraction was fixed at 3.59. The top shows the real space oscillations while the bottom shows the frequency dependence. In general, a negligible change in the field is observed. In frequency, a slight blue shift is expected (bottom right). This was actually observed in experiments (bottom left), but we originally thought the shift was due to drift in the VNA between measurements.

From the top of Fig. A.4, it is clear that the thickness of the GaAs samples is significantly smaller than the wavelength of the THz used in experiments. This small thickness may be why there is no significant change in the electric field enhancement when the sample is included. Given these results, it would indicate the correct field strength in the sample would be given by,

$$F_{\mathrm{THz}} = E_{\mathrm{eff}} \sqrt{\frac{2 R_{\mathrm{ITO}} T_{\mathrm{window}} P}{A \varepsilon_0 c}} \tag{A.4}$$

which differs from Eq. A.1 by a factor of $1/\sqrt{n}$. In GaAs, this results in an increase in

---

[5] For some unknown reason, an additional 16 GHz overall frequency shift was required to achieve adequate fit.

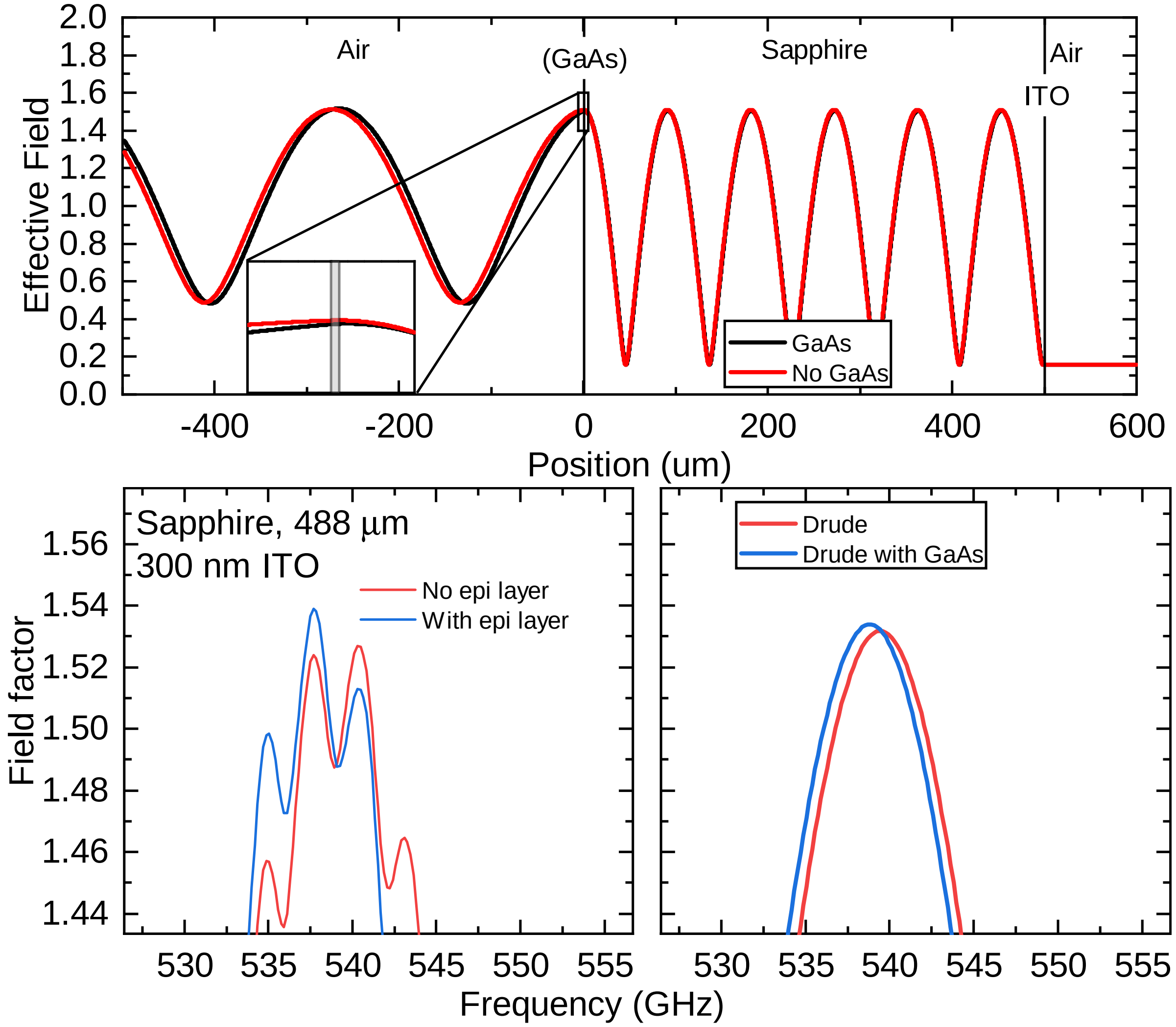

Figure A.4: Transfer matrix calculations with and without sample. (Top) calculated position dependence with (blue curve) and without (red curve) the GaAs sample using the substrate transfer matrix for S0415 from Fig. A.3. The surface of the sapphire is at position 0. The inset shows the zoom (width 10 μ) around the GaAs, observing practically no difference in the effective field in the sample. (Bottom) Shift in the frequency of one of the cavity peaks with and without the sample. The left side is measurement before and after transferring the epitaxial GaAs (technically done in a QW), and the right side is the calculated shift.

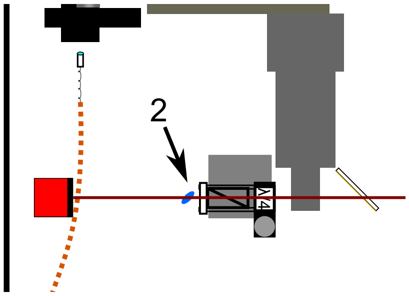

Figure A.5: Polarization measurement in the optical setup. The Thorlabs PAX (red square) can be used by removing mirror 2 and sending the NIR light in. To measure the polarization of the sidebands, the custom polarimeter is used and positioned between the cryostat and mirror 2. It is placed on a magnetic mount to be swapped in and out.

the field strength by a factor of $\sim \sqrt{3.6} \approx 1.9$. The field strengths in the sample quoted throughout this work continued to use Eq. A.1 while this issue is further investigated.

A.2.3 Polarization Measurements

An important part of this thesis has been measuring polarization states of light. Figure A.5 shows a zoom of the components which have enabled this. The red square is the Thorlabs PAX1000IR1, described in Sec. A.5.4. **Arrow 2** points to a removable mirror so the NIR laser can be sent into the PAX. It is important that no mirrors or optically active components are between the PAX and the position where the polarization state must be measured.

The PAX is not suitable to measure the polarization state of the sidebands as they are not a CW signal. To measure the polarization state of the sidebands, a custom polarimeter was designed and built which synchronizes to the FEL, see Appendix D. The polarimeter (directly behind the cryostat in Fig. A.5) is a Thorlabs K10CR1 rotation stage with a quarter-wave plate mounted within it, and a fixed polarizer mounted behind

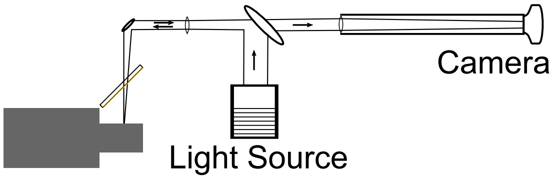

Figure A.6: (rotated) Schematic of the imaging system. A white light source provides illumination. An $f = 200$ mm lens focuses the light onto the sample while collimating the reflected light off the sample surface. A Thorlabs camera then records the reflected image.

it on 30mm cage components. The whole system is mounted on a magnetic mount (the grey baseplate) which allows it to be snapped in and out during experiments without requiring realignment.

A.2.4 Imaging System

The introduction of an imaging system, depicted in Fig. A.6, to the setup to view samples greatly eases aligning the NIR laser and sample. A light source (Thorlabs QTH10 Quartz Tungsten-Halogen Lamp) provides illumination of the sample after being reflected by an 8% pellicle beamsplitter . A 200 mm lens focuses the light onto the sample, and also collimates the reflected signal from sample surface. The light is then focused onto a CMOS camera (Thorlabs DCC1545M) using a 200 mm lens. Another pellicle directs the white light after the focusing lens onto the sample. It is mounted on a magnetic mount so it can be removed, which allows more NIR power to reach the sample.

It is possible to swap out the 200 mm sample focusing/collimating lens with a shorter focal length to achieve a higher magnification. For the transition-metal dichalcogenides studied in Chapter 4, the lens was replaced with a 60 mm lens. One complication is the tight space on the optics table in this region, and the 60 mm lens had to be placed between the pellicle and the ITO. This places it in the beam path of the NIR laser, which means it was also the focus for the NIR laser. Trying to match the focus of both the imaging system and the NIR laser is extremely difficult, and leads to poor image or beam quality. An improvement could be to move the imaging system to behind the sample on a kinematic mount which would enable fully independent alignment of the two optical systems.

A.2.5 Characterization Techniques

When new samples are received, it is important to be able to characterize them. Two simple methods are absorbance and photoluminescence (PL). Figure A.7 shows how each is implemented on the table.

A tungsten-halogen lamp (blue square in the lower left of Fig. A.2) or LED can be used for absorbance measurements. Each is fiber coupled with the output end of the fiber connecting to the absorbance (Abs) cage shown in Fig. A.7(a). The abs cage contains a 40 mm focusing lens, a 100 μm pinhole, and 60 mm collimating lens. This combination serves to spatially filter the beam to create a clean Gaussian beam profile. After filtering, a mirror and $f = 250$ mm lens (Arrow 5) focus the light to a ~ 200 μm diameter spot on the sample. A smaller focus can be achieved with a smaller pinhole in the absorbance cage or a shorter focal length lens.

After the sample, the light is re-collimated with a 60 mm lens and sent into a fiber

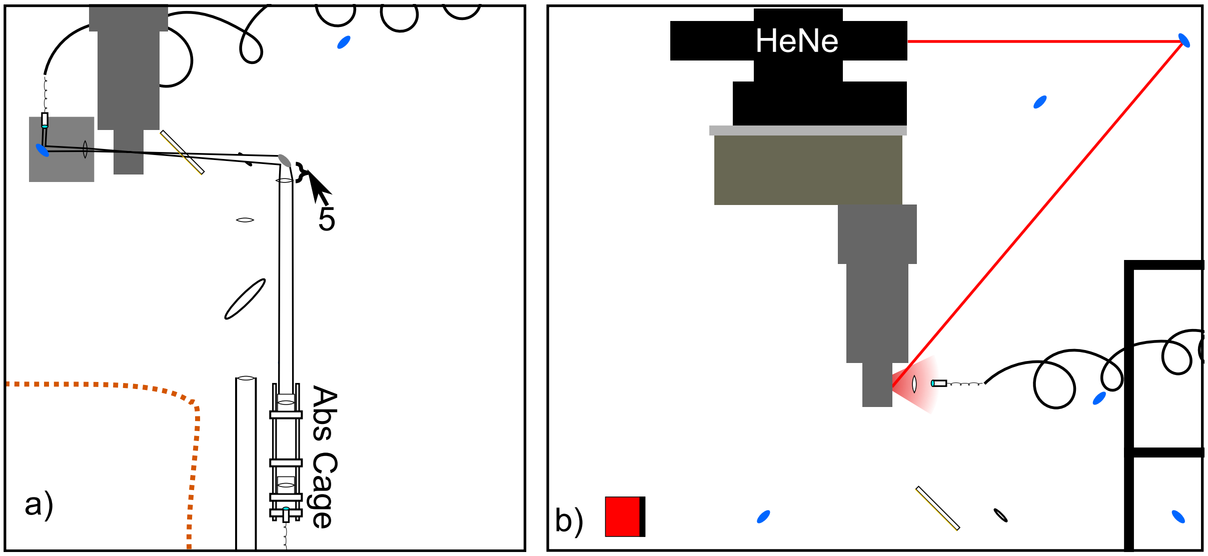

Figure A.7: Implementation of (a) absorbance and (b) photoluminescence (PL) characterization schemes. a) A white light source or LED (both depicted in Fig. A.2) fiber coupled to the absorption cage. The absorption (abs) cage is a spatial filter which then free-space propagates the light to the sample. After transmitting through the sample, the light is collected into another fiber and sent to the EMCCD. The collection optics are placed on a magnetic stage to be easily snapped in and out. Arrow 5 points to a lens and mirror which snap down as they are in the path of the SPEX. b) For PL, the cryostat is moved out of the standard position for HSG. A helium neon laser (HeNe) excites samples from the front surface. A fiber coupler collects the PL signal and sends it to the EMCCD. Optionally, a lens can be placed between the sample and fiber to improve collection efficiency.

coupler. The lens, alignment mirror and fiber coupler are placed on a magnetic mount to be swapped in and out quickly. Typical absorbance spectra take a reference image by sliding the cryostat out of the beam and then inserting the sample and cryostat. Since this does not take in to account reflections off of surfaces, or absorption from other components, the absorbance measurements discussed here would be better called differential transmission.

Photoluminescence is typically done with a helium neon (HeNe) laser for excitation, and pulling the cryostat out of the typical beam path for easier access, Fig. A.7(b). The HeNe excites the sample from the front side, and the emitted signal is also collected from the front. An optional short focal length lens ($f \approx 60$ mm) can increase the collection efficiency. The signal is collected with a fiber.

The fiber from either the absorbance or PL system are both coupled into the spectrometer and EMCCD through the same coupler. **Arrow 4** points to a flip-up mirror which allows the light from the fiber into the spectrometer.

A.3 Pre-Preparation

There are a couple of things which can be done ahead of time to get ready for experiments.

Mount Samples

The samples to be studied need to be mounted. If the cryostat is under vacuum, make sure the valves are all closed. While wearing gloves, loosen one of the 3-axis feed-throughs.

Figure A.8: Alignment guides for samples in the current cryostat mounts. Align the copper sample mount on the bar pictured above. The two black horizontal lines mark the range within which the laser can hit.

Wiggle it very slightly to let air slowly leak in. Make sure to keep a hand on the front cryostat window to catch it when it falls once the chamber is at atmospheric pressure.

Remove the cap to the hood of the cryostat, and the cold shield cap.

Remove the sample block from the cold finger. It should be held on with two flat-head screws. One screw is shorter than the other to make space for other cryostat components, so keep track of them (the short one should be colored slightly blue). Samples are mounted using Elmer's rubber cement. Using a wooden swab, place a small dab on the copper mount. Align the sample at the correct crystal orientation. Figure A.8 is an image which, when printed on 8.5"×11" paper, shows where the laser is capable of hitting the sample when mounted. Carefully push down on the sample to ensure it's snug and level against the bar.

Apiezon Z grease is used to ensure good thermal contact between the sample mount and cold finger. It's also viscous enough that it will hold the sample to the mount while you attach it. Make sure there's enough grease on the sample block, and add a very small amount if necessary by applying a small amount to a toothpick and smearing it on either the back of the sample mount or the coldfinger.

Double check the laser is able to hit the portion of the sample you want to study. If not, remove and remount the sample, otherwise reattach cryostat parts.

Close the valve to the cryostat, attach the vacuum line, and start the rough pump to pump down the vacuum line. Hold the window in place and slightly crack the valve on the cryostat until it raises the pressure. Wait for it to pump a bit before slowly opening the valve more.

Wait for the rough pump for at least 15 minutes, probably an hour (should get to about 3e-2 torr) before starting the turbo pump. The cryostat can be started about an hour later, but there will likely be issues getting the temperature to the lowest levels, or with it staying low. Overnight pumping is generally better.

The NIR laser and filters can be aligned a day early as well. I point the interested reader to Appendix A of Hunter's thesis which explains the process quite well.

A.4 Calibrations/Starting up

On the day of experiments, there's plenty of set-up to do early. Before turning on the cryostat, open the valves for the Broida equipment cooling (Sec A.5.3). Turn on the cryostat, the switch is on the back top corner, on the face opposite to the outlet valves. Once the sample temperature reaches 77K, cryo-pumping starts to become significant and it is best to close off the valves to the vacuum to prevent potential backflow of oil from the pumps. It takes 45-50 minutes to reach 77K from room temperature once the cryostat is turned on. The turbo pump can be turned off (stop button on the front of the cart). The rough pump needs to be left on for 20 minutes before turning it off, allowing the turbo to spin down. Otherwise, the backflow of air when the rough pump is turned off can damage the turbo blades. After 20 minutes, the power strip on the pump cart can be turned off. The sample temperature software can be loaded to monitor the temperature (Appendix C).

The laser should be turned on early, allowing time for it to warm up and hopefully reach better stability. Simply turn the key on the Sprout and press the button once. The power will slowly ramp up to the set point. To start the laser wavelength feedback tuning, open the WS6 software on the computer. Then, open the M2 server software. The IP address in the drop down menu needs to be changed to the IP on the subdomain with the laser (*i.e.* something like 192.168.1.100). This sets up the communication between the WS6 and the laser itself. Then, in the M2 control software, press the "Connect Wavemeter" and you can choose which wavelength. Note: when the laser is being unstable for any reason, such as the pump laser misbehaving, using the wavelength feedback loop is more harmful than good. Section A.5.2 mentions how to manually tune to ∼1 pm.

The EMCCD has a thermoelectric cooler which brings the temperature of the detector down to -90°, which significantly reduces the effects of hot pixels or dark counts. Open the camera control software, and begin setting the temperature. Make sure the blue chiller is turned on (the CCD manual describes which temperatures require the chiller, as well as what temperatures are possible with the ambient temperature and humidity). It takes roughly 20 minutes for the camera to cool.

While equipment is cooling, the FEL can be tuned. Instructions for doing so are outside the scope of this appendix.

Once the sample is cold, the ThorCAM software can be used to align the NIR to the sample. Because of thermal expansion of the components in the cryostat, it must be done cold.

Once the FEL is tuned, wiregrids and pyro detector can be calibrated. Begin by inserting the Thomas Keating detector and turning it on. Using the wiregrid calibration software, determine the correction factors (see Appendix C). To calibrate the pyroelectric detector, open the Pyro Cal software. Because the time constants on the two detectors is so different ($\sim \mu$s for the pyro, ∼ms for the TK), two oscilloscopes are required to get suitable time resolution on each detector. The software will compare the absolute energy measured by the TK for each pulse to the voltage measured on the pyro, and determine the scale factor. This allows extraction of pulse to pulse absolute energy measurements of the FEL with the pyroelectric. Because of possible misalignments of the pyro, and the frequency dependence of the mylar beamsplitter to the pyro, its good to do this calibration every day.

After all of the setup is done, data collection can proceed. The standard operation of software is descibed in Appendix C.

A.5 Equipment

Here, I will outline a couple of the important pieces of equipment and any necessary notes/maintenance/care that should be taken for them.

A.5.1 Chillers

There are three chillers in the room for equipment:

1. EMCCD (Blue Oasis), on the optics table
2. MSquared SolsTiS (ThermoTEK), on the floor
3. Sprout Chiller, on the floor

On the top of the EMCCD chiller, a fridge magnet covers the valve to add water when the system says the level is low. Add a splash of IPA as well for anti-organism protection.

The SolsTiS and Sprout chillers should be replaced twice a year. An opaque white bottle sits on top of the Sprout for replacing both coolants. Fill to the bottom line with IPA, then fill to the top of the sticker with distilled water. Do not use de-ionized water, which can damage both systems. Distilled water must be purchased from a grocery store. Each chiller requires one bottle's worth, which is about a 10% IPA solution. The manuals for each have instructions for refilling the water, outlined below.

To replace the ThermoTEK water, turn off the chiller and unplug the power. Remove the screw cap on the top, and invert the system to drain the coolant. The quick release valves can be detached from the back, but be careful to not spill water as the lines drain. Reconnect the lines and refill the reservoir from the squirt bottle. Plug the chiller back in and ensure the lines refill and water flows.

For the Spout, turn off and unplug the laser. Lift the laser onto a step stool and place a bucket beneath the drain spout. Unscrew the water reservoir cap and connect the short quick-release tube to begin draining the coolant. The laser may need to be tilted forward slightly to fully drain it. Once completed, remove the tube and begin filling with the squirt bottle. There are two faint black lines on the side of the coolant reservoir closer to the side of the laser, but it is roughly a full bottle. Turn the laser back on and ensure water flows.

Both chillers also have cleanable air filters. The Sprout's is held in place by the metal grid on the front. Remove the grid (magnetically attached), and vacuum the foam filter. The ThermoTEK filter is the blue mesh running around three of the four edges. Remove it (attached by large velcro), vacuum it, and reattach it.

A.5.2 MSquared SolsTiS and Lighthouse Sprout

The NIR laser used in these experiments is an MSqured SolsTiS Ti:sapph laser, pumped by a DPSS 532nm laser. The laser is nominally hands-off, with the only interaction being setting the wavelength. Normal operation is:

- Turn key on the pump
- Press button once to start ramping power
- Open SolsTiS software on computer (192.168.1.224 in a web browser)
- Open the WS6 control software.
- Open the "Wavemeter_TCP" software from MSquared
- Make sure the IP address is the ICEBLOK's (192.168.1.100)

- On the SolsTiS control page, under “Wavemeter link”, click “On”
- Type in the desired wavelength and watch it go.

Unfortunately, over time the lasers have required more care. One point is adjusting the pump alignment into the SolsTiS. Between the Sprout head and the SolsTiS head, there is a coupling box which includes a single mirror with external controls. Only the tip-tilt directions on the mirror should ever be adjusted, never the z-axis (the corner of the L). Using the power meter directly after the laser output, adjust the tip and tilt very carefully to maximize power. The WS6 wavelength feedback should be disabled, and the etalon should be unlocked, or the power will be unstable as it tries to re-lock.

Sometimes, power instabilities of the Sprout cause issues with the SolsTiS and make it impossible to lock the etalon, which defeats the ‘Dial-a-wavelength’ (or dial-in-lambda, DIL) functionality which maintains a set wavelength. Fortunately, grad-student feedback is quite good at keeping the wavelength constant to within 1.5 pm. The WS6 monitor needs to be up, as well as the web-scope of the SolsTiS: at the bottom of the SolsTiS control page, select Monitor A as ‘Etalon lock error’, and click ‘Web scope’. The window which pops up displacys an oscilloscope trace of various feedback and control signals of the SolsTiS, and the etalon lock error is a control signal on the etalon. Figure A.9 shows screenshots of the etalon lock error under two different operation modes to be described later.

The wavelength can be tuned within 0.5nm using the coarse birefringent filter steps, using the big ‘+’ and ‘−’ buttons under ‘Target λ’. The etalon tune can be used to

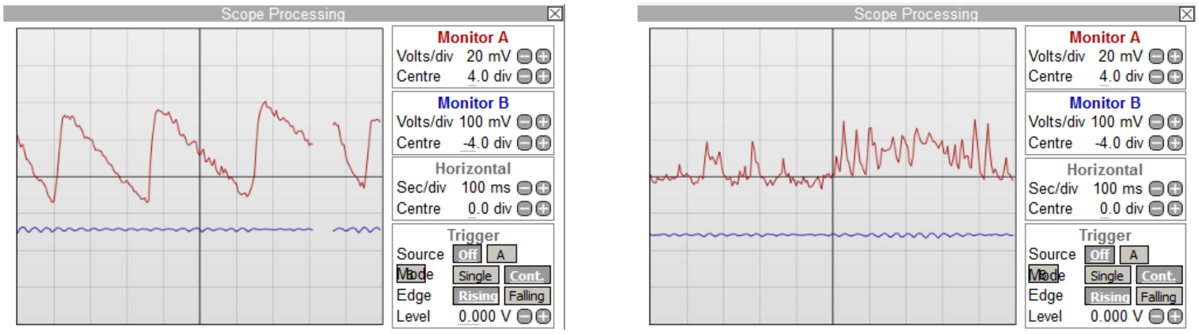

Monitor A
Volts/div 20 mV
Centre 4.0 div
Monitor B
Volts/div 100 mV
Centre -4.0 div
Horizontal
Sec/div 100 ms
Centre 0.0 div
Trigger
Source Off
Mode Cont.
Edge Rising
Level 0.000 V

Figure A.9: Screenshots of the SolsTiS control software when the laser is in two different operating regimes. (Left) The etalon is unstable, usually from large changes in its value. Each period of the sawtooth causes the wavelength to jump by one FSR of the etalon. The period of the saw tooth tends to increase within a few moments, and the etalon can be tuned to correct for the jumps from the sawtooth until the etalon eventually stabilizes. (Right) The laser etalon is mostly stable, but begins to drift towards the edge of its free spectral range. The spikes up and down correspond to it jumping back and forth. The etalon should be tuned by 0.01% to center the etalon lock signal between the two extrema of these spikes.

bring the wavelength closer to the desired wavelength, by stepping in increments of 1%, 0.1%, or 0.01% (of overal etalon voltage, I believe), where 1% will change by $\sim$ 0.07nm (3 GHz), 0.1% changes by $\sim$ 0.014 nm (800 MHz), and 0.01% moves the etalon within its FSR without changing the wavelength. When making large changes in wavelength, the etalon is not stable, which is visible as the saw-tooth pattern in the etalon lock error, as shown in the left of Fig. A.9. Each jump in the saw-tooth corresponds to the etalon jumping by one FSR. To tune to an arbitrary wavelength:

- Tune to within 0.5nm using the coarse BRF
- Change the etalon by 1% to get it within a few picometer
- Use changes of 0.1% to counter the changes in wavelength from the etalon instabilities

- The etalon should begin stabilizing within a minute, and 0.01% changes can be used to bring the wavelength to the desired wavelength, within 800 MHz.
- The etalon lock error signal can be monitored to correct for slow drifts over the course for tens of minutes to hours.

Once the etalon is stable, it should produce a flat etalon lock error signal which does not drift significantly from trace to trace of the webscope. However, it will slowly drift over long periods. When it reaches the edge of its FSR, it will jump between two adjacent modes. This is depicted on the right side of Fig. A.9. Simply adjusting the etalon by 0.01% can place the etalon in a position that will remain stable for a long period.

The above steps can keep the wavelength within 800 MHz (1.4pm at 800nm), it does not control the wavelength to 0.1pm. While the DIL seems to maintain this level of precision (when functioning), the abilities to control the cavity to that level are not provided in the SolsTiS control page. However, this level os precision is far greater than anything needed for HSG experiments, and isn't likely an issue.

Finally, some issues with the Sprout should be mentioned. In many discussions with MSquared technicians, "pump instabilities" has been a common problem for many SolsTiS users. It is often attributed to causing power fluctuations, which interfere with the etalon locking mechanisms. To first order, this problem has been remedied for a period by contacting MSquared, who is able to remotely connect to the computer and diagnose the Sprout. Typically, the temperature dependence of one of the double crystals needs to be retuned. When MSquared is unable to fix an issue, Lighthouse can be contacted directly. They will, again, remotely connect to try and diagnose an issue. Both technicians will use the ‘Lighthouse Photonics’ software which is currently on the desktop of the computer. It also has a feature for starting a ‘Test Run’, which can be useful to send to Lighthouse when asking for assistance. It will record the operating parameters of the Sprout over time. In order to download the files from the Sprout, the key must be turned into the standby position. Note that the Lighthouse software must be plugged directly into the computer, it does not work when plugged into a USB hub.

A.5.3 Broida Water

Currently, the Broida equipment cooling water is used to cool the cryostat compressor. It is relatively low-maintenance, but there is a water filter which must be replaced every 6 months. At the back of the room at shin level, a blue water trap houses the filter.

1. Close the shutoff valves before and after the filter
2. Place a bucket below the filter to catch water
3. Press the red relief valve on top of the filter
4. Unscrew the housing unit (may require a wrench)
5. Dump the water and filter into the bucket
6. Replace the filter with a fresh one from the stock room (1 μm)
7. Screw the housing unit back on and tighten

8. Open the shutoff valves, and write the date on the sheet taped to the wall
9. Open the valves to the cryostat and let it flow for 10 minutes. Ensure there are no leaks from the filter

Opening the fitler introduces a lot of air into the lines. Running the cryostat water for 10 minutes pushes the bubbles through the lines. Also note that if the filter is not replaced soon enough, it can become sufficiently clogged to prevent water flow, which seems to happen by 7 to 8 months after a replacement.

A.5.4 PAX1000IR1

One of the most useful tools for doing polarimetry has been the Thorlabs PAX1000IR1, a fast, small and accurate polarimeter. While it cannot be used to measure sidebands directly, because it requires monochromatic, DC signal, it provides an extremely quick way of determining the NIR polarization during experiments, and provides an absolute scale to calibrate the home-built polarimeter to. However, there are some quirks which should be kept in mind when using it.

- While the spec sheet claims it can handle 30mW of NIR power, I've found the results vary drastically if you increase the NIR power from 10 mW to 30 mW, likely from the internal photodiode beginning to saturate. I try to attenuate power into the detector to ∼1 mW.
- The PAX has a very handy 'Alignment Assitant' under the tools tab. It should be used often to make sure it hasn't been bumped. I aim for >97%

- Two common bugs in their software: Sometimes the software will open but will not connect to the device. Simply unplug and re-plug the USB cable. The second is that it will not auto-scale the power level. Manually select a power level, and then recheck the auto-scale button.

- Note: The PAX measures the polarization of light as defined by looking *at* the source, **not** looking *with* the source. This has been confirmed by the Weld lab, using spin-sensitive transitions in their cold atoms.

Some special mention should also be made for attenuators in relation to the first point above. I have found that several attenuators in lab can change the polarization state slightly. Ensure the filter is at normal incidence by using the back-reflection of the spot, and I typically only use the blue NE20A ND filter.

A.5.5 Acton Spectrometer

The spectrometer has three gratings currently installed. The details are below:

Grating No.	Groove Density (g/mm)	Approx. Bandwidth (800nm) (nm)
1	1800	11.5
2	1200	23
3	600	53

The Acton spectrometer has developed an unfortunate skipping problem. Occasionally, when moving the wavelength, the spectrometer does not actually go to that position, and is off by ~1 nm. It seems especially prevalent with center wavelengths around 720-

730 nm, and has not been confirmed on gratings 1 or 2, only on grating 3. Looking at sidebands has been the most efficient method for checking whether the spectrometer is in the same place. Some success to correct it has come from moving the spectrometer far away (600 nm), and then moving back. If this does not fix it, the software handles adding an offset to correct for it (`spectrometer_offset`parameter). The spectrometer has an internal backlash correction which does not seem to correct it, and a custom software backlash correction does not always fix it. Brief communication with the manufacturer was not able to remedy the issue, and the next course of action would be sending the spectrometer to Massachusetts for repair.

Appendix B

Fabrication Steps

B.1 ITO Deposition

Indium tin oxide (ITO) is a material which has enabled higher field experiments when the sapphire substrate is back-side coated with a thin film of ITO, relative to without. Figure B.1 shows the effective field enhancement, as measured by a vector network analyzer (VNA), at the surface of the sapphire substrate used for many of the experiments in this thesis. Evidently, there are spectral regions where the field is enhanced beyond unity, allowing higher field experiments. One down side, which was emphasized in Fig. 4.1, is the damage induced to the ITO from the strong THz field from the FEL. The mechanism for such damage is not fully understood, although similar mechanisms have been reported elsewhere (see ref. [2]). Growing thicker ITO films or taking better care to protect and prevent damage to the film may delay damage from occurring, but it has not been investigated significantly.

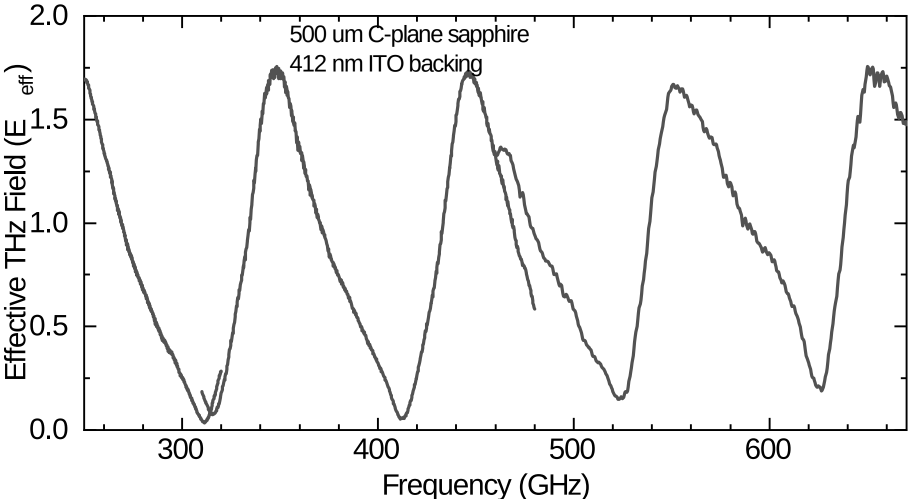

Figure B.1: Measured electric field at the surface of a 500 μm sapphire substrate backed by 412 nm of ITO. The ITO reflects the THz field off the back surface of the substrate which coherently sums to a larger field at the surface for certain frequencies. The artifacts at 320 GHz and 480 GHz occur at the edges of the frequency bands of the VNA where the signal is weak and a slight phase shift occurred between scans.

B.1.1 Fabrication Steps

ITO can be deposited in the UCSB nanofab facility on E-Beam #2. It is also advised to simultaneously deposit onto a dummy SiO_2 piece for characterization. Begin by preparing both surfaces with a standard solvent clean, followed by an O_2 plasma descum.

For a good ITO film (i.e. low resistance and optically transparent), the substrate must be heated to 290 °C. Before deposition begins, a flow of 30 sccm of oxygen should be entering the chamber which results in a better ITO growth.

The growth rate needs to be kept very slow and controlled. The first 10 nm of the film should be deposited at 0.1 Å/s. After 10 nm, the rate can be increased to 0.3 Å/s. After 50 nm, the rate can be bumped to the final value of 0.5 Å/s. Further rate increases have not been tested or investigated, but could result in thicker films faster.

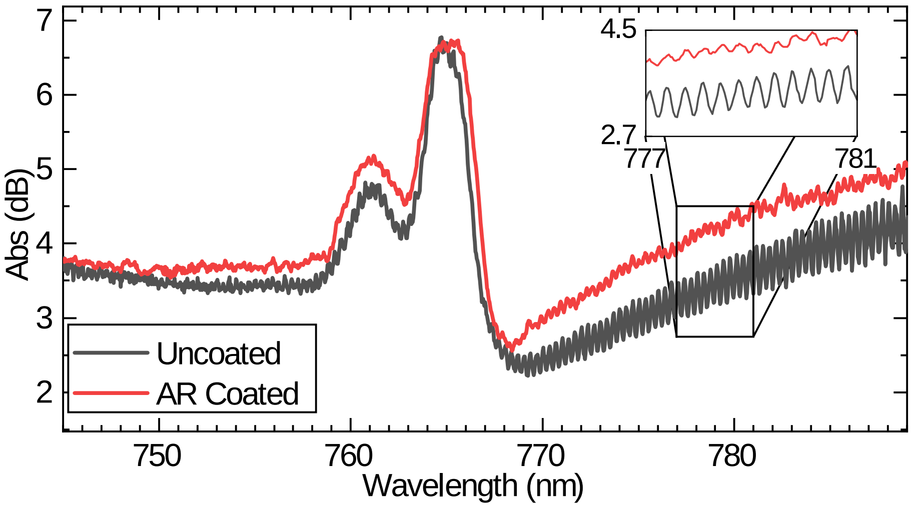

Figure B.2: Demonstration of the benefit of the anti-reflection (AR) coating. The grey curve shows the absorbance spectra of a 10 nm AlGaAs QW transfered to a sapphire which is backed by ITO alone. At low energies, large Fabrey-Perot oscillations are seen. The red curve shows a 10 nm AlGaAs QW transferred to a sapphire-ITO substrate which also has a thin film of SiO_2 as an AR coating. The FP oscillations are substantially lessened, as seen in the zoomed in inset.

Characterizing the thickness of the ITO is best accomplished with the Filmetrics in the cleanroom, which has built-in recipes for ITO on Si. A more thorough analysis can be done on the ellipsometer, if desired. Characterization of the THz field, as in Fig. B.1 can be done with the VNA. Refer to the Appendix of the Bachelor's thesis of Andrew Pierce for measurement instructions.

B.2 Silicon Dioxide Deposition

The mismatch in indices of refraction between the sapphire, ITO and air result in rather large Fabrey-Perot (FP) oscillations. These oscillations have had significant impact on experiments where the NIR frequency is tuned, as seen in Fig. 4.3(a). They are also obvious in the absorbance spectra of the samples, as shown in the grey curve of Fig. B.2. To lessen the magnitude of the oscillations, an anti-reflection coating was designed. A 160 nm thin film of SiO_2 is suitable to substantially reduce the oscillations, as seen in the red curve of Fig. B.2.

B.2.1 Fabrication Steps

SiO_2 can also be deposited in E-Beam #2. It is also more convenient than ITO as the substrate does not need to be heated. As before, a fresh Si test piece is useful for characterizing[1]. It is very important to clean both samples ahead of deposition, including a O_2 plasma descum, as the SiO_2 films have delaminated off the ITO film when improperly cleaned.

The SiO_2 can be deposited at a rate of 2 Å/s, regardless of thickness. Once finished, the Filmetrics or ellipsometer can be used to characterize film thickness. Alternatively, the absorbance of the sample can be measured to compare the strengths of the FP oscillations before and after the coating.

B.3 Epitaxial Transfer

After the substrates have been fully prepared, the epitaxial (epi) layers can be transfered. The general procedure is to protect the epi layer with a protective black wax (Apiezon W), strip the backside substrate and etch stop and Van der Waal bond the epi to the

---

[1] Reusing the Si piece from the ITO deposition will likely lead to complications as the Filmetrics will not have the appropriate thin-film recipe for characterization.

substrate. Before beginning, the final mounting substrate, typically a sapphire substrate which has the above ITO and SiO_2 films, should be diced to the appropriate dimensions and the epi sample should be cleaved. When noted, sample handling should be done on Berkshire wipes to prevent lint from ruining the bond.

Preparing the sample (Berkshire):

1. Clean the epi side of the sample with tergitol, acetone, isopropanol, rinse with distilled water and blow dry with N_2. Clean the surface in the O_2 plasma descum, 100 W for 1 minute.
2. Place the sample on an aluminum weigh boat on a hot plate set to 100 °C. Place a small piece of black wax on the surface and allow it to flow to cover the surface. Do not let the black wax flow over the edge of the sample surface, otherwise it will interfere with the final bonding.
3. Stretch one quarter of the gel pack[2] across the plastic vacuum flange and secure it[3].
4. Remove the sample from the hot plate and allow it to cool to room temperature. Adhere it to the gel-pak carrier by lowering the gel-pak over the sample.

Backside removal

1. Etch the sample in 10:1 H_2O_2:NH_4OH for roughly 50 minutes. The etch is anisotropic, attacking the (111)Ga face more slowly than the As face [7]. Thus, the side etched

---

[2] DGL-45-X8-SP2 from gelpak.com

[3] C10516394 and H02124037 from edwardsvacuum.com

slower is the [011] direction.

2. The 10:1 solution is quick, but non-selective. A 30:1 solution of H_2O_2:NH_4OH is slower but more selective to the etch stop region. Etch in the 30:1 solution until the GaAs substrate is fully removed, determined by the appearance of a colorful thin-film interference of the etch stop layer[4].
3. The etch stop can be removed in HF (either buffered HF or 50% HF). Submerge the sample for 30s in HF, then 30s in water, and 30s again in HF.

Van der Waal Bonding (Berkshire):

1. While the sample backside is etching, the sapphire substrate should be thoroughly cleaned with tergitol, acetone, isopropanol, rinse with distilled water and blow dry with N_2. O_2 plasma descum at 200 W for 2 minutes.
2. Position the sample above the sapphire substrate. Gently press down on the black wax side of the sample, pushing the gel-pak film, until the sample makes contact with the substrate. Ideally, a single point should contact and bond. Over the course of a day, the bond should propagate outwards until the full sample is bonded.
3. Slight pressure can be used to improve the bond or remove bubbles which form.
4. After a satisfactory bond, the black wax can be removed in chloroform. After the BW is removed, the sample can be *very* gently scrubbed in isopropanol and tergitol

---

[4] The 30:1 cannot efficiently remove the oxide layer which forms when the substrate is exposed to air for any period of time. The sample must be transfered directly from the 10:1 (such as quickly submerging it if the sample is exposed to air), or by squirting the sample directly with a few drops of NH_4OH

to clear the surface of debris. A final O_2 plasma descum can be done at 100 W for 1-2 minutes.

B.4 Hugins Software

While processing samples, I've found it's very useful to have full-size images of the sample at intermediate steps to determine how the process is proceeding, as well as one at the end to compare experimental positions and sample degradations over time. Since the samples are rather large, the field of view of the cleanroom microscopes isn't sufficient to capture a full sample in a single image. Instead, several images are required which must be stitched together. A straightforward way to do this is to manually overlap the images in Gimp or another photo-editting software, but I've found an easier method, with better results, results from using better software. "Hugin" is a software package intended for stitching together panoramic images for photographers, but it adapts well to our microscope slides, with some tweaking. In addition to stitching images together, it also balances exposures between images and merges them into a single, smooth image without shearing from stitching images together. Here, I'll outline the basic steps for using the software. In general, the software starts by analyzing images to find control points (CPs), which are edges or spots of high contrast which are common between two images. It then analyzes all of the images to determine what transformations of the images (moving them along the surface of a sphere) minize the distances between all control points.

(Optional) Linear CP Finder

The default CP finder for Hugin is Hugin's CPFind. As mentioned above, it finds control points between any two images. This isn't always ideal in our case, because we know some images are not at all related, but the software may still find CPs between them due to sample defects. Assuming each image of the sample is taken as a raster scan across the sample (*e.g.* each image is only well correlated to the image directly before and after), it's better to set up a CP finder which only looks at neighboring pairs.

1. Select File ⇒ Preferences
2. Under 'Control Point Detectors', select 'New...'
3. Give it a description (*i.e.* 'linear cpfind')
4. Set the Program as 'cpfind.exe'
5. Set the arguments as

   ```
   --linearmatch -o %o %s
   ```
6. Type should be left as 'All images at once' and it is a 'One step detector'
7. Press OK

B.4.1 Stitching an image

Make sure you're using Expert mode (Interface ⇒ Expert). This provides additional options and controls needed for tweaking the controls. It's also useful to open the fast view (View ⇒ Fast Preview Window). These first steps refer to usage in the "Hugin - Panorama Stitcher" window.

1. Under Photos, press 'Add Images...' and select all the images
2. Enter 5 for the HFOV[5]
3. (Optional) Under 'Feature Matching', select the linear cpfind created above
4. Under Optimize ⇒ Geometric, select 'Custom Parameters'
5. Press 'Create control points'
6. Under the 'Optimizer' tab, de-select all 'Yaw', 'Pitch' and 'Roll' parameters (right click on the column header), and select 'X' and 'Y'[6]
7. Press 'Optimize now!'

These steps should do a good job and aligning the image. It can be checked in the 'Fast Panorama preview' window. If the images don't look right, you can look at the 'Control Points' tab un the Hugin window, and manually remove bad control points, or add them if there isn't good overlap or enough features for the stitcher. It's much easier to do this with a linear cpfind, since you only need to consider consecutive images, instead of all pairs. To finish up, open the Fast Panorama preview.

1. Under the assistant tab, select a Lens type of Equirectangular

---

[5] Entering 5 for the HFOV isn't really tested, and could be tweaked to make things work better.

[6] Selecting X and Y as optimization parameters, instead of Yaw, Pitch, and Roll, forces the software to confine the images to a flat plane, instead of trying to optimize on the surface of a sphere.

2. The right side shows the image that will be output. Using the blue sliders on the bottom/right side will reduce the ‘FOV’, effectively zooming in on the image. Use them to get a closer image

3. Next, select the Crop tab. Now, mousing over the right image brings up handles for further cropping the image to the appropriate size.

4. In the Hugin window, select the Stitcher tab, and press Stitch!

Appendix C

Experiment Software

I've written a lot of Python3 code for data collection and analysis. In this appendix, I will try to give overviews of both generic usage of the software, as well as hints and tips for potentially extending the software.

C.1 EMCCD Software

The potentially biggest piece of software is the EMCCD software, which controls the Andor camera and Acton spectrometer, and ties in with the pyro oscilloscope, the wiregrid attenuators and the Thorlabs rotation stage.

C.1.1 Standard Usage

General Camera Settings Figure C.1 shows the first tab to open when the camera is first opened, and displays the overall settings and controls for the camera and

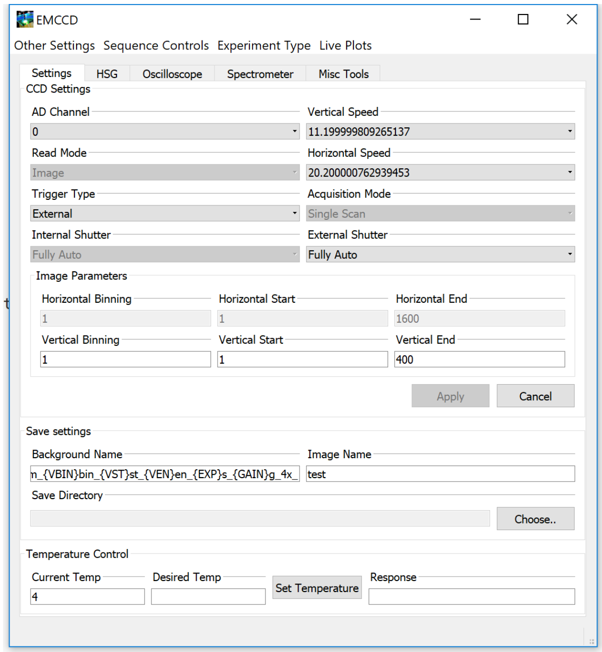

CCD Settings

AD Channel: 0

Vertical Speed: 11.199999809265137

Read Mode: Image

Horizontal Speed: 20.200000762939453

Trigger Type: External

Acquisition Mode: Single Scan

Internal Shutter: Fully Auto

External Shutter: Fully Auto

Image Parameters

Horizontal Binning: 1

Horizontal Start: 1

Horizontal End: 1600

Vertical Binning: 1

Vertical Start: 1

Vertical End: 400

Save settings

Background Name: n_{VBIN}bin_{VST}st_{VEN}en_{EXP}s_{GAIN}g_4x_

Image Name: test

Save Directory:

Temperature Control

Current Temp: 4

Desired Temp:

Response:

Figure C.1: Settings and first page for the EMCCD software

for data saving. AD Channel controls which analog to digital converter is used by the camera, changing the read-out speed of the camera. 0 is slow and low noise, while 1 is fast and higher noise. Vertical speed and horizontal speed allow finer control of read-out speeds. However, some settings are unreliable and none are thoroughly tested. Switching the ADC between 0 and 1 will automatically update the read speeds to the correct values, and manually selecting those speeds should not be done. Read Mode, Acquisition mode, and internal shutter are not used in experiments, and they have been disabled. Detailed descriptions of their function can be found in the Andor manual.

Programming Project: *Add Vertical and Horizontal Speed to the greyed-out options*

Trigger Type toggles between internal and external. External is desired for experiments, as there is a physical port on the camera which is connected to the FEL triggering system. When the pyro-oscope is used as well, the software will ensure FEL pulses are counted properly. Internal switches the camera to trigger off the 60Hz AC line. This is very helpful when aligning to the laser, where you don't need to be restricted to the FEL rep rate.

The external shutter interfaces to the shutter attached to entrance slit of the Acton Spectrometer to which the camera is attached. Fully Auto results in the shutter opening when an exposure begins, and closing when it is completed (it will be closed during the read-out sequence, which can be helpful on slow reads, such as 0 ADC and no binning on the camera).

The Image Parameters sub-section allows for specifying a subset of the camera chip to read out, as well as binning (Refer to the Andor manual for a detailed description). Both features result in faster read-out speeds, as fewer pixels of the camera are read out. Furthermore, binning substantially increases the SNR as the signal from several pixels are integrated before noisy amplification sequences are applied. Horizontal parameters have been greyed-out because some of the analysis software is not equipped to handle input arrays which are not 1600 pixels long.

Programming Project: *Trace through the analysis software to find out where the analysis breaks with horizontal binning (Hint: There are a lot of hard-coded* `[:1600]` *slices, and the pixel to wavelength converter has issues)*

None of the above settings are implemented until the Apply button is pressed. It will become enabled when settings are changed from the current value in the camera. Cancel will reset the values to the original parameters.

The Save Settings straightforwardly chooses save information. The Background Name gets passed through a quick python string formatter, allowing the files to be saved with the current parameters to quickly tell which background file is desire for which experiment. The Image Name does not have this feature implented. When a Save Directory is chosen, provding an Image Name then creates a sub-folder within the chosen Save Directory. This is to keep various images from different sweeps localized to separate folders.

Programming Project: *Implement string formatting for the Image Name*

(The previous programming project is a little more difficult than it sounds. See the discussion in the Details on code section below.)

The final option on this page controls the temperature of the camera. The camera is equipped with a TE cooler, which can significantly lower dark count and leads to higher effective gains from the amplifying circuitry. Typical experiments occur at -90°C, which is the lowest temperature possible in our room. Refer to the Andor manual for the allowable temperatures depending on room temperature, humidity, and chiller water temperature. Enter a desired temperature, and click Set Temperature. The software will disable camera settings while the camera cools (camera gain is strongly dependent on temperature, so this is to prevent accidently taking meaningless data), and begin a loop which monitors the cooling of the camera. A warning will pop up to remind you to turn on the chiller. When the chilling sequence is begun, an option becomes available in the (Menubar)Other Settings>Break temperature loop. This will stop the software-side temperature monitoring so data can be collected (such as for aligning). This does not stop the camera from cooling, the internal camera software will continue to cool the camera.

When the camera is cold, and the software is opened (such as after a crash or software restart), the software will read the camera temperature, check if it is cold, and begin re-stabilizing the temperature if needed. Furthermore, under (Menubar)Other Settings>Exit without shutdown provides an option to exit the software without causing the camera to warm up. Be very careful with this, the python software (or the Andor software) should be opened shortly afterwards to prevent damage to the camera. However, this feature can be very helpful when the software crashses, or communication with an instrument breaks, and the software needs to be restarted quickly. Otherwise, the appropriate way to close the software is to press the standard red × at the top-right of the application. The software will start warming up the camera, displaying a dialog indicating that the camera is still warming. When the dialog disappears, it is safe to press the red × again to fully close the software.

Taking Images Experiment controls and camera readback is done on the second tab of the UI, labeled as whichever experiment is running. The panel for HSG experiments is shown in Fig. C.2. In the window, there are many places to input experimental parameters which get saved in data files as a header. The `Series` tag is used by processing software to group data files together, such as different spectrometer steps, or as labels when stitching sweeps together. Entering a '{' will pop down an autocompleter which shows the various keys which can be used, automatically setting the series tag to the

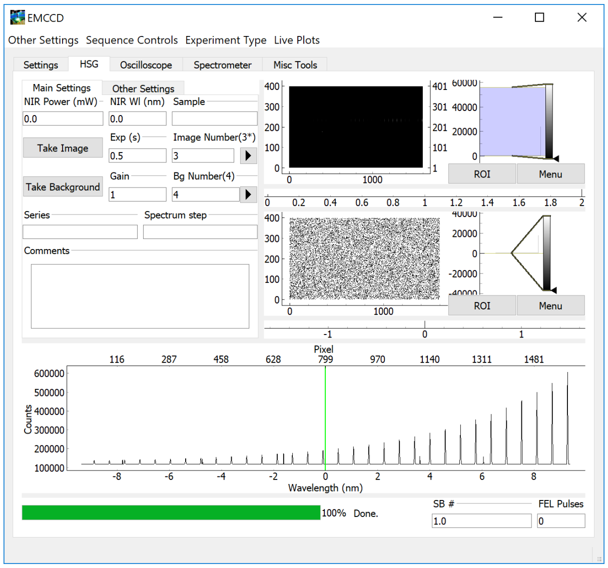

NIR Power (mW): 0.0
NIR Wl (nm): 0.0
Sample:
Exp (s): 0.5
Image Number(3*): 3
Gain: 1
Bg Number(4): 4
Series:
Spectrum step:
SB #: 1.0
FEL Pulses: 0

Figure C.2: Example panel for data collection. The layout for an HSG experiment is displayed.

value in a separate text field.

The `Spectrum Step` field is used by processing software to combine spectra with the same series tag, and sorts spectra assuming lower `Spectrum Step` values correspond to lower-order sidebands.

> ***Programming Project:*** *The Spectrum Step field could likely be done away with by sorting only on the spectrometer wavelength. This would prevent issues from accidentally forgetting to change or update the field manually.*

The `Exposure` and `Gain` settings are sent to the camera itself. Pressing either `Take Image` or `Take Background` will update the settings, and begin an immage acquisition. An acquisition can be aborted from (Menubar)Other Settings>Abort Acquisition. After an image is taken the software will prompt if the image should be saved. This allows discarding of images with large cosmics, or if no signal is observed for any reaon. The same prompt is not provided for background images.

As images (or backgrounds) are taken and saved, a counter is incremented on the `Image Number` (`Bg Number`) fields, indicating how many images have been stored for the current sequence. While the values in text box correspond to the total number of images (and used in saving to prevent overwriting images), sets of images are required for cosmic ray removal, averaging, and statistical information. Pressing the button under `Image Number` (`Bg Number`) will process the data, and remove the '`*`' from beside the number of images in the sequence, indicating the data has been processed.

The top image plot shows the camera read as an image, while the background is shown below it. The left-axis displays the dimensions of the array, starting from zero, with each 'pixel' counting as 1 unit (that is, it does not account for binning on the camera). This axis is useful for determining what region of the camera chip to integrate over in software, as determined in the `Other Settings` tab, `y_min` and `y_max`. The right axis displays the actual pixels on the camera, where it accounts for offsets from camera binning and starting readout away from pixel 1.

The bottom plot shows the integrated image plot for the pixels specified by `y_min` and `y_max`. If the `NIR Wl(nm)` and `FEL Freq (cm-1)` (under the `Oscilloscope` tab) are set, the green bar can be dragged and the `SB #` text will update to display which sideband is under the green cursor. Alternatively, a sideband order can be entered in the textbox, and the green cursor will jump to it.

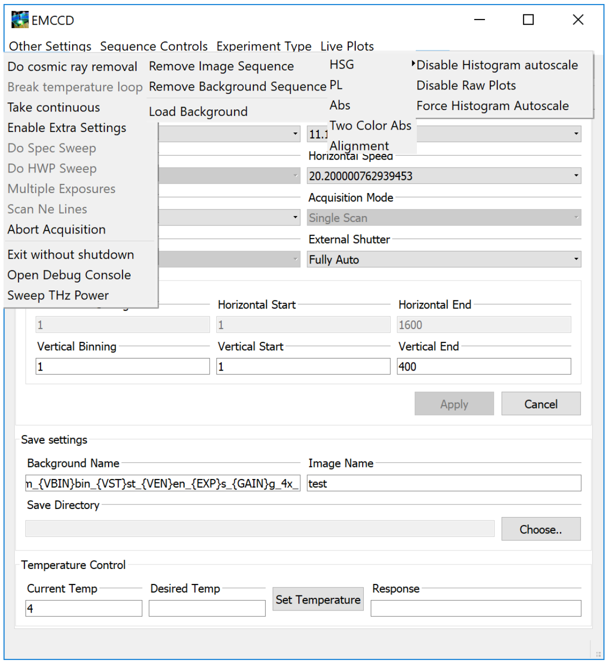

Horizontal Speed: 20.200000762939453
Acquisition Mode: Single Scan
External Shutter: Fully Auto
Horizontal Start: 1
Horizontal End: 1600
Vertical Binning: 1
Vertical Start: 1
Vertical End: 400

Save settings
Background Name: n_{VBIN}bin_{VST}st_{VEN}en_{EXP}s_{GAIN}g_4x_
Image Name: test
Save Directory

Temperature Control
Current Temp: 4
Desired Temp
Response

Figure C.3: Available options in menubars for controlling the data collection settings.

Menubar items What follows will be a brief description of all of the items which appear in the top menubar. The list of actions are shown in Fig. C.3.

Other Settings This menu item is a catch-all for various useful tools for experiments. `Do cosmic ray removal` refers to doing old-school, 2D cosmic ray removal. It is not useful for the binned images most often used in experiments, so it is default disabled. However, if the camera chip remains largely unbinned, and long exposures are taken, enabling it could be used. This does not affect the cosmic ray removal which occurs when processing an image sequence.

`Break Temperature Loop`, as mentioned above, stops the software loops which monitor setting the temperature on the camera, and is enabled when such a loop begins.

`Take continous` is a feature added for alignment. It will constantly set an acquisition and read images from the camera. It disables the prompt for image quality, and doesn't save images. Note, you should almost always set the shutter on the camera to `Permanently Open` (Under `External Shutter` on the CCD settings) to prevent excess wear of the mechanism.

Programming Project: *Set the camera to automatically keep the shutter open when a continous acquisition is started*

`Enable Extra Settings` enables the 4 options below it. It was originally implemented to prevent accidental use of experimental software features.

Programming Project: *HWP sweeps and Multiple exposures are mostly robust procedures. Remove them from the list of initially disabled features.*

`Do HWP Sweep` is the feature used for polarimetery. The user will be prompted of a starting angle, a step size, and ending angle, and a number of images to take at each angle.

`Multiple Exposures` will ask for a number of images desired, and take that many (without processing). This is mostly useful for taking several long exposures without needing to pay direct attention to the software. Holding Shift while pressing this item will take background images instead of standard images.

`Scan Ne Lines` A neon (Ne) calibration source was purchased for calibrating the camera and spectrometer. The software has a list of the Ne emission lines. Selecting this action will prompt which wavelength range to scan over, and then will center the spectrometer at every emission line within the specified region, take a set of images, and a set of backgrounds. This feature can be useful for recalibrating the spectrometer, and/or analyzing the spectrometer slippage, see Appendix A, section A.5.5.

`Abort Acquisition` Tells the camera to stop acquiring an image. Useful to prevent damage if a long exposure was accidentally selected which may damage the camera. No readout of the image is performed.

Programming Project: *Abort Acquisition does not also terminate a sweep, such as for the QWP or multiple exposures. Try adding that functionality so aborting an acquisition will also terminate sweeps.*

`Exit without shutdown` This function will close the software, without first waiting for the camera to warm up, as discussed in Sections C.1.1 and C.1.3. This has been helpful for many of the bugs mentioned in Sec. C.1.4 where restarting the software is necessary, butout waiting half an hour for the camera to warm and cool. Take care with this feature, it has not been tested how long the camera will stay cool with no software control, so only use this option when the software will be quickly reopened.

`Open debug console` This software isn't perfect. The debug console exposes all of the functionality of the camera software, so a small amount of debugging can be done without restarting the camera.

`Sweep THz Power` Another sweep feature, where the wiregrid attenuator will be stepped to the angles provided after selecting this option. This sweep was initially set up in a very coarse fashion, which is why it is separated from the other sweeping functions, and also not enabled/disabled via `Enable Extra Settings`.

Programming Project: *Improve this sweep function. Add it to the UI file directly. Prompt for how many images to take, as it is hardcoded to 4 images*

Sequence Controls These menu items are for controlling image sequences, which are sets of images taken under identical experimental conditions to be averaged together for statistics and cosmic ray removal.

`Remove Image (Background) Sequence` When images (backgrounds) are taken, the "Image (Bg) Number" label will indicate how many images have been taken which need to be processed together. Removing the sequence removes them from software memory without processing them together. The files are still saved as raw image files. This functionality helps keep data folders clean by removing the need to process images to get them out of the image buffer.

Programming Project: *Add a `Remove Reference Sequence` to absorbance experiments*

`Load Background (Reference)` This functionality allows loading of background images or references. It can handle loading of a processed pair, *e.g.* the `*_seq.txt` and `*_std.txt` files for the mean and std of a processed sequence, respectively. Alternatively, any number of raw background images can be loaded so further images can be taken and added to the sequence, or to have them reprocessed.

Programming Project: *Add a `Load Images` functionality, which could be useful for starting again after a software crash, or useful in reloading old images which need to be re-processed.*

Experiment Type Selecting an option in this menu will change which experiment is to be performed. Refer to Section C.1.2.

Live Plots These options control the image plots which plot the result of the camera.

`Disable Histogram autoscale` When an image is taken, the colorbar defaults to autoscaling such that the highest value is colored white, and the lowest is colored black. Selecting this option prevents this autoscaling, which can be useful when wanting to compare consecutive images, especially around low counts where rescaling the color bar would change the contrast.

`Disable Raw Plots` Selecting this option prevents updating the image plot with the raw image from the camera. I think it was mostly intended when 2D cosmic ray removal was used, and likely doesn't have much purpose in the current stat eof the software.

`Force Histogram Autoscale` will force the contrast on the image plot to place white at the largest value, and black at the smallest. Useful for when the colors have been changed to enhance contrast at a specific region.

Programming Project: *Add the functionality to rescale the background*

C.1.2 Experiment Types

These sections will briefly outline the different experiments which can be performed with the current software.

HSG Experiments Three different types of experiments have beeen set up for doing HSG. They all ensure the oscilloscope is open, and use it for counting pulses/normalizing data. There are also places to input the parameters of the NIR laser to be saved in the headers of data files.

`FVB` (Full Vertical Binning) was attempting to take advantage of a camera setting which would fully bin the camera vertically. This functionality is no longer necessary, as it was determined it is better to specify a desired binning region on the first page, instead of binning across the entire chip.

`Image` is the standard method of running the camera, where the full chip is read out (or as-binned specified on the settings page). An image of this data collection experiment is shown in Fig. C.2.

`Photon Counting` was an attempt to implement the photon counting mode of the camera. It has not been fully developed.

PL Experiments Photoluminesence experiments can be performed in this setup. There is no communication with the oscilloscope since there is no FEL for a standard PL experiment. There are places to input the parameters of the NIR.

Programming Project: *Normalization does not occur in this software for PL. It should likely be normalized by exposure time*

Abs Experiments Absorption experiments can be performed here. There is a new button for taking reference images, an an absorbance spectra is defined as

$$\mathrm{Abs} = -10\log\left(\frac{\mathrm{img}-\mathrm{bg}}{\mathrm{ref}-\mathrm{bg}}\right)$$

. The image and reference are both shown in the top image pane, while their binned images are both shown in the bottom, along with the absorbance itself, once both are taken. There are places to input the settings of an LED, when abs experiments were done using an LED driven at some current and held at some temperature.

Programming Project: *Normalization is not performed in absorbance images, but it really should be.*

Two Color Abs Experiments Two color absorbance experiments with a THz driven absorbance. Works with the oscilloscope to log FEL information, and normalizes by number of FEL pulses. As with absorbance, there are places to input parameters of the LED used for absorbance.

Alignment Experiment The alignment widget is helpful for aligning the laser or signals to the camera. Fonts are enlarged to increase their visiblity from across the room. Data is not saved to a file, and there is no prompt to confirm quality.

A button to `Add Vertical Line` and `Add Horizontal Line` have been added, which will add the respective lines to the image plot, and the slice of data along those lines is shown in the bottom plot. By default, the slices are scaled between 0 and 1. This was originally used to look at the white light on the camera, and compare the widths and positions of the white light across the chip. The lines on the image plot are also useful to mark positions on the chip, such as the edges of the slits when aligning to the spectrometer.

Holding `Ctrl` while clicking one of the buttons will add a line which is not normalized between 0 and 1. Futhermore, changing the `Slits` value will integrate that many pixels on both side of the line.

Programming Project: *This slits trick was a quickly needed feature, but has unintended behavior since it will change the value of the slits in the other experimental widgets. Make an independent (and better explained) place to change the integration region.*

Holding `Shift` will clear those lines from the plot.

Other Equipment interfaces There are four other pieces of with which the software communicates, the oscilloscope, the spectrometer, the wiregrid motor, and the Thorlabs Rotation stage. All but the spectrometer will be discussed in future sections. The spectrometer is controlled through the “Spectrometer” tab, while the attenutator and Thorlabs Rotator are controlled under the “Misc Tools” tab.

Programming Project: *Rearrange the software so the spectrometer and “misc tools” are in the same tab in software, to keep things together. The extra tools are added to the UI dynamically, and are not directly in the UI files.*

The spectrometer operation is straightforward. Specify a wavelength and **press Set**. When calculations are done for the wavelengths of each pixel, the value specified by the user in `Center wavelength` is used, not the `Current wavelength` as readback by the spectrometer. This is a legacy from when the spectrometer calibration was done in software and told to go to an incorrect position. The spectrometer has since been calibrated directly.

Programming Project: *Change the calculations for the wavelength to the value read by the spectrometer to prevent accidental errors from forgetting to hit* `Set`

The spectrometer is currently equipped with 3 gratings of various groove densities. See Appendix A, section A.5.5 for details on the gratings. As with the center wavelength, the `Set` button must be pressed for the hardware to be updated.

Whenever the value for the center wavelength or grating is changed, the software will calculate the starting and ending wavelengths for those values. If an HSG experiment is being performed, and a NIR wavelength and THz wavelength is entered (in the oscilloscope tab), it will also calculate the corresponding sideband orders to assist determining which center wavelength is desired.

The THz Attenuator is the first item under the Misc Tools tab. When the oscilloscope is used during an experiment, such as in HSG experiments, it will pull the attenuation value from this tool to calculate the field on the sample. If the motor has not been opened (such as when the EMCCD software is opened after a different tool which uses the motor), it defaults to 0.0 transmission and will give incorrect values for the field strength and field intensity.

Programming Project: *Make a popup or some warning occur if the oscilloscope is running but the attenuator software is closed, to prevent saving incorrect data*

The Thorlabs Rotator is the second item under Misc Tools. It controls the Thorlabs K10CR1 rotation stage. It will interface with the EMCCD software to do automated polarimetry experiments by rotating the motor and taking HSG images at defined steps. If the stage is not plugged in when the EMCCD software is started, hold `Shift` while pressing the `Open` button, which will cause the software to referesh the device list before opening.

C.1.3 Details on code

Camera control Controlling the camera was all done using the `.dll` provided by Andor, and following the SDK provided. To access it in python, the `ctypes` library was used. All of this was wrapped up in `class AndorEMCCD`. `registerFunctions` will create python handles to all of the appropriate functions from the dll which are needed for operation. The optional flag, `wantFake`, provides the ability create handles to fake functions (implemented in `fAndorEMCCD`). This does a lot of debug output for determining function call orders, but allows the software to be run without the camera. It also gets run when communication with the camera cannot be started, such as it not being plugged in, or two instances of the EMCCD software running. On top of registering all of the C functions, the `AndorEMCCD` class then has more pythonic functions to quickly get/set values to the camera without having to expose the internal `ctypes` functionality.

Camera Settings One the first settings page, keeping track of which settings have been updated is done on a software-side flag which simply tracks when values have been changed from the last set value. However, after the apply button is pressed, each setting is updated, checked that it was set properly, and raises a warning if it was not.

File Names The background name and series tag have custom autocompleters attached to their `QTextEdits`. They were designed in Python2, and the functionality seems to have broken in Python3.

Programming Project: *Fix the autocompleter to work again*

To extend this functionality to the Image Name, it is important to understand how folders are handled. When an Image Name is entered (and enter is hit, or focus is lost), and a Save Directory is provided, an appropriate folder is generated. If a string formatter is applied to Save Image strings, this functionality would have to be delayed until an image is actually taken, so the desired settings to format the folder with are actually known. This would likely need to add a check at every image save whether the desired folder exists, and creating it if not.

Temperature control When a temperature is first set, a dialog box pops up reminding you to turn on the chiller. The software starts a `QThread` which calls the temperature set of the Andor, which is a blocking thread until the temperature stabilizes. A `QTimer` is also started, which updates the GUI with the current temperature and readback from the camera, so you can always know where it is in the process.

One feature I added to try and make things easier is that, when you press the red × to close the software while it's cold, you can set it to go to 20°C, but it's safe to turn off the camera > 0°C. There's a flag that gets passed around, `killFast`, which causes the Andor loop to stop monitoring the temperature once it's above 0°C. I feel like this was done in a rather dirty way. A better way might have been to have the `AndorEMCCD` to have a member variable on whether it should loop a temperature thread, and have the GUI EMCCD software toggle that thread once it reaches the desired temperature.

Another important feature is the persistent cooler mode. When communication with software stops, the camera will stop maintaining a temperature. If the camera is cold, this can lead to it warming too quickly and potentially cracking the camera chip (detail can be found in the Andor manual). This caused problems when the software would crash (or need to be restarted). Thankfully, the SDK provides the `SetCoolerMode` funcionality, which seems to maintain the camera temperature when the software is closed. This function is called as soon as the Andor class is intialized; the software would occassionally crash during UI initialization or other start-up processes while testing new software, so this ensured the camera would stay cold.

Taking Images When either an image or background is taken, the software begins preparing for an exposure. First, it checks whether the value of the gain or exposure has changed, updating if needed. One poorly done feature is that it compares it relative to what the software has stored in memory for those values from the last exposure, and not the actual camera settings. This has not yet caused problems, but there are better ways to do it.

Programming Project: *Have the software query the camera to figure out what the current exposure/gain settings are, instead of relying on a memory value.*

Gain controlls are performed using the EM (electron-multiplying) gain. There is apparently funtionality for a "conventional" gain process, which has not been explored.

Loops Looping image collection, such as the Continuous Image feature, Polarimetry Sweep, or scanning THz Power, were all developed quickly and not very intelligently or in an extendable manner. All of the loops get pushed to a single thread instance, `thSpectrometerSweep`; sweeping the spectrometer grating was the first loop created, and all of the following reused the same code.

Programming Project: *Give a better name for the name of the thread used for all sweeps*

Whenever a sweep is requested, a function gets called to set up the sweep, such as `startHWPSweep` (which is a misnomer and should be relabeled as `startPolarimetry`). These functions prompt for the sweep parameters and start a thread which runs the actual loop.

Each loop is written with its own function to do the things required of the loop. Typically, the function will move a separate instrument via mimicking button presses. After the device finishes moving, the loop will then emulate pressing the `Take Image` button the desired number of times. More details will be discussed in Sec. C.1.4

Cosmic Ray Removal There are two ways of doing cosmic ray removal (CRR) in the software. The original method uses the `comics_hsg.py` script, which includes references to the paper the algorithm comes from. It can remove cosmic rays from a single image, but requires a 2D image to scan across. When we moved to full-vertical binning, that algorithm would not function and a second was devised.

Each image, reference, or background which gets taken is stored within a `ConsecutiveImageAnalyze`

This stores the raw image data from the camera as well as the normalization parameter. For HSG experiments, or experiments with the FEL, it normalizes to the number of FEL pulses which occurred during the exposure. It currently does not do anything for exposure times, such as for PL or absorbance, which may be useful features for combining absorbance images with longer signal integrations compared to the reference.

Programming Project: *Add normalization based on exposure time when FEL pulses is not appropriate*

When a 1D sequence is being processed for cosmic rays, a set of images must be considered. A cutoff is defined by,

$$\text{cutoff} = r_c * \text{median} + r_\delta * \delta$$

where the median is the pixel-wise median of the image set, δ is a rough estimate of the noise, and r_c and r_δ are adjustable scale parameters. The noise is estimated by the average noise between images for the first several pixels of the image. The values of the scaling factors were chosen by looking at many data sets to determine what good values are. Any data point which deviates from the median by more than this cutoff is considered a cosmic and removed.

Since cosmic rays tend to be skewed Gaussians or even one-sided exponentials, sometimes the noise floor is raised by a very large cosmic ray whose tail is not within the cutoff. Thus, an improved cosmic removal algorithm may try to fit the exponential tail of the cosmic rays to also remove.

Programming Project: *Experiment with changing the removal criteria for CRR*

Implementing Different Experiment Types One of the most significant parts of the software may come from the ability to relatively quickly add new experimental schemes, especially if they can be derived from existing experiments to subclass. The first step to create a new experimental widget is to create the UI for it. Each experimental widget is saved first as a Qt Designer `.ui` file (Qt Designer is installed with Anaconda python distributions), which can be converted to a python UI file via the `pyuic5` command, which should be in the Anaconda path.

For software, the new widget should subclass `BaseExpWidget` (or one of its subclasses) within the `ExpWidgs.py` file. Further processing and data handling is done in the subclasses of `EMCCD_image` in the `image_spec_for_gui.py` folder. Each subclass of `BaseExpWid` has several flags: `hasNIR`, `hasTHz` and `hasSample`. These are used by the `BaseExpWid` for determining which settings from the widget must be saved, or preparing for an acquisition which must count FEL pulses. The `name` class variable defines which name is shown for the tab in the main EMCCD window. The class variable `DataClass` should be a reference to the class in `image_spec_for_gui.py` which handles the data processing required.

After that, the next steps depend on what new functionality is needed. The best thing to do would look at the currently existing extensions to determine what is needed for a new experiment.

C.1.4 Known bugs/workarounds

Graph Freezing Over time, I have noticed that the `pyqtgraph` image plots would occasionally stop responding to controls, requiring a camera restart. This was most often seen when using `Continuous Mode`. There were some indications it would happen more often when switching the software to different tabs. The software disables other tabs when `Continuous Mode` is enabled. I have not been able to determine the cause of the bug, those the occurrences of it are extremely rare.

Oscilloscope failing to re-open On occasion, upon switching the CCD software to a experiment which doesn't use the oscilloscope (*i.e.* `Alignment`) and back to one which does, the oscilloscope would not properly open, causing that tab to not appear, nor the appropriate experimental tab. The work around is to restart the software, without warming up if necessary. Preliminary investigations indicate it is from garbage collection or invalidation of the VISA `ResourceManager`. Unfortunately, debugging on a different computer (which does not use VISA) has been unable to reproduce the issue to correct it. However, it may be fixed by re-instantiating the `ResourceManager` class.

Programming Project: *Fix the oscilloscope bug by re-instantiating the `ResourceManager` instead of referencing the stored `rm`*

Pausing QWP Sweeps A pause function on the QWP sweeps was implemented to allow a pause when, for example, the FEL or NIR laser required retuning during a scan. Unfortunately, while it seems to work well on an office computer, it fails rather reliably on the lab computer, causing the software to immediately crash. I am unsure of the cause, but suspect thread-unsafe code was introduced. Reloading the software is the only course of action.

Take Image greyed out If an error occurred during an image readout or processing, sometimes the software will not re-enable the `Take Image` and `Take Background` buttons, nor any of the camera control settings. One option is to restart the software. However, it can often by fixed by opening the console ((Menubar)Other Settings>Open Debug Console), and typing `self.getCurExp().toggleUIElements(True)` and hitting Enter. The console can be closed afterwards.

Taking images not starting I have noticed an occasional issue where `Take Image` or `Take Background` will be pressed, and the buttons will become greyed out, but the progress bar does not proceed and the image collection never occurs. This seems to come from an occasional bug where the oscilloscope will timeout and stop communication with software, but the EMCCD software does not see this and instead waits for the trigger, which never comes. To fix it immediately, open the console ((Menubar)Other Settings>Open Debug Console), and type `self.getCurExp().thDoExposure.terminate()`, which will stop the thread which is waiting for the trigger. The elements can be re-enabled with `self.getCurExp().toggleUIElements(True)`. Restarting the oscilloscope thread can be achieved by either switching to an experiment without the oscilloscope (*e.g.* Alignment) and back. Alternatively, switching the GPIB of the oscilloscope to `Fake` or `None` should also resolve the issue.

Programming Project: *Fix the miscommunication errors with the oscilloscope*

A more long-term solution would be to fix the communication error with the oscilloscope (see Sec. C.3). Secondly, the EMCCD software could check to ensure the oscilloscope is functioning. In the `doExposure` function of the `BaseExpWidet` class, there is a loop which checks to see if it should wait on the oscilloscope before proceeding with pulse counting and the progress bar. An extra check could be performed, such as checking if the thread of the oscilloscope widget, which queries the oscilloscope for data, is running.

Incorrect absorbance plots When taking absorbance data sets, an image without the sample (reference) and with (image) are both required, and it can be helpful to see both of these raw signals in addition to the absorbance of the data. Unfortunately, this functionality broke at some point, so the image data is plotted twice (once background subtracted and once not) instead of plotting the reference and image spectra independently.

Synchronization Issues As discussed above, most sweeping loops function by emulating button presses and waiting for completion (of a hardware move, or image exposure, ...). This has led to significant synchronization issues; the looping thread emulates a button press, which must be handled by the main thread, which then inherently spawns a third thread which is what the looping thread must wait for. Often, this has been accomplished by waiting a small period of time after the button press emulation before waiting on the other thread which is assumed to have begun. However, this has led to problems for short activities (such as short exposures or small moves of the QWP) where the wait is longer than it takes for the third thread to spawn and finish its activity, or when the computer is slow and the wait is still not enough time to spawn the third thread. The former issue puts a lower limit on how short of exposures can be safely used for looping, while the later can result in fewer images collected than requested as the sweeping thread mis-counts how many threads have executed.

When setting up the looping functionality, image collection could most easily be achieved by calling the `BaseExpWidget.takeImage()` function, or the `BaseExpWidget.doExposure()` function directly. `doExposure` starts an image acquisition from the camera and would be synchronous with looping, since it will wait for the image to finish, but `takeImage` does extra preparation, such as disabling some elements, and resetting FEL pulse counting statistics. Therefore, `takeImage` is called, which results in the present synchronization issues.

Programming Project: *Fix synchronization issues when performing loops*

One method to fix these issues is to call `doExposure` instead. This would require separating the acquisition preparation from the thread functionality in `takeImage`, and taking care to not change UI elements in different threads.

Programming Project: *Add better code reusage in looping functions*

Another significant improvement which could be done for loops is to reuse some of the identical code chunks. Each loop added to the software was done with very little time where it was faster to copy and paste a previous loop and simply change what happens after one set of images is taken. A better way would be to improve the Consecutive Images functionality to fix the synchronization issues above. Then, each looping function could call this function, instead of changing each loop directly. The code written for University Regensburg, which is in the 'regensburg' branch of the Github repository, attempted to fix several of these issues.

Spectrometer issues There are two significant issues which happen with the spectrometer which are worth pointing out. The first is a long-standing bug, which I have not been able to figure out. When communication with the spectrometer is started, the current wavelength and grating value are queried to update the UI. Unfortunately, an error occasionally occurs (it is unclear what the error actually is). It is a very rare issue, and not easily reproducible, and the only notice is the command prompt will loudly exclaim their might be an error. Reopening communication, such as by selecting 'None' or 'Fake' as an instrument, have always fixed the issue.

The second significant issue is a hardware problem where the grating shifts slightly from the set position either when it is first told to go to a wavelength, or even spontaneously after previously moving to the correct position. Again, this issue is also discussed in Appendix A, section A.5.5.

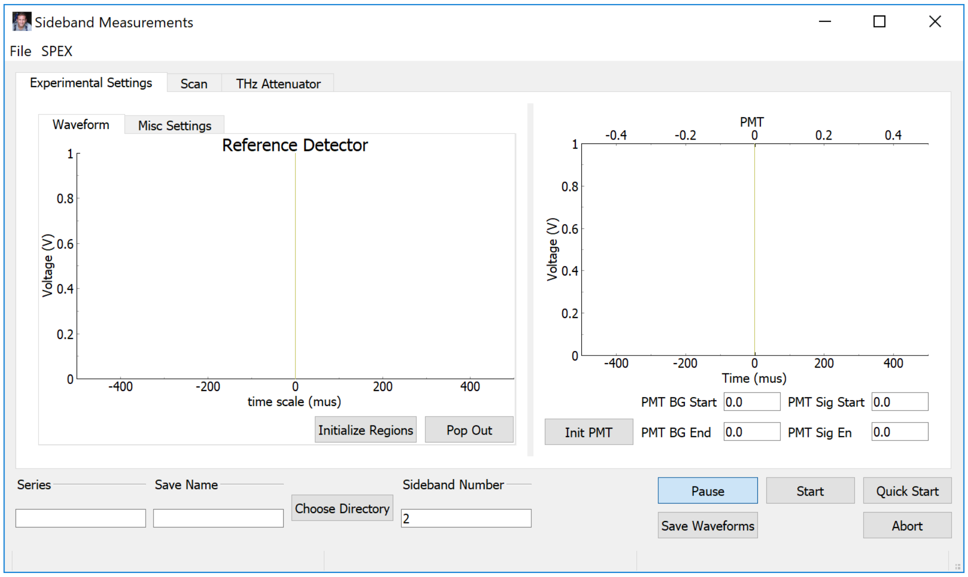

PMT BG Start 0.0

PMT Sig Start 0.0

PMT BG End 0.0

PMT Sig En 0.0

Sideband Number 2

Figure C.4: View of the front panel of the PMT/SPEX software for measuring sidebands. The left panel is the reference pyroelectric detector and the right is the voltage from the PMT.

C.2 PMT/SPEX Software

Measuring sidebands close in frequency to the NIR laser requires higher rejection than possible with the Acton Spectrometer. Instead, the SPEX spectrometer is used with a PMT has a detector. The software for controlling these two items is far less complicated than the EMCCD software. The main software is shown in Fig. C.4.

C.2.1 Standard Usage

Operation of this software is straightforward. On the left side of the software, the oscilloscope control and readback for the pyroelectric detector can be seen, which is identical to what is used in the EMCCD software and discussed in Sec. C.3. The right side shows the oscilloscope channel for the PMT and controls for boxcar integration.

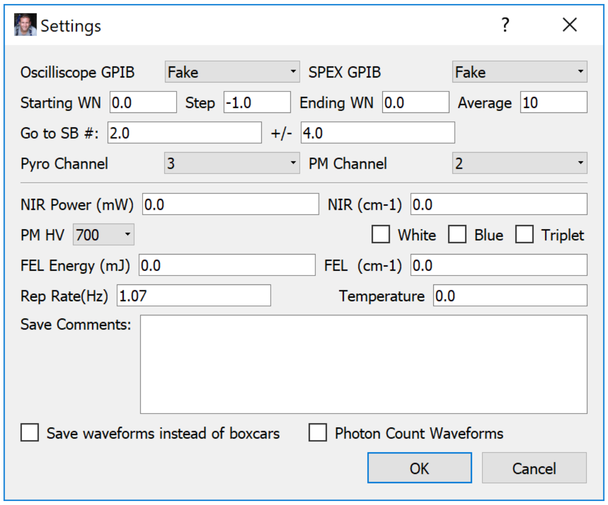

Oscilliscope GPIB: Fake
SPEX GPIB: Fake
Starting WN: 0.0
Step: -1.0
Ending WN: 0.0
Average: 10
Go to SB #: 2.0
+/-: 4.0
Pyro Channel: 3
PM Channel: 2
NIR Power (mW): 0.0
NIR (cm-1): 0.0
PM HV: 700
☐ White ☐ Blue ☐ Triplet
FEL Energy (mJ): 0.0
FEL (cm-1): 0.0
Rep Rate(Hz): 1.07
Temperature: 0.0
Save Comments:
☐ Save waveforms instead of boxcars
☐ Photon Count Waveforms

Figure C.5: The settings available to the SPEX/PMT software.

To start, the settings for the experiment should be entered by clicking File>Settings. The window shown in Fig. C.5 should appear. The GPIB addresses should default to the correct values. The next line ("Starting WN"...) specify the frequencies over which the SPEX should sweep for a single sideband, in wavenumbers (cm^{-1}). If the NIR and THz frequencies are entered below, the "Go to SB #" will calculate the correct bounds for the frequencies for the specified sideband. The next line specifies which channel of the oscilloscope the pyroelectric detector and the PMT are connected to.

The "PM HV" menu specifies the voltage of the power supply on the PMT, while the "White", "Blue" and "Triplet" checkboxes are used to indicate which filters are in place. The software will scale the data by the calibrated transmission of the filters or gain from the PMT power supply voltage.

Programming Project: *A 1kV potential on the power supply is a factor of 10 gain* *over 700V. According to the manual, 700V is a gain of 10 over 500V. Adding support for 500V could allow for fewer filters in place.*

Programming Project: *The software relies on the user correctly updating the voltage when the hardware is changed. It could be useful to have the software confirm it is correct, or set the voltage directly to prevent user errors.*

The settings for the FEL will update the corresponding values in the oscilloscope settings of the main window.

The two bottom-most checkboxes control different experiment conditions which are often not used. “Save waveforms...” will save the raw waveforms pulled from the oscilloscope instead of only the boxcar integrated values. However, it does not sweep the frequency.

“Photon count waveforms” will not integrate the waveforms, but instead attempt to count discrete peaks in the signal due to single photon events. This settings is only physically meaningful for the 1 kV setting where photons can be individually distinguished.

After settings have been specified, data collection with the software occurs on the main window of the software (Fig.C.4). “Choose Directory” specifies the base directory where data should be stored. “Save Name” obviously specifies the save name of the files, but it will create a subfolder within the chosen directory, as well as prepending file names with the save name. The “Series” textbox provides a place to put a series tag, similar to the EMCCD software; data sets with the same series tag will be processed together, and the same sideband number and series tag will be averaged together.

In the PMT graph, there are two movable regions to select the data (green region) or background (red region) for boxcar integration (the “Init PMT” button will move both regions to the center of the data, a legacy from when the data was offset by the advance trigger). The text boxes below allow moving the regions to specific values. Typically, the data boxcar is set to a width of 100 ns for cavity dumped experiments, which should fully enclose the CD signal.

The “Save Waveforms” will save the current waveforms (both PMT and reference detector, to separate files). It saves them in the base directory specified, with the filename specified by “Save Name”. It will append `referenceDetector` and `signalWaveform` to distinguish them, and auto-append a counter to prevent overwriting files.

Starting a scan can be done with “Start” or “Quick Start”. Quick start will immediately being a scan with the settings specified in the settings dialog (Fig. C.5). “Start” will bring up a dialog to easily modify the often changed settings to make data collection more efficient.

While a scan is performed, the “Scan” tab will show the current progress as a black trace. It will automatically calculate the average of the current number of pulses and display the trace. The statusbar of the window will display a message `wnCurr/wnEnd. No.  H(M)/T`, where `wnCurr` is the current wavenumber, `wnCurr` is the final wavenumber of the scan, `H` is how many FEL pulses have been counted at this wavenumber, `M` is the number of misses (legacy from when the FEL would frequently miss pulses) and `T` is how many hits are desired for the wavenumber.

When a scan is complete (or “Abort” is pressed), the data is automatically saved. The filename includes the “Save Name” and appends the sideband number and a counter for how many files have been saved. The first line in the save file is the sideband number, which is used for data processing. The “Scan” tab will add a new curve for the completed scan, including error bars (calculated as the standard error of the mean).

A final useful tool is the ability to open the SPEX controls directly, under the “SPEX” menu, “Open SPEX Settings”. Here, the SPEX can be sent to a specific wavenumber (such as for aligning). If the wavelengths of the lasers are provided to the software settings, it can go directly to sideband numbers. The GPIB control is greyed out, as it is controlled by the other settings page.

Whenever the SPEX loses power, its memory is cleared and it needs to be re-initialized and told what wavelength it is currently at. In the SPEX window, the File>Initiate SPEX option does this initialization. When prompted, enter the wavenumber the SPEX is at, which is on the dials on the side of the instrument. Enter the number exactly as is, and the software will handle the ~ 4.2 cm^{-1} offset.

C.2.2 Known bugs/workarounds

The code for the SPEX and PMT is significantly less complicated than the EMCCD, and it has fewer significant bugs. One of the issues is the poor handling of the attenuator, similar to the EMCCD software. If the device is not opened, it will give incorrect FEL parameters and does not warn the user.

One minor issue arises where the software will not recognize the wavelengths input, preventing the "goto SB #" functionalities. I believe the error occurs after restarting the software, and the wavelengths being reloaded as strings and not floats. The easiest fix is to re-enter the wavelengths in the settings tab.

One significant bug which has happened (only once that I am aware of) involved the SPEX no longer accepting commands. Any command issued was not recognized and no response was received. In the end, it was determined that the ASCII commands sent to the SPEX were terminated with a carriage return and new line (`\n\r`). While this worked for a long time, the SPEX stopped accepting this and only carriage returns were allowed. The software has been corrected to use the correct line endings.

C.3 Pyro OScope

C.3.1 Standard Usage

The final significant piece of code used during data collection is the oscilloscope software, which monitors the FEL during experiments and is used by both the EMCCD and SPEX software.

The software requires three regions be specified in the pulse for calculating characteristics of each pulse. Shown in the left of Fig. C.6, the red region should highlight the background of the pyro (the DC offset before the pulse), the blue region should cover the front porch (FP), and the green should cover the cavity dump (CD). The end of the front

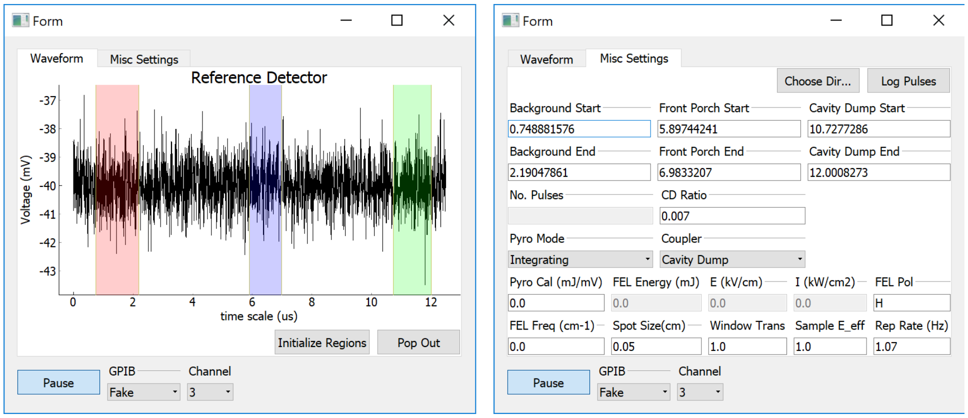

GPIB: Fake
Channel: 3

Background Start: 0.748881576
Front Porch Start: 5.89744241
Cavity Dump Start: 10.7277286
Background End: 2.19047861
Front Porch End: 6.9833207
Cavity Dump End: 12.0008273
No. Pulses:
CD Ratio: 0.007
Pyro Mode: Integrating
Coupler: Cavity Dump
Pyro Cal (mJ/mV): 0.0
FEL Energy (mJ): 0.0
E (kV/cm): 0.0
I (kW/cm2): 0.0
FEL Pol: H
FEL Freq (cm-1): 0.0
Spot Size(cm): 0.05
Window Trans: 1.0
Sample E_eff: 1.0
Rep Rate (Hz): 1.07
GPIB: Fake
Channel: 3

Figure C.6: (Left) Main panel of the oscilloscope widget. The Red, blue and green regions depict the background, front porch, and cavity dump portions of the pulse, respectively. (Right) All of the settings available to control pulse counting.

porch region should extend to directly before the large jump from the CD signal, but the front portion can be placed anywhere within the FP signal. The CD region should be placed to start directly after the spike from the CD. Similar to the PMT software, the “Initialize Regions” button will move the regions to the center of the data. “Pop Out” will create a new window with the oscilloscope trace alone. The window will be borderless and float on top of all other windows (move the window by holding `Shift` before dragging the window with the mouse). This is a useful tool to allow the pyro trace to be monitored at all times during experiments.

On the settings panel (right of Fig. C.6), there are six text boxes to provide the positions for the pulse regions, if desired. The “CD Ratio” is a value used for controlling whether a trace from the pyro counts as a pulse or not. The value (in volts) specifies the minimum height of the cavity dump region to count as the FEL successfully firing. This prevents the code from breaking or logging missed pulses. The comparison with the cavity dump signal, instead of the front porch, can be useful for occasions when the CD

YAG laser fails and the FEL pulses, but the cavity dump does not actually occur.

The “Pyro Mode” drop-down tells the software whether the pyro is in the slow, integrating mode (where the time constant of the detector is much longer than the FEL pulse) or an instant mode (where the time constant is shorter than the pulse time scale).

The “Coupler” drop-down changes whether the FEL is operating with the hole coupler (HC) or the cavity dump coupler. When using the HC, the blue region on the pyro trace is hidden (since there is no longer a front porch). The green region should then be placed at the end of the trace, which determines the amplitude of the pulse. The waveform is fit to a Sigmoid function to extract the width of the pulse.

The “Pyro Cal” text box should contain the calibration parameter for the pyro, which is sensitive to FEL frequency and alignment. It is found by using the Pyro Calibration software, which measures the voltage on the pyro and the energy measured from the TK.

The “FEL Energy” is the energy (in the cavity dump portion, not including the front porch) in a given pulse. The field strength and intensity are calculated using the spot size and field factors specified in the bottom row. “FEL Pol” is a field stored in data files for the FEL polarization. The “FEL Freq” is similarly only a stored value.

The spot size should be specified after measured with the Pyrocam or some THz-sensitive camera. The “Window Trans” is measured with the VNA, and the “Sample E_eff” is the effective field enhancement, again measured by the VNA.

Programming Project: *Both the window transmission and field enhancement are measured and stored as text files. It is possible that the FEL Freq information could be* *used to look up this information and populate the fields automatically.*

.

Finally, every pulse can be logged to a file. The “Choose Dir...” (a misnomer for what should be Choose File...) specifies which file data should be logged to. However, data is not saved until “Log Pulses” is toggled on.

C.3.2 Details on code

One of the most important parts of this software is calculating parameters of the FEL pulse. For the cavity dump, the front porch region is fit to a line. The start of the pulse is defined by where this line intersects with the background (as specified by the red region). The end of the pulse is the end of the specified front porch region. This is why the front edge of the pulse does not significantly matter (as long as enough of the pulse is included for a good linear fit), but the end of the region is significant. The cavity dump region should be selected within a small region directly after the pulse, as the average of the specified region is taken as the value for the cavity dump.

The pyro is calibrated with the TK, which provides the total energy in the pulse. Only the CD portion is of interest, so the energy in the CD is calculated by the ratio of the voltage in the CD vs FP.

For either the CD or the HC, the software needs to be aware of the wiregrid attenuator. Often the pyro oscope software is slaved to the EMCCD or SPEX/PMT software. When the pyro software is started, it checks whether is is initialized as a part of either of these software packages. If it is, the pyro keeps a reference to the FEL attenuator to include that attenuation in the calculations.

C.3.3 Known bugs/workarounds

There are, unfortunately, several known bugs for this software which have eluded squishing. One straightforward one which must be kept in mind is that the pulse logging is not saved when the software is restarted. The "Log Pulses" button must be re-enabled.

The physical oscilloscope will often display an empty screen when the software is communicating with it. This is an artifact of the oscilloscope communication protocol, wherein the software must tell the scope to begin waiting for a trigger event (which clears the screen) then the software waits for the oscilloscope to be triggered. Once a trigger is received, a readout occurs and immediately renews the waiting period. This means the physical scope is often cleared. I have not found a way to fix this.

Another communication error I have been unable to figure out causes the software to stop communicating with the scope. This is often accompanied by the physical scope displaying an error of 'Unterminated Query'. I have yet to figure out why this error occurs, but it unfortunately causes the software querying threads to crash. To fix it, the GPIB address should be changed to None before set to the correct device.

The hole coupler mode has some minor quirks which have persisted since it is not often used. The background and signal regions should be set to the edges of the region, and the scope must be set to 500 ns/div. If this is not done, the pulses will not be fit, and

I am not sure why. Furthermore, the fitting routine is rather slow (noticeably slowing the computer) when there is no pulse. It could be possible to resolve this by first coarsely checking if the pulse is valid before doing the numerical fitting routine.

As a final note, the 'Integrating' mode is not thoroughly tested for either the HC or CD. Use with caution.

C.4 HSGAnalysis

In addition to collecting all of the data, significant code has been written to process all of the data, contained in the `HSG-turbo` GitHub repository. Going through all of the code is a several hundred page document in itself, so here I will try to outline some of the most important functions, and the interested user can follow the code to learn more details.

One of the best places to start for understanding how all of the code works together is the `proc_n_plotCCD` function, which is also typically the first function called when processing a data set. When passed a folder of CCD data, the function will open all the data files and load them, find and fit the sideband peaks, all of which is done as a part of the `HighSidebandCCD` class and its methods.

The next function to consider is `hsg_combine_spectra`, passing it the list of `HighSidebandCCD` objects returned by `proc_n_plotCCD`. In typical experiments, several different experimental conditions are measured (such as laser powers or frequencies, temperatures, polarizations, etc., which are denoted in the 'Series' portion of the data collection). For each experimental condition, there can be multiple CCD images taken at different wavelength ranges (or center wavelengths on the Acton Spectrometer, denoted by the ‘Spec step’ portion of the software). `hsg_combine_spectra` parses the list of `HighSidebandCCD` objects and combines data sets. It begins by combining all of the data sets with the same series tag. It then orders these sets by increasing spec step, and combines the spectra together (the workhorse of which is done by `stitch_hsg_dicts`).

If PMT data is taken, it can be processed in the aptly named `proc_n_plotPMT`. To combine PMT and CCD together, the objects returned from `hsg_combine_spectra`, which are now `FullHighSideband` objects, have an `add_pmt` function, which will add the PMT data and renormalize the data sets to overlap the sideband conversion efficiencies. Note that, as this is not a commonly done procedure (since a full PMT data is not often taken), there is not a stock function which compares the series tag of the CCD data with the PMT data and adds them automatically. The processing script must manually ensure that the proper CCD data sets are added together.

Appendix D

Pulsed Polarimetry

In order to measure the polarization of the sidebands, a full Stokes polarimeter needed to be designed and implemented. Most of the inspiration came from Ref. [37]. Chapter 16 has a discussion of building a Stokes polarimeter, and Chapter 15 has sections on measuring the optics which compose the polarimeter. I'll briefly discuss the operation and caveats of polarimetry, and some of the nitty-gritty details of aligning/ calibrating/ troubleshooting our polarimeter.

D.1 Stokes vectors and Mueller calculus

To begin, I'll re-emphasize some of the important characteristics of Stokes vectors and its corresponding matrix space with Mueller matrices. The standard Stokes vector is defined as,

$$\vec{S}_{\text{in}} = \begin{pmatrix} S_0 \\ S_1 \\ S_2 \\ S_3 \end{pmatrix} \tag{D.1}$$

with S_0 the intensity of the light, S_1 the horizontal/vertical component, S_2 is the ±45° component, and S_3 is the left hand circular (LHC)/or right hand circular (RHC) component. Mueller matrices are 4×4 matrices used for describing how an optical element will change a Stokes vector. Important examples of Mueller matrices are an arbitrary wave retarder of retardance δ with a fast axis at an angle θ given by,

$$\mathbf{M}_R = \begin{pmatrix} 1 & 0 & 0 & 0 \\ 0 & \cos^2(2\theta) + \cos(\delta)\sin^2(2\theta) & \cos(2\theta)\sin(2\theta) - \cos(2\theta)\cos(\delta)\sin(2\theta) & \sin(2\theta)\sin(\delta) \\ 0 & \cos(2\theta)\sin(2\theta) - \cos(2\theta)\cos(\delta)\sin(2\theta) & \cos(\delta)\cos^2(2\theta) + \sin^2(2\theta) & -\cos(2\theta)\sin(\delta) \\ 0 & -\sin(2\theta)\sin(\delta) & \cos(2\theta)\sin(\delta) & \cos(\delta) \end{pmatrix} \tag{D.2}$$

and the matrix for a linear (horizontal) polarizer:

$$\mathbf{M}_H = \frac{1}{2}\begin{pmatrix} 1 & 1 & 0 & 0 \\ 1 & 1 & 0 & 0 \\ 0 & 0 & 0 & 0 \\ 0 & 0 & 0 & 0 \end{pmatrix} \tag{D.3}$$

Sending light through various optical components is equivalent by matrix multiplying the matrices and the input Stokes vector. For example, the resulting Stokes vector after propagating through a retarder followed by a horizontal polarizer is given by

$$\vec{S}_{\text{out}} = \mathbf{M}_H \mathbf{M}_R \vec{S}_{\text{in}} \tag{D.4}$$

Since the final element is a horizontally oriented polarizer, only the S_0 and S_1 parameters are nonzero, but not necessarily equal if the light is not perfectly polarized. If the intensity of the light is measured after these optics, the resulting $\left(\vec{S}_{\text{out}}\right)_0$ would be given by,

$$\begin{aligned}\left(\vec{S}_{\text{out}}\right)_0 =& S_0 + \frac{S_1}{2}(1+\cos(\delta)) - S_3\sin(\delta)\sin(2\theta) + \\ & \frac{S_1}{2}(1-\cos(\delta))\cos(4\theta) + \frac{S_2}{2}(1-\cos(\delta))\sin(4\theta)\end{aligned} \tag{D.5}$$

Equation D.5 is the fundamental equation in doing Stokes polarimetry in our lab. We send our light through a rotating retarder, then a polarizer (called the analyzer), and measure the resulting signal as a function of the retarder rotation angle. I've termed such a plot of intensity vs. retarder angle a "polaragram". Fitting the polaragram to Eq. D.5 then extracts the full Stokes vector. One caveat is the choice of wave retarder; a quarter-wave plate ($\delta = 0.5\pi$) or a half-wave plate ($\delta = \pi$) are standard optics. A half-wave plate cancels the S_3 term in Eq. D.5, making you insensitive to circular polarization, so a quarter-wave plate is required for a complete extraction of the Stokes parameter.

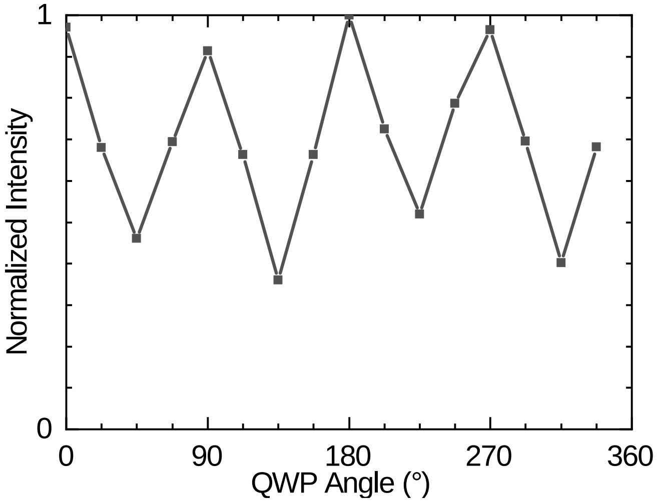

Figure D.1: Example polaragram for the NIR laser. Y-axis shows the normalized intensity after passing through the QWP followed by a horizontal polarizer. The x-axis is the angle the QWP fast axis makes with respect to horizontal in the lab frame. The backed out polarization state is $\alpha = 89.1 \pm 2.7°$, $\gamma = 2.3 \pm 1.3°$. According to the PAX, the polarization state was $\alpha = 87.0°$, $\gamma = 0.2°$.

Figure D.1 shows a typical plot of intensity of light after a horizontal polarizer as a function of QWP rotation angle, a "polaragram". The fit to Eq. D.5 is shown.

D.2 Polarization Ellipse and Jones Calculus

To describe perfectly polarized light, we make use of the polarization ellipse, see Fig. D.2. To determine if light is perfectly polarized from a Stokes vector, the degree of polarization (DOP) can be calculated,

$$\mathrm{DOP} = \frac{\sqrt{S_1^2 + S_2^2 + S_3^2}}{S_0} \tag{D.6}$$

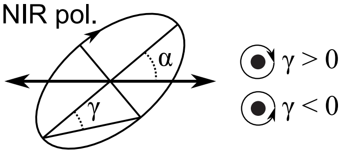

Figure D.2: Definition of parameters of the polarization ellipse. α is the angle of the major-axis of the ellipse, γ is the ratio of minor- to major-axis, also called ellipticity. The sign of γ encodes left handed versus right handed polarizations.

where DOP=0 corresponds to unpolarized, and DOP=1 is fully polarized. If the light is perfectly polarized, α and γ can then be calculated from,

$$\tan(2\alpha) = \frac{S_2}{S_1} \tag{D.7}$$

$$\tan(2\gamma) = \frac{S_3}{\sqrt{S_1^2 + S_2^2}} \tag{D.8}$$

While measurements are done to find the Stokes vector, we end up using the Jones calculus in practice. A Jones vector is a 2 component complex vector describing the electric field,

$$\vec{J} = \begin{pmatrix} E_x \\ E_y \end{pmatrix} \tag{D.9}$$

It is only valid when the light is perfectly polarized, while Stokes vectors are valid for partially/unpolarized light. Calculating a Jones vector if α and γ are known is possible from,

$$\vec{J} = \begin{pmatrix} \cos\alpha & -\sin\alpha \\ \sin\alpha & \cos\alpha \end{pmatrix} \begin{pmatrix} \cos\gamma \\ i\sin\gamma \end{pmatrix} \tag{D.10}$$

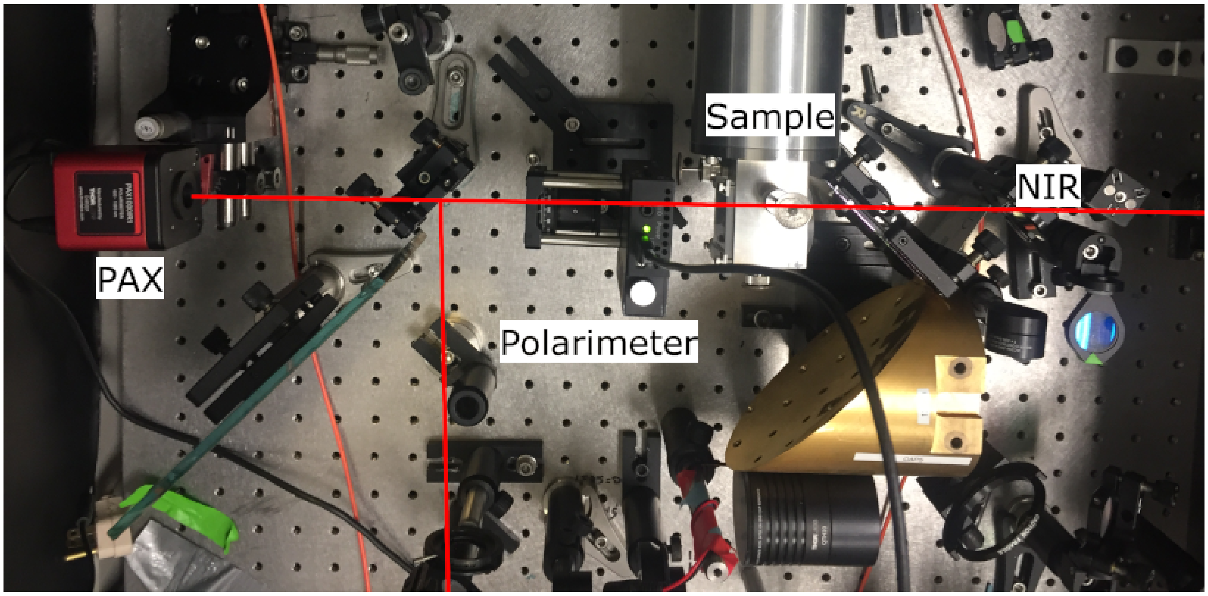

Figure D.3: Image of our optics table around the sample. Shows the rough size of our polarimeter (screw spacing on the table is 1"). The mirror after the polarimeter is on a kinematic magnetic mount which snaps in and out of place, allowing measurement of the NIR polarization with the PAX.

D.3 Experimental Implementation

Figure D.3 shows the polarimeter built at UCSB on our optics table. It is composed of an automated Thorlabs rotation stage (K10CR1), fitted with an achromatic QWP (AQWP05M-980). Cage mounts mount a glan-laser polarizer directly behind it. Python3 software has been written which interfaces the rotation stage with the CCD collection software to handle rotating the QWP while taking HSG images. It is also important to note that **no** optical component can be placed between the QWP and polarizer.

We've also purchased an off-the-shelf polarimeter from Thorlabs (the PAX instrument). It is used to measure the NIR laser more quickly than our home-built polarimeter can measure it, as well as more accurately. The PAX is better calibrated than our system,

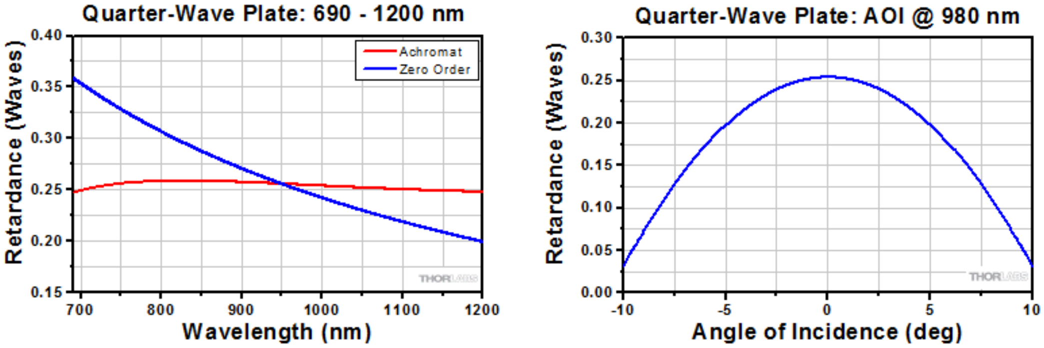

Figure D.4: (Left) Example retardance of the AQWP used in our experiments. (Right) The retardance as a function of angle of incidence.

for reasons discussed in Sec. D.4 below, but has provided a good check when testing our system. The PAX requires a monochromatic light source, and is not able to pull spectral information from sidebands directly; it purely serves to help calibrate the home-built polarimeter, and quickly determine the NIR polarization during experiments.

D.4 Pitfalls of Polarimetry

Before discussing how to calibrate and align the polarimeter, it is helpful to understand some of the difficulties of polarimetery to know how to work with a polarimeter and troubleshoot it. Two of the biggest issues with polarimeters relate to the angle of incidence of light on the QWP/polarizer, and the deviations of the QWP from $\delta = \pi/2$. From Thorlabs, the specified retardance of the QWP used at UCSB has a wavelength dependence shown in Fig. D.4. While it is close to $\delta = \pi/2$, it does deviate. Furthermore, the retardance is very sensitive to angle of incidence, as also shown in Fig. D.4.

In theory, one can measure $\delta(\lambda)$, the retardance as a function of wavelength and using that in Eq.D.5. This is discussed in Sec. D.5.3, but has difficulties (at least in our setup). The AOI dependence seems to be resolved by using the back reflected (BR) light off the surface of the QWP to ensure a normal AOI.

D.5 Aligning and Calibrating the Polarimeter

One of the most important parts of a polarimeter is ensuring it is well aligned and calibrated. This section will finally describe all I've learned to ensure our polarimeter is aligned. Characterizing the polarimeter depends heavily on the NIR laser and the PAX, as well as the white light source which must be made co-linear with the NIR. The general procedure involves putting a polarizer into the sample position of Fig. D.3, and potentially a retarder to add ellipticity. The NIR laser can be used with the PAX to align the polarizer and retarder at specific wavelengths, while the white light allows characterizing across a wide spectral range. Unfortunately, the white light does not follow the NIR beam path exactly, which limits the trustworthiness of its results, and a large number of surface reflections leads to several Fabrey-Perot oscillations which add significant noise to backed out values when using the white light.

D.5.1 Determining the fast axis

The first step of aligning the polarimeter is determining the fast axis (FA) of the QWP. While the optic has the FA marked, it must be determined with respect to the home of the rotation motor. In short, the retarder is placed between two crossed polarizers and rotated to minimize the transmitted light, which occurs when the FA is parallel to one of the polarizer axes.

In practice, there's the question of how to cross two polarizers, as trivial as it sounds. Some of the possible ways in our setup:

- Set one polarizer, rotate the second to minimize the power of the NIR going through
- Set one polarizer, rotate the second to minimize signal on the CCD when using the white light
- Set one polarizer to 0° as defined by the PAX, and the second to 90° as defined by the PAX

I typically go with the final option; one of the polarizers is the analyzer, which is attached to the retarder, while the second is the sample position polarizer. Crossing the polarizers by the first two methods would require removing the retarder from the polarimeter to cross them, and then re-inserting the retarder. By using the PAX, the polarimeter mount can be snapped in and out to align each polarizer to the PAX. Ideally, a polarizer would be placed behind the polarimeter to cross them without relying on the PAX, but it does not fit in the current setup.

When the FA of the optic is misaligned, it results in a deviation of the measured α from the real by twice the deviation of the FA. That is, if the FA is off by 1°, the measured α's will be off by 2°. I use this as the final metric for ensuring the FA is fully aligned.

D.5.2 Angle of incidence

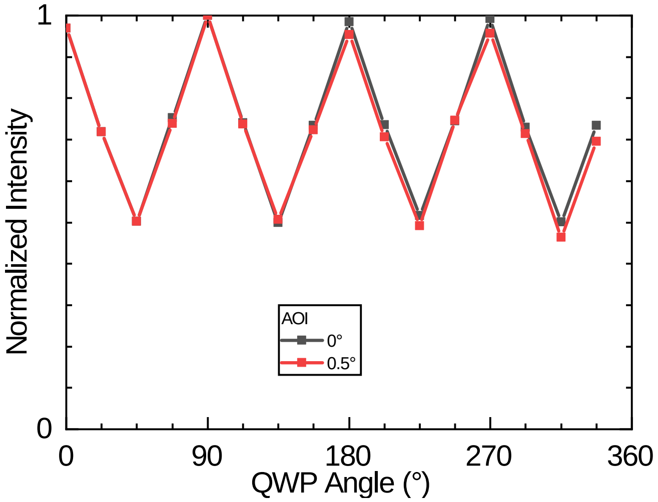

Figure D.5: Indication of angle of incidence issues with the polarimeter. The black curve shows the polaragram produced with a 0° angle of incidence on the QWP, while the red curve shows a 0.5° AOI, as measured by a back reflection. The 'tilt' of the peaks is a classic indication of an AOI misalignment. For the normal incidence, the measured angle was $\alpha = -0.6 \pm 0.9°$, $\gamma = -0.2 \pm 0.5°$, while the off-normal was $\alpha = -0.4 \pm 1.6°$, $\gamma = -0.4 \pm 0.8°$ (PAX: $\alpha = -0.5°$, $\gamma = 0.6°$). So while both were correct within error bars, the error bars are smaller on the normal incidence data.

As shown in Figure D.4, the retardance of a QWP depends heavily on the angle of incidence (AOI). Furthermore, the change in retardance is different whether the AOI deviation come from a tilt relative to the fast axis or slow axis. This results in complicated polaragrams, as depicted in Fig. D.5. Here, two polaragrams are shown, where the angle of incidence differs by 1° with respect to each other. The light is affected by the retardance due to a rotation about the slow axis, and then fast axis, as the QWP rotates, resulting in an overall slant or tilt to the polaragram. From eq. D.5, there should only be frequencies oscillating at 2θ and 4θ, and an AOI deviation results in components at other frequencies. Thorlabs PAX "Alignment Assistant" works on this principle to assist alignment.

In the home built polarimeter, the same process must be done; take polaragrams of linearly polarized light and ensure each peak is of equal height. After that, the back reflection off the surface of the optic can be used to more quickly determine a normal incidence. The one caveat with back reflections is that, due to imperfections in the mounting of the QWP, rotating the optic will trace out a cone of the back reflected spot. Thus, the optic must always be at the same angle (such as the fast axis aligned horizontally) when aligning to the back reflection.

Another caveat to angle of incidence is light entering the polarimeter should be collimated, otherwise there is again a slight angle of incidence on the beam. This is not strictly done in the current setup (as seen in Fig. D.3 due to space constraints). However, the focusing onto the sample is quite slow for standard experiments ($f = 500$ mm), and is hopefully a second order correction. If faster optics are used to achieve a smaller focus on the sample, there may need to be additional corrections in the polarimeter.

D.5.3 Backing out $\delta(\lambda)$

Chapter 15 in Ref. [37] discusses measuring the retardance of an optic. Start with vertically polarized light, and then send it through a retarder with fast axis aligned at 45°, and then a crossed (horizontal) polarizer. If the intensity with just the vertical polarizer is defined as I_D, and the intensity of the light with the retarder and second polarizer is I_{45}, the retardance of the optic is given by,

$$\delta = \cos^{-1}\left(1 - \frac{2I_{45}}{I_D}\right) \tag{D.11}$$

as calculated by the appropriate Jones matrices (I believe Goldstein either has a typo, or we disagree on the definition on I_D, and Eq. D.11 here has an additional 2).

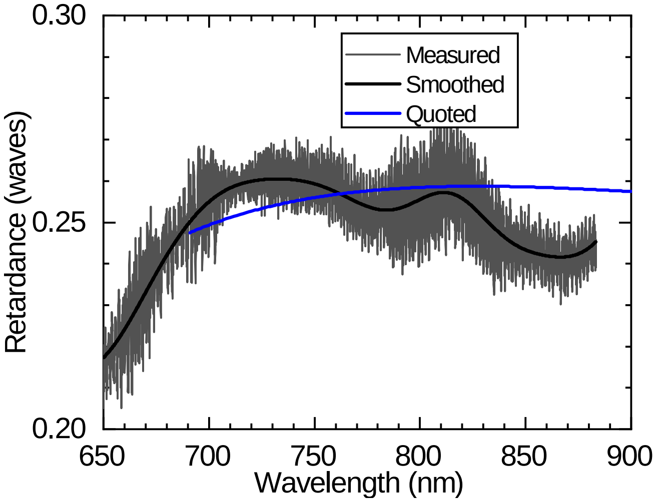

Figure D.6: Retardance of an achromatic QWP. The retardance measured in our setup and backed out using Eq. D.11 (gray). Significant Fabrey-Perot oscillations can be observed. An FFT filter was applied to smooth the data (black). Also shown is the expected retardance quoted from Thorlabs (blue).

This is not straightforward to measure in our spectrometer, especially across a large bandwidth. The first problem is the spectrometer is polarization sensitive, so the measurement of I_D and I_{45} require a half-wave plate to match the polarization to the spectrometer, which can slightly alter their intensities independent of the retarder under question. Furthermore, Fabrey-Perot oscillations between various optics in the setup add significant noise to the measurement. Figure D.6, thin grey curve, shows the measured retardance calculated from Eq. D.11. Significant oscillations are seen with two characteristic frequencies corresponding to cavity lengths of 1.3 mm and 0.13 mm in air (n=1). Smoothing through liberal applications of an FFT low-pass filter is overlain in black. Also shown is the quoted retardance provided by Thorlabs, calculated from the material parameters of the optic.

To compare the difference of an assumed ideal QWP versus the measured, Fig. D.7 shows the backed out α, γ and DOP. The dependences of these figures of merit on the retardance are not straightforward. For Fig. D.7, a white light was coupled through the setup following the NIR beam path. A polarizer was inserted directly before the polarimeter, and a (nonachromatic-)waveplate was optionally placed after the polarizer. The polarization of the white light was measured in an arbitrary frequency range, and

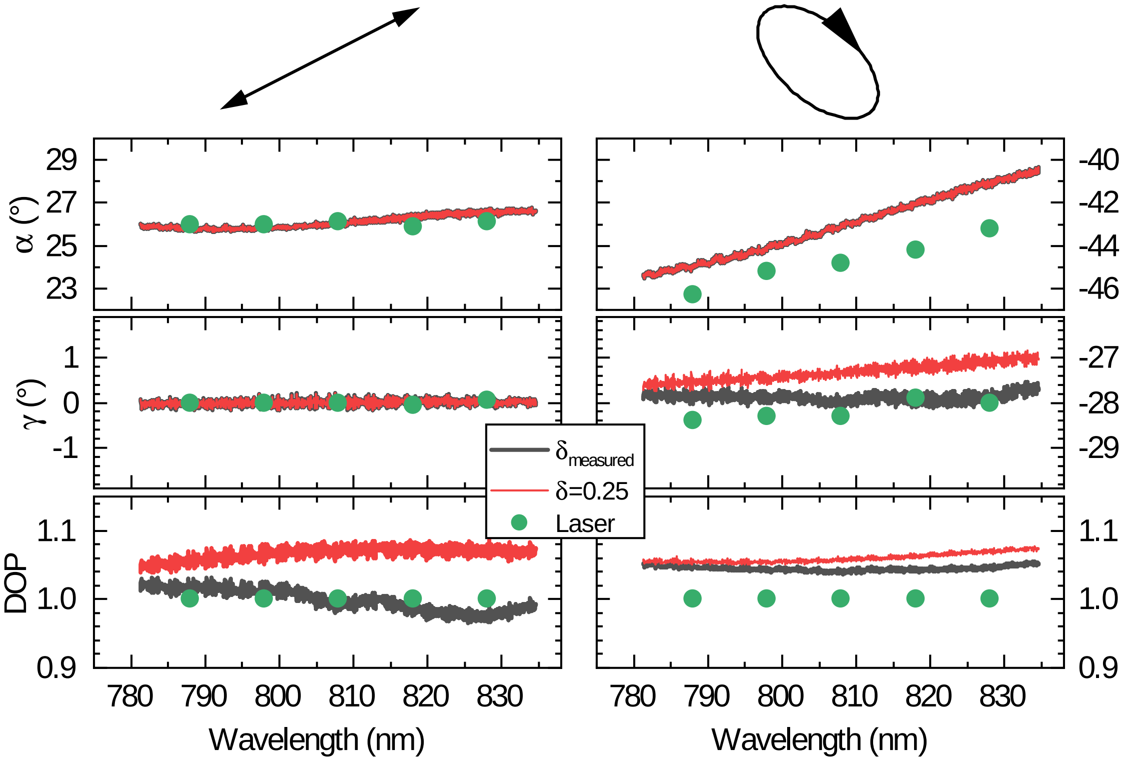

Figure D.7: Polarimetry results depending on the retardance used in Eq. D.5. Two different polarization states were measured, and are depicted schematically at the top of the figure. (Left) Linearly polarized light at $\alpha \approx 26°$. (Right) Elliptically polarized light at $\alpha \approx -43°$, $\gamma \approx -28°$. The backed out α, γ, and DOP are plotted below. The red curve shows the backed out values when $\delta = 0.25$ is used in Eq. D.5, while the grey uses the values shown in Fig. D.6. The green dots in the α and γ plots show the measured value of the NIR laser at the specified wavelengths for comparison.

two states are shown in Fig. D.7. The left side shows linearly polarized light at $\alpha \approx 26°$, while the right side shows elliptical polarization of $\alpha \approx -43°$, $\gamma \approx -28°$, with slight dispersion due to the non-achromaticity of the wave plate used. The states at a few select wavelengths was confirmed using the NIR laser and the PAX instrument, plotted as the green dots for the α and γ data. The DOP for the laser was 1 ± 0.01. The polarization states were calculated in two ways; the first assumed $\delta = 0.25$ in Eq. D.5 (red curves) while the second used the measured values from Fig. D.6 (grey curves). The top plot shows the measured α angle. For the linearly polarized case (left), the two different measurement methods are nearly identical, and agree with the laser within $< 0.5°$. The same is true of the γ angle. A clear difference between the two, however, can be seen in the DOP. Here, the measured value is closer to the laser line, and also is more physically reasonable, since DOP> 1 has no significance.

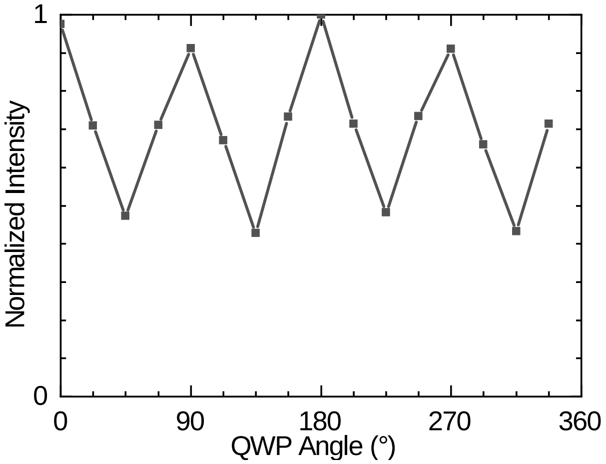

Figure D.8: Example polaragram using one of Thorlabs' superachromatic quarter-wave plates in the polarimeter. According to the PAX, the NIR laser was polarized with $\alpha = -2.3°$, $\gamma = -0.1°$. The light was linearly polarized, but the peaks when the QWP was set to 0° or 90° were unequal. While this type of polaragram is expected for slightly elliptical light ($\gamma = 1.5°$), the expected polaragrams for linearly polarized light were never observed.

The results are slightly different when considering elliptical light (Fig. D.7, right). The α angles again agree exactly whether $\delta = 0.25$ or the measured values. However, they both seem to be $\sim 2^\circ$ from the laser line. It is unclear exactly why this is the case, though a likely culprit may be the imperfect matching of the white light beam path to the laser's beam path. With finite ellipticity, the two backed out γ values do not agree as they did in the linear case. Assuming $\delta = 0.25$ results in a slight dispersion, while the backed-out γ using Fig. D.6 produces much better agreement with the laser data than the $\delta = 0.25$ assumption. Finally, the DOP is slightly better with the measured value of δ, though it is still slightly above the physically meaningful 100% degree of polarization. It is not immediately clear why this result is occurring. One solution might be to use a constrained fit of the polaragrams to Eq. D.5 such that the degree of polarization is $\leq 100\%$.

As an aside, the Thorlabs PAX documentation claims a zero-order QWP is easier to calibrate and is less sensitive to angle of incidence deviations, relative to an AQWP. This has not been tested here. However, it should be pointed out that Thorlabs' "Super-achromatic" quarter-wave plates (SAQWP) are not suitable for polarimetry (at the time of writing). Figure D.8 shows a measured polaragram for the NIR laser where the state determined by the PAX is given by $\alpha = -2.3^\circ$, $\gamma = -0.1^\circ$. For linearly polarized light, all four peaks at $\theta = 0^\circ,\ 90^\circ,\ 180^\circ$, and 270° should all be equal. It is unclear exactly why they are not, but it is a result common to all SAQWPs and makes them unfit for polarimetry. Furthermore, the SAQWP introduced a lateral displacement of the beam, which significantly affected the alignment of the beam as a polaragram was measured.

D.5.4 Analyzer direction

Equation D.5 assumes the analyzer is aligned horizontally. A vertical analyzer can also be used (but take care to derive the new equation, a few signs will change). Figure D.9 shows the backed out polarization states for two different input polarizations for a vertical or horizontal analyzer. Similar to Fig. D.7, a white light was sent into the polarimeter

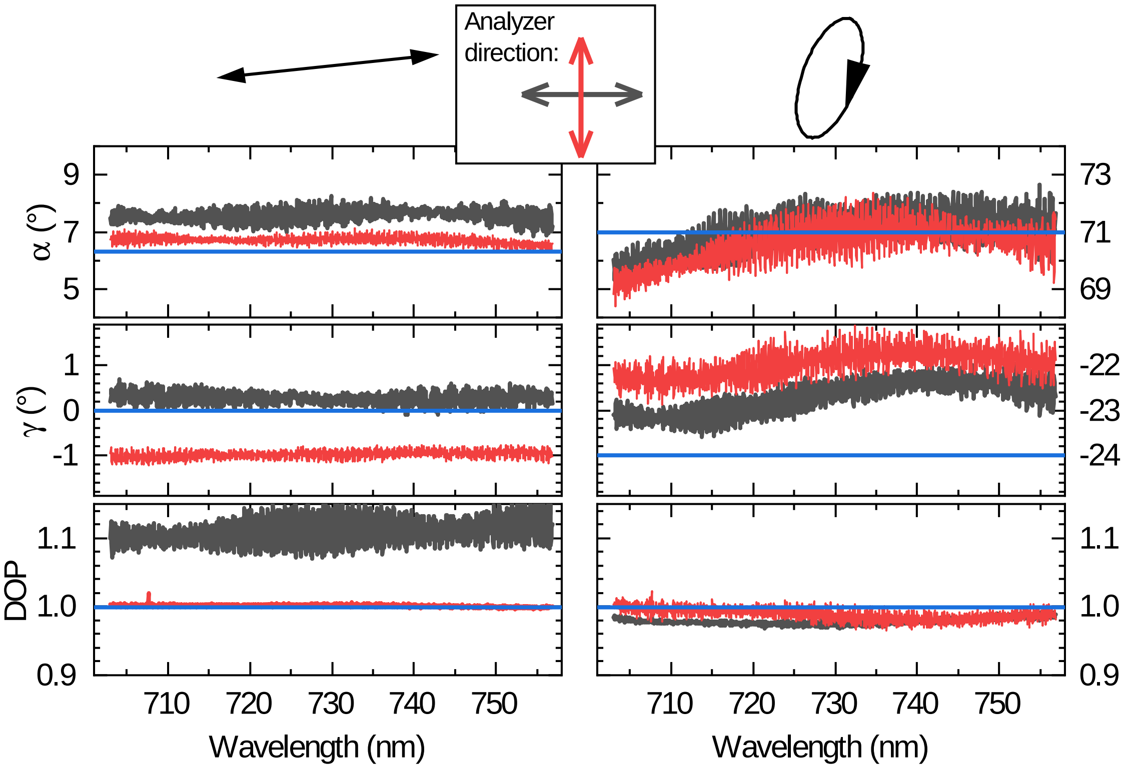

Figure D.9: Polarimetry dependence on analyzer direction for white light. Two polarization states were measured. (Left) Linearly polarized light at $\alpha = 6.3°$, $\gamma = -0.1°$. (Right) Elliptically polarized light at $\alpha = 71°$, $\gamma = -24°$. The grey curves are the backed out α (top), γ (middle), and DOP (bottom) show the results for a horizontal analyzer, while the red curves are the results for a vertical analyzer. For a perpendicular (to the major axis of the incident light) polarizer provides slightly better results for linearly polarized light, but the results are less drastic for elliptically polarized light.

with only a linear polarizer to produce perfectly linear polarization (left side fig. D.9), or with an additional achromatic QWP at an angle to produce an arbitrary elliptical state (right side fig. D.9). The polarimeter was operated with the the analyzer aligned horizontally (grey curves) with fits done with Eq. D.5, or a vertically aligned analyzer (red curves) which required fits to a modified version of Eq. D.5. These measurements were performed using Thorlabs' SAQWP in the polarimeter before the issues discussed at the end of Sec. D.5.3 were discovered, but the results are consistent when a standard achromatic QWP is used. To calculate these angles it was assumed that $\delta = 0.25$ as it had not been measured for this optic.

For the linearly polarized light, the α angle was more accurate when the analyzer was near-perpendicular to the input polarization, while the γ angle was slightly more accurate when the analyzer was near-parallel. The DOP, however, was quite good when the analyzer was near-perpendicular to the input polarization, but displayed unphysical results when the analyzer direction was rotated. For the elliptically polarized light, α was quite accurate, regardless of the direction of the analyzer. The γ angles were close, with the near-perpendicular analyzer being slightly more accurate, though both deviate from the value measured by the PAX by $\sim 1^\circ$. As shown in Fig. D.7, this may be from an incorrect δ. The DOP in either case are also quite similar, not showing the difference seen for the linear polarization, nor the "super-polarized" light (DOP>100%) also observed with the linear polarization.

To better understand the DOP dependence on analyzer direction,

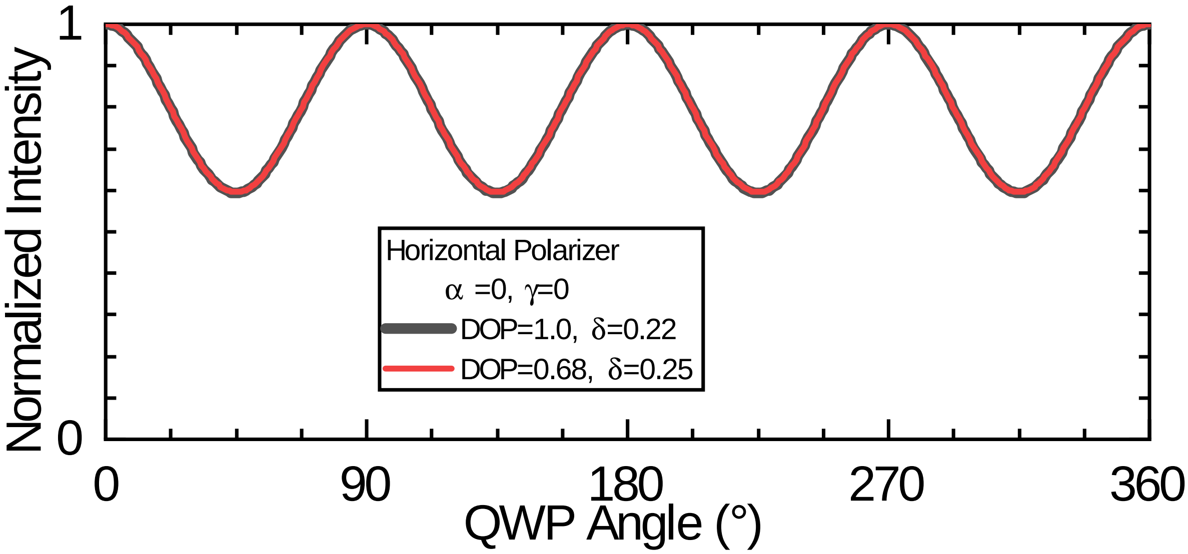

Figure D.10: Calculated normalized polaragrams for linear horizontally polarized light with a horizontal analyzer. Compares perfectly polarized light (DOP=100%) with an imperfect QWP ($\delta = 0.22$) (grey curve) with imperfectly polarized light (DOP=68%) with a perfect QWP ($\delta = 0.25$) (red curve). The two polaragrams are nearly identical.

Figure D.10 shows two different calculated polaragrams. One with perfectly polarized light (DOP=100%) with an imperfect QWP ($\delta = 0.22$) (grey curve), the other imperfectly polarized light (DOP=68%) with a perfect QWP ($\delta = 0.25$) (red curve). When the polaragrams are normalized, as done in standard processing, the two polaragrams are identical due to a degeneracy between DOP and δ for linearly polarized light which is near parallel to the analyzer direction. From this, Fig. D.10 indicates the source of superpolarized light seen for the linearly polarized, near-paralllel analyzer seen in Fig. D.9 is due to an incorrect δ which was assumed to be 0.25. While an accurate measurement of δ would significantly lessen this error, it is only a significant problem for linearly polarized light parallel to the analyzer. When the light is perpendicular, such as the red curve, lower left of Fig. D.9, or elliptically polarized, such as the lower right of Fig. D.9, the

DOP is accurate because the degeneracy no longer exists in these cases. This degeneracy also only exists if a **normalized** polaragram is analyzed. If the absolute intensity is known, the two cases can be separated by normalizing the polagram with respect to the total intensity.

D.5.5 Number of points

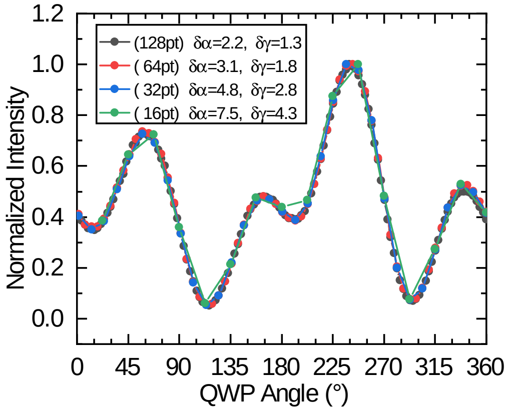

Figure D.11: Polaragrams with increasing amount of sampling. Each curve fully samples the same curve, and the legend shows the errors for each, taken as the covariance of the fits. The asymmetry between the peak heights at 60° and 240° are because the Thorlabs SAQWP was used for this measurement, before its faults were known.

The polaragrams show so far have had 16 points taken. Nyquist's theorem would indicate we only require 8 points, since the highest frequency is 4 "Hz". Figure D.11 shows four different polaragrams of the same elliptically polarized light, but with 16, 32, 64, or 128 points taken. Each of the different number of subsamples well reproduces the underlying curve. The inset shows the error associated with each measurement. Since the error is only the covariance of the fits to Eq. D.5, increasing the points decreases the error since the covariance scales inversely with the number of points. While 8 samples could be taken, 16 was chosen to reduce the errors, while not requiring the high stability from the FEL which would be required for more points. It could be fruitful, however, to drop the number of points and increase the exposure time to get better resolution on sidebands. This has not been fully explored.

D.6 Reference frame

When dealing with polarized light, it is important to distinguish whether the parameters of the polarization ellipse are defined as viewed traveling with the light, or viewing towards the source. The standard right hand rule shows these two differences would result in a sign-flip of γ, as well as α. The PAX defines it by viewing towards the source. Ours measures the opposite polarization state as the PAX, which indicates it measures along the point of view of propagation. The simplest way is to measure he polarization using the PAX, and then measuring with the home-built polarimeter. Without a PAX, it could be checked by setting a polarizer to a known angle, and measuring the polaraization behind it. Note that reversing the rotation direction of the QWP will change which reference frame the measurement is in.

D.7 Potential Improvements

Rounding out this appendix, I want to point out some of the improvements which could be done to better the polarization measurements.

D.7.1 Measuring $\delta(\lambda)$

Section D.5.3 discusses how the retardance of the QWP used in the experiments is currently performed, as well as the issues with it. One of the biggest issues stems from the need to measure vertical and horizontally polarized light, while the spectrometer is polarization sensitive. It could be possible to use a polarization insensitive detector, such as a power meter. Without spectral information, a wavelengths could be measured and values inbetween interpolated. Alternatively, it might be possible to fiber couple the white light used for Eq.D.11, which would scramble the polarization and remove the polarization sensitivity on the spectrometer. However, the white light does not follow the NIR beam path directly, and is not perfectly collimated, which might result in a slightly incorrect retardance. Finally, as noted at the end of Sec. D.5.3, it may be useful to attempt measurements with a zero-order QWP which may be less difficult to work with.

D.7.2 Error Analysis

One of the most poorly developed areas of polarimetery in this work has been on a thorough treatment of errors. The simple solution has been taken by taking the errors from the covariance of fits to Eq. D.5, and propagating those through to α, γ, and DOP. This likely does not fully account for some of the systematic errors which have been discussed here. Figures D.7 and D.9 show deviations of the polarization states measured with a white light from the same state measured for the NIR. Furthermore, Figs. D.7 and D.9 also show that the deviations can depend significantly on the actual polarization, including the rotation angle relative to the analyzer, or the ellipticity, as well as the retardance of the QWP, which is an input to Eq. D.5. These types of errors are not included in the errors from the covariance, which result in an underestimate of the true errors. In the past, errors have been cited as $\delta\alpha = \delta\gamma \approx 2^\circ$ and $\delta\mathrm{DOP} \sim 10\%$, which come from data such as that shown in Figs. D.7 and D.9, where the measurements from the polarimeter can be directly compared to the PAX, which claims an error of $< 0.1^\circ$.

Bibliography

[1] Nikolay I. Agladze, J. Michael Klopf, Gwyn P. Williams, and Albert J. Sievers. Terahertz spectroscopy with a holographic fourier transform spectrometer plus array detector using coherent synchrotron radiation. *Appl. Opt.*, 49(17):3239–3244, Jun 2010.

[2] M. B. Agranat, O. V. Chefonov, A. V. Ovchinnikov, S. I. Ashitkov, V. E. Fortov, and P. S. Kondratenko. Damage in a Thin Metal Film by High-Power Terahertz Radiation. *Physical Review Letters*, 120(8):085704, feb 2018.

[3] J. Appenzeller, Y.-M. Lin, J. Knoch, Z. Chen, and P. Avouris. Comparing Carbon Nanotube TransistorsThe Ideal Choice: A Novel Tunneling Device Design. *IEEE Transactions on Electron Devices*, 52(12):2568–2576, 2005.

[4] Ashish Arora, Maciej Koperski, Karol Nogajewski, Jacques Marcus, Clément Faugeras, and Marek Potemski. Excitonic resonances in thin films of WSe ₂ : from monolayer to bulk material. *Nanoscale*, 7(23):10421–10429, jun 2015.

[5] Ashish Arora, Karol Nogajewski, Maciej Molas, Maciej Koperski, and Marek Potemski. Exciton band structure in layered MoSe ₂ : from a monolayer to the bulk limit. *Nanoscale*, 7(48):20769–20775, dec 2015.

[6] N.W. Ashcroft and N.D. Mermin. *Solid State Physics.* Saunders College, Philadelphia, 1976.

[7] A. G Baca. *Fabrication of GaAs devices.* EMIS processing series ; no. 6. Institution of Engineering and Technology, London, pbk. ed. edition, 2009.

[8] Hunter B. Banks, Andrea Hofmann, Shawn Mack, Arthur C. Gossard, and Mark S. Sherwin. Antenna-boosted mixing of terahertz and near-infrared radiation. *Applied Physics Letters*, 105(9):092102, 2014.

[9] Hunter B. Banks, Qile Wu, Darren C. Valovcin, Shawn Mack, Arthur C. Gossard, Loren Pfeiffer, Ren-Bao Liu, and Mark S. Sherwin. Dynamical birefringence: Electron-hole recollisions as probes of berry curvature. *Phys. Rev. X*, 7:041042, Nov 2017.

[10] Hunter B. Banks, Benjamin Zaks, Fan Yang, Shawn Mack, Arthur C. Gossard, Renbao Liu, and Mark S. Sherwin. Terahertz Electron-Hole Recollisions in GaAs Quantum Wells: Robustness to Scattering by Optical Phonons and Thermal Fluctuations. *Physical Review Letters*, 111(26):267402, dec 2013.

[11] Gerald Bastard. *Wave mechanics applied to semiconductor heterostructures*. Monographies de physique. Les Editions de Physique ; Halsted Press, Les Ulis Cedex, France : New York, N.Y., 1988.

[12] Ray H. Baughman, Anvar A. Zakhidov, and Walt A. de Heer. Carbon Nanotubes: The Route Toward Applications. *Science*, 297(5582):787, 2002.

[13] M. V. Berry. Quantal Phase Factors Accompanying Adiabatic Changes. *Proceedings of the Royal Society A: Mathematical, Physical and Engineering Sciences*, 392(1802):45–57, mar 1984.

[14] Robert W. Boyd. *Nonlinear Optics*. Academic Press, 525 B Street, Suite1900, San Diego, California 92101, 1992.

[15] Federico Brivio, Alison B. Walker, and Aron Walsh. Structural and electronic properties of hybrid perovskites for high-efficiency thin-film photovoltaics from first-principles. *APL Materials*, 1(4):042111, oct 2013.

[16] J. Cerne, J. Kono, T. Inoshita, M. Sherwin, M. Sundaram, and A. C. Gossard. Near-infrared sideband generation induced by intense far-infrared radiation in gaas quantum wells. *Applied Physics Letters*, 70(26):3543–3545, 1997.

[17] Ming-Che Chang and Qian Niu. Berry Phase, Hyperorbits, and the Hofstadter Spectrum. *Physical Review Letters*, 75(7):1348–1351, aug 1995.

[18] Ming-Che Chang and Qian Niu. Berry curvature, orbital moment, and effective quantum theory of electrons in electromagnetic fields. *Journal of Physics: Condensed Matter*, 20(19):193202, may 2008.

[19] Tawinan Cheiwchanchamnangij and Walter R. L. Lambrecht. Quasiparticle band structure calculation of monolayer, bilayer, and bulk MoS 2. *Physical Review B*, 85(20):205302, may 2012.

[20] C. Chen, Y. Lin, C. Chang, P. Yu, J. Shieh, and C. Pan. Frequency-dependent complex conductivities and dielectric responses of indium tin oxide thin films from the visible to the far-infrared. *IEEE Journal of Quantum Electronics*, 46(12):1746–1754, Dec 2010.

[21] A.Y. Cho and J.R. Arthur. Molecular beam epitaxy. *Progress in Solid State Chemistry*, 10:157 – 191, 1975.

[22] R.D. Clayton, I.C. Bassignana, D.A. Macquistan, and C.J. Miner. Scanning birefringence mapping of semi-insulating GaAs wafers. In *Proceedings of the 7th Conference on Semi-insulating III-V Materials,*, pages 211–216. IEEE, 1992.

[23] P. B. Corkum. Plasma perspective on strong field multiphoton ionization. *Phys. Rev. Lett.*, 71:1994–1997, Sep 1993.

[24] P. B. Corkum. Attosecond science. *Springer Series in Optical Sciences*, 177:3–7, 2013.

[25] John H. Davies. *The Physics of Low-dimensional Semiconductors: An Introduction.* Cambridge University Press, 1997.

[26] Stefaan de Wolf, Jakub Holovsky, Soo-Jin Moon, Philipp Löper, Bjoern Niesen, Martin Ledinsky, Franz-josef Haug, Jun-ho Yum, and Christophe Ballif. Organometallic Halide Perovskites: Sharp Optical Absorption Edge and. *The Journal of Physical Chemistry Letters*, 5:1035–139, 2014.

[27] P. Del'Haye, A. Schliesser, O. Arcizet, T. Wilken, R. Holzwarth, and T. J. Kippenberg. Optical frequency comb generation from a monolithic microresonator. *Nature*, 450:1214, Dec 2007.

[28] Scott A. Diddams, David J. Jones, Jun Ye, Steven T. Cundiff, John L. Hall, Jinendra K. Ranka, Robert S. Windeler, Ronald Holzwarth, Thomas Udem, and T. W. Hänsch. Direct link between microwave and optical frequencies with a 300 thz femtosecond laser comb. *Phys. Rev. Lett.*, 84:5102–5105, May 2000.

[29] Valerio D'Innocenzo, Giulia Grancini, Marcelo J. P. Alcocer, Ajay Ram Srimath Kandada, Samuel D. Stranks, Michael M. Lee, Guglielmo Lanzani, Henry J. Snaith, and Annamaria Petrozza. Excitons versus free charges in organo-lead tri-halide perovskites. *Nature Communications*, 5(1):3586, dec 2014.

[30] Giles E. Eperon, Samuel D. Stranks, Christopher Menelaou, Michael B. Johnston, Laura M. Herz, and Henry J. Snaith. Formamidinium lead trihalide: a broadly tunable perovskite for efficient planar heterojunction solar cells. *Energy & Environmental Science*, 7(3):982, feb 2014.

[31] M Ferray, Anne L'Hullier, XF Li, G. Mainfray, and C. Manus. Multiple-harmonic conversion of 1064 nm radiation in rare gases. *Journal of Physics B*, 21, 1988.

[32] Jarvist M. Frost, Keith T. Butler, Federico Brivio, Christopher H. Hendon, Mark van Schilfgaarde, and Aron Walsh. Atomistic Origins of High-Performance in Hybrid Halide Perovskite Solar Cells. *Nano Letters*, 14(5):2584–2590, may 2014.

[33] M. Garg, H. Y. Kim, and E. Goulielmakis. Ultimate waveform reproducibility of extreme-ultraviolet pulses by high-harmonic generation in quartz. *Nature Photonics*, 12(5):291–296, may 2018.

[34] A. K. Geim and I. V. Grigorieva. Van der Waals heterostructures. *Nature*, 499(7459):419–425, jul 2013.

[35] Shambhu Ghimire, Anthony D. DiChiara, Emily Sistrunk, Pierre Agostini, Louis F. DiMauro, and David a. Reis. Observation of high-order harmonic generation in a bulk crystal. *Nature Physics*, 7(2):138–141, 2011.

[36] Shambhu Ghimire and David A. Reis. High-harmonic generation from solids. *Nature Physics*, page 1, nov 2018.

[37] Dennis H. Goldstein. *Polarized Light*. Taylor and Francis Group, Boca Raton, FL, third edition, 2011.

[38] D. Grischkowsky, Søren Keiding, Martin van Exter, and Ch. Fattinger. Far-infrared time-domain spectroscopy with terahertz beams of dielectrics and semiconductors. *J. Opt. Soc. Am. B*, 7(10):2006–2015, Oct 1990.

[39] Feng Hao, Constantinos C. Stoumpos, Duyen Hanh Cao, Robert P. H. Chang, and Mercouri G. Kanatzidis. Lead-free solid-state organicinorganic halide perovskite solar cells. *Nature Photonics*, 8(6):489–494, jun 2014.

[40] Keliang He, Nardeep Kumar, Liang Zhao, Zefang Wang, Kin Fai Mak, Hui Zhao, and Jie Shan. Tightly Bound Excitons in Monolayer WSe 2. *Physical Review Letters*, 113(2):026803, jul 2014.

[41] Xiaowei He, Weilu Gao, Lijuan Xie, Qi Zhang, Sidong Lei, Bo Li, John M Robinson, Stephen K Doorn, Robert Vajtai, Pulickel M Ajayan, and W Wade Adams. Wafer-scale monodomain films of spontaneously-aligned single-wall carbon nanotubes. *Nature Nanotechnology*, 11(April):1–21, 2016.

[42] Laura M. Herz. Charge Carrier Dynamics in Organic-Inorganic Metal Halide Perovskites. *Annual Review of Physical Chemistry*, 67:1–26, 2016.

[43] Takuya Higuchi, Mark I. Stockman, and Peter Hommelhoff. Strong-Field Perspective on High-Harmonic Radiation from Bulk Solids. *Physical Review Letters*, 113(21):213901, nov 2014.

[44] M. Hirasawa, T. Ishihara, T. Goto, K. Uchida, and N. Miura. Magnetoabsorption of the lowest exciton in perovskite-type compound (CH3NH3)PbI3. *Physica B: Condensed Matter*, 201:427–430, jul 1994.

[45] J Hone, M Whitney, C Piskoti, and A Zettl. Thermal conductivity of single-walled carbon nanotubes J. 59(4):2514–2516, 1999.

[46] Pei-Chi Huang, Carlos Hernández-García, Jen-Ting Huang, Po-Yao Huang, Chih-Hsuan Lu, Laura Rego, Daniel D. Hickstein, Jennifer L. Ellis, Agnieszka Jaron-Becker, Andreas Becker, Shang-Da Yang, Charles G. Durfee, Luis Plaja, Henry C. Kapteyn, Margaret M. Murnane, A. H. Kung, and Ming-Chang Chen. Polarization control of isolated high-harmonic pulses. *Nature Photonics*, 12(6):349–354, jun 2018.

[47] Ulrich Huttner, Mackillo Kira, and Stephan W. Koch. Ultrahigh Off-Resonant Field Effects in Semiconductors. *Laser & Photonics Reviews*, 11(4):1700049, jul 2017.

[48] John David Jackson. *Classical electrodynamics.* Wiley, New York, NY, 3rd ed. edition, 1999.

[49] Aaron M. Jones, Hongyi Yu, Nirmal J. Ghimire, Sanfeng Wu, Grant Aivazian, Jason S. Ross, Bo Zhao, Jiaqiang Yan, David G. Mandrus, Di Xiao, Wang Yao, and Xiaodong Xu. Optical generation of excitonic valley coherence in monolayer WSe2. *Nature Nanotechnology*, 8(9):634–638, sep 2013.

[50] J. P. Kaminski, J. S. Spector, C. L. Felix, D. P. Enyeart, D. T. White, and G. Ramian. Far-infrared cavity dump coupling of the UC Santa Barbara free-electron laser. *Applied Physics Letters*, 57(26):2770, 1990.

[51] Henry C. Kapteyn, Margaret M. Murnane, and Ivan P. Christov. Extreme Nonlinear Optics: Coherent X rays from Lasers. *Physics Today*, 58(3):39–46, mar 2005.

[52] H Kataura. Optical Properties of Single-Wall Carbon Nanotubes. 103:1–4, 1999.

[53] L. V. Keldysh. Ionization in the field of a string electromagnetic wave. *Journal of Experimental and Theoretical Physics*, 20(5):1307–1314, 1965.

[54] Jungwon Kim and Youjian Song. Ultralow-noise mode-locked fiber lasers and frequency combs: principles, status, and applications. *Adv. Opt. Photon.*, 8(3):465–540, Sep 2016.

[55] Claus Klingshirn. *Semiconductor Optics.* Springer Berlin Heidelberg, Berlin, Heidelberg, third edition edition, 2007.

[56] J. Kono, M. Y. Su, T. Inoshita, T. Noda, M. S. Sherwin, S. J. Allen, Jr., and H. Sakaki. Resonant terahertz optical sideband generation from confined magnetoexcitons. *Phys. Rev. Lett.*, 79:1758–1761, Sep 1997.

[57] Jeffrey L. Krause, Kenneth J. Schafer, and Kenneth C. Kulander. High-order harmonic generation from atoms and ions in the high intensity regime. *Phys. Rev. Lett.*, 68:3535–3538, Jun 1992.

[58] Ferenc Krausz and Misha Ivanov. Attosecond physics. *Reviews of Modern Physics*, 81(1):163–234, feb 2009.

[59] F. Langer, M. Hohenleutner, U. Huttner, S. W. Koch, M. Kira, and R. Huber. Symmetry-controlled temporal structure of high-harmonic carrier fields from a bulk crystal. *Nature Photonics*, 11(March):1–6, mar 2017.

[60] F. Langer, M. Hohenleutner, C. P. Schmid, C. Poellmann, P. Nagler, T. Korn, C. Schüller, M. S. Sherwin, U. Huttner, J. T. Steiner, S. W. Koch, M. Kira, and R. Huber. Lightwave-driven quasiparticle collisions on a subcycle timescale. *Nature*, 533:225, May 2016.

[61] F. Langer, C. P. Schmid, S. Schlauderer, M. Gmitra, J. Fabian, P. Nagler, C. Schüller, T. Korn, P. G. Hawkins, J. T. Steiner, U. Huttner, S. W. Koch, M. Kira, and R. Huber. Lightwave valleytronics in a monolayer of tungsten diselenide. *Nature*, 557(7703):76–80, 2018.

[62] J Lefebvre, J M Fraser, P Finnie, and Y Homma. Photoluminescence from an individual single-walled carbon nanotube. *Phys. Rev. B*, 69(7):–, 2004.

[63] M. Lewenstein, Ph. Balcou, M. Yu. Ivanov, Anne L'Huillier, and P. B. Corkum. Theory of high-harmonic generation by low-frequency laser fields. *Phys. Rev. A*, 49:2117–2132, Mar 1994.

[64] Yilei Li, Alexey Chernikov, Xian Zhang, Albert Rigosi, Heather M. Hill, Arend M. van der Zande, Daniel A. Chenet, En-Min Shih, James Hone, and Tony F. Heinz. Measurement of the optical dielectric function of monolayer transition-metal dichalcogenides: MoS 2 , Mo S e 2 , WS 2 , and WS e 2. *Physical Review B*, 90(20):205422, nov 2014.

[65] Qianqian Lin, Ardalan Armin, Ravi Chandra Raju Nagiri, Paul L. Burn, and Paul Meredith. Electro-optics of perovskite solar cells. *Nature Photonics*, 9(2):106–112, 2015.

[66] Hanzhe Liu, Yilei Li, Yong Sing You, Shambhu Ghimire, Tony F Heinz, and David A Reis. High-harmonic generation from an atomically thin semiconductor. *Nature Physics*, 1(November):2–4, 2016.

[67] RenBao Liu and BangFen Zhu. Highorder thzsideband generation in semiconductors. *AIP Conference Proceedings*, 893(1):1455–1456, 2007.

[68] J. J. Macklin, J. D. Kmetec, and C. L. Gordon. High-order harmonic generation using intense femtosecond pulses. *Phys. Rev. Lett.*, 70:766–769, Feb 1993.

[69] Kin Fai Mak, Changgu Lee, James Hone, Jie Shan, and Tony F. Heinz. Atomically Thin MoS 2 : A New Direct-Gap Semiconductor. *Physical Review Letters*, 105(13):136805, sep 2010.

[70] C. M. N. Mateo, J. J. Ibañez, J. G. Fernando, J. C. Garcia, K. Omambac, R. B. Jaculbia, M. Defensor, and A. A. Salvador. Transitions of epitaxially lifted-off bulk GaAs and GaAs/AlGaAs quantum well under thermal-induced compressive and tensile strain. *Journal of Applied Physics*, 104(10):103537, nov 2008.

[71] Cherry May N. Mateo, Alipio T. Garcia, Flo Rykiel M. Ramos, Kristine I. Manibog, and Arnel A. Salvador. Strain-induced splitting of the valence band in epitaxially lifted-off GaAs films. *Journal of Applied Physics*, 101(7):073519, apr 2007.

[72] David P McMeekin, Golnaz Sadoughi, Waqaas Rehman, Giles E Eperon, Michael Saliba, Maximilian T Hörantner, Amir Haghighirad, Nobuya Sakai, Lars Korte, Bernd Rech, Michael B Johnston, Laura M Herz, and Henry J Snaith. A mixed-cation lead mixed-halide perovskite absorber for tandem solar cells. *Science (New York, N.Y.)*, 351(6269):151–5, jan 2016.

[73] A. McPherson, G. Gibson, H. Jara, U. Johann, T. S. Luk, I. A. McIntyre, K. Boyer, and C. K. Rhodes. Studies of multiphoton production of vacuum-ultraviolet radiation in the rare gases. *Journal of the Optical Society of America B*, 4(4):595, apr 1987.

[74] M Meckel, D Comtois, D Zeidler, A Staudte, D Pavicic, H C Bandulet, H Pépin, J C Kieffer, R Dörner, D M Villeneuve, and P B Corkum. Laser-induced electron tunneling and diffraction. *Science (New York, N.Y.)*, 320(5882):1478–82, jun 2008.

[75] E. Menéndez-Proupin, P. Palacios, P. Wahnón, and J. C. Conesa. Self-consistent relativistic band structure of the CH3 NH3 PbI3 perovskite. *Physical Review B - Condensed Matter and Materials Physics*, 90(4):1–7, 2014.

[76] J. Mintmire and C. White. Universal Density of States for Carbon Nanotubes. *Physical Review Letters*, 81(12):2506–2509, 1998.

[77] K Miyazaki and H Sakai. High-order harmonic generation in rare gases with intense subpicosecond dye laser pulses. *Journal of Physics B: Atomic, Molecular and Optical Physics*, 25(3):L83, 1992.

[78] H. Murata, A. Morimoto, T. Kobayashi, and S. Yamamoto. Optical pulse generation by electrooptic-modulation method and its application to integrated ultrashort pulse generators. *IEEE Journal of Selected Topics in Quantum Electronics*, 6(6):1325–1331, 2000.

[79] M. T. Murphy, Th. Udem, R. Holzwarth, A. Sizmann, L. Pasquini, C. Araujo-Hauck, H. Dekker, S. D'Odorico, M. Fischer, T. W. Hnsch, and A. Manescau. High-precision wavelength calibration of astronomical spectrographs with laser frequency combs. *Monthly Notices of the Royal Astronomical Society*, 380(2):839–847, 2007.

[80] Nathan R. Newbury. Searching for applications with a fine-tooth comb. *Nature Photonics*, 5:186, Mar 2011.

[81] Jun Hong Noh, Sang Hyuk Im, Jin Hyuck Heo, Tarak N. Mandal, and Sang Il Seok. Chemical management for colorful, efficient, and stable inorganic-organic hybrid nanostructured solar cells. *Nano Letters*, 13(4):1764–1769, 2013.

[82] K S Novoselov, A Mishchenko, A Carvalho, and A H Castro Neto. 2D materials and van der Waals heterostructures. *Science (New York, N.Y.)*, 353(6298):aac9439, jul 2016.

[83] Edward D. Palik. References, 1998.

[84] Alessia Pasquazi, Marco Peccianti, Luca Razzari, David J. Moss, Stphane Coen, Miro Erkintalo, Yanne K. Chembo, Tobias Hansson, Stefan Wabnitz, Pascal Del-Haye, Xiaoxiao Xue, Andrew M. Weiner, and Roberto Morandotti. Micro-combs: A novel generation of optical sources. *Physics Reports*, 729:1 – 81, 2018. Micro-combs: A novel generation of optical sources.

[85] Vasili Perebeinos, J. Tersoff, and Phaedon Avouris. Scaling of Excitons in Carbon Nanotubes. *Physical Review Letters*, 92(25):257402, jun 2004.

[86] C. Poellmann, P. Steinleitner, U. Leierseder, P. Nagler, G. Plechinger, M. Porer, R. Bratschitsch, C. Schüller, T. Korn, and R. Huber. Resonant internal quantum transitions and femtosecond radiative decay of excitons in monolayer WSe2. *Nature Materials*, 14(9):889–893, sep 2015.

[87] R. Pomraenke, J. Maultzsch, S. Reich, E. Chang, D. Prezzi, A. Ruini, E. Molinari, M. S. Strano, C. Thomsen, and C. Lienau. Two-photon photoluminescence and exciton binding energies in single-walled carbon nanotubes. *Physica Status Solidi (B) Basic Research*, 243(10):2428–2435, 2006.

[88] F Quinlan, S Ozharar, S Gee, and P J Delfyett. Harmonically mode-locked semiconductor-based lasers as high repetition rate ultralow noise pulse train and optical frequency comb sources. *Journal of Optics A: Pure and Applied Optics*, 11(10):103001, 2009.

[89] Ashwin Ramasubramaniam. Large excitonic effects in monolayers of molybdenum and tungsten dichalcogenides. *Physical Review B*, 86(11):115409, sep 2012.

[90] Gerald Ramian. The new UCSB free-electron lasers. *Nuclear Instruments and Methods in Physics Research Section A: Accelerators, Spectrometers, Detectors and Associated Equipment*, 318(1-3):225–229, jul 1992.

[91] J. Reintjes, Chiao-Yao She, and R. Eckardt. Generation of coherent radiation in XUV by fifth- and seventh-order frequency conversion in rare gases. *IEEE Journal of Quantum Electronics*, 14(8):581–596, aug 1978.

[92] Raffaele Resta. Electrical polarization and orbital magnetization: the modern theories. *Journal of Physics: Condensed Matter*, 22(12):123201, mar 2010.

[93] Jason S. Ross, Sanfeng Wu, Hongyi Yu, Nirmal J. Ghimire, Aaron M. Jones, Grant Aivazian, Jiaqiang Yan, David G. Mandrus, Di Xiao, Wang Yao, and Xiaodong Xu. Electrical control of neutral and charged excitons in a monolayer semiconductor. *Nature Communications*, 4(1):1474, dec 2013.

[94] J. J. Sakurai and Jim Napolitano. *Modern Quantum Mechanics*. Cambridge University Press, 2 edition, 2017.

[95] H. Shen, M. Wraback, J. Pamulapati, P. G. Newman, M. Dutta, Y. Lu, and H. C. Kuo. Optical anisotropy in GaAs/AlxGa1-xAs multiple quantum wells under thermally induced uniaxial strain. *Physical Review B*, 47(20):13933–13936, may 1993.

[96] Y. R. Shen. *The Principles of Nonlinear Optics*. Wiley, 1984.

[97] J. Sólyom. *Fundamentals of the Physics of Solids: Volume III: Normal, Broken-Symmetry, and Correlated Systems*. Fundamentals of the Physics of Solids. Springer Berlin Heidelberg, 2010.

[98] Catalin D. Spataru, Sohrab Ismail-Beigi, Lorin X. Benedict, and Steven G. Louie. Excitonic Effects and Optical Spectra of Single-Walled Carbon Nanotubes Catalin. *Physical Review Letters*, 92(7), 2004.

[99] Tilo Steinmetz, Tobias Wilken, Constanza Araujo-Hauck, Ronald Holzwarth, Theodor W Hänsch, Luca Pasquini, Antonio Manescau, Sandro D'Odorico, Michael T Murphy, Thomas Kentischer, Wolfgang Schmidt, and Thomas Udem. Laser frequency combs for astronomical observations. *Science (New York, N.Y.)*, 321(5894):1335–7, sep 2008.

[100] Susumu Takahashi, Dan G. Allen, Jason Seifter, Gerald Ramian, Mark S. Sherwin, Louis-Claude Brunel, and Johan van Tol. Pulsed epr spectrometer with injection-locked ucsb free-electron laser. *Infrared Physics & Technology*, 51(5):426 – 428, 2008. 4th International Workshop on Infrared Microscopy and Spectroscopy with Accelerator-Based Sources.

[101] Susumu Takahashi, Gerald Ramian, and Mark S. Sherwin. Cavity dumping of an injection-locked free-electron laser. *Applied Physics Letters*, 95(23):234102, 2009.

[102] Zhi-Kuang Tan, Reza Saberi Moghaddam, May Ling Lai, Pablo Docampo, Ruben Higler, Felix Deschler, Michael Price, Aditya Sadhanala, Luis M. Pazos, Dan Credgington, Fabian Hanusch, Thomas Bein, Henry J. Snaith, and Richard H. Friend. Bright light-emitting diodes based on organometal halide perovskite. *Nature Nanotechnology*, 9(9):687–692, sep 2014.

[103] Kenichiro Tanaka, Takayuki Takahashi, Takuma Ban, Takashi Kondo, Kazuhito Uchida, and Noboru Miura. Comparative study on the excitons in lead-halide-based perovskite-type crystals CH3NH3PbBr3 CH3NH3PbI3. *Solid State Communications*, 127(9-10):619–623, sep 2003.

[104] Nicolas Tancogne-Dejean, Oliver D. Mücke, Franz X. Kärtner, and Angel Rubio. Impact of the electronic band structure in high-harmonic generation spectra of solids. *Physical Review Letters*, 118(8):1–6, feb 2016.

[105] Sefaattin Tongay, Joonki Suh, Can Ataca, Wen Fan, Alexander Luce, Jeong Seuk Kang, Jonathan Liu, Changhyun Ko, Rajamani Raghunathanan, Jian Zhou, Frank Ogletree, Jingbo Li, Jeffrey C. Grossman, and Junqiao Wu. Defects activated photoluminescence in two-dimensional semiconductors: interplay between bound, charged and free excitons. *Scientific Reports*, 3(1):2657, dec 2013.

[106] Victor Torres-Company and Andrew M. Weiner. Optical frequency comb technology for ultra-broadband radio-frequency photonics. *Laser & Photonics Reviews*, 8(3):368–393, 2014.

[107] Th Udem, R. Holzwarth, and T. W. Hänsch. Optical frequency metrology. *Nature*, 416:233, Mar 2002.

[108] Miguel M. Ugeda, Aaron J. Bradley, Su-Fei Shi, Felipe H. da Jornada, Yi Zhang, Diana Y. Qiu, Wei Ruan, Sung-Kwan Mo, Zahid Hussain, Zhi-Xun Shen, Feng Wang, Steven G. Louie, and Michael F. Crommie. Giant bandgap renormalization and excitonic effects in a monolayer transition metal dichalcogenide semiconductor. *Nature Materials*, 13(12):1091–1095, dec 2014.

[109] Darren C. Valovcin, Hunter B. Banks, Shawn Mack, Arthur C. Gossard, Kenneth West, Loren Pfeiffer, and Mark S. Sherwin. Optical frequency combs from high-order sideband generation. *Opt. Express*, 26(23):29807–29816, Nov 2018.

[110] David A. Valverde-Chávez, Carlito S. Ponseca, Constantinos C. Stoumpos, Arkady Yartsev, Mercouri G. Kanatzidis, Villy Sundström, and David G. Cooke. Intrinsic femtosecond charge generation dynamics in single crystal CH 3 NH 3 PbI 3. *Energy Environ. Sci.*, 8(12):3700–3707, 2015.

[111] G. Vampa, C. R. McDonald, G. Orlando, P. B. Corkum, and T. Brabec. Semiclassical analysis of high harmonic generation in bulk crystals. *Physical Review B*, 91(6):064302, feb 2015.

[112] J. P. van der Ziel and A. C. Gossard. Absorption, refractive index, and birefringence of AlAsGaAs monolayers. *Journal of Applied Physics*, 48(7):3018–3023, jul 1977.

[113] David Vanderbilt. *Berry Phases in Electronic Structure Theory: Electric Polarization, Orbital Magnetization and Topological Insulators.* Cambridge University Press, 2018.

[114] F. Wang, G. Dukovic, L. E. Brus, and T. F. Heinz. The Optical Resonances in Carbon. *Science*, 308(May):838–841, 2005.

[115] G. Wang, L. Bouet, D. Lagarde, M. Vidal, A. Balocchi, T. Amand, X. Marie, and B. Urbaszek. Valley dynamics probed through charged and neutral exciton emission in monolayer WSe 2. *Physical Review B*, 90(7):075413, aug 2014.

[116] Qing Hua Wang, Kourosh Kalantar-Zadeh, Andras Kis, Jonathan N. Coleman, and Michael S. Strano. Electronics and optoelectronics of two-dimensional transition metal dichalcogenides. *Nature Nanotechnology*, 7(11):699–712, nov 2012.

[117] A.M. Weiner, A.J. Metcalf, S.A. Diddams, T.M. Fortier, and F. Quinlan. Broadly tunable, low timing jitter, high repetition rate optoelectronic comb generator. *Electronics Letters*, 51(20):1596–1598, oct 2015.

[118] Claude Weisbuch and Borge Vinter. *Quantum Semiconductor Structures*. Academic Press, San Diego, 1991.

[119] R. Bruce Weisman and Sergei M. Bachilo. Dependence of optical transition energies on structure for single-walled carbon nanotubes in aqueous suspension: An empirical Kataura plot. *Nano Letters*, 3(9):1235–1238, 2003.

[120] J. Wildenauer. Generation of the ninth, eleventh, and fifteenth harmonics of iodine laser radiation. *Journal of Applied Physics*, 62(1):41–48, jul 1987.

[121] Morten Willatzen and Lok Lew-Yan-Voon. *The k p method*. Springer, New York, NY, 2009.

[122] Q. Wu and X.C. Zhang. Freespace electrooptic sampling of terahertz beams. *Applied Physics Letters*, 67(24):3523–3525, 1995.

[123] Di Xiao, Ming Che Chang, and Qian Niu. Berry phase effects on electronic properties. *Reviews of Modern Physics*, 82(3):1959–2007, 2010.

[124] Xiao-Tao Xie, Bang-Fen Zhu, and Ren-Bao Liu. Effects of excitation frequency on high-order terahertz sideband generation in semiconductors. *New Journal of Physics*, 15(10):105015, 2013.

[125] Jie-Yun Yan. Theory of excitonic high-order sideband generation in semiconductors under a strong terahertz field. *Phys. Rev. B*, 78:075204, Aug 2008.

[126] Jie Yun Yan. Theory of excitonic high-order sideband generation in semiconductors under a strong terahertz field. *Physical Review B - Condensed Matter and Materials Physics*, 78:1–7, 2008.

[127] Jun Ye and Steven T. Cundiff (Eds.). *Femtosecond Optical Frequency Comb: Principle, Operation and Applications*. Springer, New York, NY, 1 edition, 2005.

[128] X. Yi, N. K. Fontaine, R. P. Scott, and S. J. B. Yoo. Tb/s coherent optical ofdm systems enabled by optical frequency combs. *Journal of Lightwave Technology*, 28(14):2054–2061, 2010.

[129] Yong Sing You, Jian Lu, Eric F. Cunningham, Christian Roedel, and Shambhu Ghimire. Crystal orientation-dependent polarization state of high-order harmonics. *Optics Letters*, 44(3):530, feb 2019.

[130] Peter Yu and Manuel Cardona. *Fundamentals of Semiconductors*. Springer, New York, NY, 2010.

[131] Long Yuan, Ti Wang, Tong Zhu, Mingwei Zhou, and Libai Huang. Exciton Dynamics, Transport, and Annihilation in Atomically Thin Two-Dimensional Semiconductors. *The Journal of Physical Chemistry Letters*, 8(14):3371–3379, jul 2017.

[132] B. Zaks, H. Banks, and M. S. Sherwin. High-order sideband generation in bulk gaas. *Applied Physics Letters*, 102(1):012104, 2013.

[133] B. Zaks, R. B. Liu, and M. S. Sherwin. Experimental observation of electron-hole recollisions. *Nature*, 483:580, Mar 2012.

[134] Benjamin Zaks, James Heyman, Dominik Stehr, Dan Allen, Nelson Coates, and Mark Sherwin. Single Shot High Resolution THz Upconversion Spectrometer. In *2008 33RD INTERNATIONAL CONFERENCE ON INFRARED, MILLIMETER AND TERAHERTZ WAVES, VOLS 1 AND 2*, pages 749+, 345 E 47TH ST, NEW YORK, NY 10017 USA, 2008. IEEE, IEEE. 33rd International Conference on Infrared, Millimeter and Terahertz Waves, Pasadena, CA, SEP 15-19, 2008.

[135] Benjamin R. Zaks. *Nonlinear Exciton Dynamics in InGaAs Quantum Wells*. PhD thesis, University of California, Santa Barbara, 2012. Copyright - Database copyright ProQuest LLC; ProQuest does not claim copyright in the individual underlying works; Last updated - 2016-03-11.

[136] A. Zangwill. *Modern Electrodynamics*. Modern Electrodynamics. Cambridge University Press, 2013.

[137] Hongbo Zhao and Sumit Mazumdar. Electron-electron interaction effects on the optical excitations of semiconducting single-walled carbon nanotubes. *Physical Review Letters*, 93(15):8–11, 2004.

[138] Weijie Zhao, Zohreh Ghorannevis, Leiqiang Chu, Minglin Toh, Christian Kloc, Ping-Heng Tan, and Goki Eda. Evolution of Electronic Structure in Atomically Thin Sheets of WS2 and WSe2. *ACS Nano*, 7(1):791–797, jan 2013.

[139] Bairen Zhu, Xi Chen, and Xiaodong Cui. Exciton Binding Energy of Monolayer WS2. *Scientific Reports*, 5(1):9218, aug 2015.

[140] Ayan A. Zhumekenov, Makhsud I. Saidaminov, Md Azimul Haque, Erkki Alarousu, Smritakshi Phukan Sarmah, Banavoth Murali, Ibrahim Dursun, Xiao-He Miao, Ahmed L. Abdelhady, Tom Wu, Omar F. Mohammed, and Osman M. Bakr. Formamidinium Lead Halide Perovskite Crystals with Unprecedented Long Carrier Dynamics and Diffusion Length. *ACS Energy Letters*, 1(1):32–37, jul 2016.